A UAV-BASED VNIR/SWIR MULTISPECTRAL MULTI-CAMERA SYSTEM FOR MONITORING VEGETATION

Development, Application and Evaluation on Agricultural Systems

Inaugural-Dissertation
zur
Erlangung des Doktorgrades
der Mathematisch-Naturwissenschaftlichen Fakultät
der Universität zu Köln

Vorgelegt von
Alexander Gerhard Josef Jenal
aus Saarlouis

Köln 2022

Berichterstatter:	Prof. Dr. Georg Bareth
	Prof. Dr. Karl Schneider
	Prof. Dr. Jens Bongartz
	Prof. Dr. Uwe Rascher
Tag der mündlichen Prüfung:	04.05.2022

Nothing is more conducive to creativity than spending a boring ten-hour intercontinental flight with a pen and a cocktail napkin.

— ANECDOTE —

Erklärung

(gemäß der Promotionsordnung vom 12. März 2020)

Hiermit versichere ich an Eides statt, dass ich die vorliegende Dissertation selbstständig und ohne die Benutzung anderer als der angegebenen Hilfsmittel und Literatur angefertigt habe. Alle Stellen, die wörtlich oder sinngemäß aus veröffentlichten und nicht veröffentlichten Werken dem Wortlaut oder dem Sinn nach entnommen wurden, sind als solche kenntlich gemacht. Ich versichere an Eides statt, dass diese Dissertation noch keiner anderen Fakultät oder Universität zur Prüfung vorgelegen hat; dass sie—abgesehen von unten angegebenen Teilpublikationen und eingebundenen Artikeln und Manuskripten—noch nicht veröffentlicht worden ist sowie, dass ich eine Veröffentlichung der Dissertation vor Abschluss der Promotion nicht ohne Genehmigung des Promotionsausschusses vornehmen werde. Die Bestimmungen dieser Ordnung sind mir bekannt. Darüber hinaus erkläre ich hiermit, dass ich die Ordnung zur Sicherung guter wissenschaftlicher Praxis und zum Umgang mit wissenschaftlichem Fehlverhalten der Universität zu Köln gelesen und sie bei der Durchführung der Dissertation zugrundeliegenden Arbeiten und der schriftlich verfassten Dissertation beachtet habe und verpflichte mich hiermit, die dort genannten Vorgaben bei allen wissenschaftlichen Tätigkeiten zu beachten und umzusetzen. Ich versichere, dass die eingereichte elektronische Fassung der eingereichten Druckfassung vollständig entspricht.

Folgende Teilpublikationen liegen vor:

Jenal, A., Bareth, G., Bolten, A., Kneer, C., Weber, I., & Bongartz, J. (2019). Development of a VNIR/SWIR Multispectral Imaging System for Vegetation Monitoring with Unmanned Aerial Vehicles. *Sensors*, 19(24), 5507. `https://doi.org/10.3390/s19245507`

Jenal, A., Lussem, U., Bolten, A., Gnyp, M. L., Schellberg, J., Jasper, J., Bongartz, J., & Bareth, G. (2020). Investigating the Potential of a Newly Developed UAV-based VNIR/SWIR Imaging System for Forage Mass Monitoring. *PFG – Journal of Photogrammetry, Remote Sensing and Geoinformation Science*, 88(5), 493–507. `https://doi.org/10.1007/s41064-020-00128-7`

Jenal, A., Hüging, H., Ahrends, H. E., Bolten, A., Bongartz, J., & Bareth, G. (2021). Investigating the Potential of a Newly Developed UAV-Mounted VNIR/SWIR Imaging System for Monitoring Crop Traits—A Case Study for Winter Wheat. *Remote Sensing*, 13(9), 1697. `https://doi.org/10.3390/rs13091697`

Die Bedeutung der Publikationen im Zusammenhang mit dieser Dissertation ist in Abschnitt 1.3 erläutert. Der Eigenanteil an den Publikationen ist wesentlich und in den Anhängen A, B und C detailliert aufgeführt. Die in der Dissertation verwendeten Primär- und Analysedaten sowie die zur Auswertung notwendigen Skripte werden am Geographischen Institut der Universität zu Köln auf Servern der AG GIS & Fernerkundung vorgehalten und können bei Bedarf eingesehen werden.

Köln, den 26. Mai 2022

Alexander Jenal

Abstract

A growing world population with limited or even declining resources and intensifying climate change are putting increasing pressure on global food production and, in particular, on the agricultural sector. Driven by technological innovations, precision agriculture, and smart farming are upcoming management strategies essential for counteracting these negative impacts. Both trends aim to use site-specific management practices to selectively account for multifaceted plant variability within croplands to maximize yields with minimal inputs, which should also lead to more sustainable agricultural management practices. However, since one cannot manage what one cannot measure, timely information on current in-field conditions is of the utmost importance for effectively implementing these agronomic management strategies.

In this regard, optical remote sensing systems based on unmanned aerial vehicles (UAVs) can significantly contribute to airborne spectral vegetation analysis of small and medium-sized agricultural areas, both in research and in agricultural applications. Specifically, multispectral multi-camera systems are often used to acquire spectral image data sets for deriving established vegetation indices (VIs), which are then used as the basis for non-destructive estimation of specific crop traits to support—for example, site-specific crop management decisions in precision agriculture. These imaging systems can be effortlessly integrated into various UAV systems, and the spectral image data obtained has a high spatial resolution. Furthermore, these acquired data sets can be processed in photogrammetric workflows to derive spectral orthomosaics and 3D structural information. However, these commercial or experimental systems consist exclusively of multiple silicon-based image sensors. Moreover, they are in most cases self-contained and not adaptable to different applications, thus limiting their spectral resolution to a small number of primarily broad spectral bands in the visible (VIS) and near-infrared (NIR) domain (400 to 1000 nm).

However, these multi-camera systems do not cover the short-wave infrared (SWIR) range from 1000 to 1700 nm, which contains crucial spectral absorption features related to biomass, water, and biochemical leaf constituents such as lignin, starch, and nitrogen (N). Furthermore, as observed in hyperspectral imaging applications, there is already a need for narrowband SWIR imaging, especially with the more feasible UAV-based multispectral multi-camera systems. Their application in agricultural systems, with adapted spectral sensitivity in the SWIR, would be ideal for detecting site-specific, subtle spectral vegetation features in high spatial resolution. Similarly, for multispectral Earth observation satellite missions, the SWIR has minimal, still very broadband, coverage with spatial resolutions unsuitable for site-specific applications or phenotyping, resulting in a spatial and spectral sampling gap in this area. Similarly, hyperspectral missions that could compensate, at least, for this spectral shortfall, are currently only on a limited scale operational and also have lower ground resolution.

Thus, to detect light of the (SWIR) domain, a different sensor type—namely, one based on the semiconductor material InGaAs—is required. However, until recently, these sensors were not performant enough to be incorporated into miniaturized camera modules. In addition, due to technical limitations, InGaAs sensors were comparatively expensive compared to their silicon counterparts. However, these shortfalls have improved and therefore, this research (1) developed a UAV-based 2D imaging prototype of a narrowband two-channel multispectral multi-camera system, based on InGaAs sensors, with a spectral response from VIS to SWIR (approximately 600 nm to 1700 nm) and (2) evaluated the potential of this camera system prototype for estimating crop traits of two different agricultural vegetation types from the acquired spectral image data sets. These outcomes were accomplished through the objectives pursued in the context of three peer-reviewed studies published in scientific journals.

The first study focused on the development process, including selecting dedicated parts for the optical components, suitable InGaAs camera sensor modules, and a powerful computing unit. Interchangeable filter assemblies have been developed to acquire a freely selectable narrow wavelength band with each integrated sensor. Two options for this critical part were implemented and tested for suitability to be operated in the system's optical path. Subsequently, several custom mechanical and electronic components were designed and fabricated to build the integrated multi-camera system. Finally, successful tests of the individual components and the overall system in a climate chamber and an integrating sphere in a spectral laboratory, as well as an initial test flight, completed the overall development process.

The subsequent two case studies evaluated the potential of the newly developed SWIR-based multi-camera system for estimating vegetation traits in a permanent grassland field trial and a winter wheat field trial. For this purpose, two established SWIR-based VIs were selected: the two-band normalized ratio index (NRI) and the four-band GnyLi index. The data collection took place in one flight campaign for each experimental field to acquire four spectral image datasets per trial with two UAV flights in direct succession. The resulting reflectance data sets were processed into orthomosaics for each wavelength band. The GnyLi and NRI VIs were then derived from these orthomosaics and further analyzed for their estimation accuracy in bivariate regression models using trial-specific spectral and destructively sampled ground truth data.

In summary, it was concluded that the findings of both case studies confirmed the camera system's presumed performance from the initial tests in the first study. The overall aim of developing and evaluating the narrowband VNIR/SWIR multispectral multi-camera system for UAV-based vegetation monitoring was thus successfully achieved. The derived VIs from spectral image data acquired by the camera system reached high accuracies in estimating dry matter yield in permanent grassland (R^2: 0.73–0.75) and fresh biomass, dry biomass, moisture content, N concentration, and N uptake in winter wheat (R^2: 0.81–0.87). Further multi-temporal and multi-annual investigations with refined analysis methods should be carried out to confirm the findings in this thesis. As a result, this more in-depth research could further evaluate and optimize the SWIR-based multi-camera system for potential use in application-specific UAV-based monitoring applications in the context of precision agriculture.

Kurzfassung

Eine wachsende Weltbevölkerung bei begrenzten oder sogar abnehmenden Ressourcen und der sich verschärfende Klimawandel setzen die weltweite Nahrungsmittelproduktion und insbesondere den Agrarsektor zunehmend unter Druck. Angetrieben durch technologische Innovationen sind Präzisionslandwirtschaft und Smart Farming aufkommende Managementstrategien, die diesen negativen Auswirkungen entgegenwirken sollen. Beide Trends zielen darauf ab, standortspezifische Bewirtschaftungspraktiken einzusetzen, um die vielfältigen pflanzlichen Variabilitäten innerhalb der Anbauflächen selektiv zu berücksichtigen und die Erträge mit minimalem Einsatz zu maximieren, was auch zu nachhaltigeren landwirtschaftlichen Bewirtschaftungspraktiken führen soll. Da man jedoch nicht managen kann, was man nicht messen kann, sind zeitnahe Informationen über die aktuellen Feldbedingungen von größter Bedeutung für die wirksame Umsetzung dieser agronomischen Managementstrategien.

In diesem Zusammenhang können optische Fernerkundungssysteme auf der Basis unbemannter Luftfahrzeuge (UAVs) einen wichtigen Beitrag zur luftgestützten spektralen Vegetationsanalyse kleiner und mittelgroßer landwirtschaftlicher Flächen leisten, sowohl in der Forschung als auch in landwirtschaftlichen Anwendungen. Insbesondere multispektrale Mehrkamerasysteme werden häufig zur Erfassung von Spektralbilddatensätzen für die Ableitung etablierter Vegetationsindizes (VIs) verwendet, die dann als Grundlage für die zerstörungsfreie Schätzung spezifischer Pflanzenmerkmale dienen, um z. B. standortspezifische Bewirtschaftungsentscheidungen in der Präzisionslandwirtschaft zu unterstützen.

Diese Bildgebungssysteme können mühelos in verschiedene UAV-Systeme integriert werden, und die gewonnenen spektralen Bilddaten haben eine hohe räumliche Auflösung. Außerdem können die gewonnenen Datensätze in photogrammetrischen Workflows verarbeitet werden, um spektrale Orthomosaike und 3D-Strukturinformationen abzuleiten. Diese kommerziellen oder experimentellen Systeme bestehen jedoch ausschließlich aus mehreren siliziumbasierten Bildsensoren. Darüber hinaus sind sie in den meisten Fällen in sich geschlossen und nicht an verschiedene Anwendungen anpassbar, sodass ihre spektrale Auflösung auf einige wenige, hauptsächlich breite Spektralbänder im sichtbaren (VIS) und nahen infraroten (NIR) Bereich (400 bis 1000 nm) begrenzt ist.

Diese Multikamerasysteme decken jedoch nicht den kurzwelligen Infrarotbereich (SWIR) von 1000 bis 1700 nm ab, der wichtige spektrale Absorptionsmerkmale in Bezug auf Biomasse, Wasser und biochemische Blattbestandteile wie Lignin, Stärke und Stickstoff (N) enthält. Darüber hinaus besteht, wie bei hyperspektralen Bildgebungsanwendungen zu beobachten ist, bereits ein Bedarf an schmalbandiger SWIR-Bildgebung, insbesondere bei den praktikableren UAV-basierten Multikamerasystemen.

Deren Anwendung in landwirtschaftlichen Systemen mit angepasster spektraler Empfindlichkeit im SWIR wäre ideal für die Erkennung standortspezifischer, feinster spektraler Vegetationsmerkmale in hoher räumlicher Auflösung. Auch bei multispektralen Satellitenmissionen zur Erdbeobachtung hat das SWIR immer noch nur eine geringe und nur sehr breitbandige spektrale Abdeckung mit räumlichen Auflösungen, die für ortsspezifische Anwendungen oder Phänotypisierung ungeeignet sind, was zu einer räumlichen und spektralen Detektionslücke in diesem Bereich führt. Auch hyperspektrale Erdbeobachtungsmissionen, die dieses Defizit im Spektralbereich zumindest ausgleichen könnten, sind derzeit nur in begrenztem Umfang in Betrieb und haben zudem eine geringere Bodenauflösung.
Für die Erkennung von Licht im (SWIR-)Bereich ist daher ein anderer Sensortyp erforderlich, nämlich einer, der auf dem Halbleitermaterial InGaAs basiert. Bis vor Kurzem waren diese Sensoren jedoch nicht leistungsfähig genug, um in miniaturisierte Kameramodule eingebaut zu werden. Darüber hinaus waren InGaAs-Sensoren aufgrund technischer Beschränkungen im Vergleich zu ihren Pendants aus Silizium vergleichsweise teuer. Diese Defizite haben sich jedoch verbessert, sodass im Rahmen dieser Forschungsarbeit (1) ein Prototyp eines UAV-gestützten, zweikanaligen, schmalbandigen Multispektral-Mehrkamerasystems auf der Grundlage von InGaAs-Flächensensoren mit einer spektralen Empfindlichkeit von VIS bis SWIR (ca. 600 nm bis 1700 nm) entwickelt und (2) das Potenzial dieses Kamerasystemprototyps für die Schätzung von Pflanzenmerkmalen zweier verschiedener landwirtschaftlicher Vegetationstypen anhand der erfassten Spektralbilddatensätze bewertet wurde. Diese Ergebnisse wurden durch die Zielsetzungen erreicht, die im Rahmen von drei von Experten begutachteten und in wissenschaftlichen Fachzeitschriften veröffentlichten Studien verfolgt wurden.
Die erste Studie befasste sich mit dem Entwicklungsprozess, einschließlich der Auswahl spezieller Teile für die optischen Komponenten, geeigneter InGaAs-Kamerasensormodule und einer leistungsstarken Recheneinheit. Es wurden austauschbare Filterbaugruppen entwickelt, um mit jedem integrierten Sensor ein frei wählbares schmales Wellenlängenband erfassen zu können. Zwei Optionen für dieses kritische Bauteil wurden implementiert und auf ihre Eignung für den Betrieb im optischen Pfad des Systems getestet. Anschließend wurden mehrere anwendungsspezifische mechanische und elektronische Komponenten entworfen und hergestellt, um das integrierte Multikamerasystem aufzubauen. Erfolgreiche Tests der einzelnen Komponenten und des Gesamtsystems in einer Klimakammer und an einer Ulbricht-Kugel in einem Spektrallabor sowie ein erster Testflug komplettierten schließlich den gesamten Entwicklungsprozess.
In den beiden folgenden Fallstudien wurde das Potenzial des neu entwickelten SWIR-basierten Multikamerasystems für die Schätzung von Vegetationsmerkmalen in einem Dauergrünland-Feldversuch und einem Winterweizen-Feldversuch bewertet. Zu diesem Zweck wurden zwei etablierte SWIR-basierte VIs ausgewählt: der zweibandige Normalised Ratio Index (NRI) und der vierbandige GnyLi-Index. Die Datenerfassung erfolgte in einer Flugkampagne für jedes Versuchsfeld, um vier spektrale Bilddatensätze pro Versuch mit zwei direkt aufeinander folgenden UAV-Flügen zu erfassen. Die resultierenden Reflexionsdatensätze wurden für jedes Wellenlängenband zu Orthomosaiken verarbeitet. Aus diesen Orthomosaiken wurden dann die GnyLi- und NRI-VIs abgeleitet und mit versuchsspezifischen, spektralen sowie destruktiv gesammelten Bodenwahrheitsdaten weiter auf deren Schätzgenauigkeit in bivariaten Regressionsmodellen hin analysiert.

Zusammenfassend wurde festgestellt, dass die Ergebnisse beider Fallstudien die vermutete Leistungsfähigkeit des Kamerasystems aus den initialen Tests der ersten Studie bestätigten. Das Gesamtziel der Entwicklung und Evaluierung des schmalbandigen VNIR/SWIR Multispektralkamerasystems für die UAV-basierte Vegetationsüberwachung wurde somit erfolgreich erreicht. Die aus den spektralen Bilddaten des Kamerasystems abgeleiteten VIs erreichten hohe Genauigkeiten bei der Schätzung des Ertrags der Trockenmasse im Dauergrünland (R^2: 0,73–0,75) und der frischen und trockenen Biomasse, des Feuchtigkeitsgehalts, der N-Konzentration und des N uptake bei Winterweizen (R^2: 0,81–0,87). Weitere multitemporale und mehrjährige Untersuchungen mit verfeinerten Analysemethoden sollten durchgeführt werden, um die Ergebnisse dieser Arbeit zu bestätigen. Im Ergebnis könnte diese vertiefte Forschung das SWIR-basierte Multikamerasystem für den möglichen Einsatz in anwendungsspezifischen UAV-basierten Beobachtungsanwendungen im Kontext der Präzisionslandwirtschaft weiter evaluieren und optimieren.

Acknowledgements

First and foremost, I am incredibly grateful to my direct supervisors, Prof. Dr. Georg Bareth and Prof. Dr. Jens Bongartz, for their confidence, invaluable advice, continuous support, and patience throughout my doctoral studies. Their immense knowledge, ample experience, and positive thinking encouraged me tremendously.

I would like to sincerely thank Prof. Dr. Karl Schneider for his willingness to participate as a second reviewer.

I would also like to express my gratitude to the IBG-2, particularly Prof. Dr. Uwe Rascher and Dr. Bastian Siegmann at the Forschungszentrum Jülich GmbH, for providing access to their spectral laboratory for the evaluation of the camera system prototype.

I gratefully acknowledge the partial funding received by the former Ministry of Science, Further Education and Culture (MWWK) of Rhineland-Palatinate and by the Federal Ministry of Education and Research (BMBF) [Grant number 031B0734F] as part of the research consortium "GreenGrass".

For the study in permanent grassland, I would like to thank Yara International, namely Dr. Jörg Jasper and Dr. Martin Gnyp, for the excellent collaboration, the access to the field trial, and the resulting ground truth data. Furthermore, I want to thank the student assistants of the University of Cologne for their help with the biomass sampling and the processing of the samples. I would also like to thank the Institute of Plant Science at the University of Bonn, especially Dr. Hubert Hüging, for his help with sample preparation.

For the study in the winter wheat field trial, I would like to gratefully thank the Institute of Plant Science at the University of Bonn, especially Dr. Hubert Hüging, for preparing the trial design and the sampling of ground truth data, as well as the technical staff of Campus Klein-Altendorf for handling the experimental field throughout the growing season from seeding to harvest.

I would like to thank all my colleagues from the AG GIS & Remote Sensing of the Institute of Geography for their excellent collaboration. In particular, I would like to mention Dr. Andreas Bolten, Ulrike Lussem, and Dr. Christoph Hütt, who have always been open to my questions and who have been incredibly willingness to help me move forward. I would also like to acknowledge their help during the field studies in piloting the drone (Andreas) and in acquiring the spectral ground truth data (Ulrike). Without you, this endeavor would have been much more challenging.

My special regards go to my colleagues from my second scientific base, the Application Center for Machine Learning and Sensor Technologies (AMLS) at the University of Applied Sciences Koblenz, for the years of outstanding and friendly collaboration that has taken us around the globe in ambitious projects and that laid the foundations for this work. Thank you, Immanuel and Caspar.

My appreciation goes to Daniel Grünberg and Dr. Konrad Henn for proofreading this dissertation.

My heartfelt thanks go to my family for supporting me throughout my entire life.

Finally, I would like to express my deepest gratitude to my wife for her tremendous patience, caring, and support and for motivating me, especially in this thesis's final stages.

Contents

Erklärung **I**

Abstract **II**

Kurzfassung **IV**

Acknowledgements **VII**

Contents **IX**

List of Figures **XII**

List of Tables **XIV**

Abbreviations **XV**

1 Introduction **1**
1.1 Preface and Problem Statement 1
1.2 Research Questions—Aim and Objectives 5
1.3 Outline and Study Sites 8

2 Background **10**
2.1 Digital image formation and image sensor materials 10
2.1.1 Image formation 10
2.1.2 Detector materials for image sensors 12
2.1.3 Optical filters 14
2.2 UAV-based Optical Remote Sensing of Vegetation 16
2.2.1 Unmanned aerial carrier platforms 16
2.2.2 Optical sensor systems for spectral remote sensing 18
2.2.3 Image data processing 21
2.3 Spectral Vegetation Features 23
2.4 Vegetation Indices 26

3 Development of a VNIR/SWIR Multispectral Imaging System for Vegetation Monitoring with Unmanned Aerial Vehicles **29**
3.1 Introduction 31
3.2 Hardware Design 33
3.2.1 Spectral Camera Unit (SCU) 33
3.2.2 Sensor Management Unit (SMU) 39
3.3 Methods for Preliminary Camera System Characterization 43
3.3.1 Thermal Management and Dark Noise 43
3.3.2 Evaluating the Transmission of the Optical System 44

3.3.3 Flat-Field Measurements . . . 45
3.3.4 UAV Integration of the VNIR/SWIR Imaging System . . . 45
3.4 Results of the Prototype Camera System Characterization . . . 47
3.4.1 Thermal Management and Dark Signal . . . 47
3.4.2 Properties of the Optical System and Filter Layout . . . 49
3.4.3 Flat-Field Measurements . . . 50
3.4.4 UAV Integration, System Test, and Test Flight . . . 50
3.5 Discussion and Conclusions . . . 52
3.6 Author contributions . . . 55
3.7 Funding, Acknowledgments, and Conflict of interest . . . 55
3.8 References . . . 56

4 Investigating the Potential of a Newly Developed UAV-based VNIR/SWIR Imaging System for Forage Mass Monitoring 63
4.1 Introduction . . . 65
4.2 Study site and Methods . . . 68
4.2.1 Study site . . . 68
4.2.2 Yield reference data/biomass sampling . . . 68
4.2.3 Spectroradiometer ground truth measurements . . . 68
4.2.4 Image data acquisition . . . 69
4.2.5 Image data processing . . . 71
4.2.6 Spectral data analysis . . . 72
4.3 Results . . . 73
4.3.1 Reflectance Calibration . . . 73
4.3.2 ASD-based VIs vs. DM yield . . . 74
4.3.3 Direct comparison: Camera vs. ASD data . . . 75
4.3.4 DM yield estimation: camera and ASD VIs . . . 76
4.3.5 DM yield estimation: camera VIs - all plots . . . 78
4.4 Discussion . . . 78
4.4.1 Direct comparison of spectral data sets . . . 79
4.4.2 Forage mass estimation . . . 80
4.5 Conclusion . . . 81
4.6 Acknowledgements, Funding, and Conflict of Interest . . . 81
4.7 References . . . 82

5 Investigating the Potential of a Newly Developed UAV-Based VNIR/SWIR Imaging System for Monitoring Crop Traits—A Case Study for Winter Wheat 88
5.1 Introduction . . . 90
5.2 Study Site and Methods . . . 92
5.2.1 Trial Description . . . 92
5.2.2 Biomass Sampling, Nitrogen Concentrations, and Height Measurements . . . 93
5.2.3 UAV Data Acquisition for Crop Height Analysis—Crop Height Workflow . . . 94
5.2.4 VNIR/SWIR Imaging System and Vegetation Indices . . . 95
5.2.5 Spectral Image Data Acquisition and Processing—Spectral Workflow . . . 97
5.2.6 Crop Trait Estimation Workflow . . . 98
5.2.7 Statistical Measures . . . 100
5.3 Results . . . 101
5.3.1 UAV Crop Height Data Evaluation . . . 101
5.3.2 Crop Traits Estimation Models . . . 103
5.3.3 Regression Analyses of Vegetation Indices and Biomass . . . 105
5.3.4 Regression Analyses of Vegetation Indices and N_C and N uptake . . . 108
5.3.5 Regression Analyses of Vegetation Indices and Ground Truth Data . . . 111

5.4 Discussion . . . 112
5.5 Conclusions and Outlook . . . 116
5.6 Author Contributions . . . 116
5.7 Funding, Acknowledgements, and Conflict of Interest . . . 116
5.8 Appendix . . . 117
5.8.1 P4RTK Crop Height—Bar Plots . . . 117
5.8.2 Reflectance Calibration by Grayscale Panels (ELM) . . . 118
5.8.3 WPM Calibration Method Test . . . 119
5.9 References . . . 120

6 Discussion **127**
6.1 Camera System Development and Improvement . . . 129
6.1.1 Development Process . . . 129
6.1.2 Optical Filter Considerations . . . 131
6.1.3 Improved Sensor Management Unit . . . 133
6.1.4 Extension of Spectral Channels . . . 135
6.2 Camera System evaluation . . . 137
6.2.1 Evaluation of Crop Trait Estimation Performance . . . 137
6.2.2 Reflectance integrity of image data . . . 139
6.2.3 Spectral Resolution and Bandwidth . . . 140
6.3 Prospects for PA and SF applications . . . 142

7 Conclusion and Outlook **144**

8 References for Chapters 1, 2, 6, and 7 **146**

A Author's Contribution Chapter 3 **167**

B Author's Contribution Chapter 4 **168**

C Author's Contribution Chapter 5 **169**

List of Figures

1.1 Spectral gap in available multi-camera systems. 5
1.2 General map with location of both study sites. 9

2.1 Internal photoelectric effect. 11
2.2 Schematic overview of semiconductor materials for photosensitive image sensors. . 11
2.3 Comparing the layered structure of InGaAs and enhanced InGaAs sensors. 13
2.4 Bandpass filter characteristics and Fabry-Pérot etalon 15
2.5 The MK Okto XL 6S12 multirotor UAV. 17
2.6 Spectral resolution and multi-camera system channel setup 18
2.7 Spectral gap in available multi-camera systems. 20
2.8 Flight mission planning. 21
2.9 Data workflow: from raw digital image to reflectance orthomosaics (own illustration). 23
2.10 Schematic illustration of a UAV-based optical remote sensing system 24
2.11 Spectral vegetation features and spectral response of image sensors 25
2.12 Data workflow for deriving both SWIR-based VIs GnyLi and NRI 28

3.1 Schematic overview of the complete UAV-based VNIR/SWIR imaging system. . . 33
3.2 Quantum efficiency of different InGaAs sensors. 34
3.3 Filter front-assembly approach 36
3.4 Hybrid bandpass trasnmission data from manufacturer 37
3.5 Internal filter assembly 38
3.6 Spectral camera unit 38
3.7 Sensor system diagram 40
3.8 Sensor management unit 40
3.9 Nvidia Jetson TX2 module 41
3.10 Connect Tech Elroy Carrier 42
3.11 CAD View of the custom-designed and assembled adapter PCB. 42
3.12 Climate chamber measurement setup 44
3.13 Filter transmission measurement setup 45
3.14 Integrating sphere measurement setup 46
3.15 Integration of the camera system prototype into the UAV 46
3.16 Influence of temperature management 47
3.17 Climatic chamber measurements of the average dark signal 48
3.18 Fixed-pattern noise or dark signal non-uniformities (DSNU) 49
3.19 Measured hybrid bandpass trasnmission data 49
3.20 Flat-field image data from internal assembly la 50
3.21 Testflight scenario 51
3.22 Calculations for the Ground Sampling Distance. 52

4.1 System overview VNIR/SWIR multispectral multi-camera prototype 66
4.2 Location map of the experimental site in Neunkirchen-Seelscheid 67

4.3 Reflectance calibration panels . . . 70
4.4 GnyLi VI (WPM calibration) orthomosaic and test replicates . . . 72
4.5 Empirical line calibration . . . 73
4.6 Scatterplots of spectrometer VIs and DM yield . . . 75
4.7 Direct comparison of spectral camera and spectrometer data . . . 76
4.8 Scatter plots camera VIs and DM yield for test replicates . . . 77
4.9 Scatter plots camera VIs and DM yield for all replicates . . . 79

5.1 Spectral gap of Sentinel-2A . . . 91
5.2 Location map of the winter wheat experiment at Campus Klein-Altendorf . . . 93
5.3 UAV setup for crop height analysis . . . 94
5.4 Crop height processing workflow . . . 95
5.5 Overview of the VNIR/SWIR multi-camera imaging system mounted on a UAV. 95
5.6 GnyLi and NRI orthomosaics . . . 97
5.7 Simplified scheme of the developed crop trait estimation workflow. . . . 99
5.8 Image of the 108 sampling plots . . . 99
5.9 Scatters plot for UAV and manual crop height data . . . 101
5.10 UAV-derived development of crop height (growing season 2020) . . . 102
5.11 UAV-derived CH data for June 02 . . . 103
5.12 Bar chart representation of CH derived by the UAV for row 2 for all flight dates . 103
5.13 Scatter plots of the linear regression models (crop heights against crop traits) . . 104
5.14 Scatter plots for the fresh biomass (FBM) data . . . 105
5.15 Scatter plots for the dry biomass (DBM) data . . . 107
5.16 Scatter plots for the crop moisture (CM) data . . . 108
5.17 Scatter plots for the N concentration (N_C) data . . . 110
5.18 Scatter plots for the N uptake data . . . 111
5.19 Scatter plots for the VI data . . . 112
5.20 Visualization of CH values for all relevant flight dates and all winter wheat varieties 117
5.21 Regression analyses for reflectance calibration with near-lambertian gray panels . 118
5.22 Python script for selecting reflectance panels in aerial images . . . 119
5.23 Regression analyses for validation of the near-lambertian grayscale panels . . . 119

6.1 Solution to the existing spectral gap for vegetation monitoring . . . 127
6.2 Comparison between spectral response of VNIR- and SWIR-based systems . . . 128
6.3 Transmission characteristics for investigated optical bandpass filters. . . . 132
6.4 Artifacts of filter front-assemblies . . . 133
6.5 Comparison of old and new SMU CAD design . . . 134
6.6 Results of SMU redesign . . . 135

List of Tables

2.1 Overview of commercial and experimental multispectral multi-camera systems. . 19

3.1 Specifications of the applied hybrid bandpass filters 37
3.2 Feature overview of the newly developed VNIR/SWIR imaging system. 51

4.1 Vegetation indices used in this study 69
4.2 Statistics for the reflectance prediction equation derived from the ELM 74
4.3 Summarized statistics for the SLR models of the VNIR VIs and DM yield 74
4.4 Statistics of SLR models of GnyLi and NRI against DM yield for the test replicates 78
4.5 Statistics for SLR models of the GnyLi and NRI against DM yield for all 39 replicates 78

5.1 Winter wheat varieties 92
5.2 NRI and GnyLi vegetation indices 96
5.3 Regression performance results ground truth against CH data 104
5.4 SLR analyses results camera VIs against FBM, DBM and CM 106
5.5 SLR analyses results camera VIs against N_C and N uptake 109
5.6 SLR analyses results camera VIs against sampled ground truth data 113

6.1 Comparison between implemented camera module and a state-of-the-art module. 136

Abbreviations

AGL . . . . . above ground level
ANN . . . . . artificial neural network
AOI . . . . . angle of incidence
AOV . . . . . angle of view
API . . . . . application programming interface

BW . . . . . bandwidth (see FWHM)

CAD . . . . . computer-aided design
CCD . . . . . charge-coupled device
CH . . . . . crop height
CMOS . . . . . complementary metal-oxide-semiconductor
CSM . . . . . crop surface model
CWL . . . . . center wavelength

DBM . . . . . dry biomass
DEM . . . . . digital elevation model
DM . . . . . dry matter
DN . . . . . digital number
DOP . . . . . digital orthophotos
DR . . . . . dynamic range
DSM . . . . . digital surface model
DSNU . . . . . dark signal non-uniformity
DTM . . . . . digital terrain model

ELM . . . . . empirical line method
EM . . . . . electromagnetic
EMC . . . . . electromagnetic compatibility
EMI . . . . . electromagnetic interference
EO . . . . . Earth observation
EXIF . . . . . exchangeable image file format

FBM . . . . . fresh biomass
FOV . . . . . field of view
FPA . . . . . focal plane array
FPC . . . . . Fabry-Pérot cavity
FPI . . . . . Fabry-Pérot interferometer
FPN . . . . . fixed-pattern noise
FWHM . . . . . full width at half maximum

GCP . . . . . ground control point

GIS . . . . . geographic information system
GNSS . . . . . global navigation satellite system
GPR . . . . . Gaussian process regression
GPS . . . . . Global Positioning System
GPU . . . . . graphics processing unit
GSD . . . . . ground sampling distance
GUI . . . . . graphical user interface

HgCdTe . . . . . mercury cadmium tellurium

IMU . . . . . inertial measurement unit
InGaAs . . . . . indium gallium arsenide
InP . . . . . indium phosphide
INS . . . . . inertial navigation system

LAI . . . . . leaf area index
LWIR . . . . . long-wave infrared

MCARI . . . . . modified chlorophyll absorption in reflectance index
MCT . . . . . mercury cadmium tellurium
MLR . . . . . multiple linear regression
MSI . . . . . moisture stress index
MVS . . . . . mutli-view stereopsis
MWIR . . . . . mid-wave infrared

N . . . . . nitrogen
NDNI . . . . . normalized difference lignin index
NDNI . . . . . normalized difference nitrogen index
NDVI . . . . . normalized difference vegetation index
NDWI . . . . . normalized difference water index
NFC . . . . . NIR filter assigned camera
NIR . . . . . near-infrared
NRI . . . . . normalized ratio index

OSAVI . . . . . optimized soil adjusted vegetation index

PA . . . . . precision agriculture
PCB . . . . . printed circuit board
PCC . . . . . Pearson correlation coefficient
PDA . . . . . photodiode array

RF . . . . . random forest
RGB . . . . . red green blue color image data
RPAS . . . . . remotely piloted aircraft systems
RPM . . . . . rising plate meter
RS . . . . . remote sensing
RTK . . . . . real-time kinematic
RTM . . . . . radiative transfer model

SA . . . . . smart agriculture
SCU . . . . . spectral camera unit

SF . . . . . smart farming
SFC . . . . . SWIR filter assigned camera
SfM . . . . . structure from motion
SIFT . . . . . scale invariant feature transform
SLR . . . . . simple linear regression
SMU . . . . . sensor management unit
SNR . . . . . signal-to-noise ratio
SWaP . . . . . seize, weight and power
SWaP3 . . . . . seize, weight and power, performance, price
SWIR . . . . . short-wave infrared

TCARI . . . . . transformed chlorophyll absorption reflectance index
TEC . . . . . thermoelectric cooler
TIR . . . . . thermal infrared

UAS . . . . . unmanned aircraft system
UAV . . . . . unmanned aerial vehicle

VGA . . . . . video graphics array
VI . . . . . vegetation index
VIS . . . . . visible light
VLOS . . . . . visual line of sight
VNIR . . . . . visible to near-infrared
VOx . . . . . vanadium oxide
VTOL . . . . . vertical take-off and landing

WPM . . . . . white panel method

1 Introduction

1.1 Preface and Problem Statement

The Earth's ecosystems, which provide many goods and services for the world's population, are under enormous pressure (Gitay et al., 2001; Jones et al., 2018; Ferrier, 2020). The food production sector is particularly at risk because of increasing resource scarcity caused by current population growth (Godfray et al., 2010), intensifying global climate change (Shukla et al., 2019), and the ongoing COVID-19 pandemic (Aday & Aday, 2020). In order to meet the food needs of a rapidly growing world population, industrialized nations, in particular, have successfully met these needs with the increased use of large machinery parks and the overuse of pesticides and fertilizers (Liaghat & Balasundram, 2010). The key invention in this context was undoubtedly Fritz Haber's synthesis of nitrogen from ambient air in the form of ammonia NH_3 for the production of synthetic fertilizers (Witschi, 2000; Reay, 2015). To increase production capacity to meet the growing demand for synthetic fertilizers, Carl Bosch increased what was later known as the Haber-Bosch process to an industrial scale (Kandemir et al., 2013). Without synthetic fertilizers, the world's population would likely not have increased to its current number—and it is still growing. Because of all these efforts, there has been a total increase of 240 % in cereal yields since the early 1960s (Shukla et al., 2019). The downside, however, is that this success has led to the ongoing degradation of arable land, water, and biodiversity worldwide (Foley et al., 2011). Ideally, efforts should be made to achieve a higher yield without putting more pressure on the environment through targeted and demand-based management practices (Maes & Steppe, 2019).

Before the industrial age, the manageable size of arable land made it possible to use previous experience to manually adjust such targeted cultivation to individual field sections, which accounted for the already known fact of "within-field spatial variability" (Stafford, 2000). However, this practice could no longer be maintained, and it faded away as a result of the rapid industrialization of the agricultural sector and the steady expansion of arable land due to increasing average farm sizes (Lowder et al., 2016). Consequently, there has been minimal, if any, small-scale, site-specific management of fields in recent decades. This generalized management practice has led, for example, to an excess of chemicals, like pesticides and fertilizers, that subsequently accumulate in the soil or groundwater, causing long-term harm to humans, animals, and the environment and releasing anthropogenic greenhouse gases like nitrous oxide (N_2O) (Lassaletta et al., 2014; Reay et al., 2012; Robertson et al., 2000). As a result, more and more proposals to reverse these trends have arisen, as well as an increasing number of initiatives to implement a sustainable intensification of global agriculture (The Royal Society, 2009; Li et al., 2013).

This turnaround is urgent since these issues need to be addressed vigorously in the coming decade through various measures spanning the entire food production chain to prevent self-reinforcing deterioration (e.g., tipping points) in time (Lenton, 2011; Lenton et al., 2019). However, in the initial stage of food production (i.e., the agricultural sector), demand-driven and site-specific management practices during cultivation can be crucial to ensure the success of these efforts. Precision agriculture (PA) is an increasingly established trend to overcome this uniform management to a more small-scale practice divided into zones or blocks for highly targeted use of chemicals, water, and land (Inoue et al., 2018). The concept of PA emerged in the mid-1980s (Mulla, 2013) and was primarily driven by the advent of the Global Positioning System (GPS) in the late 1970s, which put accurate positioning in the centimeter range on the horizon (Stafford, 2000; Zecha et al., 2013). Another essential development was the establishment of powerful geographic information systems (GISs), making it possible to store and process information about the previously measured in-field conditions in the first place and to derive targeted local measures from these data (Koch & Khosla, 2003; Khosla, 2010).

Since then, with increasingly advanced methods, the goal has been to transform agricultural practices to become more efficient in managing available resources, more profitable, and more environmentally friendly (Cohen & Alchanatis, 2018). After Khosla (2010), nutrition management in PA follows the four Rs, which involves "*doing the right application at the right place and the right time with the right amount*". Therefore, it is of essential importance to acquire accurate and timely information in order to identify zones of similar growth conditions within agricultural areas; with such information it is possible to implement targeted agricultural management practices in terms of fertilization, irrigation, and other agricultural measures (Cohen & Alchanatis, 2018; Liaghat & Balasundram, 2010). As an information-intensive discipline, PA has benefited massively from technological innovations over the past two decades, constantly refining and expanding its methods (Stafford, 2000) and culminating in so-called smart agriculture (SA) or smart farming (SF) (Inoue et al., 2018; Inoue, 2020).

Although still in its early stages and the subject of ongoing research, such as the BMBF[1]-funded research consortia GreenGrass (2022) or DAKIS (2022) as part of the Agricultural Systems of the Future Initiative (ADZ, 2022), SA involves an even more extensive interconnection and holistic consideration of PA's possible manifold components. It includes autonomous data acquisition, evaluation, and application in partially robotic systems using big data combined with artificial intelligence (Inoue et al., 2018; Walter et al., 2017), such as the DFG[2]-funded Cluster of Excellence PhenoRob (2022).

However, for these practices to be effective, it is essential to assess the current condition of crops grown in the field, which should necessarily be non-destructive and flexible in time—that is, as timely and automated as possible. These aspects are covered by remote sensing applications (Liaghat & Balasundram, 2010). Among various sensing techniques (Hunt & Daughtry, 2018), passive optical RS, in particular, can provide essential information related to agricultural management practices (Atzberger, 2013). More specifically, specialized optical instruments can capture spectral data from satellites or airborne carrier platforms to derive the biophysical and biochemical features of crops in agricultural areas, making possible the segmentation of those areas into

[1]German Federal Ministry of Education and Research
[2]German Research Foundation

management zones for specific application of fertilizer, irrigation, or agrotechnical operations (Cohen & Alchanatis, 2018).

In recent years, airborne carrier platforms, particularly unmanned aerial vehicles (UAVs), have expanded and significantly simplified the possibilities for in-field data acquisition (Zhang & Kovacs, 2012; Colomina & Molina, 2014). UAVs do not experience problems faced by satellites or likewise manned aircraft, which cannot provide data or even take off because of cloud cover (Mulla, 2013; Chawade et al., 2019), a particular challenge in temperate climates like Northern Europe (Rasmussen et al., 2021). Moreover, UAVs can also provide image data with an unprecedented spectral, spatial, and temporal resolution (Maes & Steppe, 2019), which is crucial for timely in-field data acquisition, providing steady and reliable up-to-date information to aid the decision-making process in SA or research (Inoue et al., 2018). In addition, unlike long-established technologies, such as data collection by satellite or from the ground, UAV-driven smart agriculture is still in its early stages, and further innovations can be expected in the coming years.

Unfortunately, because of technical limitations, satellite-based optical remote sensing systems can only provide high spatial resolution (in the meter range) with a low spectral resolution and vice versa (Alavipanah et al., 2010). For example, multispectral Earth observation (EO) satellites, such as WorldView-3, offer a commercially available spatial resolution of about 1.2 m (VNIR) to 7.5 m (SWIR), along with 16 spectral bands, which are not narrow enough, between 30 and 70 nm in the SWIR, to distinguish individual spectral features, such as proteins or substitutes for nitrogen, since this detection requires bandwidths (full width at half maximum, FWHM) in the $\leq$10 nm range at dedicated wavelengths in the electromagnetic spectrum (Kuester, 2016; Berger et al., 2020; Hunt & Daughtry, 2018). Additionally, such commercial data are costly. Depending on the plot size to be analyzed, the spatial resolution of most systems is still too low to provide information for field phenotyping or for monitoring phenological stages (Tattaris et al., 2016; Chawade et al., 2019). Free EO missions, such as Sentinel 2A, provide lower ground resolutions starting at 10 m, with also a very limited number of broad spectral bands and a spectral detection gap in the EM spectrum between 950 and 1300 nm (ESA, 2017; Park et al., 2020), where important spectral vegetation features are located related to plant moisture, above-ground biomass and plant proteins (Kumar et al., 2001; Roberts et al., 2018; Hank et al., 2019).

This spectral gap is also found in other EO satellite missions, such as in the moderate resolution imaging spectroradiometer MODIS (2021), the Landsat 7, 8, and 9 satellites (Landsat, 2021), and the ASTER (2021) instrument. In addition, these instruments also only provide ground resolutions between 15 and 1000 m. On the other hand, these EO missions can also acquire thermal infrared imagery and are well suited for global observations of fire detection, land cover and change detection, or cloud properties (Pelton et al., 2013).

Recently launched (PRISMA 2022) or planned (EnMap 2022, SHALOM 2022) hyperspectral EO missions, on the other hand, offer a high spectral resolution (6 to 12 nm) of several hundred bands; this resolution, for example, holds the potential for complementary global nitrogen (N) sensing, however still at a low spatial resolution of $\geq$20 m (Berger et al., 2020). Furthermore, depending on the temporal frequency, the spectral and spatial resolution of the image data required, high costs may be incurred that are incompatible with economic objectives for monitoring small to mid-sized areas (5 to 15 ha) and therefore are best suited for supplying time-series data over large areas or on a global scale (Emilien et al., 2021; Sun et al., 2021).

These facts point to a spatial and spectral gap for targeted small-scale and site-specific management practices. This gap is where the advantages of UAVs come into effect, as they offer a practical and flexible carrier platform for spectral sensors to deliver imagery with a very high spatial resolution for smart farming applications (Inoue, 2020).
A low or high spectral resolution can be selected by choosing appropriate multi- or hyperspectral optical instruments. However, for the vast majority of applications, a multispectral sensor, with a limited number of spectral bands, is sufficient and the device of choice as long as it can acquire narrowband spectral information (Hunt & Daughtry, 2018; Thenkabail et al., 2019). Despite the availability of different two-dimensional multispectral imaging system concepts (Aasen et al., 2018), multi-camera systems have become widely accepted (Deng et al., 2018). These offer a robust design without moving elements, which is insensitive to harsh environmental conditions. In particular, multispectral multi-camera systems can be easily integrated into UAVs and are becoming increasingly popular because of their favorable cost-benefit ratio (Singh & Frazier, 2018). These systems consist of multiple independent arrangements (on average, four to nine), each consisting of a lens, bandpass filter, and image sensor, combined in a rigid camera rig. Thus, high spatial resolution imagery with a low spectral resolution can be acquired, which is still highly effective for deriving established vegetation features.
Additionally, high-resolution crop surface models can be derived from the acquired two-dimensional spectral image data with photogrammetric analysis approaches like structure from motion (SfM) and mutli-view stereopsis (MVS) supporting biomass estimation models (Aasen et al., 2015; Bendig et al., 2015; Hunt & Daughtry, 2018). Furthermore, prototype applications in PA contexts using UAV-based multispectral multi-camera systems have been successfully evaluated (Shi et al., 2019; Thompson & Puntel, 2020; Barzin et al., 2020; Osco et al., 2020).
However, the most constraining factor of these systems is the limited spectral sensitivity of the built-in image sensors, which in existing multi-camera systems is restricted exclusively to the visible (VIS) and near-infrared (NIR), or short VNIR spectrum. These imaging systems do not fully exploit the spectral range relevant to vegetation characteristics, which extends into the shortwave infrared (SWIR) spectrum. Notably, many absorption bands for important plant traits such as biomass, nitrogen, starch, lignin, and water content are located in the SWIR (Kumar et al., 2001). For this reason, this domain provides essential information for vegetation monitoring not found in the VNIR (Goward, 1985). The few studies that use the SWIR were performed only with complex hyperspectral systems. However, multi-camera systems have not yet been developed for the SWIR because of various shortcomings, primarily technical ones. Regardless of imaging technology, however, there is a demand for increased use and for a deep exploration of SWIR for robust estimation of plant traits, such as nitrogen or biomass (Herrmann et al., 2010; Knox et al., 2010; Thenkabail et al., 2013; Gnyp et al., 2014; Berger et al., 2020). Furthermore, the spectral bands of the currently available multi-camera systems are not adaptable to different agricultural applications, and the individual wavelength-selective bandpass filters are very broadband. Therefore, a more suitable multi-camera imaging system is needed—namely, one that can provide two-dimensional, narrowband, and wavelength-adaptable spectral image data for the VNIR and SWIR (VNIR/SWIR) with a high spatial resolution.

1.2 Research Questions—Aim and Objectives

Studies in the relevant literature indicate that vegetation reflectance and absorption characteristics in the SWIR are critical contributors to the robust estimation of crop traits (Thenkabail et al., 2018; Berger et al., 2020), such as above-ground biomass, crop moisture, N uptake, and plant nitrogen content (Herrmann et al., 2010; Gnyp et al., 2014; Koppe et al., 2010; Camino et al., 2018; Berger et al., 2020a). However, the SWIR range is currently not covered by available multispectral multi-camera systems (see Figure 1.1). Nonetheless, this technology would be well suited for investigating the SWIR range of the vegetation spectrum, as these systems can be easily integrated into UAVs and provide high-spatial-resolution spectral imaging data. These data can additionally provide plant height information that is derived by photogrammetric SfM/MVS tools (Aasen et al., 2015) for combined crop trait estimation models (Bendig et al., 2015; Hunt & Daughtry, 2018). As a result, a solution was sought to investigate the above study results in combination with such a versatile but SWIR-based and additionally narrowband multi-camera system.

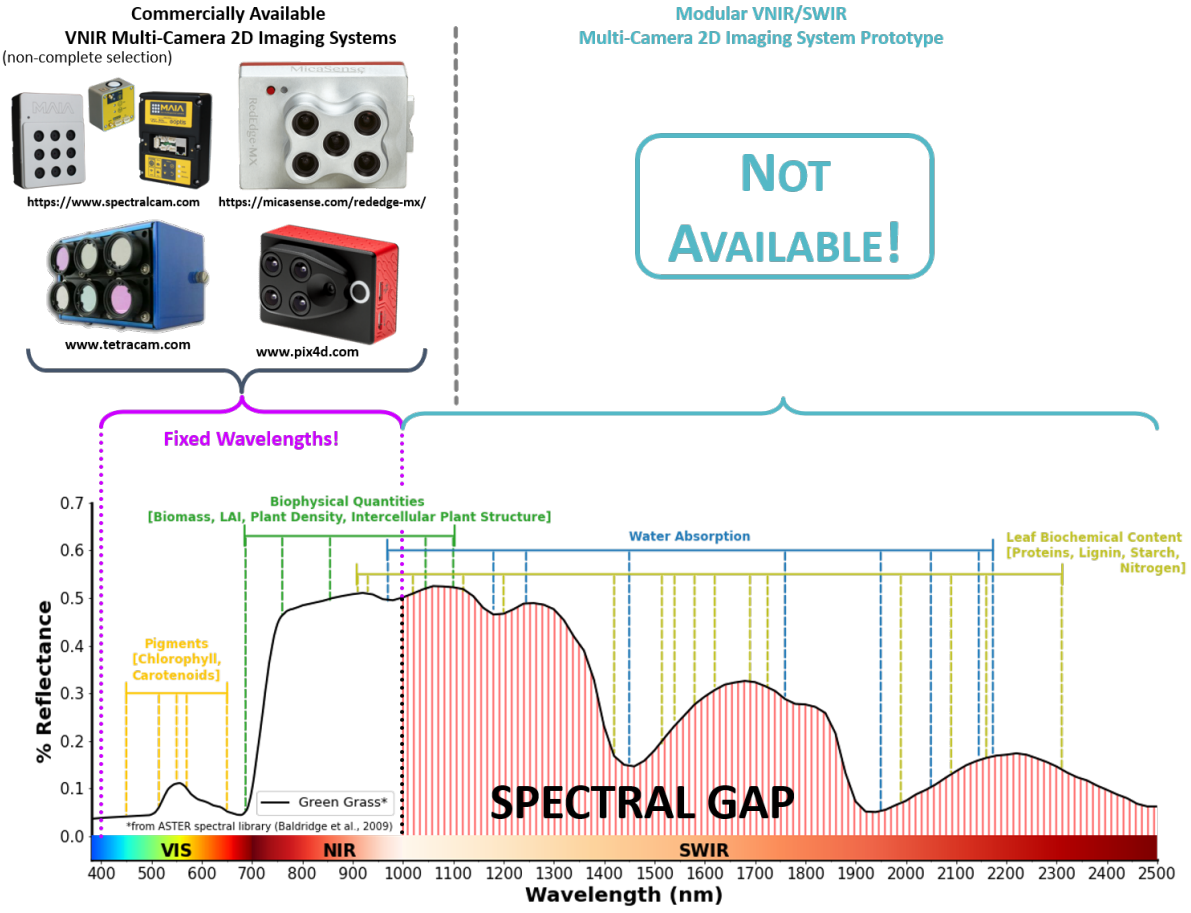


Figure 1.1: Motivation for this Work: Selection of commercial multispectral multi-camera 2D imaging systems for the VNIR spectral domain and the existing spectral gap in the SWIR for this type of camera system in relation to the spectral characteristics of vegetation (own illustration, inspired by Hank et al. 2019, Kumar et al. 2001 and Curran 1989).

The solution to this need for a SWIR-based multi-camera system was motivated and made possible in the first place by three significant technological advances in recent years. The first advance is the emergence of UAV technology, which provided the starting point for a new type of aerial carrier platform for optical RS (Colomina & Molina, 2014); it was no longer absolutely necessary to conduct complex and costly aircraft operations or satellite missions in every flight survey. Therefore, UAVs opened up the field of airborne remote sensing to a wide range of users, who previously lacked the financial resources or large-enough observation areas to use conventional aircraft (Bareth et al., 2011; Paiva et al., 2021).

The next technical milestone was the development of UAV-based multispectral multi-camera 2D imaging systems. In recent years, such camera systems have been developed, with a steadily increasing ground resolution and spectral quality and with a high degree of integration (Aasen et al., 2018; Manfreda et al., 2018). Because of their small size, low weight, and low-power consumption, these systems can be easily integrated and operated in UAVs to cover several hectares with flight times between 20 and 60 minutes (Tsouros et al., 2019). However, these commercially available multi-camera systems are limited in the number of wavelengths used because they apply one complete camera sensor per detected wavelength. Usually, four to nine sensors, filters, and prime lens combinations are used.

Furthermore, for more effortless operability, these camera instruments form a self-contained system that can no longer be adapted to different filter wavelengths, other than those used. The advantage, however, is the high spatial resolution of the spectral image data relative to the sensor resolution. This resolution has an immense advantage in simplifying further processing with photogrammetric SfM workflows of these image data and the derivation of spectral image products, like spectral orthomosaics, to evaluate specific research questions further.

The selection of filters is often based on wavelength combinations used by satellites to compare results better or complement missing satellite data because of spatial resolution, cloud cover, or significant spectral bands for vegetation monitoring (Lukas et al., 2016; Revill et al., 2020). However, a disadvantage of these instruments that cannot be neglected is that their sensors are only based on the semiconductor material silicon. Such sensors are only sensitive in the visible and near-infrared range, so more robust and indicative spectral data from the SWIR wavelengths cannot be used for detecting relevant spectral features related to above-ground biomass (Roberts et al., 2018), nitrogen-bound leaf proteins (Curran, 1989), or plant moisture (Kumar et al., 2001), to name the most important.

This fact leads to the third technological advance related to the ongoing improvement of camera sensors for the SWIR. Because of the spectral range of the SWIR, which starts approximately beyond 1000 nm, these cameras must use the semiconductor material InGaAs, with a spectral response between 900 and 1700 nm. There are special requirements in the production and the operation of these sensors, such as the usage of thermoelectric cooler (TEC) elements. As a result, InGaAs camera modules were too bulky, power-hungry, and heavy for use in UAV-based applications, let alone suitable as the basis for highly integrated multi-camera systems. These disadvantages have led to a niche existence for this technology for the last decades (Vermeiren & Merken, 2017).

However, recently, these sensor elements have caught up with silicon-based sensors in performance with regard to energy consumption, space requirements, and sensitivity (Wang et al., 2019). Due to refinements in the latest production methods, it is even possible to extend the spectral response of InGaAs down to 400 nm in the visible spectral range. These technological advances have finally made it possible to build compact industrial InGaAs camera modules that are theoretically suitable for integrating into a multi-camera system.
As a consequence, this work investigated the aforementioned technological advances in more detail to develop and evaluate a UAV-based multi-camera system capable of detecting not only the (VNIR) but mainly extending its spectral response to the SWIR. As shown in Figure 1.1, the SWIR range is not covered by current multispectral multi-camera systems based on silicon sensors, and it is only sporadically covered by multispectral EO satellite missions; thus there is a spectral gap and consequently to an under-exploitation of the SWIR domain (Berger et al., 2020).

Therefore, the two research questions relevant to this thesis are as follows:

- Given the current state-of-the-art technology, can a SWIR-based multispectral multi-camera 2D imaging system be designed to be compact, lightweight, and energy-efficient enough to be carried by a UAV?
- Can such a SWIR-based multi-camera system provide meaningful spectral data for deriving established vegetation indices for estimating relevant vegetation traits such as above-ground biomass and nitrogen concentration for different agricultural vegetation types?

The answers to both questions were pursued by the following objectives, divided into two stages:

- Camera System Development:
  - Conceptual design and construction of a potential camera system prototype.
  - Thermal and radiometric testing and evaluation in the laboratory.
  - Integration into a UAV.
  - Initial test flights with UAV-based camera prototype.
- Camera System Evaluation:
  - Acquisition of aerial spectral image data sets by the UAV-based camera system prototype of two different types of experimental agricultural sites.
  - Derivation of two SWIR-based vegetation indices from SfM-derived spectral orthomosaics.
  - Analysis of the estimation accuracy of the resulting spectral data with sampled ground truth data in bivariate regressions.

1.3 Outline and Study Sites

Chapter 1 presents the overall context in which this thesis was written. Next, chapter 2 starts with the basics of digital image formation and addresses different semiconductor materials and their suitability for different spectral ranges. Finally, the question is answered as to why sensors for detection in the short-wave infrared have only become widespread beyond their niche existence in recent years. Chapter 2 further presents the fundamental settings and methods of spectral airborne remote sensing of vegetation relevant to this thesis. In particular, UAV remote sensing with multispectral multi-camera systems and the photogrammetric workflow and its requirements are discussed, and differences from other imaging systems are specified. Finally, different spectral features of the vegetation's reflectance spectrum depending on the respective waveband are described, and the determination of these reflection or absorption features via so-called vegetation indices and their importance for estimating vegetation traits.
The results are presented in chapters 3, 4, and 5. They comprise three peer-reviewed journal articles that address the research questions posed in section 1.2 of chapter 1. The order corresponds to the chronological sequence of the elaborated objectives to answer the research questions, beginning with the development of the multi-camera system prototype (chapter 3) and followed by two field studies for evaluation of its potential for forage mass monitoring on a permanent grassland trial (chapter 4) and crop trait monitoring on a winter wheat experimental field (chapter 5). The author's contribution to the published studies was substantial and is declared in detail in Appendices A, B, and C.
Chapter 3 (Jenal et al., 2019) discusses the feasibility and development of a new multispectral multi-camera system prototype that previously did not exist, based on two VNIR/SWIR-sensitive industrial InGaAs camera modules. Problems encountered and approaches to solving them during development are presented in detail, and the most suitable system configuration was chosen for further development steps. Various measurements in a spectral laboratory on an integrating sphere and a climatic chamber were performed for characterization and calibration purposes. The non-permanent and easy-to-install integration into a suitable UAV and the results of a first test flight are also shown.
Chapter 4 (Jenal et al., 2020) investigates the application of the successfully developed UAV-borne multispectral VNIR/SWIR camera system prototype for forage mass monitoring on a permanent grassland trial. The experimental field was situated in Neunkirchen-Seelscheid (Bergisches Land region, North Rhine-Westphalia, see Figure 1.2), about 30 km southeast of Cologne. The field trial was located on a southwest-facing hillside with a constant slope of 7° on average and a total elevation change of 25 m (Lussem et al., 2018). For evaluation purposes, four spectral image data sets (910, 980, 1100, 1200 nm) were acquired with the camera system, and orthomosaics were processed from each. The two vegetation indices GnyLi (Gnyp et al., 2014b) and NRI (Koppe et al., 2010) were derived from these data. The single wavelengths and the VIs were evaluated with spectral and destructively sampled ground truth data (dry biomass). The terrestrial spectral ground truth data were acquired on 12 selected plots (i.e., three replicates) in the experimental field's 156-plot (39 replicates) chessboard configuration in parallel with the two UAV flights.

Similarly, in chapter 5 (Jenal et al., 2021), the camera system prototype was tested on a winter wheat experimental field at the research site Campus Klein-Altendorf (CKA, see Figure 1.2), which is the largest off-site laboratory experimental farm of the Faculty of Agriculture at the University of Bonn, located next to Rheinbach, near the City of Bonn, Germany. The predominantly flat area is located in the southern Lower Rhine Bight on the main Rhine terrace. The soil type is a loess-derived Haplic Luvisol (Hypereutric, Siltic), which is excellent for crop cultivation (Uni Bonn, 2022a). Long-term records from CKA weather stations (1956–2020) reveal an average temperature of 9.6 °C and average annual precipitation of 603 mm for the Atlantic climate (Uni Bonn, 2022b). Four image data sets in the same wavelengths as in chapter 4 were recorded on one survey date in two successive flights in order to evaluate the system. Spectral orthomosaics and the two VIs GnyLi and NRI could be derived from these data sets, which were then evaluated with different crop traits from destructively measured ground truth data and model functions derived from them. In addition, UAV RGB image data were acquired throughout the entire growth period to derive the crop surface models to determine crop height for the survey.
Chapter 6 discusses the research findings from chapters 3 through 5, including current limitations, further refinements of the prototype throughout this thesis, possible future improvements for a more powerful multispectral sensor system, and possible integration into PA and SF applications. Chapter 7 concludes the thesis, highlighting the relevant findings and identifying potential future research questions.

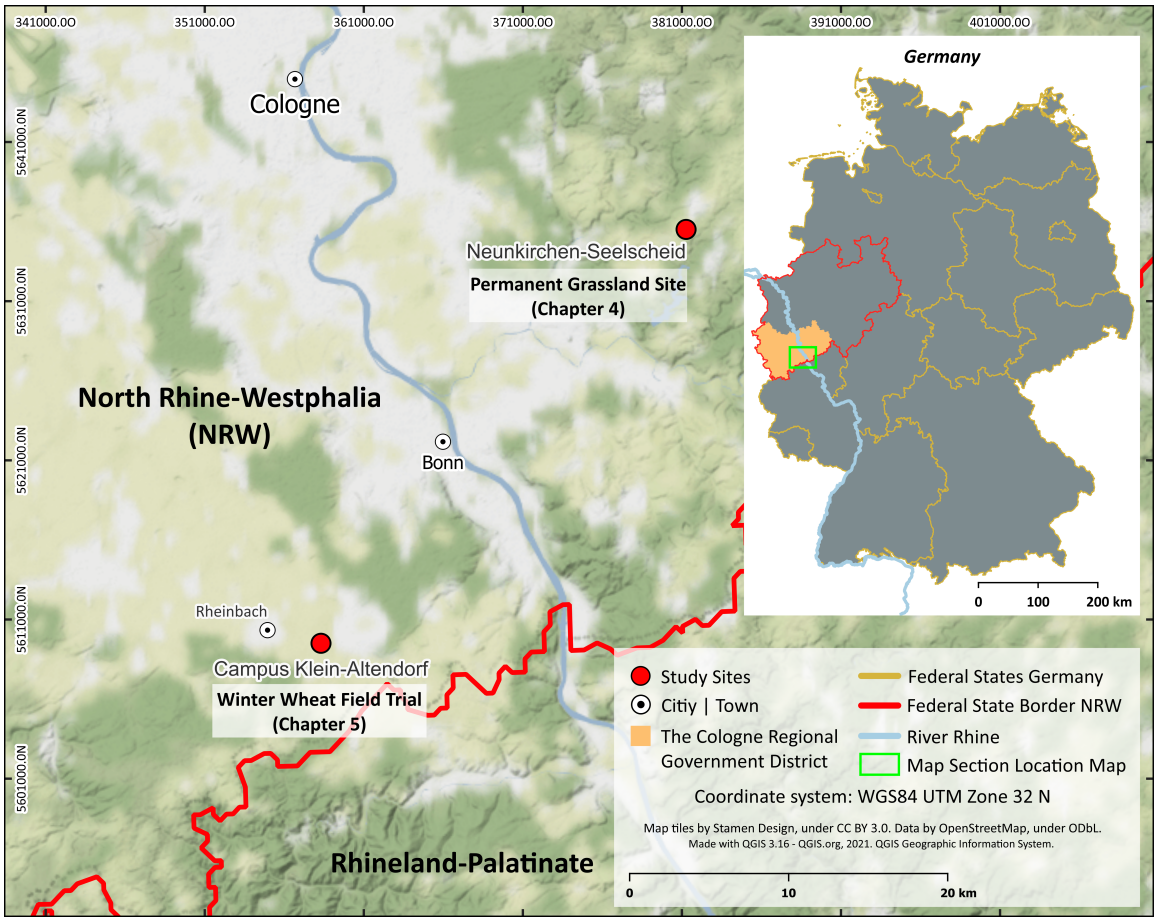


Figure 1.2: General map with location of both study sites.

2 Background

2.1 Digital image formation and image sensor materials

The imaging process used to obtain digital image data is crucial to this work. Therefore, a brief introduction to the fundamental processes of how electromagnetic (EM) radiation is detected with image sensors and the implications of this process for choosing a suitable image sensor material is given in section 2.1.1 and 2.1.2. Additionally, section 2.1.2 explains why the special image sensors used in this work have only become more widespread in recent years, even though the spectral information they provide is essential for monitoring vegetation. Finally, section 2.1.3 introduces optical filters for the selection of distinct wavelengths by spectral filtering.

2.1.1 Image formation

The EM spectrum comprises the entirety of EM radiation propagating in waves at the speed of light c (vacuum: $3.00 \times 10^8\,\mathrm{m\,s^{-1}}$). These EM waves can be distinguished by the frequency ν and the wavelength λ, connected by an inverse relationship, as shown in equation 2.1 (Jones & Vaughan, 2010).

$$\nu = \frac{c}{\lambda} \tag{2.1}$$

According to the wave-particle duality, these EM waves can also be considered as quantum particles, called photons, carrying an energy portion. A photon's energy content E_λ of a specific wavelength λ is directly proportional to its frequency ν and thus inversely proportional to its wavelength, which can be denoted with the Planck constant h ($6.63 \times 10^{-34}\,\mathrm{J\,s}$), as follows in Equation 2.2 (Maître, 2017):

$$E_\lambda = h \cdot \nu = \frac{hc}{\lambda} \tag{2.2}$$

With this energy, the incident photons can generate electron-hole pairs and thus a photocurrent in the semiconductor material of the image sensor via the internal photoelectric effect (Collet, 1986), which is directly proportional to the number of incident photons, also called the incident optical intensity or power (Paschotta, 2008). A voltage proportional to the photocurrent is then converted via complex microelectronics into digital gray values or digital numbers (DNs) for the corresponding impact location, called a pixel. However, as shown in Figure 2.1, the precondition for this process is that the impinging photons' energy is greater than the bandgap energy of the detector material to lift valence band electrons as free charge carriers to the conduction band (Janesick, 2007). This material-dependent minimum bandgap energy determines the longest (cut-off) wavelength of photons that can be detected (Maître, 2017). As shown in Equation 2.2, with increasing EM radiation's wavelengths, the energy of the photons hitting a detector element decreases.

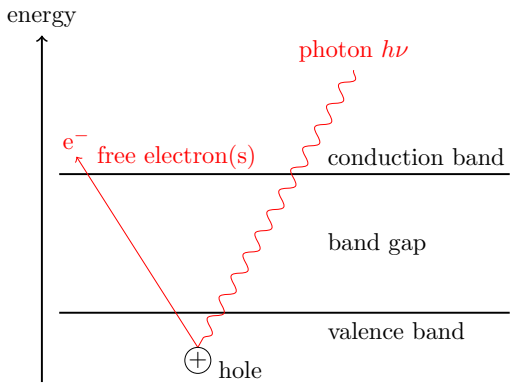


Figure 2.1: Internal photoelectric effect. Single electron-hole pair generated by a photon (own illustration, inspired by Janesick 2007).

As a result, the range of the EM spectrum observed by optical sensors in remote sensing of vegetation, about 400 nm to 2500 nm, cannot be covered by a single semiconductor material. This spectral range is further divided into three subsections: the visible (VIS), the near-infrared (NIR), and the short-wave infrared (SWIR). These are followed by mid-wave infrared (MWIR) and long-wave infrared (LWIR). The latter are also referred to as thermal infrared (TIR), as these ranges contain active thermal radiation and that can be optimally detected by cryogenic cooled photon sensors based on mercury cadmium tellurium (MCT) or HgCdTe (Hwang et al., 1979; Rogalski, 2005). In addition to the mentioned photosensors, uncooled microbolometer sensors exist for thermal infrared detection. Each pixel element consists of a thermal resistor (e.g., thermistor), usually vanadium oxide (VOx) or amorphous silicon (a-Si), whose resistance changes with the incident radiation energy between 8 and 14 µm (Rogalski, 2004; Bhan et al., 2009). Figure 2.2 shows a schematic overview of the individual EM radiation ranges and their coverage by different photosensitive sensor materials.

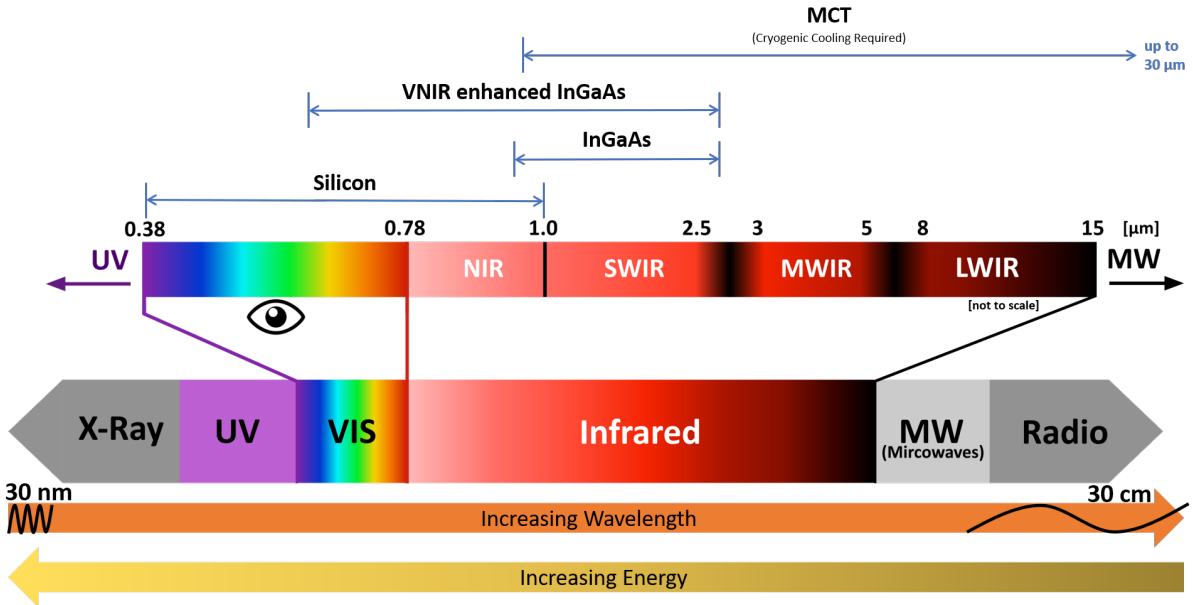


Figure 2.2: Schematic overview of the different semiconductor materials for photosensitive image sensors. (own illustration)

The limits of these three subsections, especially the NIR and the SWIR, are defined differently in various disciplines and publications, which can sometimes lead to confusion (Grant, 2016). Kumar et al. (2001) defines the NIR as ranging from 700 to 1300 nm and the SWIR from 1300 to 2500 nm. However, van Leeuwen (2009) subdivides the NIR from 700 to 1100 nm and the SWIR from 1100 to 2500 nm. This thesis's classification is based on the "sensor division scheme", which defines each wavelength range by the cut-off wavelengths of the sensors' semiconductor material. Silicon-based image sensors are sensitive up to 1000 nm and are therefore preferred for VIS and NIR (Stark et al., 2015; Martin, 2015).

2.1.2 Detector materials for image sensors

The most widely used semiconductor detector material for imaging devices is silicon, as it is best suited for VIS and NIR imaging (Chen et al., 2014), with a bandgap energy of 1.14 eV and the resulting cut-off wavelength of about 1086.8 nm (Janesick, 2007). With the advent of digital imaging in the 1970s, laborious analog photography was slowly displaced in remote sensing (Laffly, 2020). Until now, the acquisition of digital image data has been dominated by silicon-based image sensors. One important reason for this dominance might be that the photo emulsion of analog films and the quantum efficiency of silicon have approximately the same cut-off wavelength (900 to 1100 nm) (Moore, 1979; Brew & Neyland, 1980). Therefore, it was most likely apparent to also bring analog NIR photography for aerial vegetation observations into the digital age by replacing one technology for the other. In addition, silicon-based sensors were comparatively cheap to manufacture and technically easier to handle, since the semiconductor industry's production lines almost exclusively process silicon (Blanc et al., 2009). They also benefited considerably from the research and development efforts for the consumer market, which drove the development of high-performance consumer cameras and the rapid growth of the silicon-based semiconductor industry (Delamere, 2014).
The spectral range following the NIR, which is the principal focus of this thesis, is the SWIR. Hansen & Malchow (2008) define the SWIR as "the portion of the electromagnetic spectrum from the point where silicon detector response falls off to the beginning of the mid-wave infrared atmospheric transmission window", which lies between 2500 and 3000 nm. Although this spectral range has already been investigated with appropriate optical instruments for vegetation monitoring, the underutilization of the shortwave infrared, which is still prevalent today, is most likely explained by historical and manufacturing aspects (Herrmann et al., 2010).
Among a variety of detector materials suitable for SWIR applications, such as germanium (Ge), indium antimonide (InSb), or MCT/HgCdTe, detectors based on the ternary alloy indium gallium arsenide (InGaAs) have become widely adopted because of their high quantum efficiency combined with low dark current at room temperature (Hansen & Malchow, 2008). Depending on the weighting of the three semiconductor components of this composite material, the standard sensitivity range from 900 to 1700 nm can be extended up to 2600 nm (Rogalski & Ciupa, 1999; Rogalski, 2004). The standard spectral response from 900 to 1700 nm of the InGaAs-based focal plane array (FPA) detector results from the necessary combination of indium phosphide (InP) and InGaAs. During production, the InGaAs semiconductor composite material is grown on an InP layer, which is also the subsequent protection layer of such a multilayered InGaAs sensor

(see Figure 2.4). The InP substrate with a bandgap of 1.35 eV has a cut-off wavelength of about 920 nm and blocks the VIS and NIR components from the InGaAs absorption layer, while the standard InGaAs bandgap of 0.75 eV corresponds to a cut-off wavelength of around 1680 nm (Turner et al., 2008).

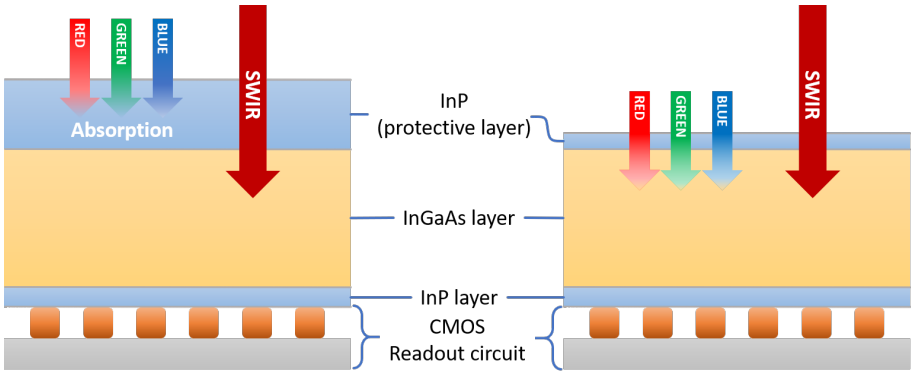


Figure 2.3: Comparing the layered structure of InGaAs and enhanced InGaAs sensors. Left: Conventional InGaAs image sensor with larger InP protective layer, which blocks VNIR wavelengths below 900 nm. Right: Improved spectral sensitivity of InGaAs image sensors is achieved by thinning the top InP protective layer (own illustration, inspired by Sony 2022).

However, this lower sensitivity limit of about 900 nm can be further reduced by thinning the InP layer in an additional etching step during production (Figure 2.3). Therefore, newer, enhanced InGaAs sensors offer even better sensitivity to the lower end of the VIS (approximately 400 nm) while maintaining high quantum efficiency and low noise characteristics over their full sensitivity range (Martin, 2015). This complex and expensive manufacturing process has a comparatively low production yield, involves long lead times, and requires materials that are occasionally difficult to source.

Therefore, in recent decades, InGaAs sensors have had a niche existence in specialized sectors like military, aerospace, astronomy, and telecommunication, but they are slowly gaining momentum for civil applications (Vermeiren & Merken, 2017). Since the early 1990s, attempts have been made to improve these sensors so that they can be operated at room temperature to open up a broader range of applications; historically, these systems have been too energy-hungry, bulky, and inconvenient to integrate into UAV-based systems (Wang et al., 2019; Rogalski, 2002). However, InGaAs photosensors also benefit significantly from the experience and sophisticated manufacturing technologies that have emerged in silicon processing (Durini & Arutinov, 2020). In this context, a critical threshold has been crossed in recent years, and the advantages and potential uses, especially in industrial applications, can no longer be denied (Delamere, 2014). Therefore, newer systems have been optimized according to the SWaP approach with regard to size, weight, and power. Because of their improved sensor and electronic performance, these systems do not necessarily require single- or multi-stage thermoelectric coolers (TECs) because of better noise characteristics and simultaneous smaller pixel-pitch, which results in higher sensor resolution. These improvements enable the design of more compact systems with lower energy consumption, which are particularly suitable for integration in UAVs (Delamere, 2014). The SWaP approach has recently even been replaced by the SWaP3 (size, weight, power, performance, and price) approach, suggesting further advancements in this area (Wang et al., 2019).

2.1.3 Optical filters

Unmodified image sensors, in the sense that they do not contain any wavelength-selective or, more precisely, frequency-selective elements in the optical path, detect all light that passes through their optics in the range of their spectral sensitivity. As a result, these so-called panchromatic image sensors can provide high-resolution and high-contrast images (Stars Project, 2022). In contrast, they cannot provide any information content for spectral examinations in which wavelength information is specifically examined that reveals characteristic properties of the examined scene or material (Earth Observing System, 2021). For the transmission of a more or less narrow waveband of the EM spectrum with simultaneous rejection of the remaining part, so-called optical filters are used. The most common example is the selective filtering of wavelengths corresponding to red, green, and blue (RGB) in digital color cameras at the pixel level by the Bayer pattern (Bayer, 1976).

Optical filters can be divided into different types depending on their physical working principle. The two relevant types in this work's context are absorption and interference filters (Dandin et al., 2007). Absorption filters block the unwanted part of the light by absorbing it through their material properties and converting the energy contained in the blocked EM radiation into thermal energy (Reichman, 2000). Interference filters, on the other hand, reflect the EM radiation to be blocked with the help of dielectric coatings that are vapor-deposited on a glass substrate. These have different refractive indices and a layer thickness of $\lambda/4$, which means that only EM radiation of a particular wavelength λ and under a certain angle of incidence (AOI) interferes constructively and can thus pass through the material (Cushing, 2011). The remaining EM radiation interferes destructively and is reflected away from the material (Madsen & Zhao, 1999; Macleod, 2010). If the angle of incidence changes, the path length traveled by the material in each layer also changes, and there may be a shift in the wavelength to be filtered, usually toward a lower wavelength and is therefore called blue-shift. Because of this phenomenon, the filter's position in the optical path is crucial and has to be tested for anomalies. If undesirable wavelength shifts occur, corrective measures must be taken (Goossens et al., 2019; Goossens & Van Hoof, 2019).

Another important wavelength-selective optical device based on interference is the Fabry-Pérot cavity (FPC), based on the Fabry-Pérot interferometer (FPI) (Vaughan, 1989). The FPI consists of two parallel, semi-transparent, highly reflective mirror plates or coatings with an air gap or spacer material in between, forming a standing wave generator (Paschotta, 2008). Given that all other parameters are fixed, the spacing of the gap, or cavity, determines the wavelength to be transmitted (Hecht, 2018; Paschotta, 2008). Wavelengths λ at which transmission takes place have to fulfill the relation in Equation 2.3 (Zorabedian, 1995):

$$2 \cdot n \cdot d \cdot \cos\theta = m \cdot \lambda \tag{2.3}$$

where: n : refraction index of spacer material
d : mirror spacing
θ : angle of incidence
m : passband order
λ : transmission wavelength

In optical filter design, the distance of this gap is fixed (etalon), and Fabry-Pérot microcavities are part of the filter design together with interference layer stacks (Born & Wolf, 2019; Bitarafan & DeCorby, 2017). In FPIs, piezoelectric elements can be used to vary the gap distance or angle of incidence—for example, to create a tunable bandpass filter, which can then be used in optical instruments (Gupta et al., 2010; Mäkynen et al., 2011).

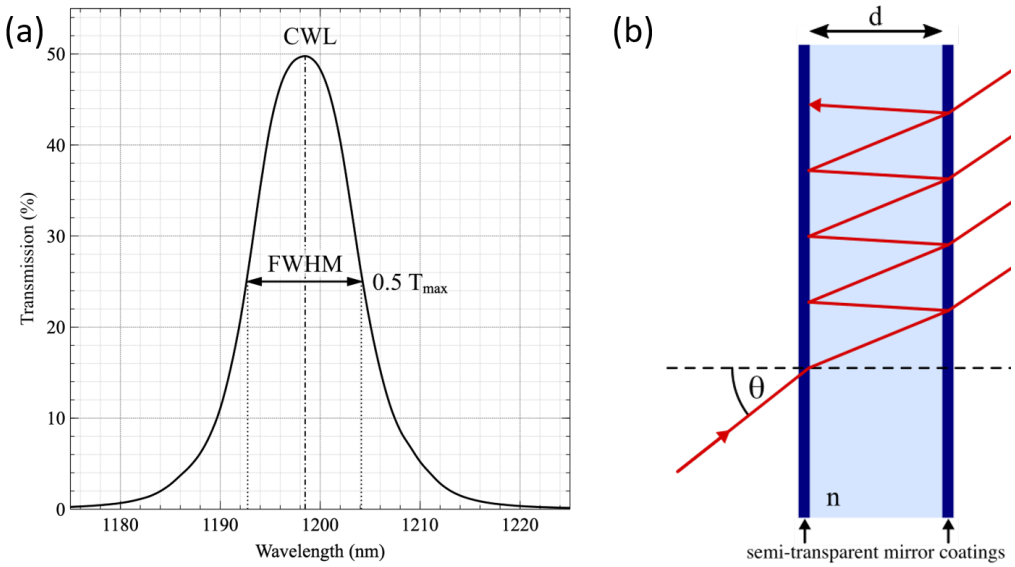


Figure 2.4: (**a**) Bandpass filter characteristics (inspired by Liang 2004). (**b**) Fabry-Pérot etalon or FPC (inspired by Vaughan 1989). (own illustrations)

Depending on their transmission characteristics, optical filters can be classified into three types: longpass, shortpass, and bandpass (Cushing, 2011). There are also further filter characteristics, but these are not relevant for this work. The difference between these three types can be explained with the help of the key terminology for optical filters. A longpass allows wavelengths above the specified cut-on wavelength, at which transmission increases to 50 % throughput, to pass (Reichman, 2000). Equivalently, a shortpass only transmits wavelengths up to its specified cut-off wavelength, at which the transmission decreases to 50 % and is blocked afterward. The essential filter type for this work is the bandpass filter, characterized mainly by two parameters (Reichman, 2000). The center wavelength (CWL)) defines the center of the spectral bandwidth over which the filter transmits (Reichman, 2000). The spectral bandwidth is also denoted as the full width at half maximum (FWHM) and is limited by the upper and lower wavelengths, at each of which the filter reaches 50 % of the peak transmission (Weik, 2001; Liang, 2003b). Bandpass filters with an FWHM $\leq$10 nm are referred to as narrowband.

A particular type of filter had to be used for the camera system developed for this research since the sensitivity range from VIS to SWIR is broad, and readily available filters with a wide range of different wavelengths for different applications had to be ensured. These so-called hybrid bandpass filters are well-matched combinations of dielectric stacks for interference, spacer layers between these stacks forming FPCs, and colored glass absorption substrates assembled in a protective ring housing (Thorlabs, 2022). In this way, a sharp and narrowband passband is created as well as an ultra-broad stopband from 400 to 2500 nm, significantly exceeding the individual components' transmission and blocking properties.

The wide range of available CWLs of these hybrid narrowband filters already enables a large number of applications. However, for applications requiring precision-tuned wavelengths or ultra-narrow bandwidths ($\leq$3 nm), customer-specific filters can be commissioned, a solution that takes more time and is also more cost-intensive.

2.2 UAV-based Optical Remote Sensing of Vegetation

There are various definitions for the concept of remote sensing (Campbell & Wynne, 2011; Laffly, 2020). Nevertheless, broadly generalized, one can define remote sensing as the science of acquiring information by instruments from a distance about objects or phenomena by measuring emitted or reflected radiation from Earth's surface (Fussell et al., 1986). These active or passive instruments, or combinations thereof, can be carried by aircraft or spacecraft (Richards & Jai, 2006). The emergence of photography around 1839 marks the starting point for the first attempts of optical remote sensing (Moore, 1979). The first documented experiments in airborne remote sensing were done around 1858 by Gaspar F. Tournachon (also known as Nadar), who used early prototypes of photo boxes from a tethered balloon 80 meters above the city of Paris (Laffly, 2020). Since these early beginnings, remote sensing has significantly evolved, and both aircraft and camera technology have advanced tremendously.

2.2.1 Unmanned aerial carrier platforms

In aircraft technology, unmanned aerial vehicles (UAVs), which emerged more than a decade ago, marked a new era in remote sensing (Sugiura et al., 2005; Maes & Steppe, 2019). Since the appearance of the first UAVs, this tool has been ambitiously adopted for remote sensing purposes and further developed as a reliable and sophisticated remotely piloted carrier platform for all kinds of instruments and remote sensing applications (Colomina & Molina, 2014). A variety of UAV concepts, mostly battery-powered, are available, which fit to different applications due to different performance parameters, such as potential payload, endurance, and size (Zhang & Kovacs, 2012; Radoglou-Grammatikis et al., 2020).

The most widespread design for smaller survey areas, which was also used in this work, is the so-called multirotor or multicopter, consisting of at least four lift-generating rotors arranged in a circular design. These are available from various manufacturers (e.g., DJI 2022, Microdrones 2022) in different sizes and configuration options (pre-installed and stabilized camera systems, real-time kinematic (RTK) global navigation satellite system (GNSS), etc.). The heavier the possible payload, the larger the number of rotors used, with six or eight being common. Fixed-wing models (SenseFly, 2022) are used less frequently but are the device of choice for longer ranges, usually at the expense of possible payloads. In addition, there are also hybrid UAVs, so-called VTOLs (vertical take-off and landing, Wingtra 2022) that combine the minimal take-off footprint of multirotors with the endurance capabilities of fixed wings. Finally, combustion-engine-powered, miniaturized, helicopter-style models are available for heavy-duty, long-range operations (Swissdrones 2022, INTRA 2022). The above examples are only a small fraction and the most prominent manufacturers of the widely diversified UAV market.

Figure 2.5 shows the multirotor UAV MK Okto XL 6S12 (HiSystems GmbH, Moormerland, Germany) used as the aerial carrier platform during all flight activities regarding the camera system prototype. For successful processing of aerial images, the camera sensors must be aligned as perpendicularly as possible to the ground (i.e., nadir), regardless of the current orientation of the aircraft. In order to accomplish this task, an electromechanical stabilization device, a so-called gimbal, was used to maintain stable orientation during flight operations.

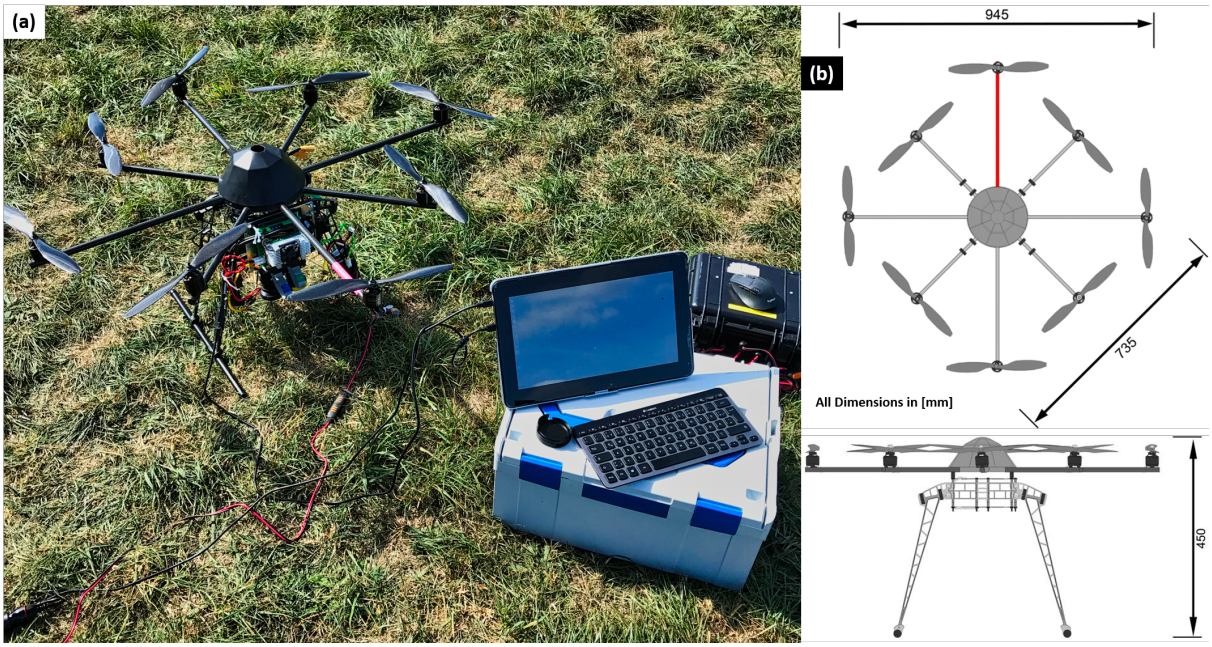


Figure 2.5: The MK Okto XL 6S12 multirotor UAV, which was used as aerial carrier system for the camera system prototype in this work. (**a**) Preflight preparations during survey in permanent grassland. (**b**) Appearance and dimensions of the MK OktoXL 6S12 (2022) aerial carrier platform.

To date, these airborne platforms primarily operate optical instruments to acquire cost-effective imaging data with a high spectral, spatial, and temporal resolution, potentially outperforming other carrier platforms, such as manned aircraft or satellites, in small to mid-scale applications (Manfreda et al., 2018). This high performance makes UAVs an integral component for supporting site-specific management decisions in precision agriculture (PA) (Singh & Frazier, 2018; Maes & Steppe, 2019), whether as a complement to delivering in-situ data to global-scale platforms like satellites (Emilien et al., 2021) or as a single-carrier platform that provides timely data for decision-making processes. In addition, UAVs can be operated mostly independent of cloud cover (Mulla, 2013) and are easily controlled by an autopilot, executing preplanned flight missions. UAVs are not only flexible in their application but can also carry multiple sensors simultaneously (Jaakkola et al., 2010; Bendig et al., 2012; Maes & Steppe, 2019; Hambrecht et al., 2019; Kandylakis et al., 2020).
However, with an average flight time of 20 to 30 minutes and existing regulations such as operating exclusively in the pilot's visual line of sight (VLOS), the potential area to be covered is still in the tens of hectares and is limited compared to manned aircraft or satellites. However, this area is also subject to constant change and improvements, and fully automated data acquisition will likely be established in the next few years (Walter et al., 2017).

2.2.2 Optical sensor systems for spectral remote sensing

On the sensor side, UAV-based passive optical instruments in agricultural remote sensing detect solar electromagnetic radiation, mainly reflected from vegetation canopies (Mulla, 2013). The most straightforward application is an off-the-shelf consumer camera with a sufficient sensor resolution. With the image data acquired by such a camera, essential height information, derived through crop surface models (CSMs), as well as spectral (broadband RGB) information, can already be obtained for vegetation monitoring (Bareth & Hütt, 2021). However, much diversification has occurred regarding dedicated spectral imaging technology for a more in-depth investigation of vegetation characteristics. The type of data acquisition from analog to digital and the digital detector systems themselves have constantly evolved and differ considerably. However, the aim of spectral imaging is always to obtain broad- or narrowband spectral information from the acquired image data that can describe distinguishing features of the captured vegetation.

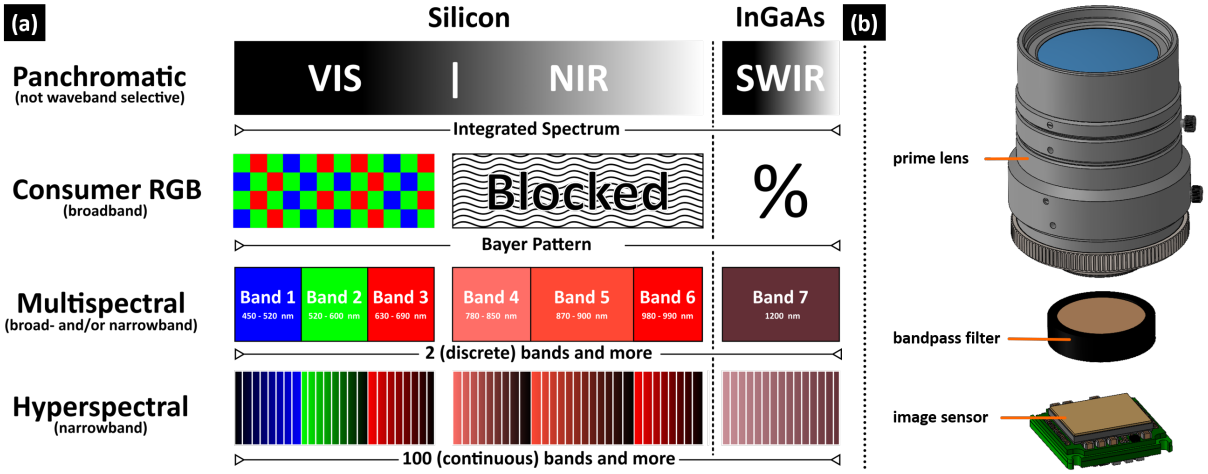


Figure 2.6: (**a**) Schematic differentiation of imaging systems based on their spectral resolution. (**b**) Simplified setup of a "spectral channel" of a multispectral multi-camera 2D imaging system (CAD files provided by Kowa 2022, Thorlabs 2022 and Allied Vision 2022b). (own illustrations)

Considering the different functional principles of the multitude of optical instruments as a black box, they differ primarily in the number and bandwidth of the spectral channels they can capture (see Figure 2.6a). Multispectral systems can usually detect between two and 10 discrete channels, while contrastingly, so-called hyperspectral systems can resolve tens to hundreds of narrow spectral bands for a more continuous coverage of the spectral domain. Relevant for this work is a particular subtype of multispectral camera systems, a multi-camera 2D imager (see Aasen et al., 2018). The underlying principle of these instruments is the use of a complete image sensor for a specific waveband selected by a bandpass filter. Such systems typically consist of four to nine fixed optical systems, or channels, each made up of a prime lens, a bandpass filter, and an image sensor arranged in a rigid camera rig configuration (see Figure 2.6b).

Although multi-camera systems can only acquire a small number of spectral channels, the two-dimensional image data offers high spatial resolution and can be further processed in a streamlined workflow. Usually, panchromatic silicon sensors are used, and the desired wavelength information is selected by optical bandpass filters integrated into the optical path. These interference filters are generally very broadband: A FWHM starting at $\geq$20 nm around their center wavelength is not uncommon (Nocerino et al., 2017; Hunt & Daughtry, 2018).

Over the years, several companies have specialized in developing these systems and have launched camera systems with up to nine cameras arranged in a grid and equipped with special bandpass filters for the VNIR domain (Dubbini et al., 2017).
Table 2.1 lists a selection of the most common commercially available and experimental multi-camera sensor systems and their spectral application range, i.e., spectral response, including further parameters. Moreover, it can be stated that no multi-camera system is available for the SWIR domain, as visualized in Figure 2.7.

Table 2.1: Overview of commercial and experimental multispectral multi-camera systems.

	Manufacturer	Sensor Name	Channels	Spectral Response	FWHM [1]	Reference
Commercial	Micasense	Redegde-MX	5	VIS - NIR	12–57	MicaSense (2019)
		RedEdge-P [2]	5		12–57	
		Altum-PT [2,3]	5		12–57	
	DJI	P4 Multispectral	6		16–26	DJI (2021)
	SAL Engineering	MAIA WV	9		40–125	MAIA (2019)
		MAIA S2	9		15–115	
		MAIA M2	2		20–125	
	Parrot	Sequoia+	5		10–40	Parrot (2020)
	Tetracam	Micro-MCA	6		25	Tetracam (2020)
Experimental	AMLS†	PanX.2	4	VIS - NIR	configurable	Jenal et al. (2022)
		PanX.3	4			
	Institute of Crop Science††	N/A	4			Geipel et al. (2016)
	IUMA‡	N/A	5[4]			Morales et al. (2020)
	Fraunhofer IPM	N/A	3			Stemmler (2021)

† University of Applied Sciences Koblenz; †† University of Hohenheim; ‡ University of Las Palmas de Gran Canaria

[1] in (nm); [2] additional panchromatic sensor; [3] additional thermal sensor; [4] one sensor with filter wheel

In contrast to these broadband and spectrally low-resolution VNIR multi-camera systems, the technology of the so-called hyperspectral scanners can produce image data with a high and narrowband ($\leq$10 nm) spectral resolution (Hunt & Daughtry, 2018), as shown in Figure 2.6a. These imaging systems usually operate on the pushbroom (line-scanning) principle, in which light rays entering the system through an optical slit are split into their spectral components, usually by an optical grating; this prism-like fanned out light is then mapped onto a pixel array detector (Goldstein et al., 2018). The detector's pixel elements are arranged in lines perpendicular to the forward motion to produce a lateral spatial resolution. A resulting aerial image, which is later created in post-processing, is acquired "line-by-line" by moving the detector array in space (Fowler, 2014). In addition, there is also the whiskbroom (point scanning) principle, which is more complex to implement and runs at slower scanning speeds than the pushbroom principle (Adão et al., 2017). The merging of the acquired line, or point, information from hyperspectral scanners into coherent aerial images and, finally, into georeferenced and orthorectified mosaics, requires additional information about the exact position of the sensor and its orientation in space to align the individual scanned lines correctly.

Thus, this alignment process of the scanner information additionally demands a high-precision inertial navigation system (INS)) consisting of a GNSS and an inertial measurement unit (IMU) (Aasen et al., 2018; Maes & Steppe, 2019). These components are expensive and inevitably lead to higher space and energy requirements, and consequently require more expensive UAV carrier platforms with a higher potential payload (Esposito et al., 2021).

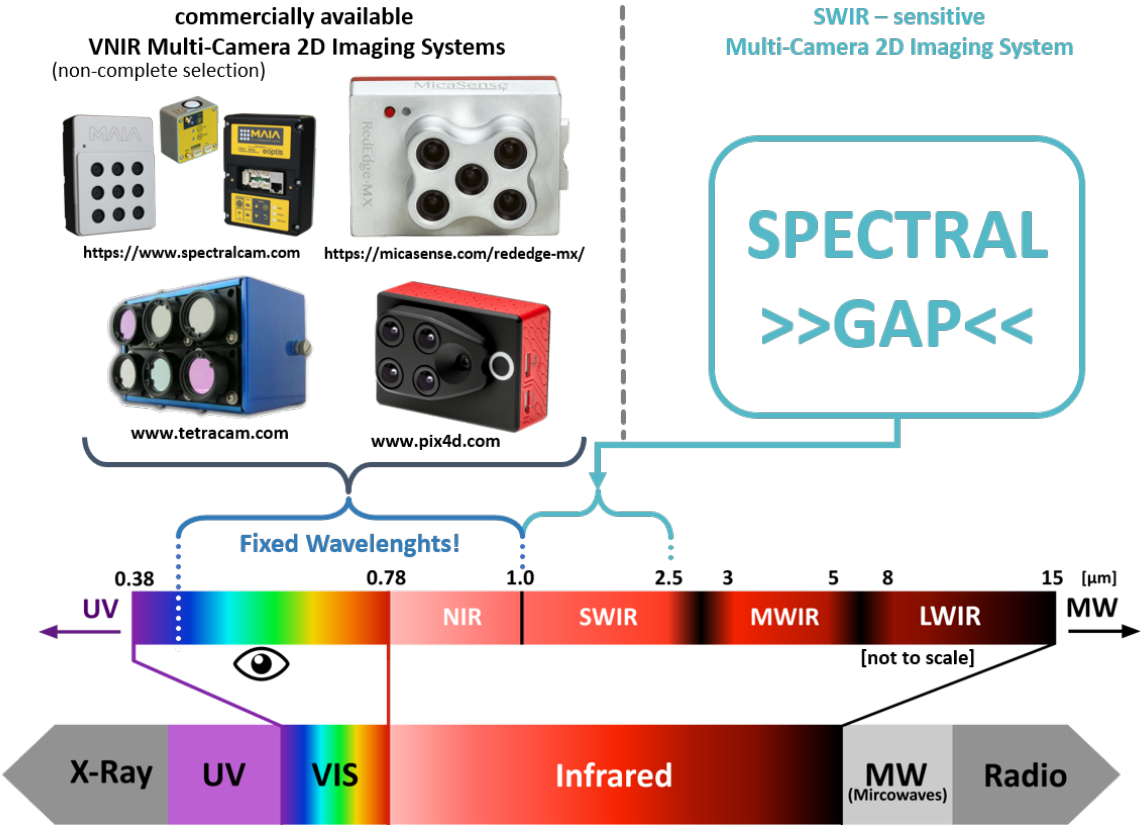


Figure 2.7: Spectral gap in available multi-camera systems: Selection of commercial multispectral multi-camera 2D imaging systems for the VNIR spectral domain and the existing spectral gap in the SWIR for this type of system (own illustration).

In addition, the use of such a hyperspectral detector generates large amounts of data in a short time. These large data sets place high demands on the size of the provided data storage and on the entire post-processing system, which must be able to cope with these data volumes. This post-processing chain usually needs expensive workstations or server capacities, which must be purchased or leased. However, it is by no means the case that the abundance of recorded spectral channels necessarily leads to a higher information gain. Many of the recorded narrow bands contain redundant information so that for specific application areas, such as vegetation monitoring, a small number of selected bands is sufficient (Curran, 1989; Thenkabail et al., 2018). Therefore, these systems are more suitable for fundamental research topics, where hitherto unanswered research questions can be investigated. In contrast, already established spectral correlations with vegetation traits can be detected most efficiently over extensive areas using specifically spectrally tuned multispectral multi-camera systems.

2.2.3 Image data processing

With a multi-camera system, optical coverage of a large area in high resolution by airborne platforms with a single image is de facto impossible. Therefore, the target area must be flown over in a precalculated grid-like flight pattern adapted to the optical sensor parameters of the multi-camera system to capture all features of the area of interest in multiple images from different perspectives (Jiang et al., 2020).

These meandering patterns (see Figure 2.8) ensure that a minimum lateral overlap of the image data on the ground does not fall below a certain percentage. Likewise, a minimal frontal overlap is recommended in the forward direction, which can be realized by GNSS-controlled trigger points or continuous image acquisition (free run) tuned to the flight speed of the UAV. For flat agricultural fields, forests, or dense vegetation, the overlap in both directions should be at least between 80 and 85 % for optimum coverage (Pix4D, 2022). The goal is to cover the area as efficiently as possible at the ground resolution required for the project. This desired ground resolution, which is often specified by the ground sample distance (GSD), determines the minimum resolvable feature size on the ground and is generally defined as the distance between the centers of two adjacent pixels measured on the ground. With nadir alignment of the image sensor, the GSD is limited by the sensor's pixel pitch, the focal length of the lens, and the altitude above ground (Roth et al., 2018). If a more in-depth assessment of the spatial and spectral optical resolving power is needed, additional parameters can be investigated as described in Joseph (2020).

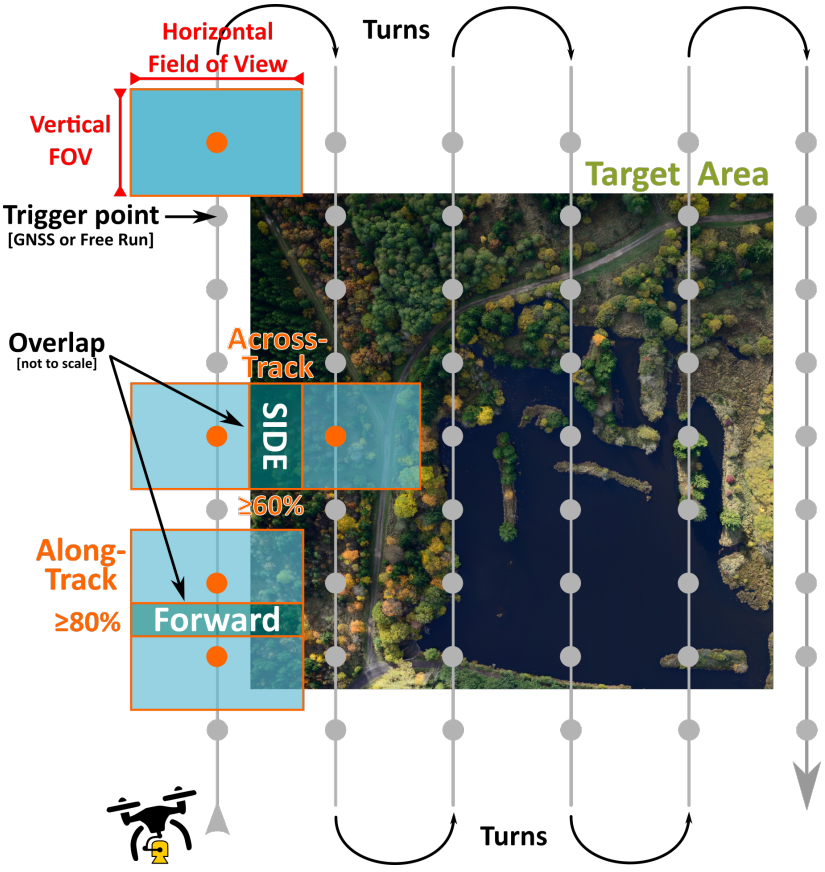


Figure 2.8: Flight mission planning (own illustration inspired by Pix4D 2022).

After successfully planning and conducting a flight mission, the resulting individual image data can be processed into orthophotos. An orthophoto differs from a standard aerial image by correcting the perspective view, lens distortion, and camera angle. In this way, the orthorectification process transforms the central projection of the raw image to a perfectly straight-down view of all objects in the image frame. With this corrected projection of constant scale, accurate distance and direction measurements can be made. These corrected orthophotos can then be stitched into a single coherent orthomosaic map of the whole flyover area. This process can be performed, for example, by photogrammetry software based on structure-from-motion (SfM) and multi-view stereopsis (MVS) algorithms in several processing steps, such as feature detection and bundle adjustment (Triggs et al., 2000; Turner et al., 2012).
SfM is the concept of capturing a three-dimensional object or area by two-dimensional images through features found in multiple overlapping areas of these images (Ullman, 1979). Lowe (1999) developed the scale-invariant feature transform (SIFT) algorithm, which allows corresponding features to be matched in a set of images even with significant variations in scale and viewpoint and under conditions of partial occlusion and changing illumination.
Snavely et al. (2006) and Goesele et al. (2007) took this concept further and firstly generated large point clouds of tourist attractions from a massive number of online community photo collections with multi-view algorithms. First applications in UAV-based remote sensing were performed and further investigated by Westoby et al. (2012), Turner et al. (2012), and Harwin & Lucieer (2012). These algorithms can be parallelized, and efficiently run on graphics processing units (GPUs). Not surprisingly, the ongoing trend of increasingly powerful GPUs has advanced this method considerably. Besides freely available command-line tools (VisualSFM, 2022) and freely available GUI-based software (Meshroom, 2022), there is also a wide range of commercial software available from various companies, such as SURE (nFrames, 2022), Inpho (Trimble, 2022), and Pix4Dmapper (Pix4D, 2022). For this work, however, the software Metashape, formerly Photoscan, (Agisoft Ltd, St. Petersburg, Russia), was used. Although the exact functionality of this software is not known because of company intellectual property, it makes use of the algorithms and procedures mentioned above. Since this software has been used by many studies (Bendig et al., 2015; Näsi et al., 2018) for data evaluation and since its functioning has been intensively and empirically examined based on the output products (Aasen & Bolten, 2017; Mamaghani et al., 2018), it can be relied upon. If the corresponding exchangeable image file format (EXIF) data is set up correctly, an advantage is obtained through the direct import of the acquired and geometrically uncalibrated raw spectral image datasets from multi-camera system's channels into the software as a rigid camera rig. In this way, the software can create multilayer orthomosaics and the corresponding end products, such as dense point clouds or digital elevation models (DEMs). Depending on the application, DEMs can be digital terrain models (DTMs) or digital surface models (DSMs).
The use of appropriate georeferenced data through high-precision ground control points (GCPs) is essential for the creation of these orthorectified mosaics, allowing accurate georeferencing for further analysis in GIS software (see Figure 2.9). In this way, the two georeferenced multilayer orthomosaics resulting from two consecutive flights for both case studies could be overlaid with high spatial accuracy and further analysis could be performed with the four aligned bands.

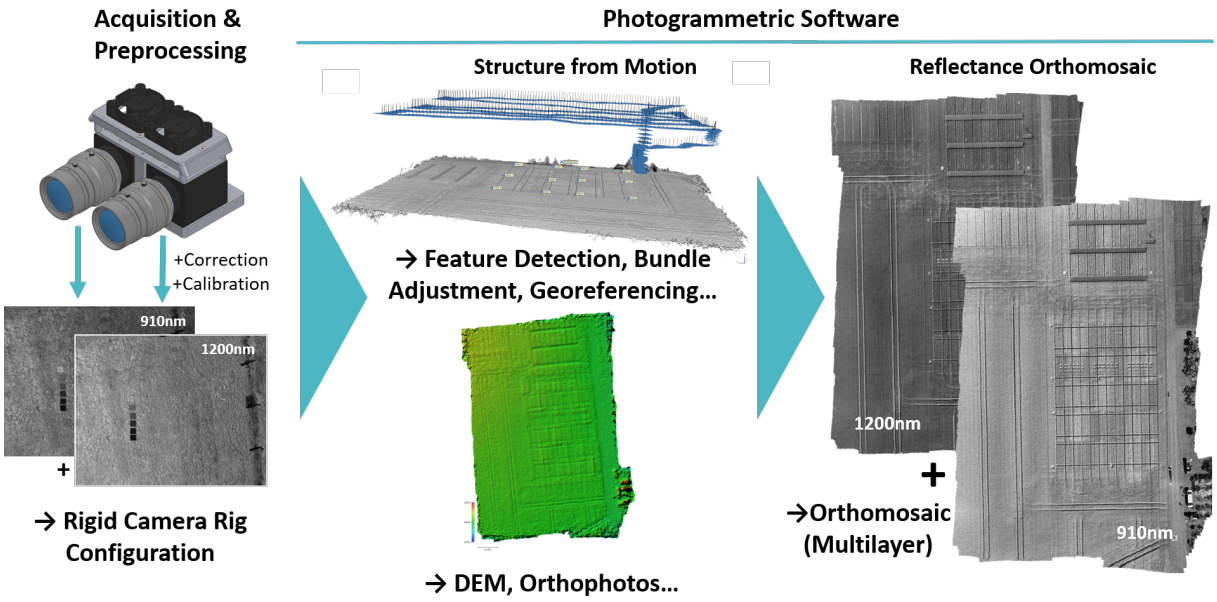


Figure 2.9: Data workflow: from raw digital image to reflectance orthomosaics (own illustration).

2.3 Spectral Vegetation Features

Figure 2.10 illustrates the process of spectral vegetation feature detection by optical remote sensing in a simplified schematic. The electromagnetic radiation emitted by the sun serves as a natural source of irradiation for the passive optical instruments used in remote sensing. Radiation reaching the canopy of vegetation through the relevant atmospheric windows ranges from about 250 to 3000 nm. Within the canopy, this radiation is reflected, transmitted, or absorbed mainly by the individual leaves but also by other parts of the plant. The most important physical process for applying passive optical instruments is, however, reflection (Grant, 2016).

Since the reflected portion of the incident radiation depends on the plant material's composition, it is possible to determine characteristic features by measuring this reflected component with optical instruments. Only a part of the reflection takes place at the surface of leaves. Since leaves are complex, multilayered objects with air and water cavities and intercellular structures, the radiation entering the leaf is scattered within the volume and thus partially reflected back toward the sensor. In addition, other processes such as absorption by pigments like chlorophyll and transmission through the leaf body take place. All these radiative properties are wavelength-dependent and can therefore determine a typical spectral response pattern of the observed canopy (Jones & Vaughan, 2010).

Since the incident radiation, like all natural processes, is non-invariant and thus fluctuating (Kumar et al., 2001), a measure independent of these external influences is needed to obtain comparable spectral reflectance data sets. Specifically, this measure must be independent of actual illumination conditions and instrument acquisition parameters (Mamaghani et al., 2019). Reflectance is such a measure and is expressed as the ratio of reflected and incident radiation, specifying how effectively a surface reflects radiant energy (Palmer & Grant, 2009).

The image sensors digitize the incoming reflected EM radiation to digital counts, often referred to as DNs. These DNs can then be converted by the empirical line method (ELM) (Smith & Milton, 1999; Wang & Myint, 2015) to reflectance values, representing a type of radiometric camera calibration (Langguth & Goesele, 2014).

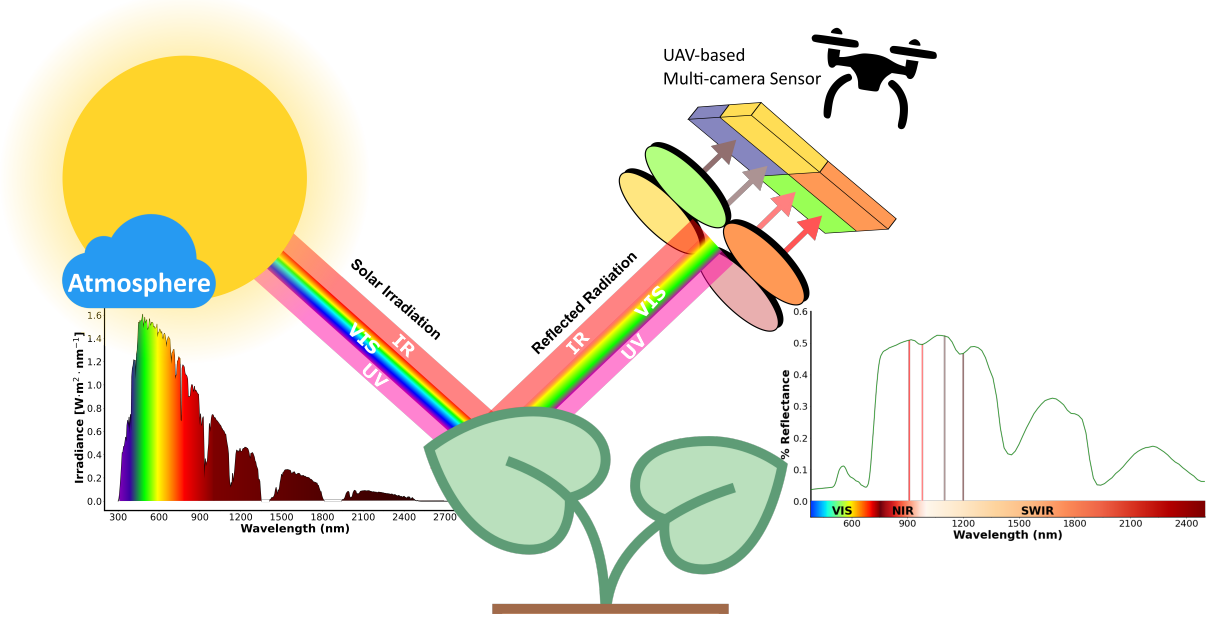


Figure 2.10: Schematic illustration of a UAV-based optical remote sensing system for detecting spectral vegetation features with a four-band multispectral multi-camera system (own illustration, inspired by Jones & Vaughan 2010).

This reflectance calibration technique is operated in various UAV-based spectral imaging applications (Berni et al., 2009; Assmann et al., 2018; Iqbal et al., 2018). It requires at least one accurate spectrally measured (near-)Lambertian reference panel to be included in the images to capture the actual illumination conditions for subsequent calibration of the image data. A surface has Lambertian reflectance properties if the energy of the incident illumination is uniformly distributed (i.e., perfectly diffuse) in all viewing directions (Koppal, 2014). Multiple panels in different shades of gray, from white to black, are more advantageous because this grayscale provides more interpolation values for the ELM and better covers the dynamic range of the optical sensors (Smith & Milton, 1999).

Vegetation has a characteristic reflectance spectrum that varies depending on plant species, health condition, and environmental factors. Figure 2.11 highlights the various plant constituents responsible for the different absorption characteristics of vegetation spectra, exemplified by green and dry grass. These absorption properties are dependent on wavelength, for example, because of foliar pigments and chemicals, intercellular plant structures, proteins, and water absorption (Curran, 1989; Fourty et al., 1996; Kumar et al., 2001).

The visual spectral range is dominated by strong absorption of pigments from chlorophyll and during leaf senescence from carotene and xanthophylls (Roberts et al., 2018). Since the energy levels in the near-infrared are lower, there is no interaction with the pigments there. However, the spectral response is influenced by intracellular plant structures, which particularly affect the transmission and reflectance of the respective electromagnetic radiation (Kumar et al., 2001).

The SWIR is dominated by water absorption so that this region is considerably attenuated by the atmosphere compared to the preceding spectral regions, and less energy reaches the ground from there. Nevertheless, water absorption bands can indicate plant water stress (Hunt & Rock, 1989) and are linked to biomass. However, despite the lower reflectance, this region also provides absorption bands of chemical constituents of the foliage.

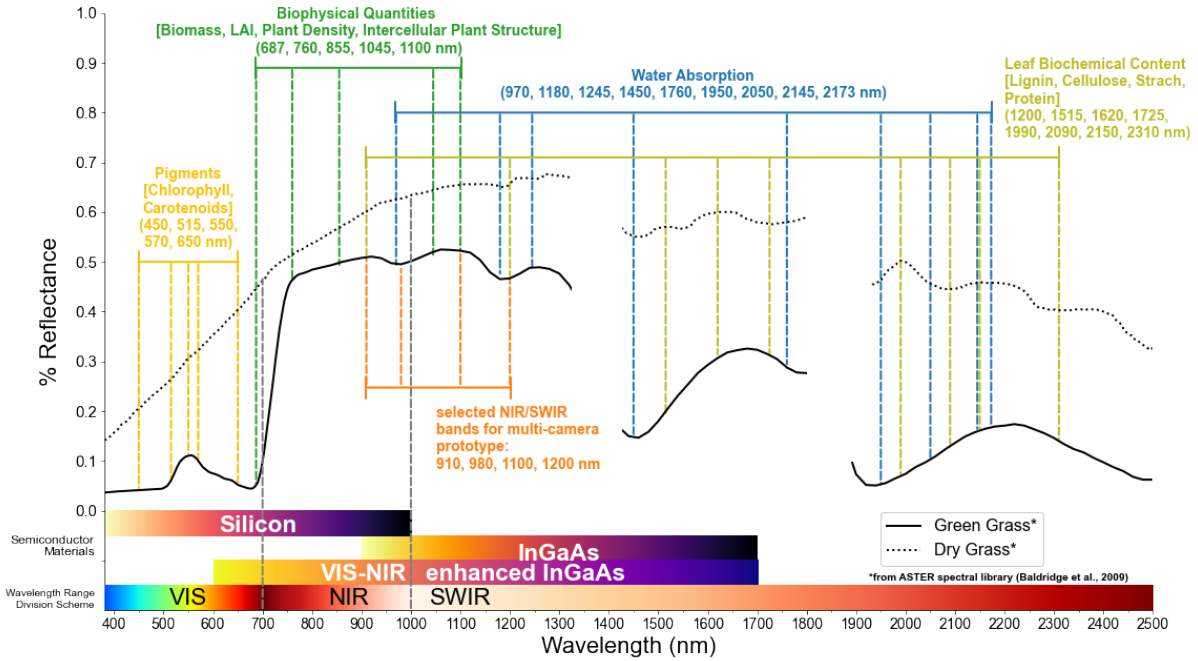


Figure 2.11: Green and dry grass reflectance spectra plotted from ASTER spectral library (Baldridge et al., 2009) and spectral features of vegetation as well as sensitivity limits of optical sensors and the narrowband filter used in the developed VNIR/SWIR multispectral multi-camera 2D imaging system (own illustration inspired and modified from Hank et al. 2019, Kumar et al. 2001 and Curran 1989)

In particular, spectral properties of important leaf components, such as proteins, cellulose, and starch, are found almost exclusively in the SWIR (Curran, 1989). These protein compounds are ideally suited for directly estimating nitrogen content, bound in the form of amino acids therein (Berger et al., 2020). Therefore, this spectral domain is of particular interest, and several studies have described it as very promising by several studies for establishing an effective N management practice in PA (Knox et al., 2010; Koppe et al., 2010; Herrmann et al., 2010; Thenkabail et al., 2013; Gnyp et al., 2014; Camino et al., 2018). Traditional optical remote sensing approaches, in contrast, estimate plant-linked N, by far the most important element for many metabolic processes in plants, through various surrogates, like chlorophyll or the leaf mass in the vegetation canopy, using the VIS and NIR (Roberts et al., 2018). However, these good estimation relationships unfortunately break down after the vegetative growth phase, after which, saturation effects also occur at high leaf area index (LAI) values (Roberts et al., 2004; Mutanga & Skidmore, 2004; Gholizadeh et al., 2017). Additionally, among other purposes, the SWIR range and the following thermal infrared ranges can be used to identify plant species to determine a spectral fingerprint (Buitrago et al., 2018). These facts make the SWIR domain an integral part of plant monitoring and should be increasingly included in vegetation analyses by multispectral imaging systems.

2.4 Vegetation Indices

Extracting useful environmental information from data acquired from airborne optical sensors is a major challenge in remote sensing. Therefore, acquiring multiple (multispectral) or a large set (hyperspectral cube) of spectral reflectance bands of vegetation raises the question of how to interpret them meaningfully. As shown in Figure 2.9, interpretation of such complex vegetation spectra is difficult, so a simplified approach to deriving vegetation characteristics is needed (Jones & Vaughan, 2010). In general, two types of approaches can be distinguished. One way to estimate biophysical features of the canopy is the application of radiative transfer models (RTMs) based on physical vegetation reflectance models, which on the one hand, provide very accurate results but on the other hand, are complex and computationally intensive, requiring a variety of input parameters that are not always available (van der Meer & de Jong, 2001; Kizel et al., 2018).
Therefore, a more simplified, empirical approach is often pursued, in which vegetation characteristics are measured using a single value derived from multiple narrow wavebands. This calculation of so-called vegetation indices (VIs) assumes that the mathematical combination of several wavelengths correlates with the relationship of biochemical or biophysical processes between electromagnetic radiation and plant material better than single wavelengths. VIs are mostly empirically designed to maximize sensitivity to vegetation features while minimizing interfering factors such as reflectance of soil, directional effects, and atmospheric effects (Jackson & Huete, 1991). Thus, in most cases, two wavelengths are combined by a simple ratio (Equation 2.4) or by a normalized ratio (Equation 2.5) calculation (Cohen & Alchanatis, 2018).

$$I = \frac{R_{\lambda_i}}{R_{\lambda_j}} \tag{2.4}$$

$$I = \frac{R_{\lambda_i} - R_{\lambda_j}}{R_{\lambda_i} + R_{\lambda_j}} \tag{2.5}$$

where: I : index value
R_{λ_j} : reflectance values in wavelength λ_i
R_{λ_j} : reflectance values in wavelength λ_j

Equation 2.5 is often referred to as an NDVI-like equation because the most commonly used VI, the normalized difference vegetation index (NDVI) (Rouse et al., 1974), also utilizes this equation and is adapted to different applications through a variety of two-band combinations in the VIS and NIR. Furthermore, there are more ways to mathematically combine the spectral information into VIs, even with more than two wavelengths. See Li et al. (2010) and Solymosi et al. (2019) for a more extensive overview.
Depending on the spectral bandwidth in which the data was recorded, VIs can be classified into broadband or narrowband. As a common rule, the VIs derived from data of multispectral instruments are mainly broadband (FWHM$\geq$10 nm). In contrast, the spectral data of hyperspectral instruments are narrowband (Roberts et al., 2018), and thereby allow to derive narrowband VIs. However, this categorization results from the fact that broadband bandpass filters are used, especially in multispectral systems. With the use of suitable optical filters (FWHM $\leq$10 nm), however, narrowband VIs can also be derived with multispectral systems (Hunt & Daughtry, 2018).

Some broadband VIs also have narrowband equivalents and can be used depending on the application (Broge & Leblanc, 2001). The advantage of narrowband VIs, in particular, is that they can be better tuned to specific spectral features by using finely resolved wavelength bands. In this way, vegetation's structural, biochemical, and physiological characteristics can be determined based on measurements of subtle individual absorption regions responsible for the characteristics of interest (Roberts et al., 2018).
Most VIs contain absorbing and non-absorbing wavelength bands. For instance, one of the most widely used indexes, the NDVI (Rouse et al., 1974), which can be used to determine the structural characteristics of vegetation, utilizes the spectral information about the chlorophyll absorption bands in the VIS and the reflective structural properties of the vegetation canopy in the NIR region. The dominant spectral domains most VIs are composed of are the VIS and the NIR. Only a few VIs use the potential of the SWIR domain. The most obvious use cases are VIs related to water content—because of the absorption properties of vegetation in the SWIR (Braga et al., 2021). Beyond that, and more importantly, narrowband SWIR-based VIs can provide essential spectral information on plant-based nitrogen and other biochemical components as well as fresh and dry biomass (Serrano et al., 2002; Koppe et al., 2012; Wang & Wei, 2016; Hank et al., 2019).
For the performed evaluation studies in this thesis, a total of four wavelengths were selected (910, 980, 1100, and 1200 nm) to be utilized with the VNIR/SWIR camera system prototype. These were used to derive two NDVI-like VIs designed explicitly for robust crop trait estimation. The first index applied was the normalized ratio index (NRI) defined by Sims & Gamon (2002), which was adopted to the SWIR domain by Koppe et al. (2010) for estimating winter wheat growth parameters. The second index applied was the four-band GnyLi index, which Gnyp et al. (2014) developed for biomass estimation in winter wheat. It also uses an NDVI-like equation as the NRI (Equation 2.6); however, the difference in the numerator and the sum in the denominator of the ratio equation consist of products of two salient features of the vegetation spectrum in the NIR and SWIR between 700 and 1400 nm (see Figure 2.11).

$$\text{GnyLi} = \frac{P_1 - P_2}{P_1 + P_2} = \frac{(R_{max_1} \times R_{max_2}) - (R_{min_1} \times R_{min_2})}{(R_{max_1} \times R_{max_2}) + (R_{min_1} \times R_{min_2})} \tag{2.6}$$

where: P_1, P_2 : products of two reflectance values
R_{max_1}, R_{max_2} : reflectance maxima
R_{min_1}, R_{min_2} : absorption minima

There are two high reflectance peaks caused by the intercellular structural composition of individual plant components around, 910 and 1100 nm (Kumar et al., 2001). The two reflectance minima are, on the one hand, moisture-related (980 nm) and, in the case of 1200 nm, originate from absorption characteristics of leaf chemicals (here, proteins) (Curran, 1989). The NRI utilizes the reflectance maxima at 910 nm and the absorption minima at 1200 nm, respectively. The wavelengths associated with both VIs in the original publications of Koppe et al. (2010) and Gnyp et al. (2014) had to be slightly modified to match available hybrid filter solutions and to minimize the number of flights required as well.

The derivation of the VI data from the four acquired spectral image data stacks is shown in Figure 2.12. Two image data stacks were acquired per flight, each covering the entirety of the experimental fields, with sufficient overlap between adjacent images to create a georeferenced multilayer orthomosaic, using SfM-based photogrammetry software (Metashape, see Section 2.2.3). These reflectance orthomosaics could then be further processed in GIS software (QGIS, 2022). Both VIs used in this work were then derived by applying the appropriate equations to process a GnyLi or NRI orthomosaic map of the experimental sites. With the help of shapefiles containing the vectorized plot boundaries of the respective field experiment, zonal statistics were then applied to the plots of interest to extract VI values from the orthomosaic raster layers. Finally, these VI data were further analyzed with different ground truth data in bivariate regression analyses for each plot.

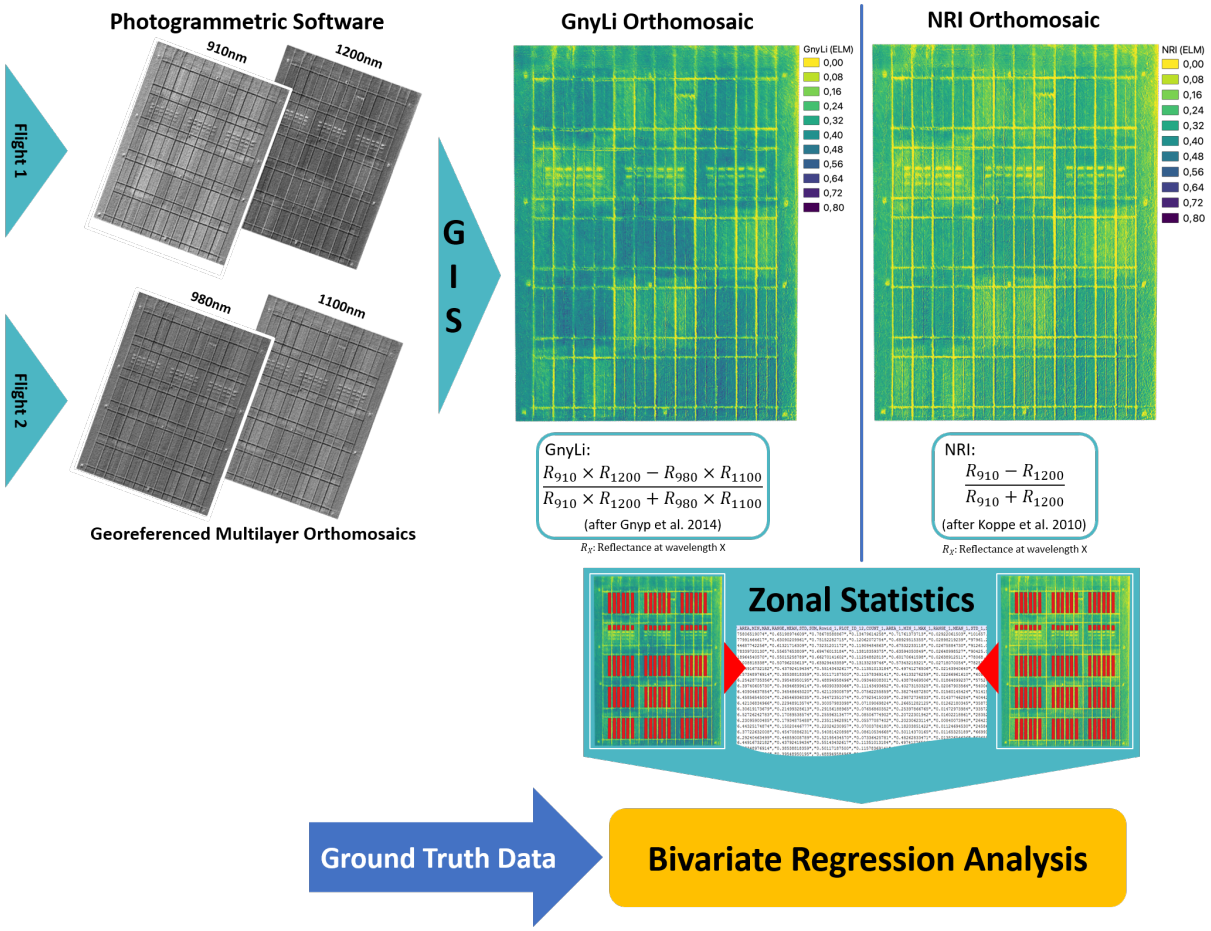


Figure 2.12: Data workflow for deriving the SWIR-based VIs, GnyLi and NRI, for the camera system prototype evaluation, with ground truth data in bivariate regression analyses.

3 | Development of a VNIR/SWIR Multispectral Imaging System for Vegetation Monitoring with Unmanned Aerial Vehicles

Alexander Jenal[1,2,*], Georg Bareth[2], Andreas Bolten[2], Caspar Kneer[1], Immanuel Weber[1] and Jens Bongartz[1]

Published in MDPI Sensors 2019, 19(24), 5507; doi.org/10.3390/s19245507

Formatting and orthography of the manuscript is adapted to the dissertation style.

1 Application Center for Machine Learning and Sensor Technology, University of Applied Science Koblenz, 53424 Remagen, Germany; kneer@hs-koblenz.de (C.K.); immanuel.weber@hs-koblenz.de (I.W.); bongartz@hs-koblenz.de (J.B.)

2 Institute of Geography, GIS & RS Group, University of Cologne, 50923 Cologne, Germany; g.bareth@uni-koeln.de (G.B.); andreas.bolten@uni-koeln.de (A.B.)

* Correspondence: alexander.jenal@hs-koblenz.de; Tel.: +49-2642-932-411

The author's contribution to this study is substantial and declared in detail in Appendix A.

Abstract

Short-wave infrared (SWIR) imaging systems with unmanned aerial vehicles (UAVs) are rarely used for remote sensing applications, like for vegetation monitoring. The reasons are that in the past, sensor systems covering the SWIR range were too expensive, too heavy, or not performing well enough, as, in contrast, it is the case in the visible and near-infrared range (VNIR). Therefore, our main objective is the development of a novel modular two-channel multispectral imaging system with a broad spectral sensitivity from the visible to the short-wave infrared spectrum (approx. 400 nm to 1700 nm) that is compact, lightweight and energy-efficient enough for UAV-based remote sensing applications. Various established vegetation indices (VIs) for mapping vegetation traits can then be set up by selecting any suitable filter combination. The study describes the selection of the individual components, starting with suitable camera modules, the optical as well as the control and storage parts. Special bandpass filters are used to select the desired wavelengths to be captured. A unique flange system has been developed, which also allows the filters to be interchanged quickly in order to adapt the system to a new application in a short time. The characterization of the system was performed in the laboratory with an integrating sphere and a climatic chamber. Finally, the integration of the novel modular VNIR/SWIR imaging system into a UAV and a subsequent first outdoor test flight, in which the functionality was tested, are described.

Keywords: short-wave infrared (SWIR); visible (VIS); near-infrared (NIR); remote sensing; unmanned aerial vehicle (UAV); multispectral; precision agriculture; phenotyping; forestry; vegetation

3.1 Introduction

Multi- and hyperspectral data acquisition with unmanned aerial vehicles (UAVs), also known as unmanned aerial systems (UASs), remotely piloted aircraft systems (RPAS), or drones has been of significant research interest in vegetation remote sensing applications during the last decade (Aasen et al., 2015; Berni et al., 2009; Colomina & Molina, 2014; Jaakkola et al., 2010; Lucieer et al., 2014). Operating systems with take-off weights below 10 kg makes them very flexible for spatio-temporal data acquisition at high to ultra-high spatial resolution. Hence, monitoring and considering phenological change patterns in a new and more appropriate way is possible. For example, water, nutrients, or other stresses can be investigated and differentiated in more detail (Calderón et al., 2013; Honkavaara et al., 2016; Näsi et al., 2015; Mahlein et al., 2019, 2013; Zarco-Tejada et al., 2012; Zheng et al., 2018).

However, most operational multi- or hyperspectral pushbroom or snapshot sensors capture wavelengths from approx. 350 to 1000 nm, in the so-called visible to near-infrared (VNIR) domain (Aasen et al., 2018). Sensors also covering the short-wave infrared (SWIR) are rarely available for UAV-based applications. To the authors' knowledge, the only exceptions are the SWIR sensor introduced by Honkavaara et al. (2016) and Tuominen et al. (2018), which is based on a tunable Fabry-Pérot interferometer (FPI) and pushbroom sensors as described in (Camino et al., 2018). In this contribution, we follow the VNIR (400 to 1000 nm) and SWIR (1000 to 2500 nm) definitions by Stark et al. (2015), which are mainly based on the spectral responses of the available image sensors (silicon and indium gallium arsenide—InGaAs, respectively). The advantage of frame sensors, in general, is that the captured images can also be used to create 3D spectral data and to correct for bidirectional reflectance distribution properties in images (Aasen et al., 2015; Aasen & Bolten, 2017). The combined analysis of structural and spectral data also seems to result in more robust estimators for vegetation traits (Tuominen et al., 2018; Bendig et al., 2015; Näsi et al., 2018; Tilly & Bareth, 2019; Saarinen et al., 2018; Waser et al., 2011; Aasen & Bareth, 2018).

The SWIR domain provides for remote sensing applications additional significant spectral absorption features, e.g., for geology (van der Meer et al., 2012; Hunt, 1979) as well as for vegetation trait retrievals (Kumar et al., 2001) using vegetation indices VIs like the normalized ratio index (NRI) introduced by Thenkabail et al. (2000). Koppe et al. (2010, 2012) showed that the two-band NRI using all possible band combinations in the VNIR/SWIR domain outperformed established VIs like normalized difference vegetation index (NDVI) for biomass monitoring of winter wheat by using a combination of NIR/SWIR wavelengths (874 nm to 1225 nm). Similar results are described by Gnyp et al. (2014), who introduced a four-band vegetation index, the GnyLi, for winter wheat biomass monitoring, which uses wavelengths of NIR/SWIR absorption characteristics (900, 955, 1055 and 1220 nm). Similar results for the GnyLi were reported for barley by Bendig et al. (2015) and Tilly et al. (2015). Besides biomass, nitrogen (N) uptake and N concentration are of crucial importance in vegetation trait monitoring. Camino et al. (2018) investigated the potential of SWIR bands to monitor N concentration in winter wheat.

The authors conclude that established VIs like the transformed chlorophyll absorption reflectance index (TCARI), the modified chlorophyll absorption in reflectance index (MCARI), or the optimized soil adjusted vegetation index (OSAVI) perform significantly better when using a SWIR version of these VIs using 1510 nm, i.e., the $TCARI_{1510}$, the $MCARI_{1510}$, and the $OSAVI_{1510}$.

Tilly & Bareth (2019) investigated the GnyLi for nitrogen and described very promising results. For the analysis of the water status of vegetation, for example, Gao (1996) introduced the normalized difference water index (NDWI). The NDWI utilizes spectral properties at 860 nm and 1240 nm in an NDVI-like equation mentioned in Haboudane et al. (2004). Similarly, the moisture stress index (MSI) performs as a simple ration index using a SWIR and NIR wavelength. Further, Serrano et al. (2002) introduced the normalized difference nitrogen index (NDNI) using 1510 nm and 1680 nm and the normalized difference lignin index (NDNI) using 1680 nm and 1754 nm. A comprehensive review of hyperspectral vegetation indices is given lately by Roberts et al. (2018). Summarizing the published studies using the VNIR/SWIR domain for determining vegetation traits, the additional usage of SWIR bands improves the detection of (i) biomass, (ii) nitrogen, and (iii) stress factors like water stress.

The research demand to evaluate and validate the true potential of the VNIR/SWIR domain for vegetation monitoring is very high due to its potential to derive more robust spectral estimators for vegetation traits also in combination with structural data analysis (Camino et al., 2018; Tilly & Bareth, 2019; Aasen & Bareth, 2018). Therefore, a VNIR/SWIR imaging system for UAVs is desired, which enables data acquisition in ultra-high spatial resolution and for certain phenological stages resulting in a daily or weekly temporal resolution. The VNIR/SWIR imaging system should also be able to capture selectable spectral bands for the purposes mentioned above, like the NDWI or GnyLi (e.g., 860, 900, 970, 1050 and 1240 nm). This paper presents the development of a novel and first VNIR/SWIR multi-camera 2D imaging system for UAVs, which combines two VNIR/SWIR sensitive cameras that are capable of selecting two wavelength bands from 400 to 1700 nm in parallel, with a custom-designed filter integration solution for fast interchanging filter setups.

The system was designed to be modular and expandable for use with a variety of airborne carrier platforms, especially for small to medium off-the-shelf UAVs (sUAVs) with a potential payload of 1.5 kg or more. In addition, the backend of the system offers additional capabilities to integrate more image sensors in the future to simultaneously acquire up to four wavelength bands. Since the VIS/NIR range is already covered by a large number of commercially available multispectral multi-camera systems (Aasen et al., 2018) (e.g., MicaSense 2019, MAIA 2019, Parrot 2019, and Tetracam 2019), this newly developed VNIR/SWIR imaging system is specially designed for wavelength detection in the SWIR spectral range. Especially already developed and validated VIs such as NDWI, NRI, or GnyLi can be examined by this system with a higher spatio-temporal resolution. Therefore, four wavelengths relevant for the NDWI, the NRI, and GnyLi (910, 980, 1100, and 1200 nm) were selected and used for the basic setup and tests. In principle, however, any filter combination from the VNIR/SWIR spectral range of 400 to 1700 nm is possible for UAV-based remote sensing applications.

Section 3.2 describes the hardware design and implementation process of the overall VNIR/ SWIR imaging system (Figure 3.1) in detail and begins with an overview of the spectral camera unit (SCU) (section 3.2.1) that is further divided into the single optical components which are the selected VNIR/SWIR camera sensors (section 3.2.1.1) and lenses (section 3.2.1.2) and the assembly layout for the optical filter placement, namely the internal filter assembly (section 3.2.1.3). Section 3.2.1.4 presents an overview of the mechanical structure of the SCU and considerations for a thermally optimized design.

The second part of the camera system, the sensor management unit (SMU), is described in section 3.2.2. There, the main components are delineated in detail. These include the selected frame grabber (section 3.2.2.1), the computer unit (section 3.2.2.1), and a custom-designed printed circuit board (section 3.2.2.3). Section 3.3 gives an insight into the methodology of the preliminary characterization of the camera system with regard to the thermal and optical properties. Section 3.4 presents the obtained test results of the individual components and the overall system outlined in section 3.2, as well as the characterization results of the parameters described in section 3.3.

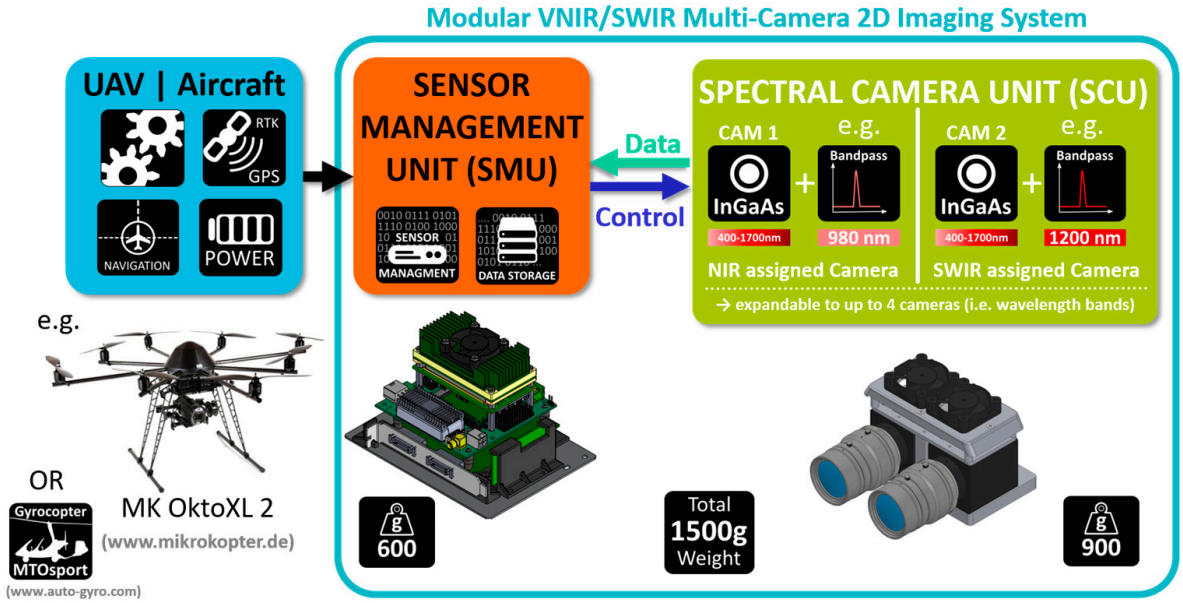


Figure 3.1: Schematic overview of the complete UAV-based VNIR/SWIR imaging system.

3.2 Hardware Design

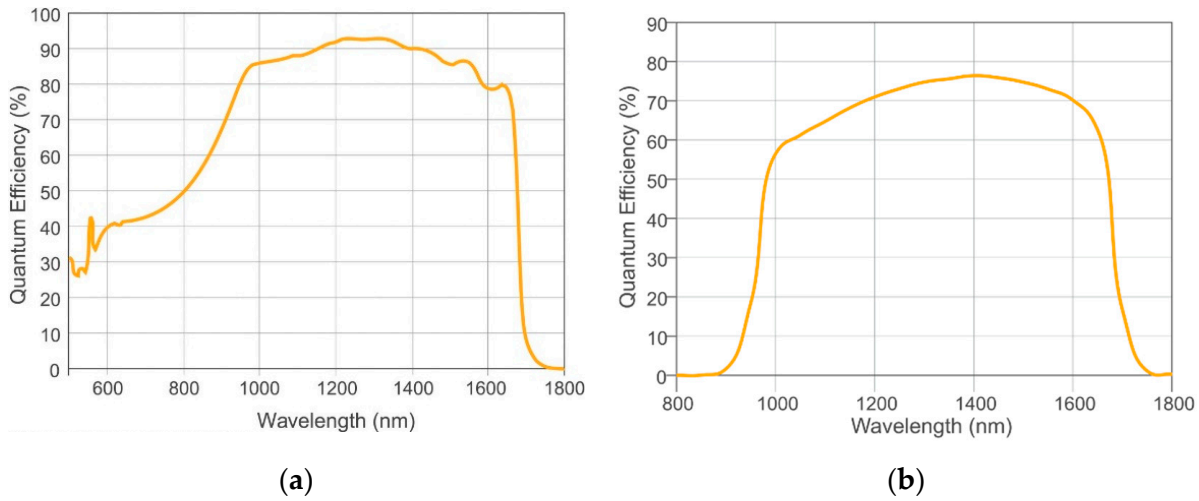
The system setup was designed modularly to improve usability for UAV-based image acquisition. Therefore, the system is divided into two modules (see Figure 3.1). The first one is the spectral camera unit (SCU), which consists of two InGaAs-based image sensors in the form of two machine vision cameras. The second part is the sensor management unit (SMU) that combines all components that are necessary to operate the system altogether. Computer-aided design (CAD) software was used to implement and adapt the system with specially developed parts. For rapid prototyping and manufacturing of the designed parts, an in-house industrial 3D production system was available.

3.2.1 Spectral Camera Unit (SCU)

3.2.1.1 VNIR/SWIR Image Sensor

SWIR sensitive camera modules were comparatively heavy in weight and complex in the past. Also, the high costs for a camera and the necessary accessories (lenses, filters) were exclusion criteria for many applications. However, due to the progress achieved in recent years both in sensor

technology and in microelectronics (Hansen & Malchow, 2008), and the increased production volume for industrial requirements, new camera modules that no longer have these disadvantages are now available. So-called SWaP cameras represent the latest trend in this optimization process, which focuses on the reduction of "size, weight and power". The Spectral Camera Unit (SCU) consists of two such OWL 640 Mini VIS-SWIR SWaP camera modules manufactured by Raptor Photonics (Raptor Photonics, 2019). The core component of each module is an indium gallium arsenide (InGaAs) photodiode array (PDA) with 640 × 512 pixels (quasi VGA) and 15 µm pixel pitch.
In contrast to the common photosensitivity of InGaAs focal plane arrays (FPA), with wavelengths between 900 nm and 1700 nm, this back-illuminated sensor has an extended sensitivity range down to approx. 400 nm (Figure 3.2) Martin (2015).



(a) **(b)**

Figure 3.2: (**a**) Quantum efficiency of the used VIS-NIR enhanced InGaAs Sensor (www.raptorphotonics.com/products/owl-640-tecless-vis-swir-ingaas/); (**b**) Quantum Efficiency of a standard InGaAs Sensor (www.raptorphotonics.com/products/owl-640-swir/).

Due to a further etching step during production, the indium phosphor (InP) passivation layer on top of the InGaAs layer is thinned out, so that also visible photons can pass through (Martin, 2015; Gardner et al., 2016; Cohen & Aphek, 2015). Due to the small bandgap of InGaAs, electrons can pass more easily from the valence band into the conduction band by thermal excitation, which leads to an increased intrinsic dark current compared to their silicon counterparts (Martin, 2015; Sullivan et al., 2013). According to the SWaP approach, however, the cameras do not have an integrated thermoelectric cooler (TEC) for temperature stabilization of the sensor. This produces a higher dark noise level. However, this increased noise floor is acceptable as the developed system is not intended for night vision applications but for bright daylight conditions, and therefore the shot noise of the photons determines both the dynamic range (DR) and the signal-to-noise ratio (SNR). The missing TEC, i.e., Peltier element, results in reduced power consumption of less than 2.5 W as well as a noticeably lower unit price. With a size of 60 mm × 42 mm × 42 mm and a weight of 170 g of a single camera module, it is compact enough to fit at least two units in an UAV-gimbal.

Both cameras output 14-bit image data via the CameraLink protocol (in base configuration). Therefore, the cameras cannot directly be connected to a computer like a USB3 Vision or a GigE Vision device. A frame grabber has to join up in circuit to transfer data from the cameras to a host computer. The frame grabber is integrated into the sensor management unit (SMU) and is described below (section 3.2.2). The SCU is therefore connected via two high-flexible CameraLink cables to the frame grabber unit. The sensor has a global shutter, which is inevitable for synchronized readout and artifact-free images (Aasen et al., 2018) during flight. Due to a universal clamping device, the camera body offers the advantage of creating even non-standard lens mounts via adaptable threaded flanges. The camera is supplied with a C-mount flange as standard. Since the two cameras are not completely identical in their properties and for the stringent allocation of the wavelengths during the measurement, each of the two cameras is allocated to a spectral range and named after it for better differentiation. The NIR filter camera (NFC) is primarily only used with NIR filters (up to 1000 nm) and the SWIR filter camera (SFC) only with filters from the SWIR spectral range (1000 – 1700 nm). In principle, the lower wavelength is always assigned to the NFC and the higher to the SFC.

3.2.1.2 VNIR/SWIR Camera Lens

Simultaneously with the selection of a suitable InGaAs camera, a suitable lens was also selected (Hansen, 2009). For each channel, the incident light passes through a Kowa LM12HC-SW lens (www.kowa-lenses.com) with a nominal wide-angle fixed focal length of 12.5 mm and a minimum f-stop of f/1.4. The lens is designed for $1''$ sensors, and the spectral transmission is optimized for the infrared range from 800 nm to 2000 nm. This wavelength range is sufficient for later use in the NIR and SWIR spectral range. However, if wavelengths below 800 nm become interesting, either a pure VIS or directly a VNIR/SWIR capable lens must be used. The wide-angle focal length was chosen to best fit the required ground sampling distance (GSD) of less than 0.1 m with regard to the flying altitudes of different aircraft like UAVs as well as microlights, e.g., gyrocopters. This helps, even for low-flying altitudes, to minimize the amount of image data while sufficient ground coverage and image overlap for structure from motion (SfM) and mutli-view stereopsis (MVS) algorithms are still guaranteed. Flight altitudes of 30 m above ground level (AGL) are envisaged for planned UAV applications. In combination with the sensor parameters, the various flight planning parameters of the system can be derived (Roth et al., 2018; O'Connor et al., 2017). The angle of view (AOV)) equals 27.51° in the vertical, 42.01° in the horizontal, and 48.79° in the diagonal. The respective field of view (FOV) at a working distance of 30 m results in 23.04 m horizontally, 14.69 m vertically, and 27.32 m diagonally with a ground sampling distance (GSD) of about 0.04 m.

3.2.1.3 Filter Assembly Layout for Spectral Band Selection

With the prime lens attached to the camera body, the imaging system is only capable of detecting the cumulated incoming light in the range of the spectral transmission of the lens as well as of the spectral response of the sensor. In order to select a specific and application-oriented spectral band out of this broadband spectrum, usually a bandpass filter with the best fitting center wavelength (CWL) and narrow bandwidth (BW) has to be integrated into the optical path.

In general, there are only two possible layouts to mount the filter in the optical path, as described by Wang et al. (2012). One solution is to mount the filter in front of the lens (front-assembly, Figure 3.3). In order to test this approach, special snap-on adapters for front-mounting the filter discs were designed and manufactured. Although this filter front-assembly is easier to implement and more practical to use, the optical characterization tests have shown that this configuration produces ring-like image artifacts. These are probably generated by mirror effects on the individual anti-reflective coatings of the filters and the individual lens. As both the exact origin and the quantification of these artifacts could not be clearly determined, this approach was not further pursued and was discarded during the development process. The second possible



Figure 3.3: (**a**) Exploded view of the developed adapter for the filter front-assembly; (**b**) Final version of the plug-in adapter with inserted filter elements and protective cap; (**c**) Flat-field image with ring-like mirroring artifacts. This design approach was discarded because of these ambiguous artifacts.

layout is the placement of the filter between the lens and the sensor (Wang et al., 2012). If the given form factor of the camera body allows it at all, this layout is more complex to realize. Also, for this solution, it is usually only possible to use existing off-the-shelf filter elements, which in turn means a limitation in both diameter and spectral properties.
Moreover, there are also two options for this internal approach. Firstly, a single interference filter mounted in a threaded ring can be screwed into the C-mount thread. However, this has the disadvantage that the blocking range of these single filter elements is not sufficient to cover the complete sensitivity of the VIS-NIR enhanced InGaAs sensor. This means that ordinary bandpass filters become transparent again to higher wavelengths above a specific cut-off wavelength, and thus light from unwanted spectral bands can reach the sensor. Fortunately, there are also hybrid filter elements with an ultra-wide blocking range available (Thorlabs, 2019). These hybrid filters consist of different filter elements, like interference and absorption filters, as well as a Fabry-Pérot cavity, which are perfectly matched to each other. Additionally, the FWHM is reduced to 10 nm for the two SWIR filters. A drawback of this filter structure is that the materials which increase the blocking range also decrease the overall transmission in the passband (Thorlabs, 2019).
Table 3.1 lists the detailed specifications of the selected filter elements so far used in the spectral camera system. The central wavelengths of the bandpass filters were selected for later use in the NIR/SWIR domain.

Table 3.1: Specifications of the applied hybrid bandpass filters (www.thorlabs.com).

CWL [1] (nm)	FWHM [2] (nm)	T [3] (%)	Blocking [4] (nm)	D [5] (mm)
910 ± 2	10 ± 2	≥50	200–2500	25.4
980 ± 2	10 ± 2	≥50	200–2500	25.4
1100 ± 2	10 ± 2	≥40	200–3000	25.4
1200 ± 2	10 ± 2	≥40	200–3000	25.4

[1] Center Wavelength; [2] Full Width Half Max; [3] Peak Transmission; [4] < 0.01% (< −40 dB); [5] Diameter.

Figure 3.4 shows the transmission data of the four used bandpass filters provided by the manufacturer (www.thorlabs.com). Compared to conventional hard-coated interference filters with typical transmissions of over 90 %, the reduced transmissions can be seen in the passband of the individual hybrid filter elements. On the other hand, these filters have an ultra-wide blocking range, which covers the entire spectral sensitivity of the sensor.

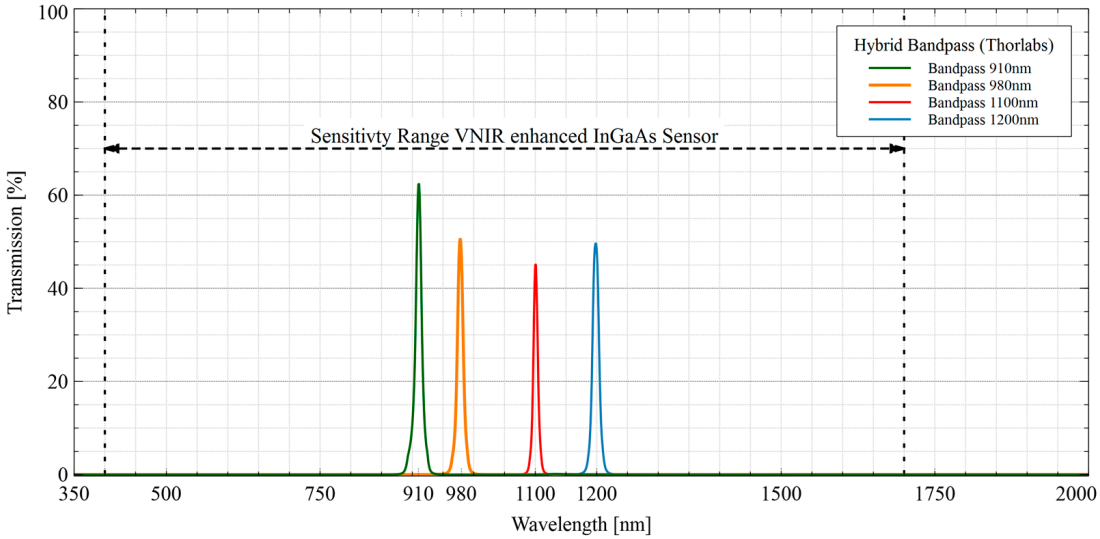
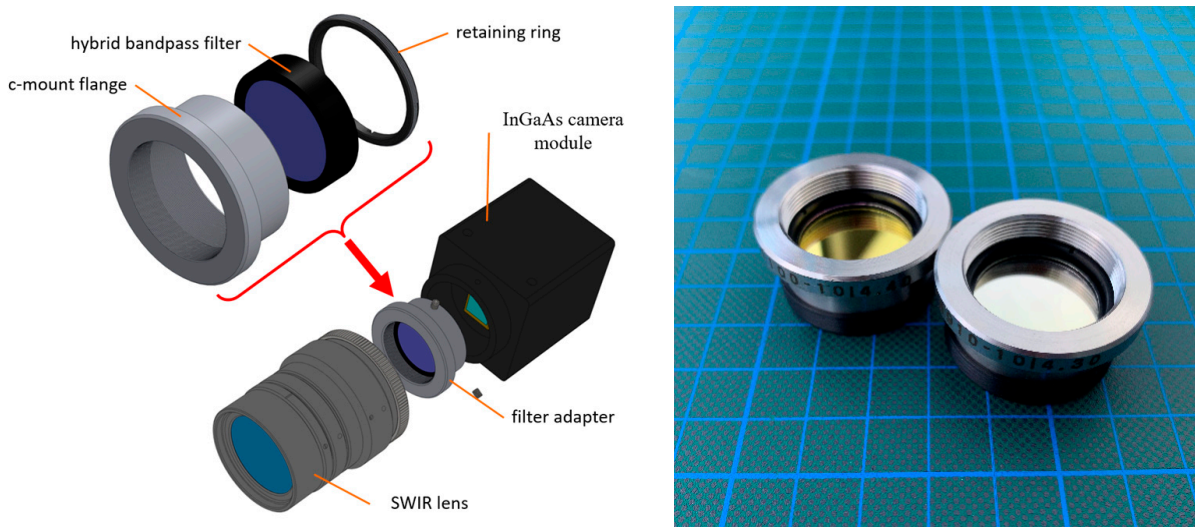


Figure 3.4: Transmission data of the used hybrid bandpass filters provided by the manufacturer (www.thorlabs.com).

Moreover, the camera mount type, here C-mount, defines the flange focal distance of a lens. Every optical component introduced into this path changes the focus characteristics of the lens, which requires compensation by appropriate measures (Wang et al., 2012). This can, for example, be achieved with an additional tube with focusing lens elements. In order to avoid these adjustments, a different solution was attempted, namely, to integrate the hybrid filters directly into the lens mount. As the lens mount of the used camera is replaceable, a custom C-mount flange could be designed (Figure 3.5). This component fulfills several tasks. The lens is mounted to it, the distance for adjusting the focus is compensated, and the individual hybrid bandpass filter element is placed as desired and is fixed with a retainer ring. A further advantage is the more parallel beam path in comparison to the wide-angle entrance area of the lens and the resulting smaller angle of incidence (AOI) on the filter. This reduces the possible blue-shift introduced by the wide-angle focal length of the lens (Stark et al., 2015). A further advantage is that these hybrid filters are also significantly cheaper than the large filter discs (50 mm), necessary for the front-assembly, due to their smaller diameter (25.4 mm).

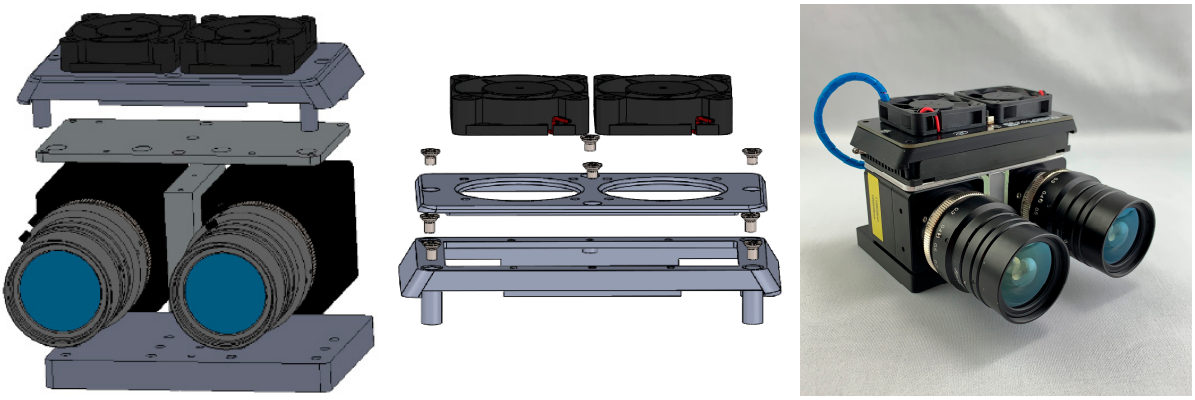


(a) (b)

Figure 3.5: (**a**) Exploded view of the custom-designed C-mount flange for the inlay filter assembly between lens and sensor; (**b**) Set of two equipped C-mount flanges with hybrid filters inserted.

3.2.1.4 Mechanical and Thermal Design

The exact parallel alignment of the two camera modules with each other is achieved by a specially designed and 3D-printed mounting plate (see Figure 3.6 a,c). This mounting plate also allows the two cameras to be easily mounted and aligned into a gimbal or on a tripod. As mentioned in section 3.2.1.1, the cameras have no integrated temperature stabilization circuit (TEC). Unlike other camera models from different manufacturers, the Owl 640 mini can be operated without a further external cooling system as long as the operating case temperature of +55 °C is not exceeded. If the camera is operated above this limit, the ohmic heat can cause permanent damage to the sensor and the electronics.



(a) (b) (c)

Figure 3.6: (**a**) Exploded view of the mechanical construction of the Spectral Camera Unit with an optional fan adapter applied; (**b**) Exploded view of the CAD model of the fan adapter of the SCU for thermal stabilization; (**c**) Current state of development of the SCU.

Moreover, sensor degradation is reduced with sensor temperatures below +40 °C, as well as the signal-to-noise ratio. Therefore, the two camera modules are thermally coupled and connected to a heat sink on top of the camera bodies (see Figure 3.6 b). To dissipate the heat more effectively, a specialized heat sink attachment that can be equipped with one or two fans was designed and 3D printed. Therefore, the system can be adapted to higher ambient temperatures. Attempts to cool the sensor with an external TEC were not successful. On the one hand, the operation of the TEC requires much energy and a correspondingly large and bulky heat sink. On the other hand, the cooling effect from outside the housing is far less effective than a TEC directly integrated into the image sensor circuit.

3.2.2 Sensor Management Unit (SMU)

The SMU (Figure 3.7) is layered from several individual components to form a compact unit (Figure 3.8), which can then be integrated as part of the overall imaging system, e.g., into a UAV. The unit consists of three main components:

- Frame grabber
- Adapter PCB
- Computing unit

and fulfills the following tasks:

- connecting the SCU to the computing unit via a frame grabber,
- providing regulated power with safety features to the overall system,
- controlling the two cameras of the SCU,
- storing the image data from the SCU,
- providing connections for additional hardware and future extensions like GNSS or IMU,
- providing enough computing power for future direct onboard image processing and machine learning tasks,
- providing further interfaces for additional cameras.

The individual components are described in detail below.

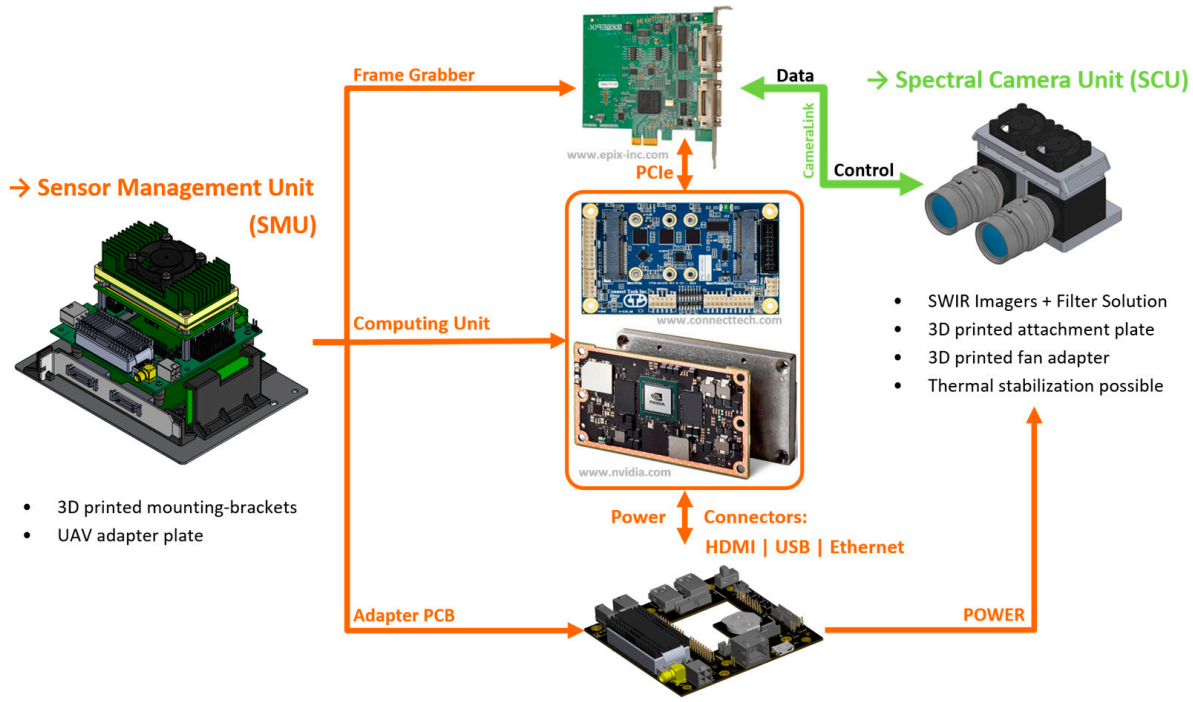
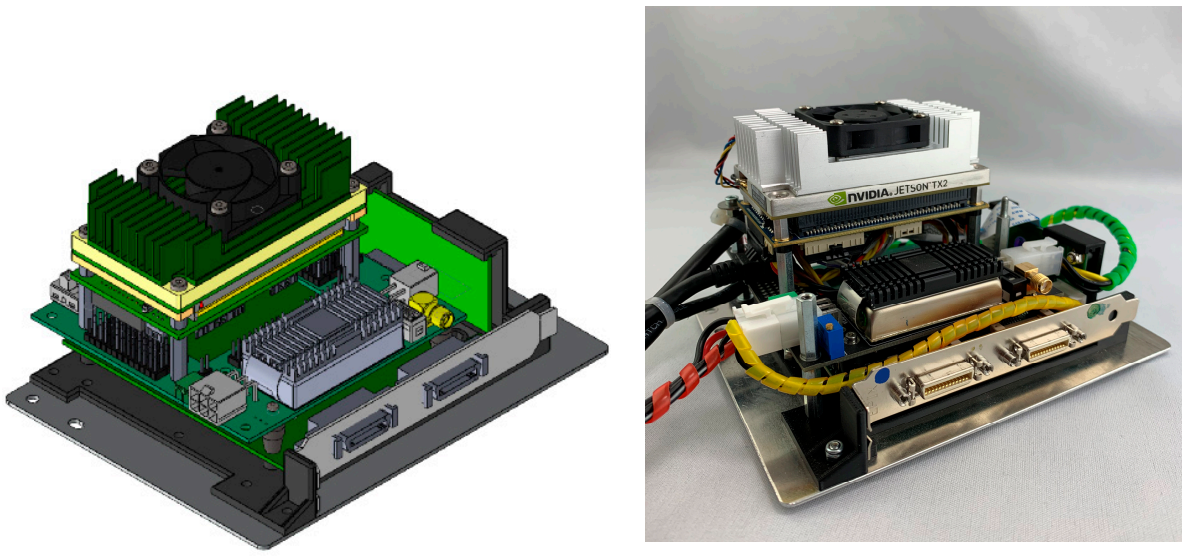


Figure 3.7: Detailed schematic view of the three main components of the Sensor Management Unit (SMU), and the interconnection of the single parts and the Spectral Camera Unit (SCU).



(a) **(b)**

Figure 3.8: (**a**) CAD side view of the assembled sensor management unit; (**b**) The current state of development of the SMU.

3.2.2.1 Frame Grabber

A dual CameraLink frame grabber card (base configuration, Epix Inc., www.epix-inc.com) serves as a bridge between the single cameras of the SCU and the computing unit. The frame grabber card is initially intended for installation in a desktop PC case and is usually connected to the mainboard via a PCI Express x1 Expansion Slot. Therefore, a mounting bracket adapted to the card was designed, and 3D printed to securely attach it to an adapter plate for the UAV integration. Epix offers a software (XCAP) to control the cameras and obtain image data via the frame grabber. Furthermore, the company provides its own "C" programming libraries (XCLIB) to access the frame grabber from self-written programs or graphical user interface (GUI) applications. These libraries are available for Windows as well as for various Linux operating systems. A GUI application has been implemented with the Epix application programming interface (API) for camera control and storing the acquired image data.

3.2.2.2 Computing Unit (CU)

The centerpiece of the computing unit is the Nvidia Jetson TX2 embedded system-on-module (SoM, www.nvidia.com, Figure 3.9). This little brick-shaped module is slightly larger than a credit card (50 × 87 mm) and weighs 85 g, including a so-called thermal transfer plate (TTP), but it combines all active processing components of a powerful computer

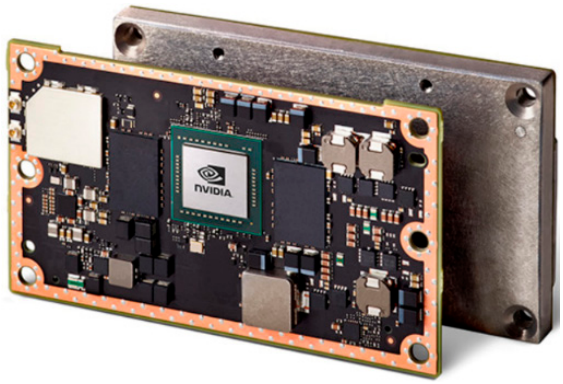
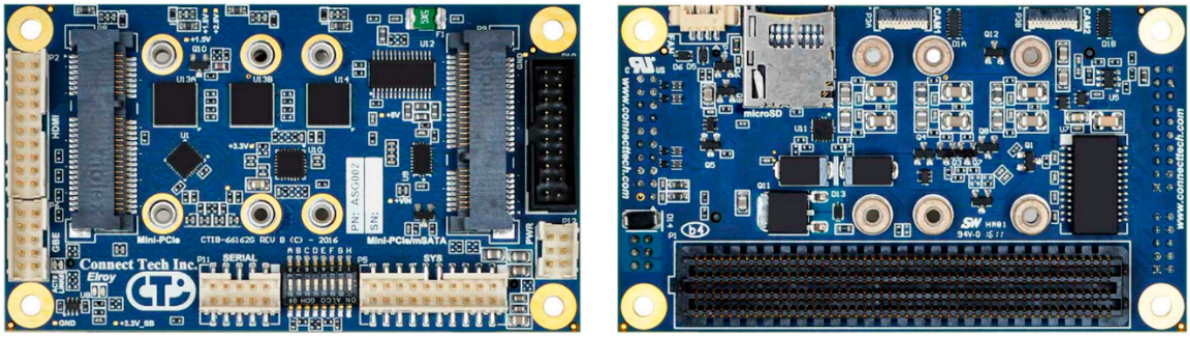


Figure 3.9: Nvidia Jetson TX2 system on module (SoM) and thermal transfer plate (TTP) (courtesy of NVIDIA).

For additional heat dumping in high-power mode, there is a fan-powered heat sink attached to the TTP. This small computer module runs with Ubuntu 16.04 LTS. The initial task for the TX2 is to run a specifically programmed software that can both control the cameras and read and store the image data from the cameras.
Since the TX2 is just a bare SoM, all signals, power rails, and the standard hardware interfaces are only accessible via a 400-pin connector. All these interconnections have to be broken out through different application-specific carrier boards provided by third-party companies. Therefore, the Elroy Carrier (EC) from Connect Tech (connecttech.com, Figure 3.10) was selected for the intended use of the TX2. In order to use the TX2, it was configured with the appropriate board support packages (BSP) for the EC and then mounted on the carrier board for the implementation in the SMU.

The Elroy Carrier matches the TX2 form-factor and provides most of the physical interfaces of the TX2. These are necessary to connect additional hardware such as SSD memory or the frame grabber card.



(a) **(b)**

Figure 3.10: (**a**) Front view of the top side of the Connect Tech Elroy Carrier; (**b**) Front view of the bottom side of the Connect Tech Elroy Carrier (courtesy of Connect Tech Inc.).

The mini-PCIe slot of the carrier can connect the Epix frame grabber via a mini-PCIe to PCIe adapter. An additional mSata slot on the EC extends the internal 30 GB memory of the TX2 with a half-sized 128 GB mSata SSD module. The remaining connections are provided by several pin-header ports that can be interconnected with prefabricated cable assemblies from Connect Tech.

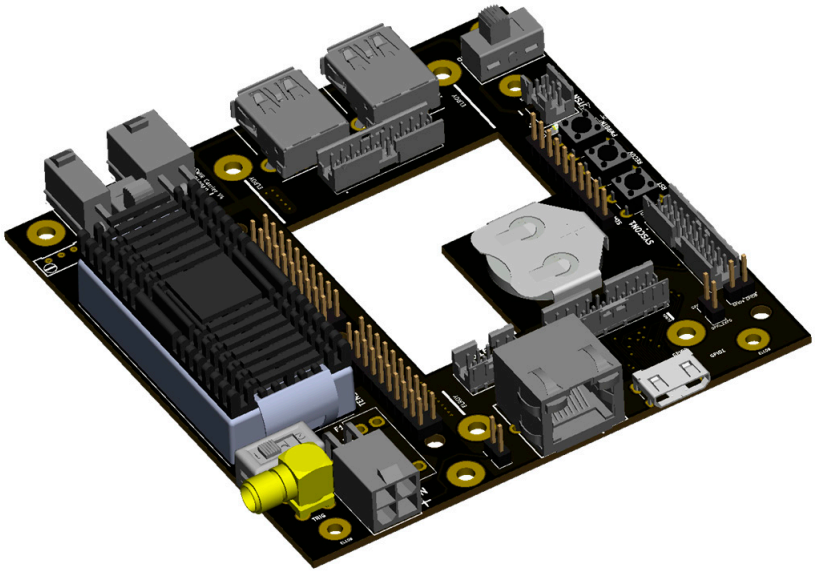


Figure 3.11: CAD View of the custom-designed and assembled adapter PCB.

3.2.2.3 Adapter Circuit

A printed circuit board (PCB, Figure 3.11) was developed to integrate the Jetson TX2 electronically and mechanically into the SMU. The latest revision (V4) fulfills three main tasks:

(1) Regulated power supply

Unlike other machine vision camera modules, the OWL 640 mini has only a very close tolerance regarding the supply voltage (12 V DC ±10%). Therefore, an isolated DC/DC converter was integrated into the PCB. This electronic part provides a constant voltage (12 V, 30 W max) for the overall system from a wide input voltage range (9 V to 36 V) and includes critical safety features like over-voltage protection, under-voltage lockout, over-temperature, and short-circuit protection.

(2) Mechanical Connection layer

The form factor of the Elroy carrier board allows direct electrical and mechanical mounting to the TX2 and forming the computing unit (CU). However, to establish a suitable mechanical connection of the CU to the frame grabber, an additional connection layer is required. Here, the board translates the drilling pattern of the frame grabber to that of the TX2.

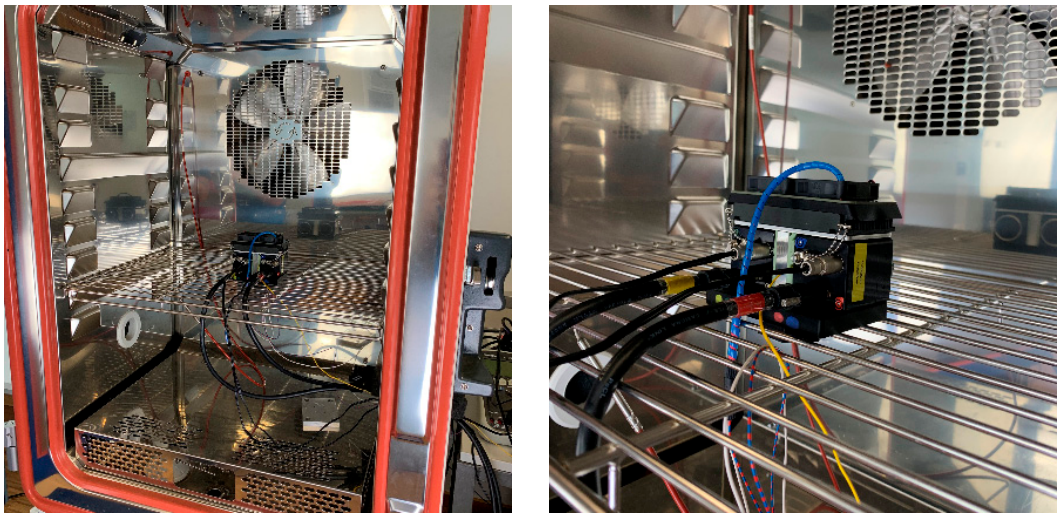
(3) Electronic connection and expansion layer

As described above, the Elroy Carrier provides the TX2 with a variety of hardware interfaces to connect the computer module to other hardware. In some cases, however, these components must be physically placed outside the Elroy Carrier and then connected via the appropriate cable connectors. Here the board is mainly used to accommodate pushbuttons, status LEDs, and interfaces such as USB, HDMI and Ethernet, which would otherwise have to be connected via bulky cables. The trigger inputs of the camera modules can be connected to the adapter board via an SMA connector with a coaxial cable. The SMA connector is connected via the PCB to one of the two GPIO inputs of the TX2. Most of the CU connectors are connected via pin-header sockets.

3.3 Methods for Preliminary Camera System Characterization

3.3.1 Thermal Management and Dark Noise

Self-heating is a determining factor for the magnitude of the various temperature-dependent sources of interference in image sensors, which in turn degrade the image quality (Sullivan et al., 2013; Strausbaugh et al., 2018; Hochedez et al., 2014). In principle, it is possible to read the temperature data of both the image sensor (CCD) and the electronics (PCB) of the OWL 640 mini camera module. This makes it possible to check the effectiveness of the implemented external thermal stabilization solution (see section 3.2.1.4) and to use the thermal information for later calibration procedures. For the thermal examinations, the SCU was inserted in a climatic chamber (Weiss WK11-180, www.weiss-technik.com, Figure 3.12). In order to check the thermal design considerations described in section 3.2.1.4, the two cameras in the SCU were operated with the external fans switched off. The resulting warm-up time of the image sensor and electronics was recorded at regular intervals with a constant ambient temperature in the climatic chamber and without a stabilized ambient temperature outside the chamber. Also, the ambient, as well as the enclosure temperatures, were logged. After a constant temperature level had been set inside the two cameras, the two external fans were activated to accelerate heat dissipation. The resulting temperature change was again recorded until a new saturation point was reached.



(a) **(b)**

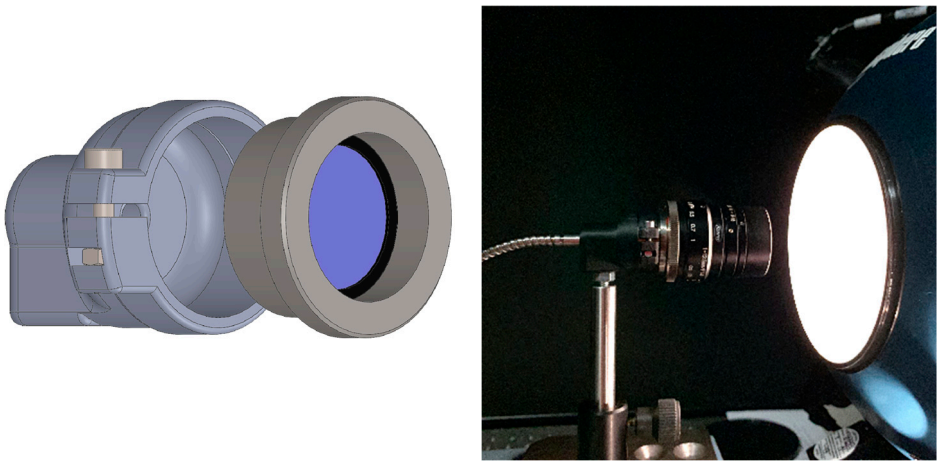
Figure 3.12: Measurement setup for thermal camera performance in a climatic chamber (Weiss WK11 180) at the test laboratory at the RheinAhrCampus of the University of Applied Science Koblenz: (**a**) Placement of the SCU in the climatic chamber; (**b**) Detailed view of the SCU into the climatic chamber.

As an ideal image sensor would not generate any signal in the absence of light and would only convert the light quanta hitting the single pixels into digital values when illuminated, real sensors, however, have undesirable effects due to various manufacturing inadequacies and material properties, which occur as disturbing effects in the image. In order to perform the most accurate and repeatable measurement possible, these imperfections must be determined at the sensor as well as at the pixel level and have to be reduced or eliminated by corrective measures. These effects can be measured in the absolute absence of light and are subsumed under the term dark signal (Theuwissen, 2011c). Subsequently, in order to determine the resulting dark signal of the two InGaAs sensors a more complex series of measurements were carried out in which several constant ambient temperatures were set in the climatic chamber (5 °C, 10 °C, 15 °C, 20 °C, 25 °C, and 30 °C). At each temperature point, a series of different exposure times were set, and 120 dark images were taken per exposure time for both sensors. Different statistical values were then calculated from these image data. These include the average dark signal and the fixed-pattern noise or dark signal non-uniformity (DSNU) (Theuwissen, 2011d,b,a). The test procedure and the calculation of the statistic values were based on the specifications of the EMVA1288 standard (EMVA, 2019) and Mansouri et al. (2005).

3.3.2 Evaluating the Transmission of the Optical System

The complete optics of the two camera channels consisting of the individual lens (2.1.2) and the particular filter combination and layout (2.1.3) were spectrally examined for compliance with the data provided by the manufacturers (see Figure 3.4). The spectral measurements were performed with an ASD FieldSpec 4 Wide-Res field spectroradiometer (www.malvernpanalytical.com), and an integrating sphere (Labsphere CSTM-USS-1200C-SL, www.labsphere.com) placed in the spectral laboratory at the Plant Sciences (IBG-2) at the research center Forschungszentrum (FZ) Jülich GmbH, Germany (www.fz-juelich.de/ibg/ibg-2).

Figure 3.13 shows the measurement setup for the internal assembly layout. For testing purposes, the fully equipped filter flanges were each mounted in a specially designed holding device (Figure 3.13 a). This is similar to the filter flange mount on the camera housing and places the front surface of the spectrometer fiber in the focal plane of the lens. This setup was then placed in front of the opening of the integrating sphere. The settings of the lens (aperture, focus) were kept constant for all measurements and are based on the settings for later use in the field.



(**a**) (**b**)

Figure 3.13: (**a**) Exploded view of the custom-designed fiber mounting adapter; (**b**) Measurement setup for transmission tests of the hybrid filter solutions (see also Figure 3.5) with an integrating sphere and an ASD FieldSpec 4 Wide-Res field spectroradiometer at the spectral laboratory at the IBG-2 at the research center Forschungszentrum Jülich, Germany.

3.3.3 Flat-Field Measurements

In a further step, the imaging properties of the entire optical system (SCU), including the sensor, were examined. Together with the filter adapters, the lenses were flange-mounted to the cameras, and the resulting imaging system was evaluated with the uniformly illuminated integrating sphere. Figure 3.14 shows the measurement setup with the front-assembly configuration as the device under test.

3.3.4 UAV Integration of the VNIR/SWIR Imaging System

The complete VNIR/SWIR imaging system was test-fitted to a Mikrokopter MK 6S12 (HiSystems GmbH, www.mikrokopter.de, Moormerland, Germany). This multi-rotor UAV has a maximum payload of around 2.5 kg. Depending on the payload and the batteries, the flight time varies between 15 and 30 min. Altitude, airspeed, and flight paths are controlled by a GNSS, a pressure sensor, and pre-defined waypoints that can be configured via the MicroKopterTool. The same system was effectively used to implement prototype sensors on a UAV (Yara-N-Sensor, Bareth et al. (2016); Cubert Firefly, Aasen et al. (2015), Aasen & Bolten (2017)). In the present study, the UAV is equipped with two 5800 mAh, 129 WH LiPo-batteries, and an additional one-hour power supply for the imaging system. The take-off weight of the complete system is around 7.2 kg. The estimated flight time is around 15 min, depending on wind speed and altitude changes.

For more details on the UAV, please refer to Aasen et al. (2015). Popular large-scale UAV like DJI Matrice 600 should reach a flight time around 30 min based on the flight time diagram on the manufacturer website (www.dji.com/matrice600).

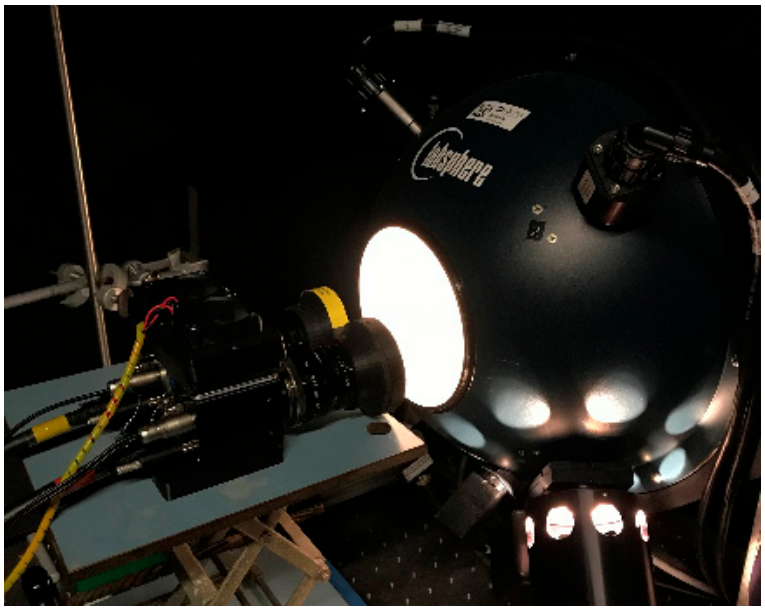


Figure 3.14: Measurement setup for the Spectral Camera Unit with the integrating sphere: for evaluation of the two different filter assemblies. The figure shows the test setup for the snap-on adapters of the front-assembly, which were no longer used due to artifacts.

The modularized two-part structure made it possible to connect the sensor managing unit (SMU) firmly to the frame of the UAV without having to change its entire structure. The spectral camera unit (SCU) was then mounted in the gimbal and connected to the SMU via flexible CameraLink ribbon cables. The gimbal uses two tilt servos to adjust pitch and roll and hold the system during the whole flight in a nadir position also outside of the balance point of the system. Figure 3.15 shows the individual parts mounted to the UAV.



(a) **(b)** **(c)**

Figure 3.15: (**a**) Front view of all adapted system components (SCU and SMU); (**b**) Spectral camera unit mounted in the gimbal of the UAS; (**c**) Side view of the SMU adapted to the frame of the UAS.

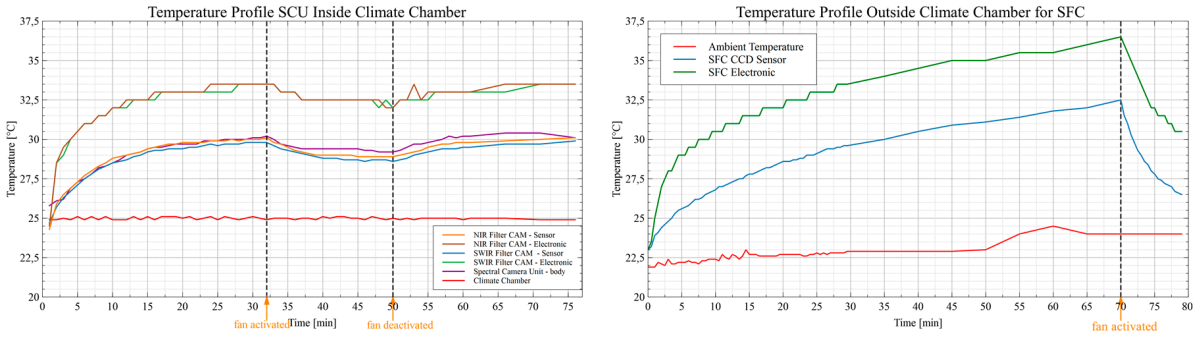
3.4 Results of the Prototype Camera System Characterization

Of utmost importance for developing a sensor system for UAV-based applications is the evaluation of the sensor itself (Mansouri et al., 2005; Jaakkola et al., 2010; Ewald et al., 2016; Lenhard et al., 2015), the integration in a UAV platform, and the validation of the complete sensing system. Therefore, we present firstly evaluation results of the newly developed VNIR/SWIR imaging system and secondly first test data captured in operational UAV mode.

3.4.1 Thermal Management and Dark Signal

3.4.1.1 Thermal Management

As described in section 3.3.1, temperature sensors can be read out at two points (sensor and control electronics) in each camera using special software. Figure 3.16 a shows the temperature profiles for both camera modules in the climatic chamber at a set ambient temperature of 25 °C. It can be observed that the two modules have settled to a constant temperature after about half an hour. Activating the fan system after 32 min hardly reduces the internal temperature. This circumstance can be explained by the way the climatic chamber works, which circulates the air in the chamber through a fan in order to keep the temperature inside constant. This airflow also effectively removes heat from the SCU and thus virtually replaces the fan system.



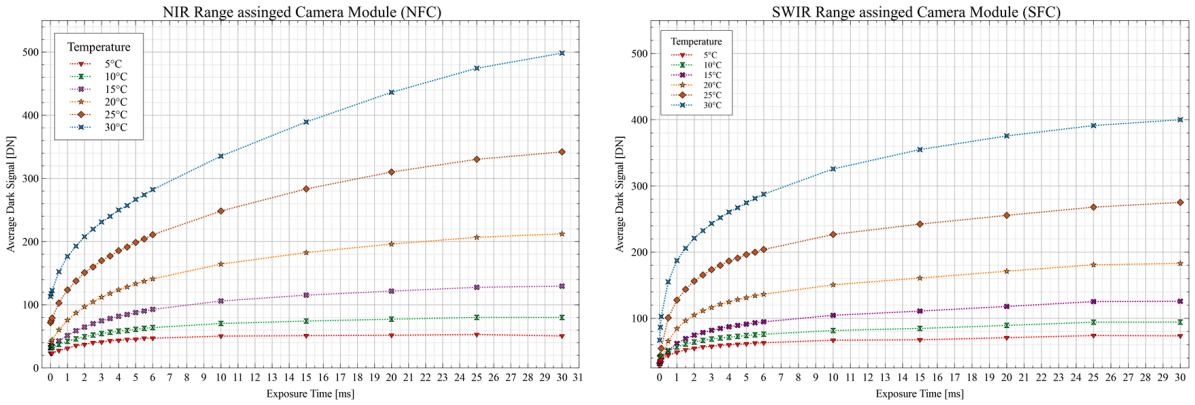
(**a**) (**b**)

Figure 3.16: Influence of the temperature management on the interior temperature of the camera: (**a**) Temperature behavior of the NIR filter assigned camera (NFC) and the SWIR filter assigned camera (SFC) at 25 °C constant ambient temperature within a climatic chamber; (**b**) Temperature behavior of the SWIR filter camera (SFC) at an unregulated ambient temperature outside a climatic chamber.

However, Figure 3.16 b shows the temperature profile of the SWIR Filter assigned Camera (SFC) outside the climatic chamber. After switching on, the temperature slowly increases until the control electronics reaches a temperature of 36.5 °C, and the fan system is activated. After the activation of the fan system, a definite temperature drop of 6 °C is to be recognized in each case, although the ambient temperature increased by 3 °C during the measurement. Hence, the self-developed cooling system works as expected. The performance of the fans used in the design is adapted in such a way that a maximum cooling effect is guaranteed with the least possible influence on the overall system by electromagnetic interference (EMI) or vibrations. During the test phase, therefore, no influence of the fan system on the cameras with regard to EMI or motion artifacts due to vibrations in the image data was detected.

3.4.1.2 Dark Signal

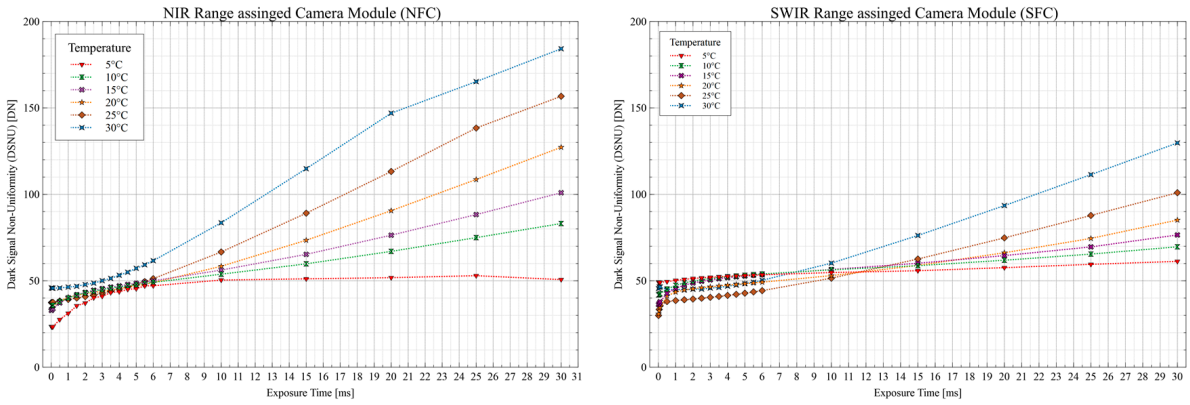
With the dark images taken at different constant temperatures with varying exposure times, the average dark signal can be determined (Theuwissen, 2011c). For each exposure time, 120 dark images were recorded and then averaged. The resulting image is then averaged pixel-wise. The results for the temperature behavior of the two sensors (NFC and SFC) are displayed in Figure 3.17. The profile of the average dark signal can be determined as a function of the exposure time and contains a fixed offset and a thermal dependent component, the so-called dark current, which in the end is the average dark signal. Based on the theoretically 14-bit (16384 digital numbers – DNs) resolution of the sensor, even the peak value determined for the average dark signal (498 DN 30 °C|30 ms) is not the decisive factor and negligible when used in daylight remote sensing applications. Here, the light signal itself, i.e., the shot noise, is the dominant factor for determining the maximum signal-to-noise ratio (SNR_{Peak}). This corresponds to the square root of the number of incoming photons or to the square root of the full well capacity of the pixels. Outdoor experiments revealed exposure times, as used in later flight scenarios, between 0.5 and 4 ms to be selected. This means that an exposure time of 30 ms is not used in later applications and that the average dark signal will be far below 500 DNs, at 30 °C and 30 ms for the NFC, in the range between 100 and 250 DN.



(a) **(b)**

Figure 3.17: Climatic chamber measurements of the average dark signal for sensor characterization: (**a**) Average dark signal for the NIR range camera module; (**b**) average dark signal for the SWIR range camera module.

Based on the average dark signal, the fixed-pattern noise (FPN), also called the dark signal non-uniformity (DSNU), which represents the variations of the dark signal between the individual pixels (Theuwissen, 2011d), can be calculated. This is the standard deviation of the pixel values for the averaged image of an exposure time at a specific set temperature. The DSNU is shown in Figure 3.18. As expected, the inter-pixel variation in the dark increases with increasing temperature and exposure time. However, also the FPN of 184 DN for the NFC sensor offers more than sufficient dynamic range for the 14-bit sensor at 30 °C and an exposure time of 30 ms, which is the upper range of the general operating limits.



(**a**) (**b**)

Figure 3.18: Fixed-pattern noise or dark signal non-uniformities (DSNU) as a function of various temperatures: (**a**) DSNU for the NIR range camera module; (**b**) DSNU for the SWIR range camera module.

3.4.2 Properties of the Optical System and Filter Layout

The more sophisticated filter integration layout is the so-called internal assembly (section 3.2.1.3) and consists of a specially designed C-mount flange that mounts only one (hybrid) filter element between lens and sensor (see Figure 3.5) for spectral band selection. The transmission curves in Figure 3.19 show the transmission properties of the four different bandpass filters used. As described in section 3.2.1.3, these consist of several different elements and thus achieve an ultra-wide blocking from 350 nm up to 2500 nm and therefore do not require any additional shortpass filter element. The measured transmissive properties are plotted in Figure 3.19 and show the advantage of these filters as well as confirm the manufacturer's specifications. Over the entire sensitivity range of the InGaAs sensor, they have an almost perfect blocking down to the desired passband ranges of the bandpass filters. Besides, the filter element can easily be inserted into the optical path via a special flange.

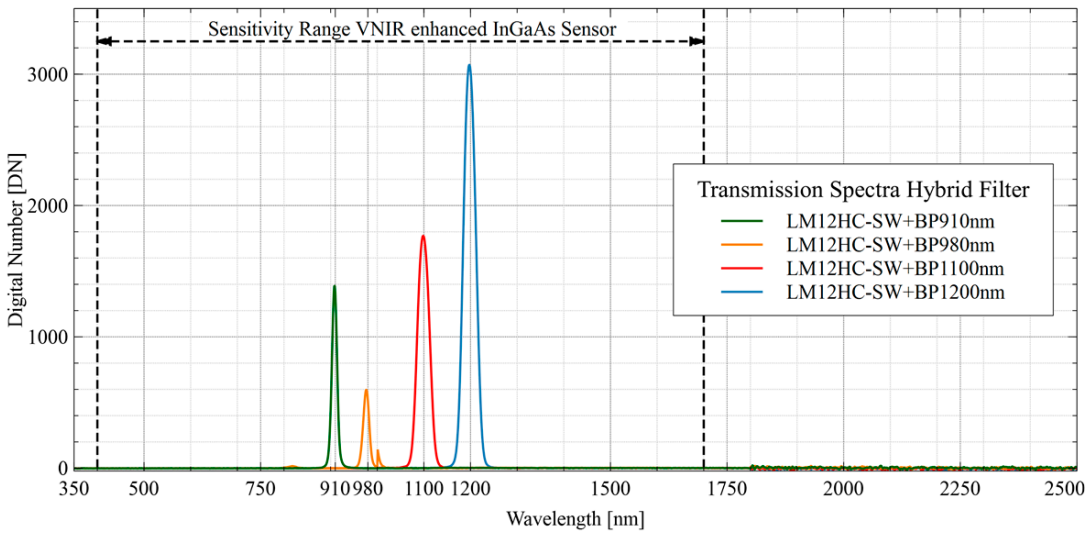


Figure 3.19: Recorded transmission data for the used SWIR lens and the four different bandpass filters (910 nm, 980 nm, 1100 nm, and 1200 nm, FWHM of 10 nm each).

3.4.3 Flat-Field Measurements

The optical characterization of the internal assembly approach was tested in a further step. For this purpose, the camera modules were equipped with the specially manufactured camera flanges (section 3.2.1.3). The hybrid filter elements were inserted beforehand into the corresponding flanges. Figure 3.20 shows the results of the flat-field measurements on the integrating sphere. In contrast to the above-mentioned, discarded front-assembly solution, no artifacts are visible for all investigated wavelengths in the flat-field data. This is also confirmed by the vertical image profiles of the individual images. Only a drop in intensity towards the edges of the image, the so-called vignetting effect, can be seen, which was expected and can be corrected.

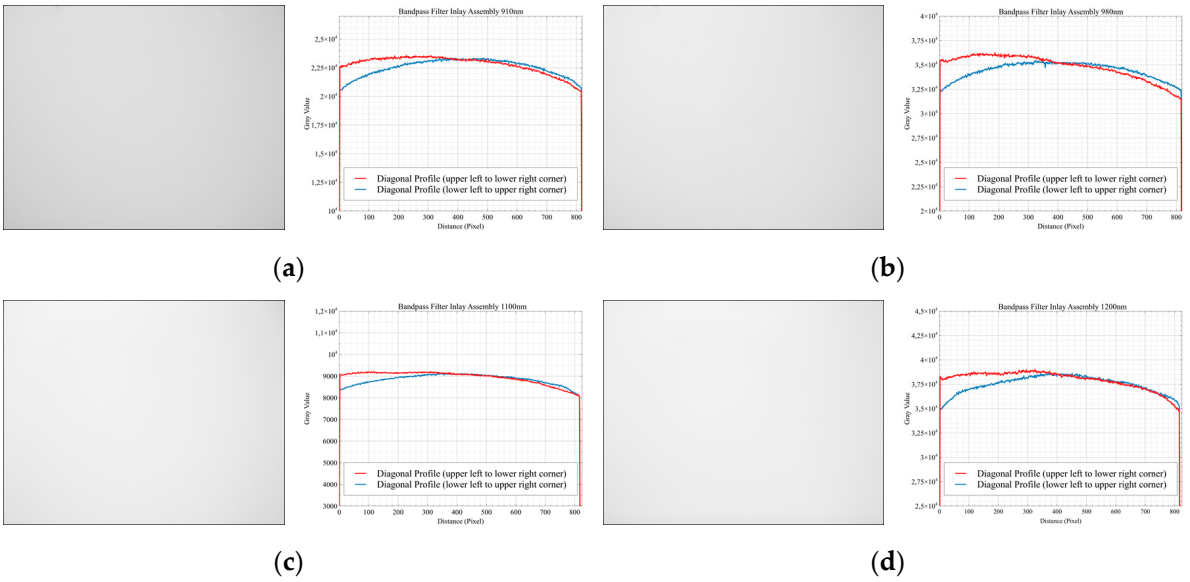


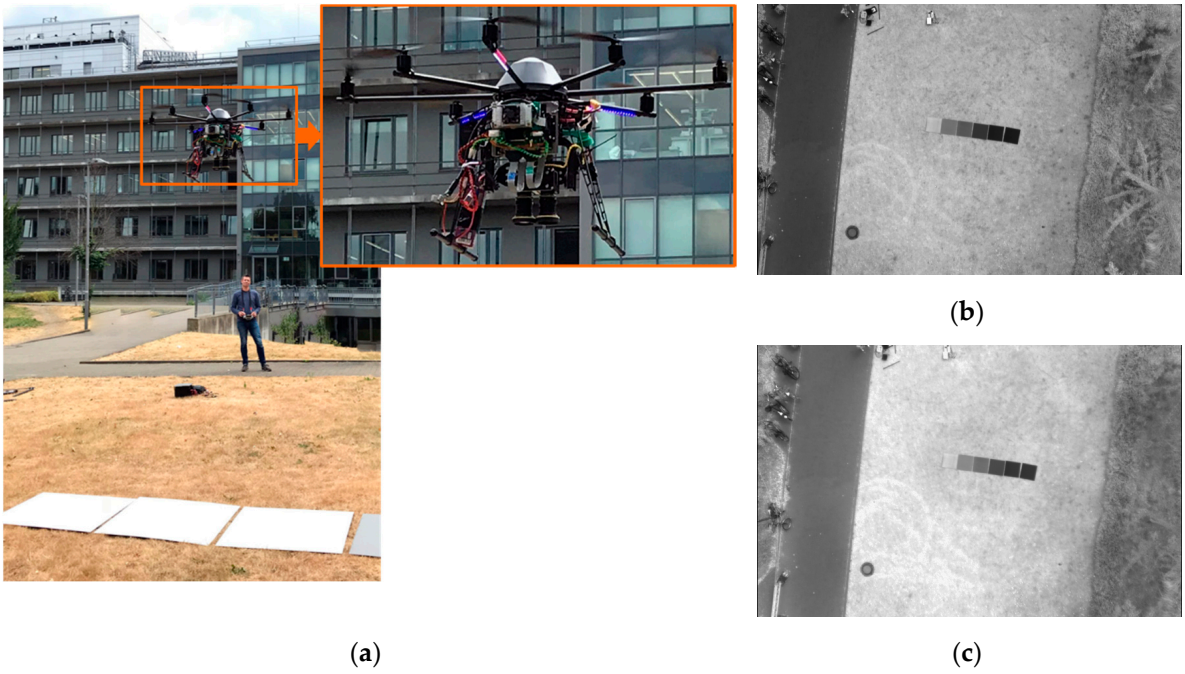
Figure 3.20: Flat-field image data from internal assembly layout with the corresponding diagonal image profiles plotted: (**a**) 910 nm; (**b**) 980 nm; (**c**) 1100 nm; (**d**) 1200 nm.

3.4.4 UAV Integration, System Test, and Test Flight of the Newly Developed VNIR/SWIR Imaging System

For the UAV integration, the SCU with the internal assembly approach of the filters was chosen. As described in section 3.2.1.3, the artifacts occurring in the front assembly layout make this spectral filter solution unusable for use in the camera system. In contrast, the internal assembly layout (section 3.2.1.3) does not generate any ambiguous artifacts (section 3.4.3) and has therefore been selected to be integrated into the SCU for further use. The main features of this newly developed VNIR/SWIR multispectral imager, as shown in Figure 3.1, are summarized in Table 3.2. After the integration of the camera system into the carrier platform as described in section 3.3.4 and successful tests in the laboratory, a first test flight at the outdoor area of the Institute of Geography (University of Cologne) was performed in the next step (Figure 3.21).

Table 3.2: Feature overview of the newly developed VNIR/SWIR imaging system.

Parameter	**Specified Value**
Sensors	InGaAs PIN-Photodiode
Data acquisition	Multi-Camera 2D imager
Spectral response	400 to 1700 nm
SNR_{Peak}	58 dB
Dynamic Range	71 dB
Shutter mode	Global Shutter
Power Supply	9 to 36 V
Power consumption	15 W @ 12 V
Weight:	
SMU	600 g
SCU	900 g



(a) **(b)** **(c)**

Figure 3.21: (**a**) The scenario for the test flight in which two image data sets with different wavelength bands were recorded; (**b**) Sample image of the acquired image data set from the 905 nm channel; (**c**) Sample image of the acquired image data set from the 1100 nm channel; The different reflection of the grass area between the wavelength and the nearly same reflection of the calibration panels and the concrete area is clearly visible.

Special attention was paid to possible shortcomings of the overall system during the flight. Particular attention was paid to the electromagnetic compatibility (EMC) of the individual components with regard to the high-current electronics of the rotor motors and to the influence of various vibration sources. Therefore, different flight situations, flight altitudes, and flight modes were tested. With the recorded test image data (Figure 3.22), the previously calculated ground resolution, the aperture settings on the lens as well as the optimal exposure time could be checked.

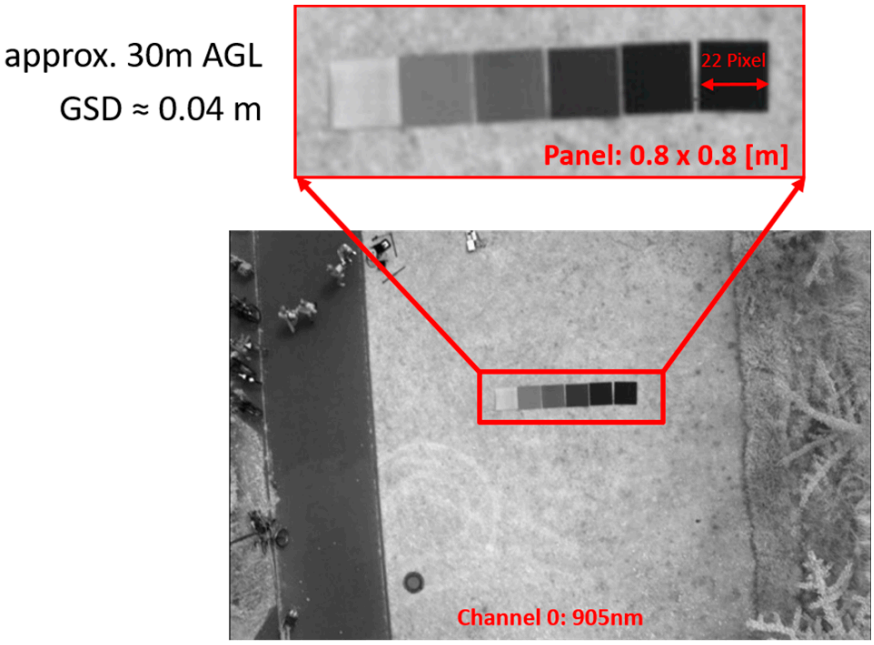


Figure 3.22: Calculations for the Ground Sampling Distance.

Based on the battery power used per time unit, a maximum flight time of around 14 min could be estimated for the whole system. Assuming a typical flight speed of 3 m s^{-1}, a ground altitude of 30 m, and an overlap of 75 % across-track, an area of 2 ha could be easily covered, which is sufficient for a typical experimental field.
In order to ensure that the image data of the two cameras of the SCU cover the same area on the ground, the SfM software Metashape (Version 1.5.5, www.agisoft.com) is currently used in combination with precisely measured ground control points. Each image data set of a specific wavelength is processed individually, and the georeferenced orthomosaics can be further processed and evaluated in a geographic information system (GIS). For single image capture, a dedicated image-to-image registration is performed, and the previous distortion corrected images of a trigger event at a certain altitude are merged into a multi-layer tiff. This is currently done with MATLAB (The MathWorks, 2015).

3.5 Discussion and Conclusions

Numerous studies indicate the higher potential for the VNIR/SWIR domain for remote sensing applications, e.g., vegetation trait estimations using wavelengths from the Red Edge to the SWIR domain (Camino et al., 2018; Bendig et al., 2015; Tilly & Bareth, 2019; van der Meer et al., 2012; Hunt, 1979; Thenkabail et al., 2000; Koppe et al., 2010; Gnyp et al., 2014; Tilly et al., 2015; Xavier et al., 2006; Thenkabail et al., 2004; Mutanga & Skidmore, 2004; Gnyp et al., 2013; Hu et al., 2019; Viscarra Rossel et al., 2006). While this spectral range is available for airborne or satellite-borne pushbroom sensing systems, for UAV platforms, only a few first studies are known (Tuominen et al., 2018; Camino et al., 2018). According to the authors, this is due to the fact that, in contrast to the VIS/NIR domain, there is currently no easy-to-use multispectral multi-camera system that also covers the SWIR spectral range.

There are different imaging systems with different sensor technologies that cover the VNIR and the SWIR spectral range for use with UAVs. Aasen et al. (2018), as well as Hagen & Kudenov (2013), provide a comprehensive review of the particular methods and systems. In the field of UAV-based SWIR imaging, especially pushbroom spectrometers (line scanners) (Lucieer et al., 2014; Calderón et al., 2013; Camino et al., 2018; Suomalainen et al., 2014; Zarco-Tejada et al., 2014) and partially sequential 2D imagers are used for data acquisition. Sequential 2D imagers use a tunable Fabry-Pérot interferometer (FPI) to set the desired spectral band (Honkavaara et al., 2016; Hakala et al., 2018; Näsi et al., 2016). The advantages are the high spatial resolution and the flexible selection of the wavelength bands. However, the scanning time depends directly on the number of bands required, which also affects other parameters such as exposure time, flight altitude, and flight speed (Aasen et al., 2018). Pushbroom scanners offer a high spatial and spectral resolution, which, however, is only achieved in complex post-processing through the individual spectrally and locally resolved line data. In addition to the scanner itself, a powerful computer with a large memory capacity for the spectral data and additional modules for exact georeferencing (GNSS, IMU) have to be used.
In contrast to pushbroom spectrometers, multispectral multi-camera imagers offer the advantage of concise and lighter sensor structures, a high spatial resolution, and more straightforward data processing and evaluation methods, however, with the disadvantage of significantly reduced spectral information. They are therefore applied to use cases where the selection of spectral channels relevant to the problem has already taken place in previous studies and has been established, e.g., in vegetation indices to facilitate further investigation of a relevant topic.
Although there are many multi-camera imaging systems for the VNIR range (MAIA, 2019; Parrot, 2019; Altum, 2019; RedEdge-Mx, 2019; Mirco-MCA, 2019), there is currently no multi-camera imaging system with a spectral response in the SWIR range (from 1000 nm upwards). Therefore, the first modular prototype of a multispectral multi-camera system using two VNIR enhanced SWIR imagers (approx. 400 to 1700 nm), and a powerful single-board computer was developed that is lightweight and compact enough to be carried by UAVs with a sensor payload capacity starting from 1.5 kg. Furthermore, the spectral image data of this newly developed VNIR/SWIR imaging system can be used for SfM and MVS analysis, resulting in spectral 3D data from one sensor (Aasen et al., 2015; Aasen & Bolten, 2017). Several authors already investigated the benefits of combined spectral and structural data analysis of vegetation (Aasen & Bareth, 2018; Pinto et al., 2017). Roberts et al. (2018) and Camino et al. (2018) show, for monitoring vegetation traits, only a few VNIR/SWIR analyses require more than two to four spectral bands.
Two mounting devices, the so-called external and internal assembly, for placing the individual filters in the optical path of the respective sensor were successfully designed, built, and tested. The external filter positioning in front of the lens, realized by a snap-on adapter, is the more straightforward and, therefore, the most used setup for multi-camera systems. During imaging tests, however, this solution has proven to be unsuitable, as ring-like mirror artifacts have occurred. Therefore, this layout was discarded for further use at an early stage of development. The so-called internal assembly solution, however, positions the individual filter between lens and sensor via a specially developed and self-manufactured stainless steel C-mount flange. Each filter used is inserted into its own flange, which is specially adapted to the optical system. This means that the entire flange is always replaced when the filter is changed.

In contrast to the rejected front-assembly layout with the developed snap-on filter adapter, this flange design has even more advantages. On the one hand, the light beams emerging from the lens are more parallel, and a significant angle-dependent wavelength shift (blue-shift) (Stark et al., 2015) could not be detected in the spectroradiometer measurements. On the other hand, there are no ring-like mirroring artifacts generated by back reflections in the images, as the flat-field measurements have shown. In addition, the hybrid filters offer excellent blocking over the entire sensitivity range of the InGaAs sensor, so that only one filter element is required instead of two for the front-assembly approach. Due to the smaller diameter (25.4 mm), this solution is also less expensive than filter discs with a larger diameter (50 mm).

The spectral camera unit (SCU) was intensively tested for various parameters, both in a climatic chamber and with an integrating sphere. The tests in the climatic chamber included a preliminary characterization of the thermal noise behavior of the individual camera sensors and their internal electronics, both at different temperatures and exposure times. The determined parameters of the Average Dark Current and the Fixed Pattern Noise provide information at the pixel level and are indispensable for further corrective measures, since InGaAs sensors in particular exhibit higher temperature-induced noise values compared to silicon sensors. During the test flight it was shown that in daylight conditions exposure times between 1 ms, cloudless sky, and 4 to 6 ms, cloudy sky, the sensors are still sufficiently illuminated so that not the noise part of the sensor, but the shot noise of the photons is the dominant part of the SNR. Furthermore, the effectiveness of the specially developed external fan system was tested.

With activated fans, a significant reduction and stabilization of the sensor temperature of 6 °C relative to the ambient temperature could be achieved. This is especially important in situations where the ambient temperature causes the internal temperature, especially the sensor temperature, to rise to a critical level. The influence of the fans on the cameras with regard to EMI or motion artifacts due to vibrations could not be detected in the image data.

The tests in the spectral laboratory included the validation of the filter characteristics of the two developed layouts (front- and internal assembly) as well as a preliminary characterization of the complete optical system (flat-field) with both filter assembly solutions. Only the internal assembly design proved to be suitable for further use, since the front-assembly layout generated ring-like artifacts in the image data due to mirroring effects. The modular system was then successfully integrated into a multirotor UAV and tested in aerial operation.

The current state of development of the system allows the simultaneous image data recording of two wavelength bands. For collecting further bands, the equipped filter combinations have to be exchanged, and the examination area has to be flown over again. In stable weather conditions, this is no problem because the image data of the newly developed prototype can easily be georeferenced via precisely measured ground control points. Additionally, spectral reference panels, as shown in Figure 3.21 b,c and Figure 3.22, should be placed for each flight to ensure spectral ground-truth data. The UAV-based acquisition of overlapping image data with 0.04 m spatial resolution with two spectral bands takes for 1 ha approx. 7 min. In total, the data acquisition of four different VNIR/SWIR bands takes about 20 min (including filter change). Larger areas of up to 10 ha can be covered in lower resolution (approx. 0.13 m) at the same time. The latter resolution would be still precious to use calibrated VNIR/SWIR data from UAV data acquisition, also for validating satellite-borne remote sensing data.

Due to the remaining payload capacity of the UAV and the backend connectivity, up to two additional cameras can be added to the system to capture four spectral bands simultaneously. Although a quadruple VNIR/SWIR camera system would be the optimal solution, the first approach could be to cover the NIR range with two additional NIR-enhanced CMOS cameras based on silicon. These cameras are cheaper to acquire and even more compact and lighter than the OWL 640 Mini.
This study presents the novel development setup and initial validation of the first VNIR/SWIR imaging system for extending the possible spectral range to the SWIR domain in the field of UAV-based multi-camera systems. This new VNIR/SWIR imaging system for UAVs will enable innovative studies for remote sensing applications, e.g., to analyze non-destructively vegetation traits with a high spatio-temporal resolution. The next steps are the validation and calibration of the newly developed system for continuous vegetation monitoring for biomass, nitrogen, and stresses to verify its suitability for mapping VNIR/SWIR-based VIs such as NRI or GnyLi. Although the prototype already performs as expected and provides image data under real test conditions, it needs to be comprehensively tested and validated in remote sensing projects. Therefore, several UAV campaigns have been conducted for a grassland experiment, where spectral ground-truth data and vegetation traits were and will be collected simultaneously. In 2020, these activities will be extended to field experiments of crops, monitoring of silvopastoral systems, and forest applications.

3.6 Author contributions

Conceptualization, A.J., G.B. and J.B.; system and software design, A.J.; system evaluation, A.J.; UAV piloting, A.B.; UAV integration, A.J., A.B.; writing—original draft preparation, A.J.; writing significant parts of section 3.1 and section 3.5, and contribution to the other parts of the manuscript, G.B.; writing—contribution to sections 3.3.4 and 3.4.4, A.B.; writing—review and editing, all authors; revision and printing of CAD parts, C.K.; Matlab scripts for data evaluation and support for software development, I.W.; J.B. reviewed the manuscript, contributed text and figures, and supported the work through essential discussions.

3.7 Funding, Acknowledgments, and Conflict of interest

Major parts of this work were funded by the Ministry of Science, Further Education and Culture MWWK of Rhineland-Palatinate (www.mwwk.rlp.de), Germany.

The authors want to thank the IBG-2, Uwe Rascher, at the research center Forschungszentrum Jülich GmbH (Germany) for providing access to their integrating sphere and the ASD Fieldspec 4 at their spectral laboratory for evaluation analysis.

The authors declare that they have no conflict of interest.

3.8 References

Aasen, H. & Bareth, G. (2018). Spectral and 3D Nonspectral Approaches to Crop Trait Estimation Using Ground and UAV Sensing. *Hyperspectral Remote Sensing of Vegetation*, volume III Title: Biophysical and Biochemical Characterization and Plant Species Studies, 103–131. CRC Press Taylor & Francis Group, (second edition ed.). https://doi.org/10.1201/9780429431180-4

Aasen, H. & Bolten, A. (2017). Multi-temporal high-resolution imaging spectroscopy with hyperspectral 2D imagers – From theory to application. *Remote Sensing of Environment*, 205(September 2017), 374–389. https://doi.org/10.1016/j.rse.2017.10.043

Aasen, H., Burkart, A., Bolten, A., & Bareth, G. (2015). Generating 3D hyperspectral information with lightweight UAV snapshot cameras for vegetation monitoring: From camera calibration to quality assurance. *ISPRS Journal of Photogrammetry and Remote Sensing*, 108, 245–259. https://doi.org/10.1016/j.isprsjprs.2015.08.002

Aasen, H., Honkavaara, E., Lucieer, A., & Zarco-Tejada, P. J. (2018). Quantitative Remote Sensing at Ultra-High Resolution with UAV Spectroscopy: A Review of Sensor Technology, Measurement Procedures, and Data Correction Workflows. *Remote Sensing*, 10(7), 1091. https://doi.org/10.3390/rs10071091

Altum (2019). *Altum-PT - MicaSense*. https://micasense.com/altum/. Last accessed on 20 January 2022.

Bareth, G., Bolten, A., Gnyp, M. L., Reusch, S., & Jasper, J. (2016). Comparison of Uncalibrated RGBVI with Spectrometer-Based NDVI Derived from UAV Sensing Systems on Field Scale. *ISPRS - International Archives of the Photogrammetry, Remote Sensing and Spatial Information Sciences*, XLI-B8, 837–843. https://doi.org/10.5194/isprsarchives-XLI-B8-837-2016

Bendig, J., Yu, K., Aasen, H., Bolten, A., Bennertz, S., Broscheit, J., Gnyp, M. L., & Bareth, G. (2015). Combining UAV-based plant height from crop surface models, visible, and near infrared vegetation indices for biomass monitoring in barley. *International Journal of Applied Earth Observation and Geoinformation*, 39, 79–87. https://doi.org/10.1016/j.jag.2015.02.012

Berni, J., Zarco-Tejada, P., Suarez, L., & Fereres, E. (2009). Thermal and Narrowband Multispectral Remote Sensing for Vegetation Monitoring From an Unmanned Aerial Vehicle. *IEEE Transactions on Geoscience and Remote Sensing*, 47(3), 722–738. https://doi.org/10.1109/TGRS.2008.2010457

Calderón, R., Navas-Cortés, J. A., Lucena, C., & Zarco-Tejada, P. J. (2013). High-resolution airborne hyperspectral and thermal imagery for early detection of Verticillium wilt of olive using fluorescence, temperature and narrow-band spectral indices. *Remote Sensing of Environment*, 139, 231–245. https://doi.org/10.1016/j.rse.2013.07.031

Camino, C., González-Dugo, V., Hernández, P., Sillero, J., & Zarco-Tejada, P. J. (2018). Improved nitrogen retrievals with airborne-derived fluorescence and plant traits quantified from VNIR-SWIR hyperspectral imagery in the context of precision agriculture. *International Journal of Applied Earth Observation and Geoinformation*, 70(February), 105–117. https://doi.org/10.1016/j.jag.2018.04.013

Cohen, N. & Aphek, O. (2015). Extended wavelength SWIR detectors with reduced dark current. 9451, 945106. https://doi.org/10.1117/12.2192103

Colomina, I. & Molina, P. (2014). Unmanned aerial systems for photogrammetry and remote sensing: A review. *ISPRS Journal of Photogrammetry and Remote Sensing*, 92, 79–97. https://doi.org/10.1016/j.isprsjprs.2014.02.013

EMVA (2019). *EMVA. European Machine Vision Association.* https://www.emva.org/. Last accessed on 17 January 2022.

Ewald, F., Kölling, T., Baumgartner, A., Zinner, T., & Mayer, B. (2016). Design and characterization of specMACS, a multipurpose hyperspectral cloud and sky imager. *Atmospheric Measurement Techniques*, 9(5), 2015–2042. https://doi.org/10.5194/amt-9-2015-2016

Gao, B.-c. (1996). NDWI—A normalized difference water index for remote sensing of vegetation liquid water from space. *Remote Sensing of Environment*, 58(3), 257–266. https://doi.org/10.1016/S0034-4257(96)00067-3

Gardner, M. C., Rogers, P. J., Wilde, M. F., Cook, T., & Shipton, A. (2016). Challenges and solutions for high performance SWIR lens design. *Electro-Optical and Infrared Systems: Technology and Applications XIII*, volume 9987, 99870C. https://doi.org/10.1117/12.2241089

Gnyp, M., Bareth, G., Li, F., Lenz-Wiedemann, V. I., Koppe, W., Miao, Y., Hennig, S. D., Jia, L., Laudien, R., Chen, X., & Zhang, F. (2014). Development and implementation of a multiscale biomass model using hyperspectral vegetation indices for winter wheat in the North China Plain. *International Journal of Applied Earth Observation and Geoinformation*, 33, 232–242. https://doi.org/10.1016/j.jag.2014.05.006

Gnyp, M. L., Yu, K., Aasen, H., Yao, Y., Huang, S., Miao, Y., & Bareth, C. . G. (2013). Analysis of Crop Reflectance for Estimating Biomass in Rice Canopies at Different Phenological Stages. *Photogrammetrie - Fernerkundung - Geoinformation*, 2013(4), 351–365. https://doi.org/10.1127/1432-8364/2013/0182

Haboudane, D., Miller, J. R., Pattey, E., Zarco-Tejada, P. J., & Strachan, I. B. (2004). Hyperspectral vegetation indices and novel algorithms for predicting green LAI of crop canopies: Modeling and validation in the context of precision agriculture. *Remote Sensing of Environment*, 90(3), 337–352. https://doi.org/10.1016/j.rse.2003.12.013

Hagen, N. & Kudenov, M. W. (2013). Review of snapshot spectral imaging technologies. *Optical Engineering*, 52(9), 090901. https://doi.org/10.1117/1.OE.52.9.090901

Hakala, T., Markelin, L., Honkavaara, E., Scott, B., Theocharous, T., Nevalainen, O., Näsi, R., Suomalainen, J., Viljanen, N., Greenwell, C., & Fox, N. (2018). Direct Reflectance Measurements from Drones: Sensor Absolute Radiometric Calibration and System Tests for Forest Reflectance Characterization. *Sensors*, 18(5), 1417. https://doi.org/10.3390/s18051417

Hansen, M. (2009). What you should ask before investing in a shortwave infrared (SWIR) lens. *Photonics Online: The Photonics Solutions Update*, 14–17.

Hansen, M. P. & Malchow, D. S. (2008). Overview of SWIR detectors, cameras, and applications. 6939, 69390I. https://doi.org/10.1117/12.777776

Hochedez, J.-F., Timmermans, C., Hauchecorne, A., & Meftah, M. (2014). Dark signal correction for a lukecold frame-transfer CCD: New method and application to the solar imager of the PICARD space mission. *Astronomy & Astrophysics*, 561, A17. https://doi.org/10.1051/0004-6361/201321607

Honkavaara, E., Eskelinen, M. A., Pölönen, I., Saari, H., Ojanen, H., Mannila, R., Holmlund, C., Hakala, T., Litkey, P., Rosnell, T., Viljanen, N., & Pulkkanen, M. (2016). Remote Sensing of 3-D Geometry and Surface Moisture of a Peat Production Area Using Hyperspectral Frame Cameras in Visible to Short-Wave Infrared Spectral Ranges Onboard a Small Unmanned Airborne Vehicle (UAV). *IEEE Transactions on Geoscience and Remote Sensing*, 54(9), 5440–5454. https://doi.org/10.1109/TGRS.2016.2565471

Hu, J., Peng, J., Zhou, Y., Xu, D., Zhao, R., Jiang, Q., Fu, T., Wang, F., & Shi, Z. (2019). Quantitative Estimation of Soil Salinity Using UAV-Borne Hyperspectral and Satellite Multispectral Images. *Remote Sensing*, 11(7), 736. https://doi.org/10.3390/rs11070736

Hunt, G. R. (1979). Near-infrared (1.3–2.4) Mm spectra of alteration minerals—Potential for use in remote sensing. *GEOPHYSICS*, 44(12), 1974–1986. https://doi.org/10.1190/1.1440951

Jaakkola, A., Hyyppä, J., Kukko, A., Yu, X., Kaartinen, H., Lehtomäki, M., & Lin, Y. (2010). A low-cost multi-sensoral mobile mapping system and its feasibility for tree measurements. *ISPRS Journal of Photogrammetry and Remote Sensing*, 65(6), 514–522. https://doi.org/10.1016/j.isprsjprs.2010.08.002

Koppe, W., Gnyp, M. L., Hennig, S. D., Li, F., Miao, Y., Chen, X., Jia, L., & Bareth, G. (2012). Multi-Temporal Hyperspectral and Radar Remote Sensing for Estimating Winter Wheat Biomass in the North China Plain. *Photogrammetrie - Fernerkundung - Geoinformation*, 2012(3), 281–298. https://doi.org/10.1127/1432-8364/2012/0117

Koppe, W., Li, F., Gnyp, M. L., Miao, Y., Jia, L., Chen, X., Zhang, F., & Bareth, G. (2010). Evaluating Multispectral and Hyperspectral Satellite Remote Sensing Data for Estimating Winter Wheat Growth Parameters at Regional Scale in the North China Plain. *Photogrammetrie - Fernerkundung - Geoinformation*, 2010(3), 167–178. https://doi.org/10.1127/1432-8364/2010/0047

Kumar, L., Schmidt, K., Dury, S., & Skidmore, A. (2001). Imaging Spectrometry and Vegetation Science. *Imaging Spectrometry: Basic Principles and Prospective Applications*, Remote Sensing and Digital Image Processing, 111–155. Springer Netherlands. https://doi.org/10.1007/978-0-306-47578-8_5

Lenhard, K., Baumgartner, A., & Schwarzmaier, T. (2015). Independent Laboratory Characterization of NEO HySpex Imaging Spectrometers VNIR-1600 and SWIR-320m-e. *IEEE Transactions on Geoscience and Remote Sensing*, 53(4), 1828–1841. https://doi.org/10.1109/TGRS.2014.2349737

Lucieer, A., Malenovský, Z., Veness, T., & Wallace, L. (2014). HyperUAS - Imaging spectroscopy from a multirotor unmanned aircraft system. *Journal of Field Robotics*, 31(4), 571–590. https://doi.org/10.1002/rob.21508

Mahlein, A.-K., Kuska, M. T., Thomas, S., Wahabzada, M., Behmann, J., Rascher, U., & Kersting, K. (2019). Quantitative and qualitative phenotyping of disease resistance of crops by hyperspectral sensors: Seamless interlocking of phytopathology, sensors, and machine learning is needed! *Current Opinion in Plant Biology*, 50, 156–162. https://doi.org/10.1016/j.pbi.2019.06.007

Mahlein, A. K., Rumpf, T., Welke, P., Dehne, H. W., Plümer, L., Steiner, U., & Oerke, E. C. (2013). Development of spectral indices for detecting and identifying plant diseases. *Remote Sensing of Environment*, 128, 21–30. https://doi.org/10.1016/j.rse.2012.09.019

MAIA (2019). *MAIA - the multispectral camera*. https://www.spectralcam.com/. Last accessed on 17 September 2019.

Mansouri, A., Marzani, F., & Gouton, P. (2005). Development of a Protocol for CCD Calibration: Application to a Multispectral Imaging System. *International Journal of Robotics and Automation*, 20(2). https://doi.org/10.2316/Journal.206.2005.2.206-2784

Martin, G. (2015). High Performance SWIR Imaging Cameras. *Raptor Photonics White Paper*, Raptor Photonics Ltd.: Milbrook, Larne, UK.

MicaSense (2019). *Home - MicaSense*. https://micasense.com/. Last accessed on 15 January 2019.

Mirco-MCA (2019). *Tetracam Micro-MCA Multispectral Camera Array*. https://www.tetracam.com/Products-Micro_MCA.htm. Last accessed on 22 January 2022.

Mutanga, O. & Skidmore, A. K. (2004). Narrow band vegetation indices overcome the saturation problem in biomass estimation. *International Journal of Remote Sensing*, 25(19), 3999–4014. https://doi.org/10.1080/01431160310001654923

Näsi, R., Honkavaara, E., Lyytikäinen-Saarenmaa, P., Blomqvist, M., Litkey, P., Hakala, T., Viljanen, N., Kantola, T., Tanhuanpää, T., & Holopainen, M. (2015). Using UAV-Based Photogrammetry and Hyperspectral Imaging for Mapping Bark Beetle Damage at Tree-Level. *Remote Sensing*, 7(11), 15467–15493. https://doi.org/10.3390/rs71115467

Näsi, R., Honkavaara, E., Tuominen, S., Saari, H., Pölönen, I., Hakala, T., Viljanen, N., Soukkamäki, J., Näkki, I., Ojanen, H., & Reinikainen, J. (2016). Uas based tree species identification using the novel fpi based hyperspectral cameras in visible, nir and swir spectral ranges. *International Archives of the Photogrammetry, Remote Sensing and Spatial Information Sciences - ISPRS Archives*, 2016-Janua(July), 1143–1148. https://doi.org/10.5194/isprsarchives-XLI-B1-1143-2016

Näsi, R., Viljanen, N., Kaivosoja, J., Alhonoja, K., Hakala, T., Markelin, L., & Honkavaara, E. (2018). Estimating Biomass and Nitrogen Amount of Barley and Grass Using UAV and Aircraft Based Spectral and Photogrammetric 3D Features. *Remote Sensing*, 10(7), 1082. https://doi.org/10.3390/rs10071082

O'Connor, J., Smith, M. J., & James, M. R. (2017). Cameras and settings for aerial surveys in the geosciences: Optimising image data. *Progress in Physical Geography*.

Parrot (2019). *Use cases*. https://www.parrot.com/us/use-cases. Last accessed on 14 November 2019.

Pinto, F., Müller-Linow, M., Schickling, A., Cendrero-Mateo, M. P., Ballvora, A., & Rascher, U. (2017). Multiangular Observation of Canopy Sun-Induced Chlorophyll Fluorescence by Combining Imaging Spectroscopy and Stereoscopy. *Remote Sensing*, 9(5), 415. https://doi.org/10.3390/rs9050415

Raptor Photonics (2019). *InGaAs SWIR VIS-SWIR SWaP 640 TEC-less Camera for Low Power Lost Cost OEMs*. https://www.raptorphotonics.com/products/owl-640-tecless-vis-swir-ingaas/. Last accessed on 20 January 2022.

RedEdge-Mx (2019). *RedEdge-MX - MicaSense*. https://micasense.com/rededge-mx/. Last accessed on 17 September 2019.

Roberts, D. A., Roth, K. L., Wetherley, E. B., Meerdink, S. K., & Perroy, R. L. (2018). Hyperspectral Vegetation Indices. *Hyperspectral Indices and Image Classifications for Agriculture and Vegetation*, (Chapter Hyperspectral Vegetation Indices). CRC Press. https://doi.org/10.1201/9781315159331-1

Roth, L., Hund, A., & Aasen, H. (2018). PhenoFly Planning Tool: Flight planning for high-resolution optical remote sensing with unmanned areal systems. *Plant Methods*, 14(1). https://doi.org/10.1186/s13007-018-0376-6

Saarinen, N., Vastaranta, M., Näsi, R., Hakala, T., Honkavaara, E., Wulder, M. A., Luoma, V., Tommaselli, A. M. G., Imai, N. N., Ribeiro, E. A. W., Guimarães, R. B., Holopainen, M., & Hyyppä, J. (2018). Assessing Biodiversity in Boreal Forests with UAV-Based Photogrammetric Point Clouds and Hyperspectral Imaging. *Remote Sensing*, 10(2), 338. https://doi.org/10.3390/rs10020338

Serrano, L., Peñuelas, J., & Ustin, S. L. (2002). Remote sensing of nitrogen and lignin in Mediterranean vegetation from AVIRIS data: Decomposing biochemical from structural signals. *Remote Sensing of Environment*, 81(2), 355–364. https://doi.org/10.1016/S0034-4257(02)00011-1

Stark, B., McGee, M., & Chen, Y. (2015). Short wave infrared (SWIR) imaging systems using small Unmanned Aerial Systems (sUAS). *2015 International Conference on Unmanned Aircraft Systems (ICUAS)*, 495–501. https://doi.org/10.1109/ICUAS.2015.7152328

Strausbaugh, R., Jackson, R., & Butler, N. (2018). Night Vision for Small Telescopes. *Publications of the Astronomical Society of the Pacific*, 130(991), 095001. https://doi.org/10.1088/1538-3873/aaca2a

Sullivan, P. W., Croll, B., & Simcoe, R. A. (2013). Precision of a Low-Cost InGaAs Detector for Near Infrared Photometry. https://doi.org/10.1086/672573

Suomalainen, J., Anders, N., Iqbal, S., Roerink, G., Franke, J., Wenting, P., Hünniger, D., Bartholomeus, H., Becker, R., Kooistra, L., Suomalainen, J., Anders, N., Iqbal, S., Roerink, G., Franke, J., Wenting, P., Hünniger, D., Bartholomeus, H., Becker, R., & Kooistra, L. (2014). A Lightweight Hyperspectral Mapping System and Photogrammetric Processing Chain for Unmanned Aerial Vehicles. *Remote Sensing*, 6(11), 11013–11030. https://doi.org/10.3390/rs61111013

Tetracam (2019). *Tetracam Multispectral and Smart NDVI Mapping Cameras.* https://www.tetracam.com/. Last accessed on 14 November 2021.

The MathWorks, I. (2015). *MATLAB and Image Processing Toolbox R2015a.* https://de.mathworks.com/products/image.html

Thenkabail, P. S., Enclona, E. A., Ashton, M. S., & Van Der Meer, B. (2004). Accuracy assessments of hyperspectral waveband performance for vegetation analysis applications. *Remote Sensing of Environment*, 91(3-4), 354–376. https://doi.org/10.1016/j.rse.2004.03.013

Thenkabail, P. S., Smith, R. B., & De Pauw, E. (2000). Hyperspectral vegetation indices and their relationships with agricultural crop characteristics. *Remote Sensing of Environment*, 71(2), 158–182. https://doi.org/10.1016/S0034-4257(99)00067-X

Theuwissen, A. (2011a). *How to measure the average dark signal ?* https://harvestimaging.com/blog/?p=795. Last accessed on 08 January 2022.

Theuwissen, A. (2011b). *How To Measure the Fixed-Pattern Noise in Dark (2).* https://harvestimaging.com/blog/?p=838. Last accessed on 08 January 2022.

Theuwissen, A. (2011c). *How to Measure the Fixed-Pattern Noise in Dark (3).* https://harvestimaging.com/blog/?p=849. Last accessed on 08 January 2022.

Theuwissen, A. (2011d). *How to measure the Fixed-Pattern Noise in Dark or DSNU (1).* https://harvestimaging.com/blog/?p=814. Last accessed on 08 January 2022.

Thorlabs (2019). *NIR Bandpass & Laser Line Filters: 700 - 1650 nm Center Wavelength.* https://www.thorlabs.com/newgrouppage9.cfm?objectgroup_id=1000. Last accessed on 13 February 2022.

Tilly, N., Aasen, H., & Bareth, G. (2015). Fusion of Plant Height and Vegetation Indices for the Estimation of Barley Biomass. *Remote Sensing*, 7(9), 11449–11480. https://doi.org/10.3390/rs70911449

Tilly, N. & Bareth, G. (2019). Estimating Nitrogen from Structural Crop Traits at Field Scale—A Novel Approach Versus Spectral Vegetation Indices. *Remote Sensing*, 11(17), 2066. https://doi.org/10.3390/rs11172066

Tuominen, S., Näsi, R., Honkavaara, E., Balazs, A., Hakala, T., Viljanen, N., Pölönen, I., Saari, H., & Ojanen, H. (2018). Assessment of Classifiers and Remote Sensing Features of Hyperspectral Imagery and Stereo-Photogrammetric Point Clouds for Recognition of Tree Species in a Forest Area of High Species Diversity. *Remote Sensing*, 10(5), 714. https://doi.org/10.3390/rs10050714

van der Meer, F. D., van der Werff, H. M. A., van Ruitenbeek, F. J. A., Hecker, C. A., Bakker, W. H., Noomen, M. F., van der Meijde, M., Carranza, E. J. M., de Smeth, J. B., & Woldai, T. (2012). Multi- and hyperspectral geologic remote sensing: A review. *International Journal of Applied Earth Observation and Geoinformation*, 14(1), 112–128. https://doi.org/10.1016/j.jag.2011.08.002

Viscarra Rossel, R. A., Walvoort, D. J. J., McBratney, A. B., Janik, L. J., & Skjemstad, J. O. (2006). Visible, near infrared, mid infrared or combined diffuse reflectance spectroscopy for simultaneous assessment of various soil properties. *Geoderma*, 131(1), 59–75. https://doi.org/10.1016/j.geoderma.2005.03.007

Wang, W., Li, C., Tollner, E. W., Rains, G. C., & Gitaitis, R. D. (2012). A liquid crystal tunable filter based shortwave infrared spectral imaging system: Calibration and characterization. *Computers and Electronics in Agriculture*, 80, 135–144. https://doi.org/10.1016/j.compag.2011.09.003

Waser, L. T., Ginzler, C., Kuechler, M., Baltsavias, E., & Hurni, L. (2011). Semi-automatic classification of tree species in different forest ecosystems by spectral and geometric variables derived from Airborne Digital Sensor (ADS40) and RC30 data. *Remote Sensing of Environment*, 115(1), 76–85. https://doi.org/10.1016/j.rse.2010.08.006

Xavier, A. C., Rudorff, B. F. T., Moreira, M. A., Alvarenga, B. S., de Freitas, J. G., & Salomon, M. V. (2006). Hyperspectral field reflectance measurements to estimate wheat grain yield and plant height. *Scientia Agricola*, 63(2), 130–138. https://doi.org/10.1590/S0103-90162006000200004

Zarco-Tejada, P. J., Diaz-Varela, R., Angileri, V., & Loudjani, P. (2014). Tree height quantification using very high resolution imagery acquired from an unmanned aerial vehicle (UAV) and automatic 3D photo-reconstruction methods. *European Journal of Agronomy*, 55, 89–99. https://doi.org/10.1016/j.eja.2014.01.004

Zarco-Tejada, P. J., González-Dugo, V., & Berni, J. A. J. (2012). Fluorescence, temperature and narrow-band indices acquired from a UAV platform for water stress detection using a micro-hyperspectral imager and a thermal camera. *Remote Sensing of Environment*, 117, 322–337. https://doi.org/10.1016/j.rse.2011.10.007

Zheng, H., Li, W., Jiang, J., Liu, Y., Cheng, T., Tian, Y., Zhu, Y., Cao, W., Zhang, Y., & Yao, X. (2018). A Comparative Assessment of Different Modeling Algorithms for Estimating Leaf Nitrogen Content in Winter Wheat Using Multispectral Images from an Unmanned Aerial Vehicle. *Remote Sensing*, 10(12), 2026. https://doi.org/10.3390/rs10122026

4 | Investigating the Potential of a Newly Developed UAV-based VNIR/SWIR Imaging System for Forage Mass Monitoring

Alexander Jenal[1,*], Ulrike Lussem[2], Andreas Bolten[2], Martin Leon Gnyp[3], Jürgen Schellberg[4], Jörg Jasper[3], Jens Bongartz[1], Georg Bareth[2]

PFG – Journal of Photogrammetry, Remote Sensing and Geoinformation Science volume 88, 493–507 (2020); doi.org/10.1007/s41064-020-00128-7

Formatting and orthography of the manuscript is adapted to the dissertation style.

1 Application Center for Machine Learning and Sensor Technology, University of Applied Science Koblenz, 53424 Remagen, Germany; bongartz@hs-koblenz.de (J.B.)

2 Institute of Geography, GIS & RS Group, University of Cologne, 50923 Cologne, Germany; ulrike.lussem@uni-koeln.de (U.L.); andreas.bolten@uni-koeln.de (A.B.); g.bareth@uni-koeln.de (G.B.)

3 Institute of Plant Nutrition and Environmental Science, Research Centre Hanninghof, Yara International ASA, Hanninghof 35, 48249 Dülmen, Germany; martin.gnyp@yara.com (M.G.); joerg.jasper@yara.com (J.J.)

4 INRES - Institute of Crop Science and Resource Conservation, University of Bonn, Katzenburgweg 5, 53115 Bonn, Germany; jk.schellberg@gmail.com (J.S.)

* Correspondence: alexander.jenal@hs-koblenz.de; Tel.: +49-2642-932-411

The author's contribution to this study is substantial and declared in detail in Appendix B.

Abstract

Remote sensing systems based on unmanned aerial vehicles (UAVs) are well suited for airborne monitoring of small to medium-sized farmland in agricultural applications. An imaging system is often used in the form of a multispectral multi-camera system to derive well-established vegetation indices (VIs) efficiently. This study investigates the potential of such a multi-camera system with a novel approach to extend spectral sensitivity from visible-to-near-infrared (VNIR) to short-wave infrared (SWIR) (400 to 1700 nm) for estimating forage mass from an aerial carrier platform. The system test was performed in a grassland fertilizer trial in Germany near Cologne in late July 2019. Within 37 minutes, a spectral response in four different wavelength bands in the NIR and SWIR range was acquired during two consecutive flights. Spectral image data were calibrated to reflectance using two different methods. The resulting reflectance data sets were processed to orthomosaics for each wavelength band. From these orthomosaics for both calibration methods, the four-band NIR/SWIR GnyLi VI and the two-band NIR/SWIR normalized ratio index (NRI), were calculated. During both UAV flights, spectral ground truth data were recorded with a spectroradiometer on twelve plots in total for validation of camera-based spectral data. The camera and spectroradiometer data sets were directly compared in resulting reflectance and further analyzed with simple linear regression (SLR) models to predict dry matter (DM) yield. In the camera-based SLRs, the NRI performed best with R^2 of 0.73 and 0.75 (*RMSE*: 0.18 and 0.17) before the GnyLi with R^2 of 0.71 and 0.73 (*RMSE*: 0.19 and 0.18). These results clearly indicate the potential of the camera system for applications in forage mass monitoring.

Keywords: Short-wave infrared (SWIR), Unmanned aerial vehicle (UAV), Precision agriculture, Forage mass, Grassland, Biomass

4.1 Introduction

Grassland ecosystem covers almost 30 % of the total land area and approx. 70 % of the global agricultural land is managed grasslands (Boval & Dixon, 2012; Gibson, 2009). Grasslands are critical "as a feed source for livestock, as a habitat for wildlife, for environmental protection and for the in-situ conservation of plant genetic resources" (Suttie et al., 2005). Furthermore, they are of high cultural and economic value (Nelson et al., 2017), comprising pastureland, rangeland, and cropland for forage production such as grass, silage, or hay (Nelson et al., 2017), and provide the base for meat, dairy, and wool production.

In managed grasslands, pastures, rangelands, and meadows, the information on sward height and growth for forage mass estimates is crucial for management decisions (Evans & Jones, 1958; Higgins et al., 2019). Consequently, the approaches for nondestructive estimation of spatial forage mass production were investigated for decades (Santillan et al., 1979; Bareth et al., 2015; Legg & Bradley, 2020). In the 1960s, the development of so-called disk-meters started (Castle, 1976) and led to the development of rising plate meters (RPMs) (Earle & McGowan, 1979), which are measuring compressed sward height as an estimator for forage mass (Sanderson et al., 2001). Such systems in modern electromechanical versions are still used by farmers and provide robust and reliable estimates. Newer technologies to measure sward height are rapid pasture meters (King et al., 2010) using light beams measurements as well as ultrasonic devices (Fricke & Wachendorf, 2013).

A completely different approach for nondestructive estimation of forage mass is optical remote sensing. A wide range of imaging sensors for different carrier systems (mobile, aerial, and satellite) are available, providing multi- and hyperspectral image data in the visible and near-infrared (VNIR) domain (approx. 300 to 1000 nm). Portz et al. (2017), Näsi et al. (2018), and Capolupo et al. (2015) have successfully investigated such optical approaches. In this context, portable field spectroradiometer studies are of essential importance for identifying the potential of significant spectral domains and for evaluating remote sensing data (Hollberg & Schellberg, 2017; Lussem et al., 2019). In the past fifteen years, numerous studies emerged where unmanned aerial vehicles (UAVs) have been used as a carrying platform for miniaturized multi- and hyperspectral sensors (Hardin & Jackson, 2005; Rango et al., 2006; Berni et al., 2009; Hunt et al., 2010; Aasen et al., 2015; Geipel et al., 2016). Such aerial mapping systems or field spectroradiometer measurements were also applied for forage mass monitoring. Lussem et al. (2019) reported varying performances of selected VNIR VIs as estimators for dry matter (DM) yield, with R^2 ranging from 0.32 to 0.86. Viljanen et al. (2018) derived similar VIs from UAV-based image acquisition. The latter study described Pearson correlation coefficients (PCCs) for DM yield ranging from 0.3 to 0.9. Capolupo et al. (2015) acquired image data with a VNIR hyperspectral UAV sensor system. The results of regression analyses against DM yield varied in R^2 values between 0.36 and 0.57. For crop monitoring, Koppe et al. (2012) and Gnyp et al. (2014) proofed the promising potential of reflectance features in the shortwave-infrared (SWIR) for biomass monitoring of winter wheat using a two-band NIR/SWIR-based normalized ratio index (NRI) and the four-band NIR/SWIR GnyLi vegetation index. In the studies by Gnyp et al. (2014b), Koppe et al. (2010), Koppe et al. (2012), Bendig et al. (2015), and Tilly et al. (2015), the NRI and GnyLi outperformed the VIs using VNIR wavelengths.

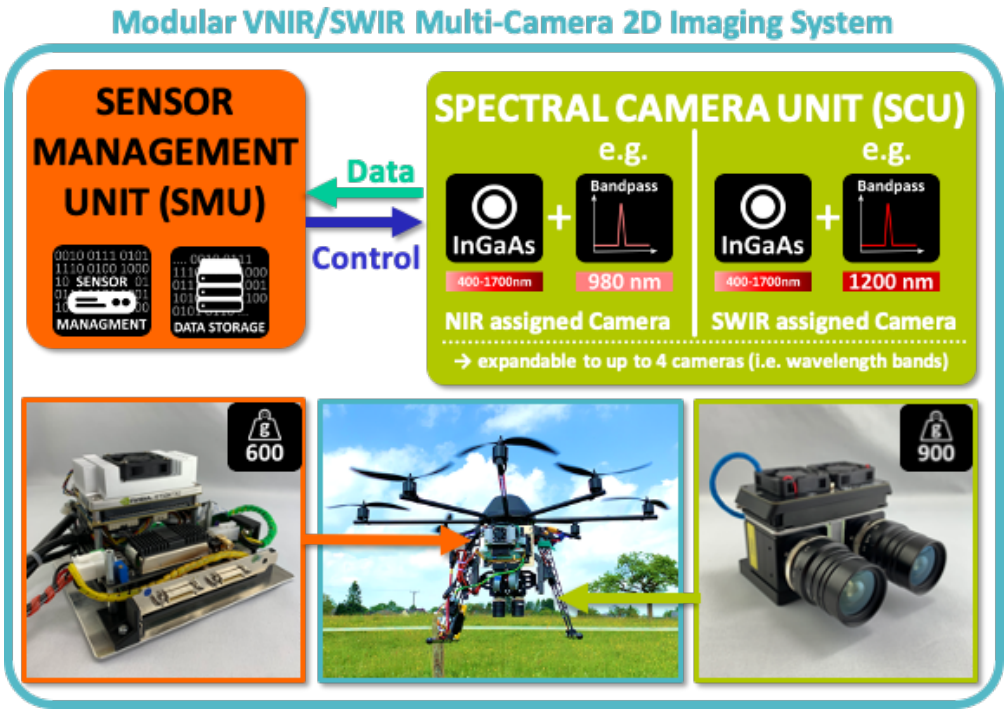


Figure 4.1: System overview of the novel, modular-designed VNIR/SWIR multispectral multi-camera 2D imaging prototype for UAV-based remote sensing applications.

Therefore, a UAV-based multi-camera imaging system covering these VNIR/SWIR bands is demanded to efficiently evaluate the potential of the VNIR/SWIR range for grassland monitoring. To the authors' knowledge, UAV-borne NIR/SWIR data of such a camera system have not yet been investigated for grassland monitoring.

In a previous study, the authors have developed a novel prototype of a UAV-based remote sensing multispectral multi-camera system. The centerpiece of the system consists of two compact scientific camera modules, based on indium gallium arsenide (InGaAs) sensors, to capture spectral image data from the VNIR and SWIR spectral range (Jenal et al., 2019). These camera modules provide a higher spectral sensitivity within the 400 to 1700 nm wavelength range, made possible by an additional etching step during the manufacturing process (Martin, 2015). Thus, vegetation indices can be derived not only within the NIR/SWIR spectral range, but also in additional combinations within the entire VNIR and SWIR wavelength range. Suitable hybrid bandpass filters select the required spectral bands for vegetation indices out of the incoming light. These filters are mounted via C-mount flanges developed explicitly for this particular system. Each bandpass filter used with the camera system is installed into a separate interchangeable flange. This filter assembly can be mounted in the optical path of each camera, between the prime lens and sensor, to achieve the best possible image data quality. This flange allows quick as well as repeatable filter changes and adapts the filter to the optical system. In Figure 4.1, the newly introduced imaging sensor system for UAVs is shown (Jenal et al., 2019). The modular camera system divides into two parts so that it can be easily integrated into many different airborne carrier platforms, especially into UAVs. The spectral camera unit (SCU) consists of two InGaAs cameras, while the sensor management unit (SMU) combines the control and storing unit.

For the spectral measurements performed in this study, the dual-camera system was equipped with four bandpass filters, for the NIR and SWIR spectral range, to derive the NRI and GnyLi VIs mentioned above. Since the prototype of the camera system currently consists of only two InGaAs-based cameras arranged in parallel, more complex VIs, which require more than two wavelength bands, have to be composed of several consecutive flights with the shortest possible time delay.

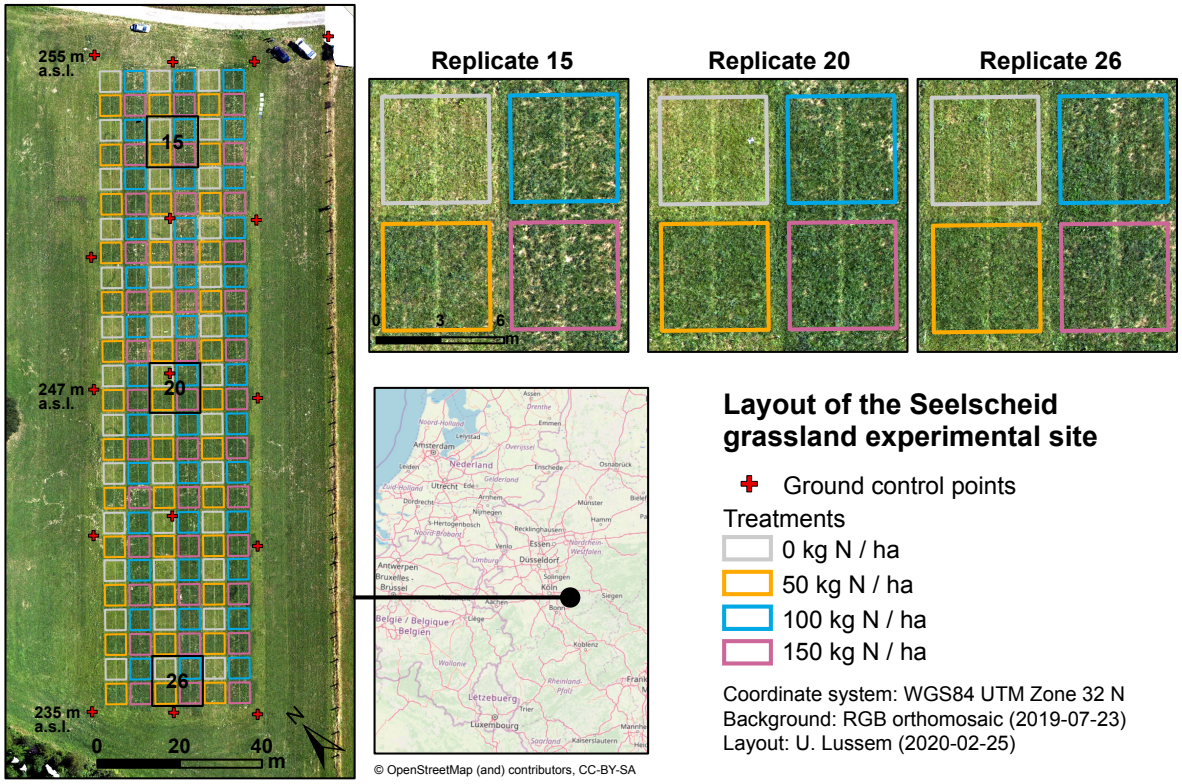


Figure 4.2: Location map and additional information of the experimental site in Neunkirchen-Seelscheid.

According to (Honkavaara et al., 2016), (Camino et al., 2018), and (Aasen & Bareth, 2018), the VNIR/SWIR domain provides an unexploited potential for UAV-based monitoring of vegetation. Therefore, the overall aim of this study is to evaluate the potential for grassland monitoring of the newly developed VNIR/SWIR multispectral multi-camera 2D imager, as described by Jenal et al. (2019). A first UAV-borne data acquisition campaign was carried out on a chessboard experiment on permanent grassland near Cologne, Germany, in July 2019. As a result, spectral data were acquired by the camera system in the NIR/SWIR spectral range, as well as narrowband hyperspectral ground truth data from a portable field spectroradiometer. Moreover, destructively measured DM yield data were obtained. With these data sets the following main objectives of this study are (i) to validate the spectral performance of the UAV-mounted multi-camera sensor system in-situ, (ii) to compare UAV-derived NIR/SWIR image data with hyperspectral ground truth measurements using a portable field spectroradiometer, (iii) to evaluate well-established VNIR VIs using the spectroradiometer data, and (iv) performing simple linear regression analyses (SLR) of destructively measured DM yield against UAV-derived NIR/SWIR VIs and the equivalent spectroradiometer VNIR/SWIR VIs.

4.2 Study site and Methods

4.2.1 Study site

This study was based on data acquired on a grassland field trial in Germany. The permanent grassland site is located in Neunkirchen-Seelscheid (Bergisches Land region, North Rhine-Westphalia), about 30 km southeast of Cologne. The mean annual temperature is 10 °C, and the mean annual precipitation about 800 mm. The experimental field was established in March 2017 on a conventionally managed permanent grassland. The field trial comprised three nitrogen (N) fertilizer application levels (50, 100, 150 kg N ha^{-1}) and one control with no fertilizer applied at all, ending up in four treatments. Each treatment comprised 39 replicates, resulting in 156 plots systematically arranged in a chessboard pattern (see Figure 4.2). Each plot covered an area of 6×6 m. The experimental field was managed as a three-cut system. The first cut was harvested in May, the second in July, and the third in October, similar to local farming practice.

4.2.2 Yield reference data/biomass sampling

For yield reference data, biomass samples were collected on August 5th, 2019. A conventional lawn mower was used to harvest a 0.54×5.46 m strip of standing biomass from each of the 156 plots. The fresh biomass samples were weighed directly, and from that, subsamples were taken for DM calculation. Subsamples were dried in a forced-air dryer to constant weight for three days at 65 °C. Subsequently, weights of dried subsamples were used to calculate dry above-ground biomass yield per hectare (t ha^{-1}).

4.2.3 Spectroradiometer ground truth measurements

The spectral ground truth data were measured with an ASD FieldSpec3 spectroradiometer (Malvern Panalytical Ltd, Malvern, United Kingdom). Three (No. 15, 20, and 26, see Figure 4.2) out of the overall 39 replicates, evenly distributed across the experimental site, were selected for spectral ground-truthing. Spectral field measurements were conducted between 10:58 am and 12:05 pm on the twelve plots of these replicates. In each plot, between 13 and 17 spectral measurements were taken to cover the complete plot area. For each spectrum obtained, ten spectra were averaged. Before starting measurements on individual plots, white (Zenith Lite™ panel) and dark reference measurements were obtained. The resulting raw spectra were transformed to reflectance and corrected for sensor offset (splice correction) using the ASD-software IndicoPro v5.0. Subsequently, the spectra were smoothed using a Savitzky-Golay filter implemented in the R package "prospectr" (Stevens & Ramirez-Lopez, 2013), R package version 0.2.0). The arithmetic mean of all spectra recorded in a plot was calculated. The averaged spectra were then used to calculate VIs in the VNIR/SWIR range (see Table 4.1). The vegetation indices listed in Table 4.1 were selected based on previous studies on biomass estimation in crops and grassland studies (Koppe et al., 2010; Gnyp et al., 2014b; Tilly et al., 2015; Capolupo et al., 2015; Viljanen et al., 2018; Näsi et al., 2018; Lussem et al., 2019). The spectral data recorded by the ASD FieldSpec3 spectroradiometer, as well as the derived vegetation indices, are marked *ASD* in the subsequent sections.

Table 4.1: Vegetation indices used in this study. Indices (**a**) to (**l**) were applied to the spectral ground truth data of the ASD Fieldspec3 spectroradiometer. Indices (**k**) and (**l**) were also applied to the spectral image data of the camera.

	Name	Equation	Reference
(a)	NDVI	$\frac{R_{800}-R_{670}}{R_{800}+R_{670}}$	(Rouse et al., 1974)
(b)	RDVI	$\frac{(R_{798}-R_{670})}{\left(\sqrt{R_{798}+R_{670}}\right)}$	(Roujean & Breon, 1995)
(c)	OSAVI	$\frac{1.16\times(R_{800}-R_{670})}{R_{800}+R_{670}+0.16}$	(Rondeaux et al., 1996)
(d)	REIP	$700+40\times\frac{\frac{R_{670}+R_{780}}{2}-R_{700}}{R_{740}+R_{700}}$	(Guyot & Baret, 1988)
(e)	NDREI	$\frac{R_{790}-R_{720}}{R_{790}+R_{720}}$	(Gitelson & Merzlyak, 1994)
(f)	MTCI	$\frac{R_{754}-R_{709}}{R_{709}-R_{681}}$	(Dash & Curran, 2004)
(g)	Cl-Green	$(R_{780}-R_{550})-1$	(Gitelson et al., 2003)
(h)	RVI	$\frac{R_{800}}{R_{670}}$	(Pearson & Miller, 1972)
(i)	PRI	$\frac{R_{512}-R_{531}}{R_{512}+R_{531}}$	(Hernández-Clemente et al., 2011)
(j)	MSAVI	$\frac{\left(2\times R_{800}+1-\sqrt{2\times R_{800}+1}\right)^2-8\times(R_{800}-R_{670})}{2}$	(Qi et al., 1994)
(k)	GnyLi	$\frac{R_{910}\times R_{1100}-R_{980}\times R_{1200}}{R_{910}\times R_{1100}+R_{980}\times R_{1200}}$	(Gnyp et al., 2014)
(l)	NRI	$\frac{R_{910}-R_{1200}}{R_{910}+R_{1200}}$	(Koppe et al., 2010)

4.2.4 Image data acquisition

With the first flight starting at 11:03 am, spectral image data were acquired with the above-described camera system around noon under clear sky conditions on July 23rd, 2019. The modular system was mounted on an MK S612 octocopter (HiSystems GmbH, Moormerland, Germany), with the spectral camera unit mounted in the gimbal and the control unit on the rigid frame of the UAV. Within 37 minutes, two UAV flights (approx. 7 minutes each) were performed in short succession. After the first flight, the filter arrangement was changed from 910 and 1100 nm to 980 and 1200 nm. When changing filters in the field, consistent image quality has to be ensured throughout the flights. Therefore, each bandpass filter was installed in its own filter flange, which was matched to the entire optical system. Moreover, these filter mounts have been mechanically designed to be always positioned in the same way as during initial flat-field calibration in the laboratory (see Jenal et al., 2019). A series of calibration images from a spectrally precisely characterized Zenith™ polymer white panel with 95 % lambertian reflectance as well as additional dark images were taken before each flight (see Figure 4.3a,b).

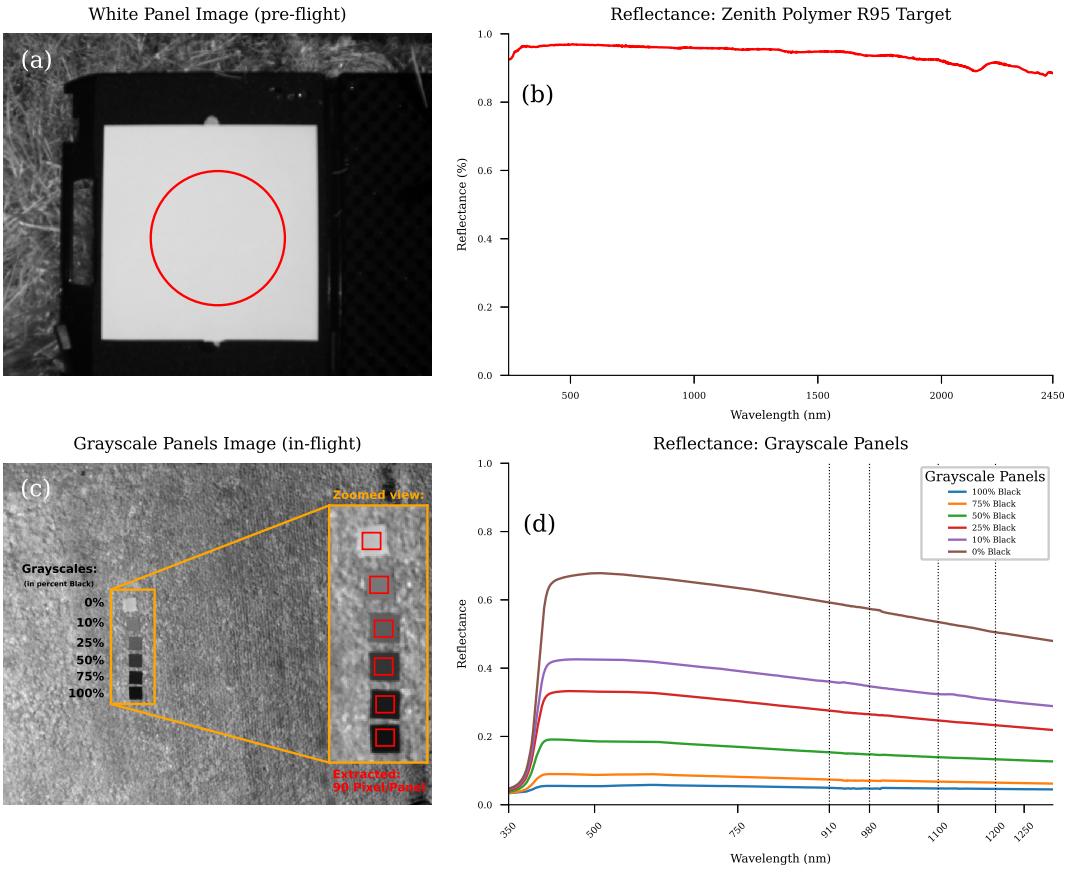


Figure 4.3: (**a**) Pre-flight image of the white calibration panel and the marked area (red circle) that is used for reflectance calibration during post-processing. (**b**) Reflectance data, provided by the manufacturer, of the spectrally precisely characterized lambertian Zenith™ polymer white panel with 95 % reflectance. (**c**) In-flight image of the six differently graded grey panels and the marked areas (red squares), which are used for reflectance calibration with the empirical line method in post-processing. (**d**) Reflectance values of the six grey panels measured by an ASD FieldSpec3 spectroradiometer.

This correction data was used in post-processing for a one-point calibration of the image digital numbers (DNs) to reflectance values and is referred to as the White-Panel-Method, abbreviated *WPM*. Besides, six differently graded and also spectrally well-characterized 80×80 cm near-lambertian grey panels were placed next to the test site. These grayscale panels (0, 10, 25, 50, 75 and 100 %.black shading) were then captured in-flight and were used, in addition to the White-Panel-Method, for reflectance calibration of the DNs according to the empirical line method published by (Smith & Milton, 1999). The reflectance data, as well as the vegetation indices derived by the empirical line method, are given the suffix *ELM* in the following.
The flight duration was about seven minutes each and resulted in around 1000 images per channel with a constant flight altitude of 30 m above ground level (AGL). The camera system's aperture and exposure settings were kept constant during both flights of the survey campaign. In combination with the lenses used, the calculated ground sampling distance (GSD) resulted in approx. 0.04 m. In order to georeference the data thereafter, fifteen ground control points were evenly distributed across the experimental site (see Figure 4.2). Then their exact geolocation was measured with high accuracy using a Real-Time Kinematic Differential Global Positioning System (RTK-DGPS) receiver (Topcon GR5).

4.2.5 Image data processing

The image data of each of the four spectral bands were individually flat-field corrected. To this end, accurate flat-field measurements at an integrating sphere and measurements for dark signal compensation in a climatic chamber have been performed in advance for accurate sensor characterization (Jenal et al., 2019). These preprocessed images were then converted from at-sensor radiance into at-surface reflectance values. This subsequent transformation was carried out using two different methods, based on the empirical line method described by Smith & Milton (1999) and empirically proven by Baugh & Groeneveld (2008). In this study, simplified empirical line procedures for UAV-based imaging sensors, derived by Wang & Myint (2015) and Iqbal et al. (2018), were applied.

Firstly, pre-flight calibration data were taken from a white calibration target for a one-point calibration, which is the simplest form of the empirical line method (see Smith & Milton, 1999). Figure 4.3a shows one of 20 white calibration images, which were acquired for the WPM immediately before a flight and averaged afterward. The red circular marking encloses the area of the image that was used for reflectance calibration of the previously flat-fielded image data. For this reason, the target must also be positioned as centrally as possible in both camera images before acquiring the images, which can be done using the control software of the SCU.

Secondly, a calibration was performed by in-flight measurements of six differently shaded grey targets for a more sophisticated approach of the empirical line method. Figure 4.3c shows one of the calibration images with the included grayscale targets during a flyover (first flight, 910 nm channel) as an example. Each red box in the zoomed view shows the pixel locations that were extracted with the OpenCV (Bradski, 2000) *imcrop tool* to determine the average digital number (DN) for every grey target. For each target, approx. 90 pixels were averaged. The mean image DN of each calibration panel was then plotted against the mean reflectance of the calibration panels determined by reference measurements with an ASD FieldSpec3 spectroradiometer (see Figure 4.3d) in a scatter plot. Linear regression was then applied to determine the calibration equation in the form of (see Iqbal et al., 2018):

$$Reflectance = slope \times DN + intercept \tag{4.1}$$

Both workflows were processed with the Python programming language using IPython (Perez & Granger, 2007) in a JupyterLab (Kluyver et al., 2016) environment. Both reflectance image data sets of each flight were imported separately in the structure from motion (SfM) software Metashape (Agisoft Ltd, St. Petersburg, Russia, v 1.6.2) with the *rigid camera rig* option to process a two-layer georeferenced orthomosaic per flight and for each calibration method. Therefore, corresponding metadata was added to the individual image data sets of each flight via the command-line application ExifTool (version 11.66) (Harvey, 2019). Due to a low image resolution of 640×512 pixel, the accuracy setting *Highest* had to be selected for successful image alignment of the two layers. This setting forces the algorithm to upscale the image size by a factor of 4. For the further processing steps, the individual settings have been switched to *Medium* mode. After the SfM process, the resulting two-layer orthomosaics of the WPM and the ELM calibration were used to calculate the orthomosaics for the GnyLi (see Figure 4.4) and the NRI VIs of both calibration methods. The applied equations for both indices are listed in Table 4.1 (k) and (l).

Subsequently, with a total of six orthomosaics per calibration method, zonal statistics were derived. The mean and the standard deviation were calculated from the raster data using vector data of the individual plot positions. Zonal statistics were performed with the Python packages *geopandas* (Jordahl et al., 2020), *rasterstats*, and *rasterio* in JupyterLab.

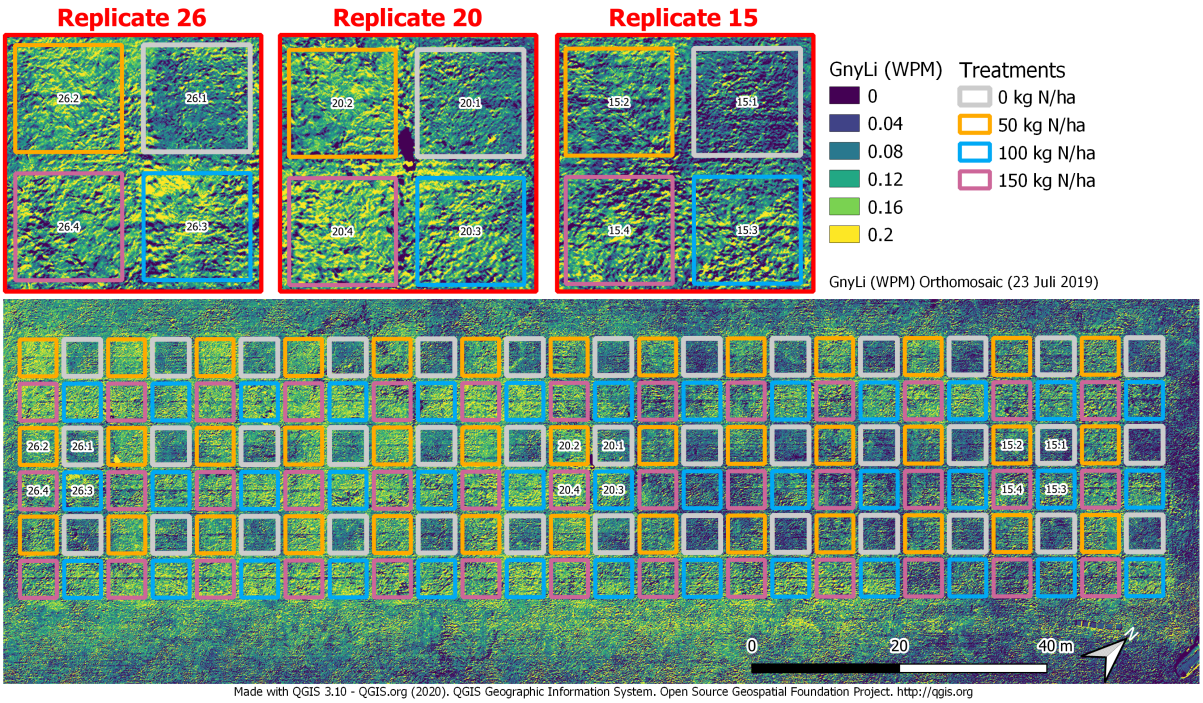


Figure 4.4: GnyLi VI (WPM calibration) orthomosaic derived from the four waveband orthomosaics processed from the camera system's spectral image data.

4.2.6 Spectral data analysis

Well-established vegetation indices from the VNIR/SWIR range (see Table 4.1) were derived from the narrowband spectral ground truth measurements of the ASD FieldSpec3 spectroradiometer to compare their prediction quality in simple linear regression (SLR) for dry matter (DM) yield with that of camera-based NIR/SWIR VIs.

To evaluate the spectral properties of the VNIR/SWIR camera system, the reflectance values of the individual spectral bands, as well as the two VIs GnyLi and NRI, were directly compared with the corresponding ASD values. Additionally, SLR analyses were performed to determine whether the two vegetation indices GnyLi and NRI, obtained from the camera system, could potentially provide a reliable prediction of DM yield. These analyses were carried out in two ways.

First, the analyses were performed with the WPM, ELM, and ASD data sets for the twelve spectral ground truth plots of replicates 15, 20, and 26. Additionally, only the WPM and ELM camera-based VIs GnyLi and NRI were analyzed in another SLR with the DM yield data of all 156 plots since no ASD spectral ground truth data were available for all plots. Quality measures, such as the coefficient of determination (R^2) and the root-mean-square error ($RMSE$), were determined for all SLR analyses.

4.3 Results

4.3.1 Reflectance Calibration

The spectral image data acquired during both flights were flat-field corrected and then converted from at-sensor radiance into at-surface reflectance values based on the empirical line method. This was done using the WPM and the ELM procedure described in section 4.2.5.

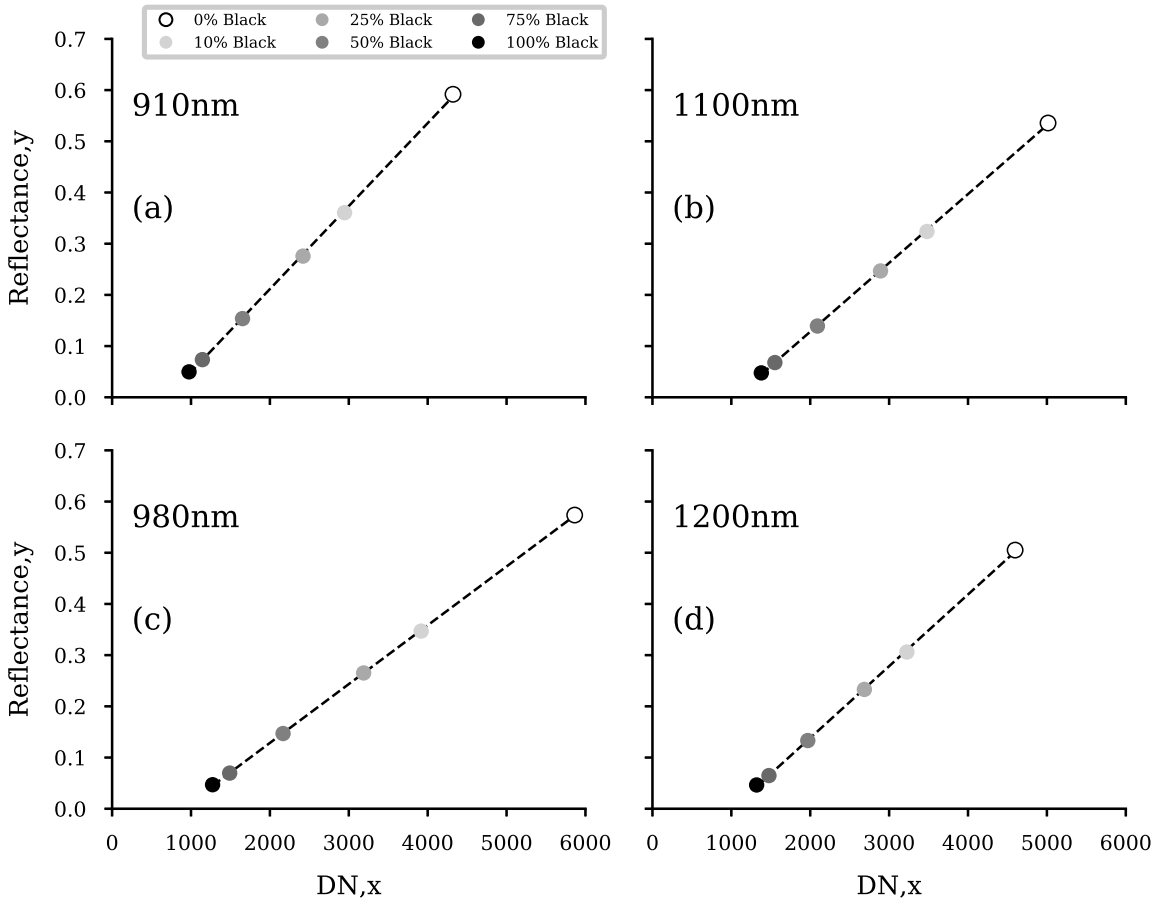


Figure 4.5: (**a**)-(**d**). The linear relationship between mean DNs of the target area in the cameras' calibration images and mean reflectance of the calibration panels measured by an ASD FieldSpec3 spectroradiometer for all four wavelength bands of the VNIR/SWIR camera system. Each data point represents one of the six calibration targets. X- and y-axes are shared among graphs ($p < 0.0001$).

Figure 4.5 displays the scatter plots with the linear relationship between the mean DNs of the camera data and the reflectance of the calibration panels for all four wavelength bands. Table 4.2 lists the calibration equations for all four wavelength channels and the quality measures derived from the applied ELM of the six calibration panels. The 910 nm band exhibits the highest *RMSE* of 0.0035. The three remaining bands were below this value, with 980 nm having the lowest *RMSE* of 0.0012.

Table 4.2: Summarized statistics for the reflectance prediction equation derived from the empirical line method. ($p < 0.0001$)

Channel	Prediction Equation	R^2	*RMSE*
910 nm	$y = 0.0002x - 0.1126$	0.9997	0.0035
1100 nm	$y = 0.0001x - 0.1407$	0.9998	0.0021
980 nm	$y = 0.0001x - 0.1012$	1.0000	0.0012
1200 nm	$y = 0.0001x - 0.1419$	0.9997	0.0025

4.3.2 ASD-based VIs vs. DM yield

Vegetation indices were derived according to Table 4.1 based on ASD data. Each VI data set of the twelve spectrally measured plots was correlated with DM yield data in an SLR analysis. Table 4.3 concisely summarizes the statistical parameters of this analysis.

Table 4.3: Summarized statistics for the linear regression models of the twelve VNIR VIs and the DM yield ($p < 0.001$).

	VI	Equation	R^2	*RMSE*
(a)	NDVI	$y = 6.98x - 5.11$	0.86	0.12
(b)	RDVI	$y = 6.68x - 3.03$	0.94	0.08
(c)	OSAVI	$y = 6.48x - 3.92$	0.92	0.09
(d)	REIP	$y = 0.12x - 82.28$	0.81	0.14
(e)	NDREI	$y = 4.85x - 0.92$	0.79	0.15
(f)	MTCI	$y = 0.43x - 0.43$	0.77	0.16
(g)	Cl-Green	$y = 7.2x + 5.5$	0.93	0.09
(h)	RVI	$y = 0.07x - 0.16$	0.88	0.11
(i)	PRI	$y = -13.26x - 2.47$	0.59	0.21
(j)	MSAVI	$y = -2x - 2.08$	0.93	0.09
(k)	GnyLi	$y = 11.62x - 0.38$	0.90	0.10
(l)	NRI	$y = 10.26x + 0.29$	0.83	0.13

As shown in Table 4.3, the VIs used for the SLR analyses, except for the PRI, consistently show a good to an excellent level of accuracy (R^2: 0.77 to 0.94) for the estimation of DM yield. Figure 4.6 displays the twelve scatter plots of the ASD derived VIs (see Table 4.1) against the DM yield. The performance of the two ASD VIs GnyLi and NRI was very good (R^2 of 0.90 and 0.83). The results of both VIs are compared with the camera-based WPM and ELM VIs and displayed below.

4.3.3 Direct comparison: Camera vs. ASD data

Figure 4.7a-d directly compares the calibrated reflectance data recorded by the camera system (WPM, ELM) per plot to the corresponding ASD reflectance data. As can be seen in Figure 4.7, the three reflectance values for each plot differed only slightly. Averaged over all plots of a measured wavelength, the mean relative difference of the WPM values differ from the reference values of the ASD by 5.72 % and the mean relative difference of the ELM values by only 3.28 %. A clear pattern of the two methods of over- or underestimating the reference values was not apparent. The standard deviation (SD) of the mean ASD reflectance data was lower (0.013 to 0.044) as compared to WPM (0.024 to 0.059) and ELM (0.030 to 0.073) data. This can be explained by the higher spatial resolution of the image data compared to the point measurements of the spectroradiometer. From the VNIR/SWIR image data, approx. 17,200 pixel values were averaged per plot. From the ASD, between 13 and 17 spectra were averaged per plot, each providing a footprint of about 0.6 m.

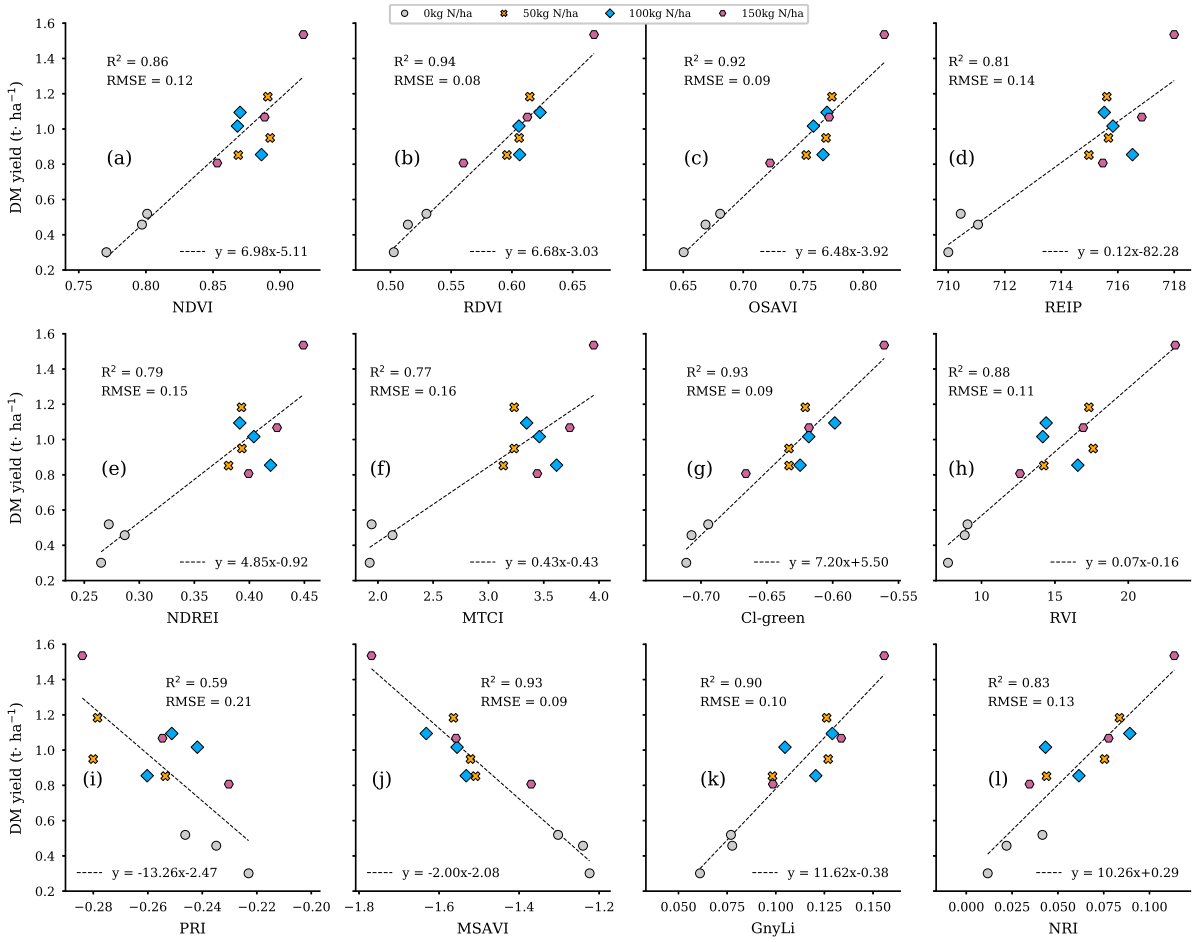


Figure 4.6: (**a**)-(**l**). Scatter plots of the individual VIs listed in Table 4.1 derived from the ASD data and the DM yield. Regression Lines and quality measures from an SLR are added ($p < 0.001$).

Based on the processed GnyLi and NRI orthomosaics, the mean values for both indices of the WPM and ELM were calculated pixel-wise per plot of each replicate via zonal statistics. These data were then compared for each plot of the three replicates with the indices calculated from the ASD data.

Figure 4.7 shows a comparison of three modalities per plot of the three spectral reference replicates for the GnyLi (Figure 4.7e) and the NRI (Figure 4.7f). With the GnyLi index, the three values per plot were relatively close together. A mean relative difference of 11 % for the WPM and 10 % for the ELM method from the ASD reference value was found. For the NRI, the WPM method led to a significant difference of more than 63 %. The ELM method reveals an average relative difference of 37 % to the ASD derived indices. Both GnyLi data sets (WPM, ELM) of the camera system show that there was no clear trend in under- or overestimating the ASD-based VI values. However, it is also visible that NRI WPM and ELM values permanently and indefinitely underestimated ASD reference values.

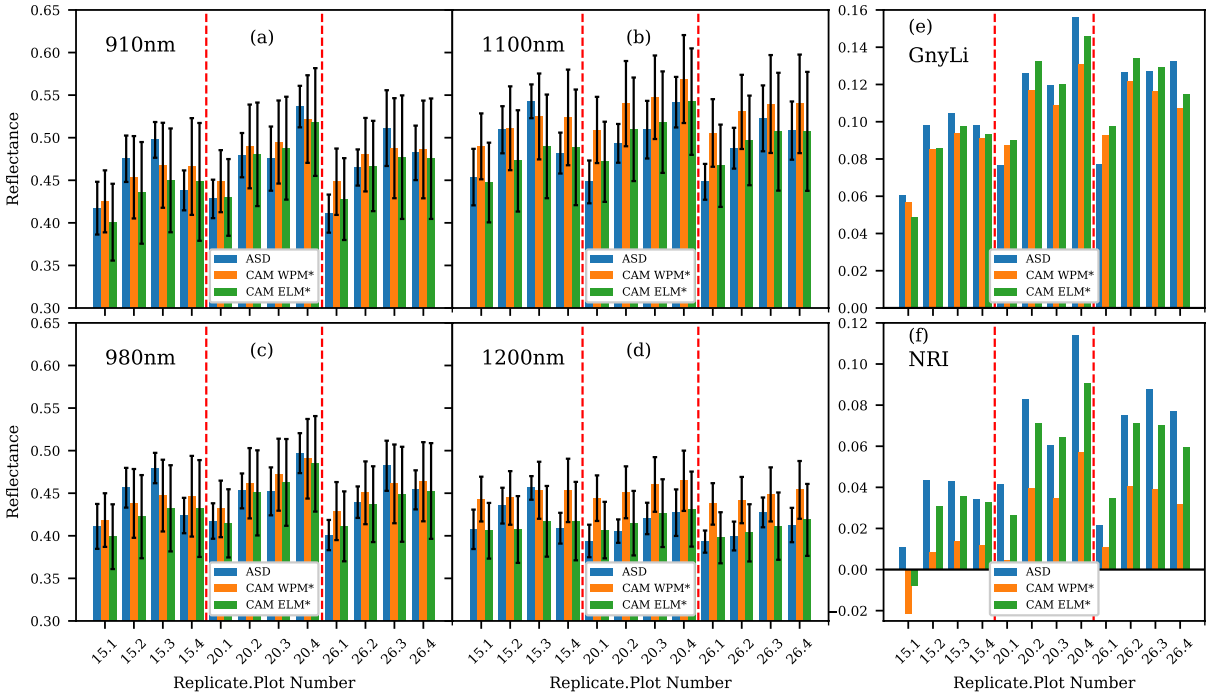


Figure 4.7: (**a**) - (**d**) Direct comparison of the spectral ground truth data of the ASD and the spectral camera reflectance data (WPM, ELM) for each plot of the three replicates and wavelength band. Error bars represent standard deviation. Comparison of the (**e**) GnyLi VI and the (**f**) NRI for the two calibration methods (WPM and ELM) of the camera data and the spectral ground truth ASD data for each plot of the three measured replicates. The y-axes represent the individual plot number of the three replicates and are shared among the subplots

4.3.4 DM yield estimation: camera and ASD VIs

SLR analyses were performed from the three GnyLi and NRI spectral data sets (WPM, ELM, and ASD) against the DM yield data derived from destructive biomass sampling. Table 4.4 lists the predictor equations and the statistical results R^2 and *RMSE* of the six regression models. Figure 4.8 shows the six scatter plots with regression lines as well as R^2 and the *RMSE* as performance measures. As can be seen in Table 4.4, the two indices based on the ASD data provided a higher R^2 (between 23 to 28 % compared to the GnyLi and 6 to 10 % to the NRI) and a lower *RMSE* compared to camera-based indices. When comparing the two calibration methods of the camera-based indices with each other, the WPM shows slightly better values for R^2 and *RMSE*, both about 6 %, compared to the ELM method.

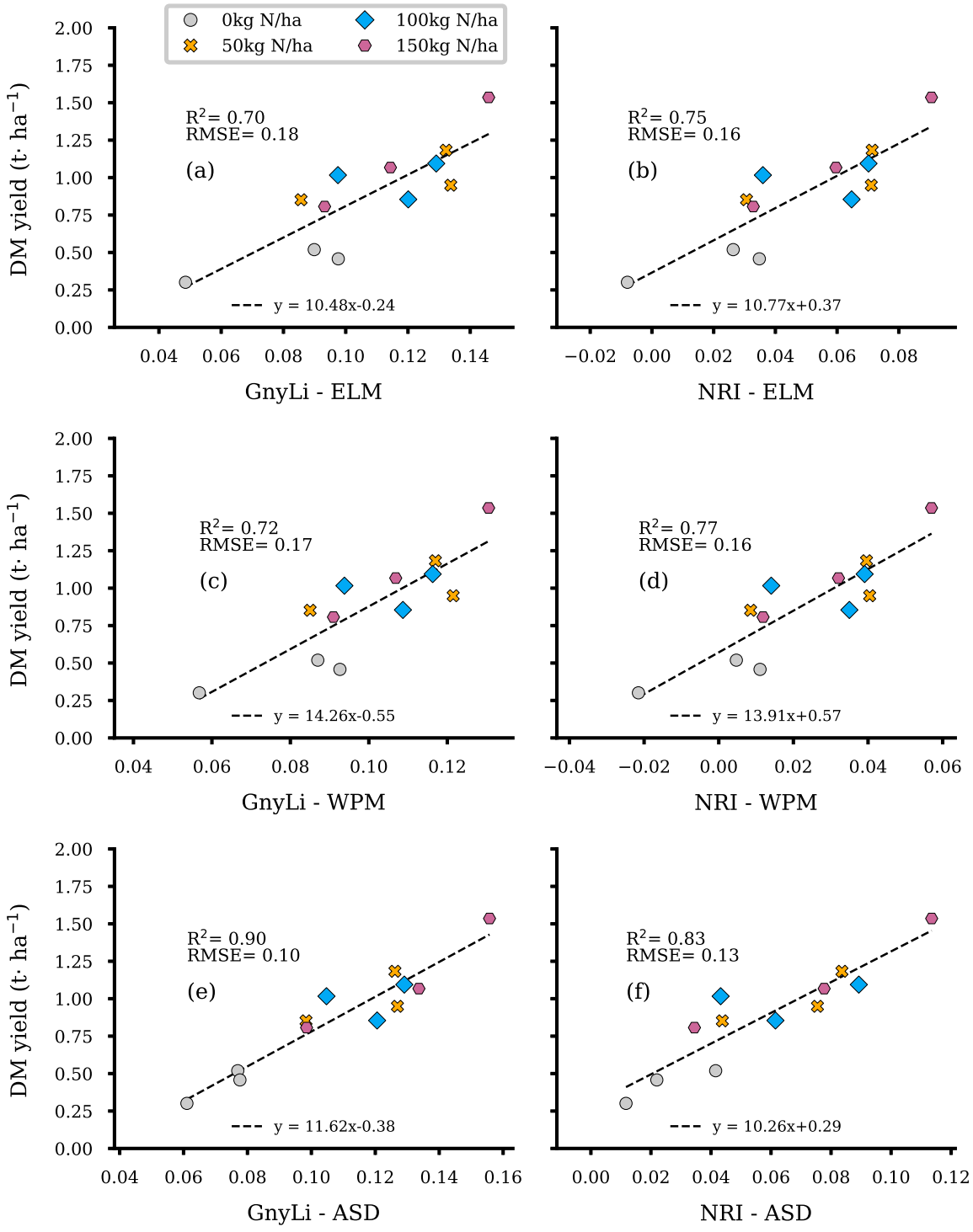


Figure 4.8: Simple linear regression ($p < 0.001$) (**a**)-(**c**) for DM yield versus GnyLi VI derived from two different camera calibration methods (WPM, ELM) with ASD data and (**d**)-(**f**) for measured DM yield and NRI derived from two different camera calibration methods (WPM, ELM) and the ASD data. Y-axes are shared among graphs.

Table 4.4: Summarized statistics of simple linear regression models of the two NIR/SWIR VIs GnyLi and NRI (WPM and ELM camera data as well as from ASD data) against DM yield for the twelve plots of the three replicates ($p < 0.001$).

VI	Equa tion	R^2	*RMSE*	n
GnyLi (ELM)	$y = 10.48x - 0.24$	0.70	0.18	12
GnyLi (WPM)	$y = 14.26x - 0.55$	0.72	0.17	12
GnyLi (ASD)	$y = 11.62x - 0.38$	0.90	0.10	12
NRI (ELM)	$y = 10.77x + 0.34$	0.75	0.16	12
NRI (WPM)	$y = 13.91x + 0.57$	0.77	0.16	12
NRI (ASD)	$y = 10.26x + 0.29$	0.83	0.13	12

4.3.5 DM yield estimation: camera VIs - all plots

The GnyLi and the NRI VIs derived from camera data (WPM and ELM) of all 156 plots were correlated with the DM yield via SLR. Figure 4.9 shows the four resulting scatter plots with regression lines and the corresponding statistical quality characteristics R^2 and *RMSE*. As described in section 4.2, spectral ground truth data are only available for three replicates (twelve plots). Therefore, the two indices calculated on the ASD data are not applicable here. However, these plots are marked separately in Figure 4.9 (a) to (d) and are referred to as "spectral plots" in the respective legend. Table 4.5 summarizes this information. Compared with the results for R^2 and the *RMSE* from Table 4.4, the R^2 for the GnyLi indices performed better, albeit only slightly. For the NRI, however, they have declined to a minor extent.

Table 4.5: Statistics for SLR models of the two NIR/SWIR VIs GnyLi and NRI (WPM and ELM) and the DM yield for all 156 plots of the 39 replicates (n=156, $p < 0.001$).

VI	Equation	R^2	*RMSE*
GnyLi (ELM)	$y = 8.96x - 0.003$	0.71	0.19
GnyLi (WPM)	$y = 11.84x - 0.244$	0.73	0.18
NRI (ELM)	$y = 8.79x + 0.527$	0.73	0.18
NRI (WPM)	$y = 11.09x + 0.692$	0.75	0.17

4.4 Discussion

The study aimed to validate the spectral performance and to investigate NIR/SWIR image data of a newly developed VNIR/SWIR multi-camera prototype for forage mass monitoring. For this purpose, spectral data were acquired on an experimental grassland site near Cologne, Germany, under clear sky conditions in July 2019. The forage mass expressed in dry matter (DM) yield used in the study was obtained by destructive biomass sampling 14 days after the flight date. The weather situation during this period was warm and dry, with occasional short rainfall, so that despite the two-week offset, it can be assumed that the additional growth is still representative of the date of flight and does not have a significant effect on the analyses.

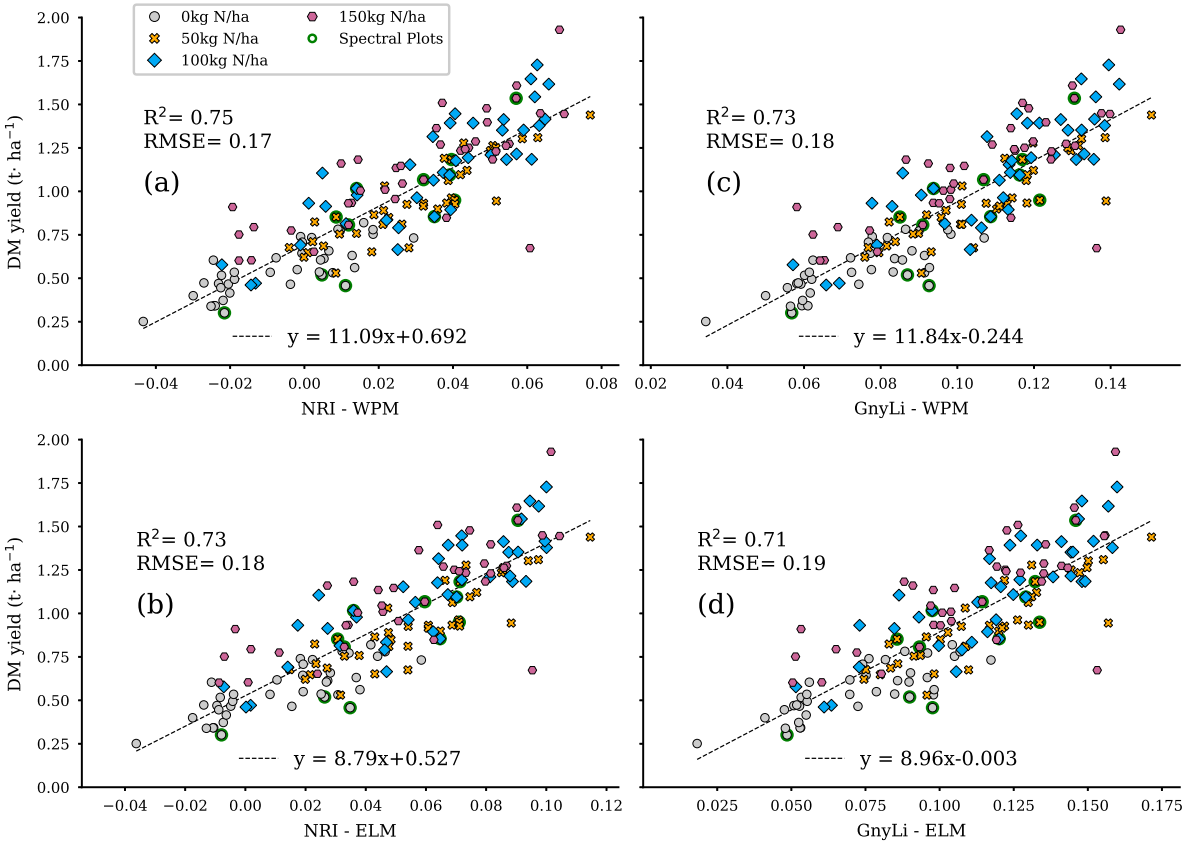


Figure 4.9: Simple linear regression analysis of the NRI: (**a**) WPM and (**b**) ELM and of the GnyLi VI: (**c**) WPM and (**d**) ELM) with DMY; for all 156 plots of the experimental site ($p < 0.001$ for all). Markers of plots with available ASD data (called "spectral plots", see legend) are highlighted with a green circle.

4.4.1 Direct comparison of spectral data sets

The acquired spectral image data were compared to near-ground data of a portable field spectroradiometer. By directly comparing the camera reflectance data with the ASD data, a clear pattern of under- or overestimation could not be detected. A significant difference in the standard deviation (SD) of the individual reflectance values per plot could be observed. The SD of the ASD values is relatively low (ASD: 0.013 to 0.044) compared to the UAV-derived reflectance data (approx. factor 1.5 to 2, WPM: 0.024 to 0.059, ELM: 0.030 to 0.073). One reason could be that for each plot, 13 to 17 ASD spectra were captured and averaged in contrast to approx. 17,200 spectral pixels for the mean camera reflectance values (WPM, ELM) per plot. The overall spectral performance compared to the ASD data and the very high correlation to grayscale panels of $R^2 > 0.99$ for the empirical line method are considered to be very good and prove the suitable application of the newly introduced VNIR/SWIR imaging system for UAV-based vegetation monitoring (see Jenal et al., 2019).

4.4.2 Forage mass estimation

For the estimation of forage mass, three approaches were investigated for the spectral data evaluation:

(i) Narrow-band VIs (see Table 4.1) were calculated from the ASD FieldSpec3 recorded spectra for selected plots and evaluated against (DM) yield using simple linear regression analysis (SLR). The results listed in Table 4.3 show a good to excellent performance with R^2 from 0.59 to 0.94 and *RMSE* from 0.08 to 0.21 t ha^{-1} for the narrowband VIs as a predictor of biomass. In contrast to studies in crops, the two investigated NIR/SWIR VIs do not outperform VNIR VIs (Gnyp et al. 2014 and Tilly et al. 2015). However, both NIR/SWIR VIs, the GnyLi and NRI, show very high R^2 values of 0.83 and 0.9, respectively, using the ASD spectral data. In their studies, Viljanen et al. (2018) and Näsi et al. (2018) used, amongst more sophisticated methods, the SLR in biomass estimation of grass, based on spectral VNIR data acquired with a drone-based FPI camera. With derived VIs similar to our study, the former reached comparable levels in PCCs varying from 0.23 to 0.95 throughout four flight dates. The latter reached a PCC of 0.79. Lussem et al. (2019) used narrowband VIs based on ASD data as a reference and observed that the spectroradiometer VIs, compared to camera-based ones, performed better-having cross-validation R^2 between 0.44 and 0.87 for bivariate linear regression. Similar results can be described from this study using the spectral data of the UAV-borne VNIR/SWIR imaging system.

(ii) The estimations of forage mass via the simple linear regression analyses for all three spectral data sets (WPM, ELM, ASD) of the twelve selected plots performed well. For the camera-based VIs, the NRI data with R^2 of 0.75 for the ELM and R^2 of 0.77 for WPM performed better compared to the GnyLi data (ELM R^2: 0.70 and WPM R^2: 0.72). As expected, the SLR analyses based on the spectral ground truth ASD-derived GnyLi (R^2: 0.9) and NRI (R^2 of 0.83) indices outperformed the respective camera-based VIs. Comparing the two approaches, WPM and ELM for reflectance calibration, the WPM performed slightly better but did not outperform the ELM. Both methods have to be investigated further for the robustness of calibration in future and multi-temporal campaigns.

(iii) The SLR analyses results for the spectral camera data of all 156 plots show robust and good results with R^2 of 0.73 (ELM) and 0.75 (WPM) for the NRI, which means a non-significant decline in performance. The GnyLi, however, showed slightly better accuracies – but also non-significant ones – with an R^2 of 0.71 (ELM) and 0.73 (WPM) compared to the evaluation method (ii). Schut & Ketelaars (2003) applied a hyperspectral line scanner (404–700 nm) with 5 nm spectral resolution on grass swards and reported similar R^2 of 0.59 and for an exponential function 0.82. The latter usually performs better for multi-temporal data sets, which is also reported by Gnyp et al. (2014) for the GnyLi. The authors document R^2 between 0.8 and 0.85 for a multi-temporal and multi-experiments study on winter wheat. Similar results have been presented by Tilly et al. (2015) and Bendig et al. (2015) for winter barley, the NIR/SWIR indices clearly outperformed the VNIR VIs. Geipel et al. (2016) also used SLR for above-ground biomass estimation with a prototype VNIR multispectral camera system and found similar accuracies for the NDVI and REIP as estimators (R^2 of 0.7 to 0.84) for different growth stages in winter wheat.

Finally, only a few published studies highlight the potential of using the SWIR wavelength domain, additionally to the VNIR one. Jacques et al. (2014) document the best potential of MODIS SWIR bands for monitoring dry vegetation masses.Ramoelo et al. (2013) even conclude a very high potential of SWIR imaging data for detecting nitrogen and phosphorus in savannah grasses using airborne HyMap data. Similar findings have been reported by Mutanga & Skidmore (2004) and Mutanga et al. (2005). This study clearly shows the suitable potential of NIR/SWIR bands for forage mass monitoring. However, VNIR VIs also perform similarly or better using ASD data. Further studies have to be conducted to investigate whether UAV-based NIR/SWIR data can be used to develop more robust and better-performing estimators of forage mass monitoring.

4.5 Conclusion

In this study, a newly developed VNIR/SWIR multi-camera prototype was tested for its suitability for vegetation monitoring in grassland, especially for forage mass monitoring. To the authors' knowledge, this was the first flight campaign of a UAV-based VNIR/SWIR capable multi-camera 2D imaging system. The promising results, which are derived from a single flight campaign, indicate the potential of the newly developed VNIR/SWIR camera system to monitor vegetation and especially forage mass. The biomass estimation via both VIs, GnyLi and NRI, correspond well with the results of UAV- and RPM-derived sward height as forage mass estimators in the studies from Lussem et al. (2019) and Lussem et al. (2020). Lussem et al. (2019) found R^2 in the range of 0.56 to 0.75 for UAV-derived sward height and R^2 in the range of 0.61 to 0.88 for RPM derived compressed sward height. For Lussem et al. (2020) R^2 resulted from 0.54 to 0.88 for UAV-derived sward height and from 0.52 to 0.89 for RPM measurements.
Concluding from relating studies, the next research aims towards the application of the newly developed VNIR/ SWIR imaging system for UAVs in multi-temporal campaigns for monitoring grass sward development during several growth periods in a year throughout multiple years. This will also lead to a continuous improvement of the camera system and calibration routines. Furthermore, the potential for detecting nitrogen concentration, more precisely crude protein content, should be further investigated. For the latter, the results reported in the literature should be investigated using full range spectral data (350 - 2500 nm) from field measurements using field spectroradiometers. From this data analysis, characteristic spectral bands can be identified, and appropriate spectral filters applied to this novel VNIR/SWIR multi-camera system for more efficient, area-wide vegetation monitoring by UAVs.

4.6 Acknowledgements, Funding, and Conflict of Interest

The authors would like to thank Mr. Mosler for making his field available for the permanent grassland trial. Further, thanks go to the Yara field team for the N-fertilization and the help in biomass sampling. Furthermore, we would like to thank the student assistants of the University of Cologne for their help with the biomass sampling and the processing of the samples. We would also like to thank the Institute of Plant Science at the University of Bonn, especially Hubert Hüging, for his help with sample preparation.

Open Access funding provided by Projekt DEAL. Alexander Jenal and parts of this work were funded by the Ministry of Science, Further Education and Culture MWWK of Rhineland-Palatinate, Germany.

Ulrike Lussem was supported by the German Federal Ministry of Education and Research (BMBF) [Grant number 031B0734F] as part of the consortium research project "GreenGrass".

The authors declare that they have no conflict of interest.

4.7 References

Aasen, H. & Bareth, G. (2018). Spectral and 3D Nonspectral Approaches to Crop Trait Estimation Using Ground and UAV Sensing. *Hyperspectral Remote Sensing of Vegetation*, volume III Title: Biophysical and Biochemical Characterization and Plant Species Studies, 103–131. CRC Press Taylor & Francis Group, (second edition ed.). https://doi.org/10.1201/9780429431180-4

Aasen, H., Burkart, A., Bolten, A., & Bareth, G. (2015). Generating 3D hyperspectral information with lightweight UAV snapshot cameras for vegetation monitoring: From camera calibration to quality assurance. *ISPRS Journal of Photogrammetry and Remote Sensing*, 108, 245–259. https://doi.org/10.1016/j.isprsjprs.2015.08.002

Bareth, G., Aasen, H., Bendig, J., Gnyp, M. L., Bolten, A., Jung, A., Michels, R., & Soukkamäki, J. (2015). Low-weight and UAV-based Hyperspectral Full-frame Cameras for Monitoring Crops: Spectral Comparison with Portable Spectroradiometer Measurements. *Photogrammetrie - Fernerkundung - Geoinformation*, 2015(1), 69–79. https://doi.org/10.1127/pfg/2015/0256

Baugh, W. M. & Groeneveld, D. P. (2008). Empirical proof of the empirical line. *International Journal of Remote Sensing*, 29(3), 665–672. https://doi.org/10.1080/01431160701352162

Bendig, J., Yu, K., Aasen, H., Bolten, A., Bennertz, S., Broscheit, J., Gnyp, M. L., & Bareth, G. (2015). Combining UAV-based plant height from crop surface models, visible, and near infrared vegetation indices for biomass monitoring in barley. *International Journal of Applied Earth Observation and Geoinformation*, 39, 79–87. https://doi.org/10.1016/j.jag.2015.02.012

Berni, J., Zarco-Tejada, P., Suarez, L., & Fereres, E. (2009). Thermal and Narrowband Multispectral Remote Sensing for Vegetation Monitoring From an Unmanned Aerial Vehicle. *IEEE Transactions on Geoscience and Remote Sensing*, 47(3), 722–738. https://doi.org/10.1109/TGRS.2008.2010457

Boval, M. & Dixon, R. M. (2012). The importance of grasslands for animal production and other functions: A review on management and methodological progress in the tropics. *animal*, 6(5), 748–762. https://doi.org/10.1017/S1751731112000304

Bradski, G. (2000). The OpenCV library. *Dr. Dobb's Journal of Software Tools*.

Camino, C., González-Dugo, V., Hernández, P., Sillero, J., & Zarco-Tejada, P. J. (2018). Improved nitrogen retrievals with airborne-derived fluorescence and plant traits quantified from VNIR-SWIR hyperspectral imagery in the context of precision agriculture. *International Journal of Applied Earth Observation and Geoinformation*, 70(February), 105–117. https://doi.org/10.1016/j.jag.2018.04.013

Capolupo, A., Kooistra, L., Berendonk, C., Boccia, L., & Suomalainen, J. (2015). Estimating Plant Traits of Grasslands from UAV-Acquired Hyperspectral Images: A Comparison of Statistical Approaches. *ISPRS International Journal of Geo-Information*, 4(4), 2792–2820. https://doi.org/10.3390/ijgi4042792

Castle, M. E. (1976). A simple disc instrument for estimating herbage yield. *Grass and Forage Science*, 31(1), 37–40. https://doi.org/10.1111/j.1365-2494.1976.tb01113.x

Dash, J. & Curran, P. J. (2004). The MERIS terrestrial chlorophyll index. *International Journal of Remote Sensing*, 25(23), 5403–5413. https://doi.org/10.1080/0143116042000274015

Earle, D. F. & McGowan, A. A. (1979). Evaluation and calibration of an automated rising plate meter for estimating dry matter yield of pasture. *Australian Journal of Experimental Agriculture*, 19(98), 337–343. https://doi.org/10.1071/ea9790337

Evans, R. A. & Jones, M. B. (1958). Plant Height Times Ground Cover versus Clipped Samples for Estimating Forage Production1. *Agronomy Journal*, 50(9), 504–506. https://doi.org/10.2134/agronj1958.00021962005000090003x

Fricke, T. & Wachendorf, M. (2013). Combining ultrasonic sward height and spectral signatures to assess the biomass of legume–grass swards. *Computers and Electronics in Agriculture*, 99, 236–247. https://doi.org/10.1016/j.compag.2013.10.004

Geipel, J., Link, J., Wirwahn, J., & Claupein, W. (2016). A Programmable Aerial Multispectral Camera System for In-Season Crop Biomass and Nitrogen Content Estimation. *Agriculture*, 6(1), 4. https://doi.org/10.3390/agriculture6010004

Gibson, D. J. (2009). Grasses and grassland ecology. *Annals of Botany*, 104(6), ix–ix. https://doi.org/10.1093/aob/mcp219

Gitelson, A. & Merzlyak, M. N. (1994). Quantitative estimation of chlorophyll-a using reflectance spectra: Experiments with autumn chestnut and maple leaves. *Journal of Photochemistry and Photobiology B: Biology*, 22(3), 247–252. https://doi.org/10.1016/1011-1344(93)06963-4

Gitelson, A. A., Gritz, Y., & Merzlyak, M. N. (2003). Relationships between leaf chlorophyll content and spectral reflectance and algorithms for non-destructive chlorophyll assessment in higher plant leaves. *Journal of Plant Physiology*, 160(3), 271–282. https://doi.org/10.1078/0176-1617-00887

Gnyp, M., Bareth, G., Li, F., Lenz-Wiedemann, V. I., Koppe, W., Miao, Y., Hennig, S. D., Jia, L., Laudien, R., Chen, X., & Zhang, F. (2014a). Development and implementation of a multiscale biomass model using hyperspectral vegetation indices for winter wheat in the North China Plain. *International Journal of Applied Earth Observation and Geoinformation*, 33, 232–242. https://doi.org/10.1016/j.jag.2014.05.006

Gnyp, M. L., Miao, Y., Yuan, F., Ustin, S. L., Yu, K., Yao, Y., Huang, S., & Bareth, G. (2014b). Hyperspectral canopy sensing of paddy rice aboveground biomass at different growth stages. *Field Crops Research*, 155, 42–55. https://doi.org/10.1016/j.fcr.2013.09.023

Guyot, G. & Baret, F. (1988). Utilisation de la Haute Resolution Spectrale pour Suivre L'état des Couverts Vegetaux. *Spectral Signatures of Objects in Remote Sensing*, 287, 279–286. http://adsabs.harvard.edu/abs/1988ESASP.287..279G

Hardin, P. J. & Jackson, M. W. (2005). An Unmanned Aerial Vehicle for Rangeland Photography. *Rangeland Ecology & Management*, 58(4), 439–442. https://doi.org/10.2111/1551-5028(2005)058[0439:AUAVFR]2.0.CO;2

Harvey, P. (2019). *ExifTool by Phil Harvey*. https://exiftool.org/. Last accessed on 03 March 2020.

Hernández-Clemente, R., Navarro-Cerrillo, R. M., Suárez, L., Morales, F., & Zarco-Tejada, P. J. (2011). Assessing structural effects on PRI for stress detection in conifer forests. *Remote Sensing of Environment*, 115(9), 2360–2375. https://doi.org/10.1016/j.rse.2011.04.036

Higgins, S., Schellberg, J., & Bailey, J. S. (2019). Improving productivity and increasing the efficiency of soil nutrient management on grassland farms in the UK and Ireland using precision agriculture technology. *European Journal of Agronomy*, 106, 67–74. https://doi.org/10.1016/j.eja.2019.04.001

Hollberg, J. L. & Schellberg, J. (2017). Distinguishing Intensity Levels of Grassland Fertilization Using Vegetation Indices. *Remote Sensing*, 9(1), 81. https://doi.org/10.3390/rs9010081

Honkavaara, E., Eskelinen, M. A., Pölönen, I., Saari, H., Ojanen, H., Mannila, R., Holmlund, C., Hakala, T., Litkey, P., Rosnell, T., Viljanen, N., & Pulkkanen, M. (2016). Remote Sensing of 3-D Geometry and Surface Moisture of a Peat Production Area Using Hyperspectral Frame Cameras in Visible to Short-Wave Infrared Spectral Ranges Onboard a Small Unmanned Airborne Vehicle (UAV). *IEEE Transactions on Geoscience and Remote Sensing*, 54(9), 5440–5454. https://doi.org/10.1109/TGRS.2016.2565471

Hunt, E. R., Hively, W. D., Fujikawa, S. J., Linden, D. S., Daughtry, C. S. T., & McCarty, G. W. (2010). Acquisition of NIR-Green-Blue Digital Photographs from Unmanned Aircraft for Crop Monitoring. *Remote Sensing*, 2(1), 290–305. https://doi.org/10.3390/rs2010290

Iqbal, F., Lucieer, A., & Barry, K. (2018). Simplified radiometric calibration for UAS-mounted multispectral sensor. *European Journal of Remote Sensing*, 51(1), 301–313. https://doi.org/10.1080/22797254.2018.1432293

Jacques, D. C., Kergoat, L., Hiernaux, P., Mougin, E., & Defourny, P. (2014). Monitoring dry vegetation masses in semi-arid areas with MODIS SWIR bands. *Remote Sensing of Environment*, 153, 40–49. https://doi.org/10.1016/j.rse.2014.07.027

Jenal, A., Bareth, G., Bolten, A., Kneer, C., Weber, I., & Bongartz, J. (2019). Development of a VNIR/SWIR Multispectral Imaging System for Vegetation Monitoring with Unmanned Aerial Vehicles. *Sensors*, 19(24), 5507. https://doi.org/10.3390/s19245507

Jordahl, K., Joris Van den Bossche, Wasserman, J., McBride, J., Fleischmann, M., Gerard, J., Tratner, J., Perry, M., Farmer, C., Hjelle, G. A., Gillies, S., Cochran, M., Bartos, M., Culbertson, L., Eubank, N., Bilogur, A., & maxalbert (2020). *Geopandas/geopandas: V0.7.0*. Zenodo. https://doi.org/10.5281/zenodo.3669853

King, W. M., Rennie, G., Dalley, D., Dynes, R., & Upsdell, M. (2010). Pasture mass estimation by the C-DAX pasture meter: Regional calibrations for New Zealand. *Proceedings of the Australasian Dairy Science Symposium*, Proceedings of the 4th Australasian Dairy Science Symposium, 233–238. http://www.sciquest.org.nz/node/149545

Kluyver, T., Ragan-Kelley, B., Pérez, F., Bussonnier, M., Frederic, J., Hamrick, J., Grout, J., Corlay, S., Ivanov, P., Abdalla, S., & Willing, C. (2016). Jupyter Notebooks—a publishing format for reproducible computational workflows. *Proceedings of the 20th International Conference on Electronic Publishing*, 4. https://doi.org/10.3233/978-1-61499-649-1-87

Koppe, W., Gnyp, M. L., Hennig, S. D., Li, F., Miao, Y., Chen, X., Jia, L., & Bareth, G. (2012). Multi-Temporal Hyperspectral and Radar Remote Sensing for Estimating Winter Wheat Biomass in the North China Plain. *Photogrammetrie - Fernerkundung - Geoinformation*, 2012(3), 281–298. https://doi.org/10.1127/1432-8364/2012/0117

Koppe, W., Li, F., Gnyp, M. L., Miao, Y., Jia, L., Chen, X., Zhang, F., & Bareth, G. (2010). Evaluating Multispectral and Hyperspectral Satellite Remote Sensing Data for Estimating Winter Wheat Growth Parameters at Regional Scale in the North China Plain. *Photogrammetrie - Fernerkundung - Geoinformation*, 2010(3), 167–178. https://doi.org/10.1127/1432-8364/2010/0047

Legg, M. & Bradley, S. (2020). Ultrasonic Arrays for Remote Sensing of Pasture Biomass. *Remote Sensing*, 12(1), 111. https://doi.org/10.3390/rs12010111

Lussem, U., Bolten, A., Menne, J., Gnyp, M. L., Schellberg, J., & Bareth, G. (2019). Estimating biomass in temperate grassland with high resolution canopy surface models from UAV-based RGB images and vegetation indices. *Journal of Applied Remote Sensing*, 13(3), 034525. https://doi.org/10.1117/1.JRS.13.034525

Lussem, U., Schellberg, J., & Bareth, G. (2020). Monitoring Forage Mass with Low-Cost UAV Data: Case Study at the Rengen Grassland Experiment. *PFG – Journal of Photogrammetry, Remote Sensing and Geoinformation Science*. https://doi.org/10.1007/s41064-020-00117-w

Martin, G. (2015). High Performance SWIR Imaging Cameras. *Raptor Photonics White Paper*, Raptor Photonics Ltd.: Milbrook, Larne, UK.

Mutanga, O. & Skidmore, A. K. (2004). Integrating imaging spectroscopy and neural networks to map grass quality in the Kruger National Park, South Africa. *Remote Sensing of Environment*, 90(1), 104–115. https://doi.org/10.1016/j.rse.2003.12.004

Mutanga, O., Skidmore, A. K., Kumar, L., & Ferwerda, J. (2005). Estimating tropical pasture quality at canopy level using band depth analysis with continuum removal in the visible domain. *International Journal of Remote Sensing*, 26(6), 1093–1108. https://doi.org/10.1080/01431160512331326738

Näsi, R., Viljanen, N., Kaivosoja, J., Alhonoja, K., Hakala, T., Markelin, L., & Honkavaara, E. (2018). Estimating Biomass and Nitrogen Amount of Barley and Grass Using UAV and Aircraft Based Spectral and Photogrammetric 3D Features. *Remote Sensing*, 10(7), 1082. https://doi.org/10.3390/rs10071082

Nelson, C., Moore, K. J., & Collins, M. (2017). Forages and Grasslands in a Changing World. *Forages*, volume 1, 432. Wiley. https://www.semanticscholar.org/paper/Forages-and-Grasslands-in-a-Changing-World-Nelson-Moore/144a1772b84ffd519eb60b89de0a6932d9c01368

Pearson, R. L. & Miller, L. D. (1972). Remote Mapping of Standing Crop Biomass for Estimation of the Productivity of the Shortgrass Prairie. *Proceedings of the Eighth International Symposium on Remote Sensing of Environment*, 1355. http://adsabs.harvard.edu/abs/1972rse..conf.1355P

Perez, F. & Granger, B. E. (2007). IPython: A System for Interactive Scientific Computing. *Computing in Science & Engineering*, 9(3), 21–29. https://doi.org/10.1109/MCSE.2007.53

Portz, G., Gnyp, M. L., & Jasper, J. (2017). Capability of crop canopy sensing to predict crop parameters of cut grass swards aiming at early season variable rate nitrogen top dressings. *Advances in Animal Biosciences*, 8(2), 792–795. https://doi.org/10.1017/S2040470017001364

Qi, J., Chehbouni, A., Huete, A. R., Kerr, Y. H., & Sorooshian, S. (1994). A modified soil adjusted vegetation index. *Remote Sensing of Environment*, 48(2), 119–126. https://doi.org/10.1016/0034-4257(94)90134-1

Ramoelo, A., Skidmore, A. K., Schlerf, M., Heitkönig, I. M. A., Mathieu, R., & Cho, M. A. (2013). Savanna grass nitrogen to phosphorous ratio estimation using field spectroscopy and the potential for estimation with imaging spectroscopy. *International Journal of Applied Earth Observation and Geoinformation*, 23, 334–343. https://doi.org/10.1016/j.jag.2012.10.009

Rango, A., Laliberte, A., Steele, C., Herrick, J. E., Bestelmeyer, B., Schmugge, T., Roanhorse, A., & Jenkins, V. (2006). Research Article: Using Unmanned Aerial Vehicles for Rangelands: Current Applications and Future Potentials. *Environmental Practice*, 8(3), 159–168. https://doi.org/10.1017/S1466046606060224

Rondeaux, G., Steven, M., & Baret, F. (1996). Optimization of soil-adjusted vegetation indices. *Remote Sensing of Environment*, 55(2), 95–107. https://doi.org/10.1016/0034-4257(95)00186-7

Roujean, J.-L. & Breon, F.-M. (1995). Estimating PAR absorbed by vegetation from bidirectional reflectance measurements. *Remote Sensing of Environment*, 51(3), 375–384. https://doi.org/10.1016/0034-4257(94)00114-3

Rouse, W., Haas, R. H., Schell, J. A., & Deering, D. W. (1974). Monitoring vegetation systems in the Great Plains with ERTS. *Third Earth Resources Technology Satellite-1 Symposium (NASA SP-351)*, 309–317.

Sanderson, M. A., Rotz, C. A., Fultz, S. W., & Rayburn, E. B. (2001). Estimating Forage Mass with a Commercial Capacitance Meter, Rising Plate Meter, and Pasture Ruler. *Agronomy Journal*, 93(6), 1281–1286. https://doi.org/10.2134/agronj2001.1281

Santillan, R. A., Ocumpaugh, W. R., & Mott, G. O. (1979). Estimating Forage Yield with a Disk Meter1. *Agronomy Journal*, 71(1), 71–74. https://doi.org/10.2134/agronj1979.00021962007100010017x

Schut, A. G. T. & Ketelaars, J. J. M. H. (2003). Monitoring grass swards using imaging spectroscopy. *Grass and Forage Science*, 58(3), 276–286. https://doi.org/10.1046/j.1365-2494.2003.00379.x

Smith, G. M. & Milton, E. J. (1999). The use of the empirical line method to calibrate remotely sensed data to reflectance. *International Journal of Remote Sensing*, 20(13), 2653–2662. https://doi.org/10.1080/014311699211994

Stevens, A. & Ramirez-Lopez, L. (2013). An introduction to the prospectr package. *R Package*.

Suttie, J., Batello, C., & Reynolds, S. (2005). *Grassland of the World*, volume 34 of *Plant Production and Protection Series*. The Food and Agriculture Organization. http://www.fao.org/3/y8344e/y8344e00.htm#Contents

Tilly, N., Aasen, H., & Bareth, G. (2015). Fusion of Plant Height and Vegetation Indices for the Estimation of Barley Biomass. *Remote Sensing*, 7(9), 11449–11480. https://doi.org/10.3390/rs70911449

Viljanen, N., Honkavaara, E., Näsi, R., Hakala, T., Niemeläinen, O., & Kaivosoja, J. (2018). A Novel Machine Learning Method for Estimating Biomass of Grass Swards Using a Photogrammetric Canopy Height Model, Images and Vegetation Indices Captured by a Drone. *Agriculture*, 8(5), 70. https://doi.org/10.3390/agriculture8050070

Wang, C. & Myint, S. W. (2015). A Simplified Empirical Line Method of Radiometric Calibration for Small Unmanned Aircraft Systems-Based Remote Sensing. *IEEE Journal of Selected Topics in Applied Earth Observations and Remote Sensing*, 8(5), 1876–1885. https://doi.org/10.1109/JSTARS.2015.2422716

5 Investigating the Potential of a Newly Developed UAV-Based VNIR/SWIR Imaging System for Monitoring Crop Traits—A Case Study for Winter Wheat

Alexander Jenal[1,3,*], Hubert Hüging[2], Hella Ellen Ahrends[4], Andreas Bolten[1], Jens Bongartz[3], Georg Bareth[1]

Published in MDPI Remote Sensensing 2021, 13(9), 1697; doi.org/10.3390/rs13091697

Formatting and orthography of the manuscript is adapted to the dissertation style.

1 Institute of Geography, GIS & RS Group, University of Cologne, 50923 Cologne, Germany; andreas.bolten@uni-koeln.de (A.B.); g.bareth@uni-koeln.de (G.B.)

2 INRES - Institute of Crop Science and Resource Conservation, University of Bonn, Katzenburgweg 5, 53115 Bonn, Germany; h.hueging@uni-bonn.de (H.H.)

3 Application Center for Machine Learning and Sensor Technology, University of Applied Science Koblenz, 53424 Remagen, Germany; bongartz@hs-koblenz.de (J.B.)

4 Department of Agricultural Sciences, Faculty of Agriculture and Forestry, University of Helsinki, Koetilantie 5, 00790 Helsinki, Finland; ellen.ahrends@helsinki.fi (H.E.A.)

* Correspondence: alexander.jenal@hs-koblenz.de; Tel.: +49-2642-932-411

The author's contribution to this study is substantial and declared in detail in Appendix C.

Abstract

UAV-based multispectral multi-camera systems are widely used in scientific research for non-destructive crop traits estimation to optimize agricultural management decisions. These systems typically provide data from the visible to near-infrared (VNIR) domain. However, several key absorption features related to biomass and nitrogen (N) are located in the short-wave infrared (SWIR) domain. Therefore, this study investigates a novel multi-camera system prototype that addresses this spectral gap with a sensitivity from 600 to 1700 nm by implementing dedicated bandpass filter combinations to derive application-specific vegetation indices (VIs). In this study, two VIs, GnyLi and NRI, were applied using data obtained on a single observation date at a winter wheat field experiment located in Germany. Ground truth data were destructively sampled for the entire growing season. Likewise, crop heights were derived from UAV-based RGB image data using an improved approach developed within this study. Based on these variables, regression models were derived to estimate fresh and dry biomass, crop moisture, N concentration, and N uptake. The relationships between the NIR/SWIR-based VIs and the estimated crop traits were successfully evaluated (R^2: 0.57 to 0.66). Both VIs were further validated against the sampled ground truth data (R^2: 0.75 to 0.84). These results indicate the imaging system's potential for monitoring crop traits in agricultural applications, but further multitemporal validations are needed.

Keywords: unmanned aerial vehicle (UAV); near-infrared (NIR); short-wave infrared (SWIR); biomass; nitrogen concentration; nitrogen uptake; crop moisture; crop height; winter wheat; precision agriculture

5.1 Introduction

In light of the increase in the global population, food security will be a significant concern in the next decades (Foley, 2011). This security can be enhanced by good decision support in crop management, and for that purpose, non-destructive imaging technologies are of key importance, especially when it comes to diagnosing in-season site-specific crop status (Huang et al., 2017; Weiss et al., 2020; Atzberger, 2013). In this context, the most promising research area is precision agriculture that utilizes proximal and remote sensing technologies (Mulla, 2013). In the last decade, remote sensing of crops changed significantly in two ways: (i) open access satellite data enabled the analysis of large multi-temporal data sets in spatial resolutions of at least 10 to 20 m (Veloso et al., 2017; Hütt et al., 2020) and (ii) progress in new data acquisition and analysis approaches were facilitated by the fast development of unmanned aerial vehicles (UAVs) as sensor carrying platforms for RGB, multi- and hyperspectral, LiDAR, or thermal sensing systems (Aasen et al., 2015; Bendig et al., 2015; Candiago et al., 2015; ten Harkel et al., 2020; Sagan et al., 2019).

Studies on UAV-based sensing of crops have demonstrated the potential of such non-destructive approaches in determining crop traits (Bareth et al., 2011; Maes & Steppe, 2019; Aasen & Bareth, 2018). As shown in many studies since 2013, robust crop height data, which have a strong link to biomass, can be derived from stereo-photogrammetric and GIS analyses (Bendig et al., 2013; Bareth & Schellberg, 2018; Gilliot et al., 2020). A general problem is that estimation of nitrogen concentration (N_C) from spectral data over different plant constituents is only indirectly possible, since N_C has no unique spectral features in the VNIR-SWIR range. According to Berger et al. (2020), most studies only use the VNIR (400 to 1000 nm) to determine crop traits, especially nitrogen, in relation to chlorophyll. However, this approach neglects the foliar biochemical contents, such as plant proteins, which have faint spectral components in the short-wave infrared (SWIR) and whose link to different crop traits has hardly been studied so far, leading Berger et al. (2020) to recommend including this domain explicitly.

Likewise, Stroppiana et al. (2018) state that this wavelength range has the potential to reveal new approaches or indices for vegetation monitoring. Herrmann et al. (2010) attribute the under-exploration of this domain to traditional and to technical aspects. Those aspects have meant that expensive and heavyweight equipment, such as portable field-spectroradiometers or hyperspectral scanner systems on various airborne platforms, have been used so far. As a result of technological advances in recent years, however, these former shortcomings are increasingly being overcome, enabling new application scenarios. Exemplary in this context, Kandylakis et al. (2020) developed a methodology for estimating water stress in vineyards using the unfiltered spectral response (900 to 1700 nm) of a SWIR imager combined with a VNIR multispectral multi-camera system (Parrot Sequoia; Parrot Drone SAS, Paris, France) using a UAVs. However, no multi-camera system based on VIS-enhanced InGaAs (600 to 1700 nm) cameras with application-specific applicable narrowband bandpass filters appear to have been used.

Within the latest research activities on UAV-based monitoring of crops, Jenal et al. (2019) presented a new and unique sensing system for UAVs, a VNIR/SWIR imaging system that enables the acquisition of two filter-selectable wavelengths in the range of 600 to 1700 nm. This research's primary motivation is driven by several publications indicating two- or four-band NIR/SWIR vegetation indices (VIs) as robust estimators for crop traits.

To predict winter wheat biomass, Koppe et al. (2010) fitted the normalized ratio index (NRI) to the best-performing wavelengths, 874 and 1225 nm, from hyperspectral satellite data. Gnyp et al. (2014) also investigated winter wheat introducing a four-band vegetation index (VI), the GnyLi. Bendig et al. (2015) and Tilly et al. (2015) evaluated the GnyLi on barley biomass data sets showing high R^2 and outperforming VNIR VIs.

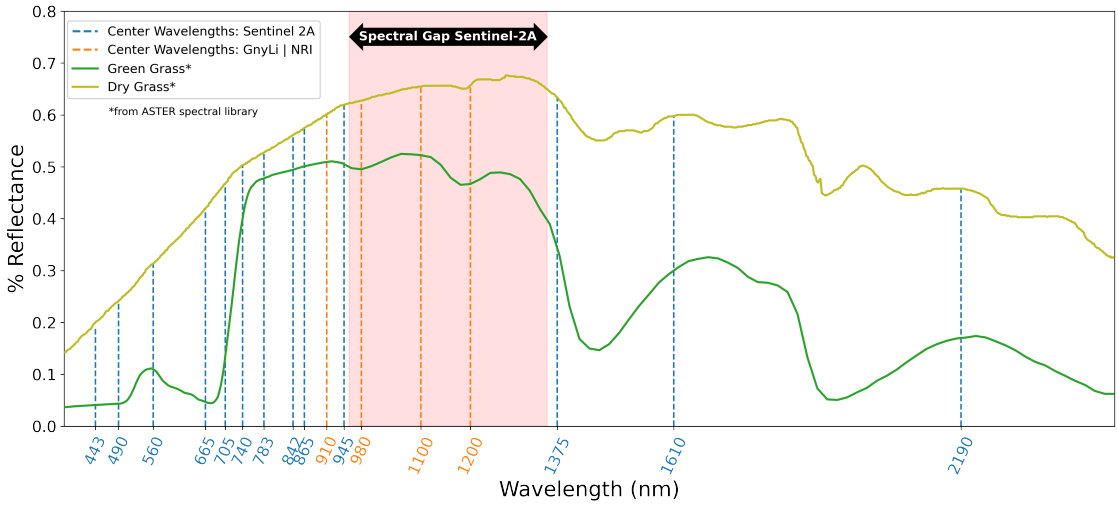


Figure 5.1: Typical reflectance spectra for green and dry grass plotted from the ASTER spectral library (Baldridge et al., 2009), the center wavelengths of Sentinel-2A (ESA, 2017) (dashed vertical blue lines), and the applied center wavelengths of the VNIR/SWIR multi-camera system for the GnyLi and the NRI (dashed vertical orange lines).

Camino et al. (2018) investigated VNIR/SWIR imaging for N retrieval in wheat and concluded that VIs centered at 1510 nm outperform chlorophyll and structural indices. While these wavelength bands have been successfully applied in field studies, they are not covered by comparable multispectral Earth observation (EO) missions, such as Sentinel-2 (see Figure 5.1). Three of the four selected wavebands in this study are located in the "spectral gap" from 955 and 1355 nm indicated in Figure 5.1. This gap in the Sentinel spectral sensitivity might contribute to the low number of studies investigating the use of these wavelengths for precision agriculture.

According to Kumar et al. (2001), the vegetation compounds' spectral characteristics are present in this segment and are of interest for further investigations. Absorption minima caused by canopy moisture, cellulose, starch, and lignin can be found at around 970 and 1200 nm (Curran, 1989; Kumar et al., 2001; Roberts et al., 2018). Reflectance maxima lie roughly at 910 and 1100 nm and are caused by components of protein content, lignin, and intercellular plant structures (Curran, 1989; Kumar et al., 2001). Roberts et al. (2018) provide a detailed review on VIs for retrieving data on vegetation structure, canopy biochemistry, e.g., pigments or moisture, or plant physiology.

This study aims to evaluate and validate a novel VNIR/SWIR multi-camera system's performance and potential to assess crop traits using a winter wheat field trial at the Campus Klein-Altendorf (North Rhine-Westphalia, Germany) as a case study. More specifically, the objectives are to (i) regress UAV-based and manually measured crop heights against ground truth data, (ii) apply resulting regression models to estimate crop traits (fresh and dry) biomass, crop moisture, N_C, and N uptake, and (iii) evaluate and validate the relationship between NIR/SWIR-based vegetation indices and crop traits.

5.2 Study Site and Methods

5.2.1 Trial Description

Winter wheat was grown in an experimental field (50°37′11.85″N and 6°59′45.47″E) at the research site *Campus Klein-Altendorf* (CKA, www.cka.uni-bonn.de, last accessed on March 2021), which is located near the City of Bonn, Germany. The CKA is the largest off-site laboratory experimental farm of the Faculty of Agriculture at the University of Bonn. The winter wheat trial is managed by the Institute of Crop Science and Resource Conservation (INRES, University of Bonn, Germany). The soil type can be described as a Haplic Luvisol on loess. The site is characterized by an Atlantic climate with a mean annual precipitation of 603 mm and a mean annual temperature of 9.6 °C (1956—2020). The crops are grown under conventional management with regular application of pesticides, fungicides, and growth regulators. A crop rotation of "winter barley—winter barley—sugar beet—winter wheat" is maintained in the experimental field. At the time of sowing, the pH value averaged 6.7, and the humus content was 1.4 %. Per 100 g of soil portion, P_2O_5 content was 20 mg, K_2O content was 13 mg, and MgO content was 7 mg. Mineralized nitrogen (N_{min}) content was 10 kg ha^{-1} at a soil depth of 0 to 30 cm, 32 kg ha^{-1} at 30 to 60 cm, and 18 kg ha^{-1} at 60 to 90 cm. The winter wheat trial can be described as a split-plot design divided into five rows (see Figure 5.2). Each row is, in turn, subdivided into three nitrogen treatments (N1-N3). Each nitrogen treatment contains six different winter wheat varieties, first released in 1935 (see Table 5.1, Ahrends et al., 2018). On November 11, 2019, these varieties were randomly sown in plots measuring 7.0×1.5 m using a row spacing of 11.3 cm, resulting in a total number of 18 plots per row. Cultivars were grown under three different nitrogen levels, receiving either 0 (N1), 120 (N2), or 240 kg N ha^{-1} (N3). The 18 randomized crop-treatment combinations were replicated in the five rows, leading to 90 plots for the field trial. Nitrogen was supplied as calcium ammonium nitrate, with the first application during wheat tillering (March 17), the second at the beginning of stem elongation (April 16), and the third during the late booting stage (May 18) in 2020.

Table 5.1: Winter wheat varieties

No	Variety	Year of release
1	Heines II	1935
2	Heines VII	1950
3	Heines Rot	1949
4	Jubilar	1961
5	Sperber	1982
6	Tommi	2002

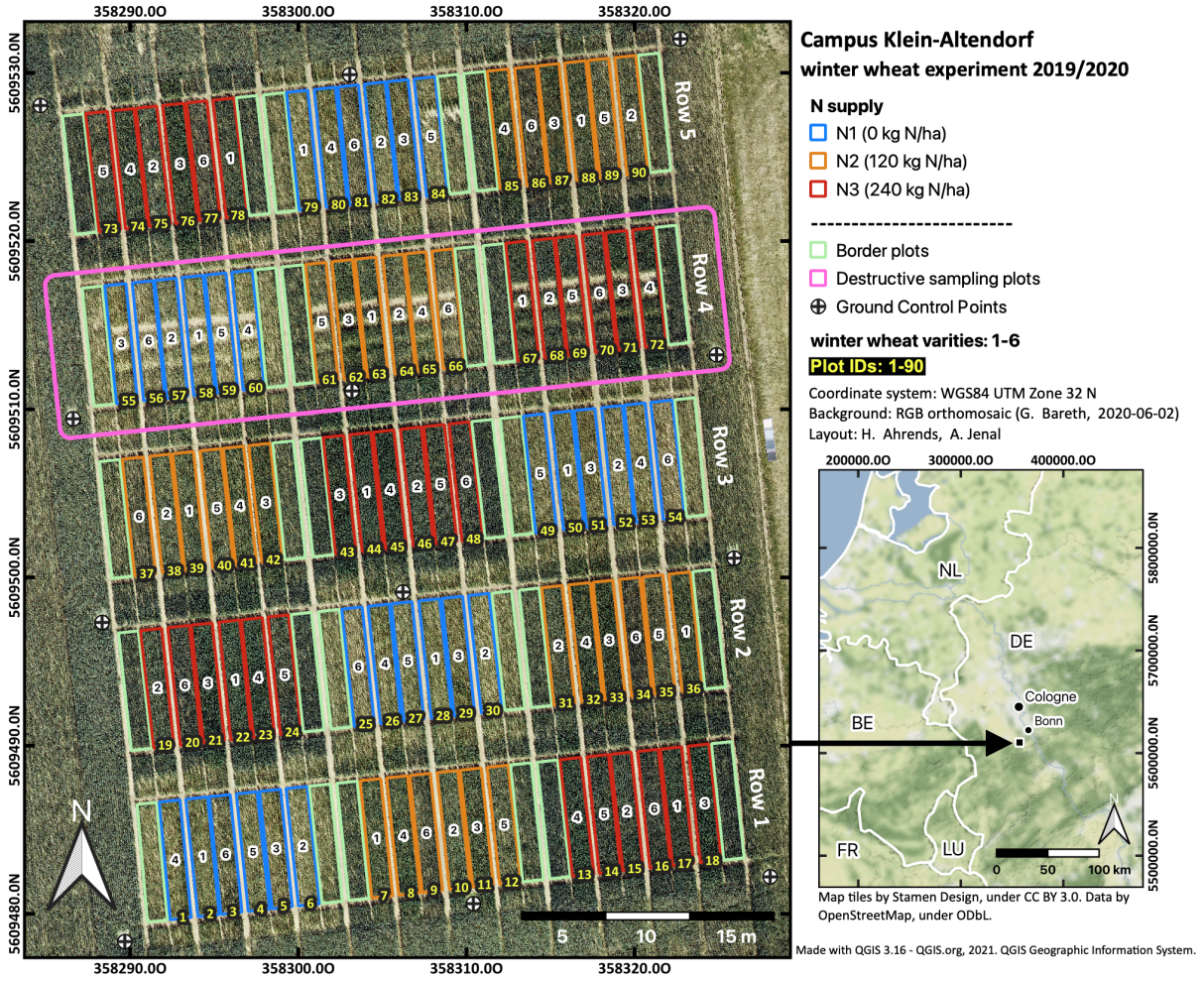


Figure 5.2: Location map and additional information of the winter wheat experiment at Campus Klein-Altendorf (2019/2020).

5.2.2 Biomass Sampling, Nitrogen Concentrations, and Height Measurements

Biomass sampling was performed destructively within one of the five rows (no. 4, see Figure 5.2) approximately every two weeks, resulting in a total number of six observation dates (April 08, April 28, May 13, May 26, June 09, and July 02). During these observation dates, the complete plant biomass was cut using standard scissors at a length of 50 cm along three different sowing rows, with three replicates for each plot. We excluded the two outermost rows from sampling to avoid edge effects. After measuring each sample's fresh biomass (FBM) weight, sub-samples were oven-dried (at 105 °C for 1–2 days) to calculate the plant dry biomass (DBM) (g). The remaining plant biomass samples were oven-dried at 60 °C until reaching a constant weight and ground for the subsequent analysis of carbon (C) and N_C (%) using a C/N analyzer (EuroEA3000, EuroVector S.p.A., Italy). Manual height measurements of all 90 plots were taken on the first five observation dates by holding a folding rule in the center of each plot and visually reading the crop height at the head of that plot.

5.2.3 UAV Data Acquisition for Crop Height Analysis—Crop Height Workflow

UAV-derived crop heights (CHs) were produced using a DJI© Phantom 4 RTK (P4RTK). The P4RTK is equipped with a 1″ global shutter CMOS sensor providing 20 megapixels in RGB. The P4RTK connects to an RTK base station for precise geotagging of the image data. Figure 5.3 displays the P4RTK during take-off, the base station, and the flown flight path pattern. The same flight plan was used for all UAV campaigns on nine dates: March 26, April 07, April 28, May 13, May 26, June 02, June 12, July 01, and July 21. For each date, approx. 400 photos were acquired from a flight altitude of 25 m above ground level (AGL). Besides the UAV data acquisition, 12 ground control points (GCPs) were permanently installed and georeferenced with an RTK-GPS (Topcon GR-5).

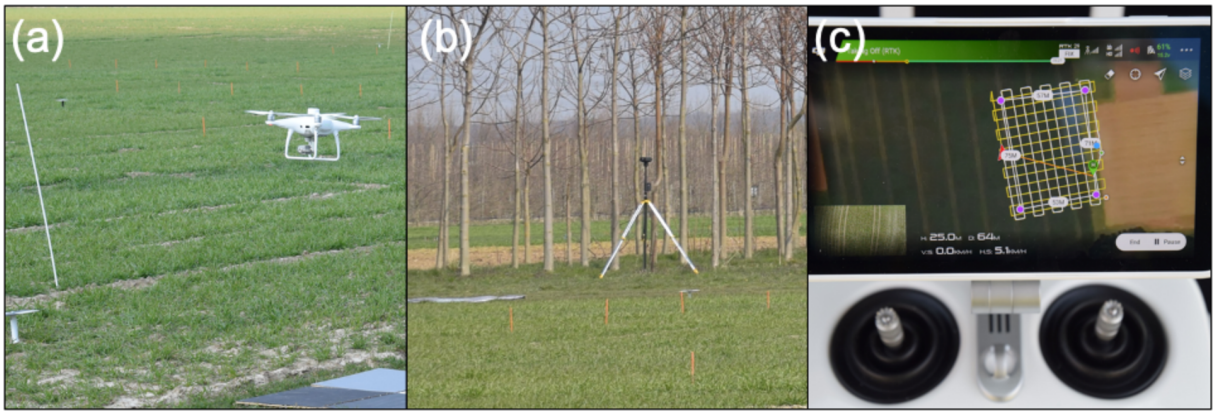


Figure 5.3: The utilized UAV for crop height analysis is (**a**) a DJI© Phantom 4 RTK, which can be operated in RTK mode using (**b**) a base station. Flight planning is also possible (**c**).

Numerous studies have proven that UAV-derived image data for structure from motion and multi-view stereopsis (SfM/MVS) analysis provide a robust method to derive CH (Viljanen et al., 2018; Geipel et al., 2014; Bareth & Schellberg, 2018). Therefore, we essentially followed the crop surface model (CSM) approach introduced by Hoffmeister et al. (2010) for terrestrial laser scanning data, which was successfully applied on a UAV data set for winter barley by Bendig et al. (2013). The latter used Agisoft Photoscan for SfM/MVS analysis to generate 3D data and digital orthophotoss (DOPs). For this study, we used Metashape (Version 1.5.2, Agisoft LLC, St. Petersburg, Russia) for SfM/MVS analysis. We exported the DOPs and digital surface models (DSMs) into ESRI's ArcGIS software to compute CH from the DSMs. In this study, however, accounting for the suggestions by Lussem et al. (2017), we tested a newly elaborated analysis workflow: (i) we used the direct RTK-georeferenced P4RTK images and batch-processed them directly in Metashape without using GCPs, (ii) we georeferenced DOPs and DSMs to the GCPs in ArcGIS, (iii) we normalized the elevation of all DSMs to the same take-off point of each UAV campaign in ArcGIS, and (iv) we computed crop heights in ArcGIS, subtracting the digital terrain model (DTM) from March 26 from all other dates. Step (iii) was intended and necessary due to appropriately setting the same x,y,z-data of the P4RTK base station on March 26 and April 28. The ground sampling distance was approx. 0.007 m for the DOPs and approx. 0.013 m for the DSMs. Figure 5.4 shows the DSM from March 26, the CSM from June 12, and the CH, computed by subtracting the March 26 DSM from the June 12 CSM.

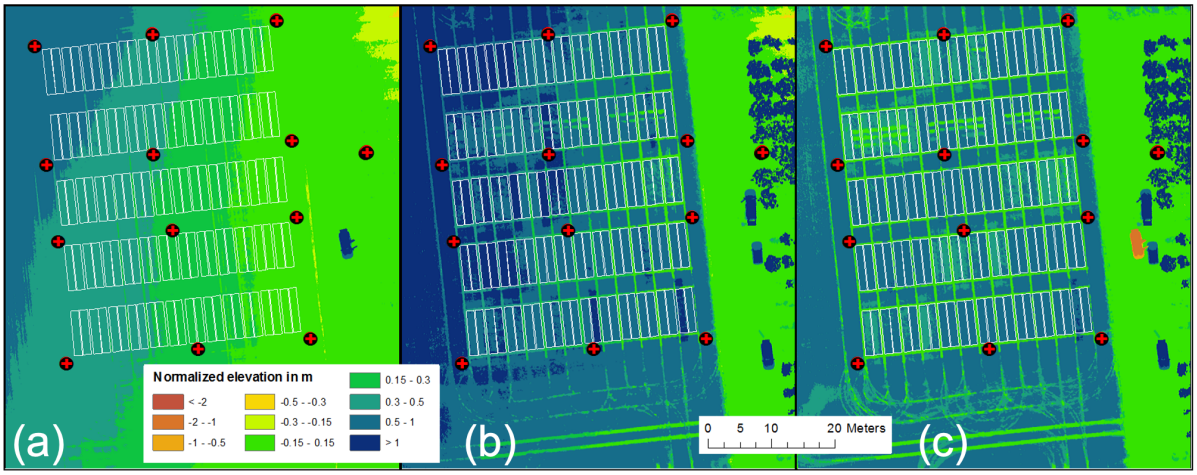


Figure 5.4: Visualization of (**a**) the normalized base Digital Surface Model (DSM) at the beginning of the growing season 2020 on March 26. In the middle, (**b**) represents a normalized Crop Surface Model (CSM) for June 12, and (**c**) is the CH computed by subtracting (**a**) from (**b**).

5.2.4 VNIR/SWIR Imaging System and Vegetation Indices

This study's evaluation applies a novel VNIR/SWIR multi-camera system (Jenal et al., 2019), *camSWIR*. In a permanent grassland trial, Jenal et al. (2020) successfully tested this prototype for its suitability in estimating forage mass. The system's modular two-part design means it can be integrated into various aerial remote sensing platforms, focusing on UAV-based multi-rotor vehicles (see Figure 5.5). The centerpiece consists of the spectral camera unit (SCU), which combines two VNIR enhanced SWIR cameras based on the semiconductor material InGaAs. Two single-wavelength image data sets are captured per flight. For this, each camera of the system is adopted with an application-specific bandpass filter via specially designed inter-changeable filter flanges to derive well-established VIs in the VNIR/SWIR spectral range.

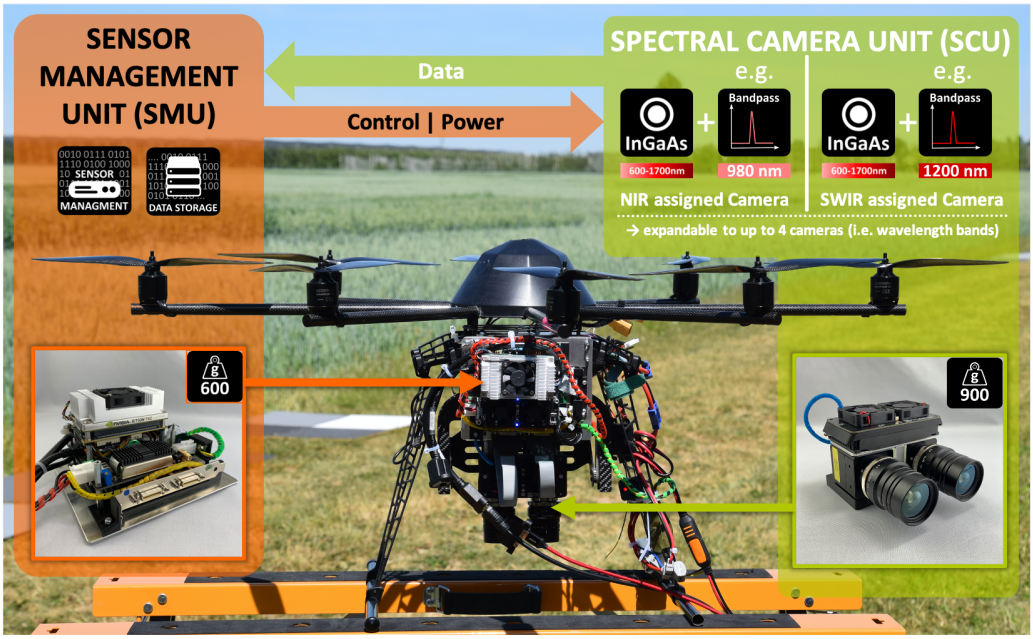


Figure 5.5: Overview of the VNIR/SWIR multi-camera imaging system mounted on a UAV.

Table 5.2 summarizes the two NIR/SWIR-based VIs, GnyLi and NRI, which were chosen to evaluate the system's spectral performance in this study. The four-band GnyLi was developed by Gnyp et al. (2014) using hyperspectral narrowband vegetation indices in winter wheat. This VI uses two local minima and maxima in the reflectance spectrum of vegetation between 900 and 1300 nm (see Figure 5.1). Absorption by canopy moisture, moisture stress, and plant water content dominate these two minima (Roberts et al., 2018). Overtone bands of starch (around 970 nm) as well as cellulose, starch, and lignin (around 1200 nm) also affect both absorption ranges (Curran, 1989; Kumar et al., 2001; Roberts et al., 2018). The two reflectance maxima around 910 and 1100 nm are dominated by the plant leaves' intercellular structures and to a minor extent by overtone bands of protein and lignin (Curran, 1989; Kumar et al., 2001; Hank et al., 2019). Thus, there are two biomass-related and two moisture-sensitive spectral components in the GnyLi equation.
In contrast to the bandpass wavelengths selected by Gnyp et al. (2014), commercially available, narrowband hybrid bandpass filters were selected at center wavelengths of 980 and 1200 nm for the reflectance minima and 910 and 1100 nm for the reflectance maxima, with a spectral bandwidth (full width at half maximum, FWHM) of (10 ± 2) nm each. This bandwidth already meets the spectral resolution, at least in the SWIR, of some hyperspectral sensors, especially in the field of EO satellite missions. A comprehensive overview can be found in Berger et al. (2020).

Table 5.2: NIR/SWIR vegetation indices derived from the camera system and used in this study. The wavebands used differ from the original selection of Gnyp et al. (2014) and Koppe et al. (2010). One reason is the limited range of readily available narrowband and high-performance bandpass filters for this application.

Name	Equation	Reference
GnyLi	$\frac{(R_{910} \cdot R_{1100}) - (R_{980} \cdot R_{1200})}{(R_{910} \cdot R_{1100}) + (R_{980} \cdot R_{1200})}$	Gnyp et al. (2014)
NRI	$\frac{R_{910} - R_{1200}}{R_{910} + R_{1200}}$	Koppe et al. (2010)

The second VI uses an NDVI-like equation. This so-called normalized ratio index (NRI) is widely used with different wavelengths, mainly in the VNIR domain (Thenkabail et al., 2000; Sims & Gamon, 2002). Koppe et al. (2010) extended this index to the NIR/SWIR range by empirical testing with Hyperion data and found high coefficients of determination between this narrowband VI and above-ground biomass in winter wheat. In this study, the wavelengths of 910 and 1200 nm applied in the GnyLi VI were also used for the two-band NRI to cover the biomass and the moisture part of the winter wheat reflectance spectrum. A key advantage of both SWIR-based VIs over VNIR-based VIs, such as NDVI, is that they are not as susceptible to saturation issues due to increasing biomass density or leaf cover (Mutanga & Skidmore, 2004; Haboudane et al., 2004; Aklilu Tesfaye & Gessesse Awoke, 2020; Li et al., 2010), which typically reaches nearly 100 % in the mid-vegetative stage of crops (Tilly et al., 2015). As a result, it is possible to monitor the increasing amount of biomass beyond this stage.

5.2.5 Spectral Image Data Acquisition and Processing—Spectral Workflow

The camSWIR system acquired the spectral image data around noon on June 02, 2020. It took 28 min to perform two consecutive flights to collect the four necessary spectral bands. The first flight took off at 11:31 a.m. CET. Each flight lasted about 9 minutes. The remaining time was required for the bandpass-filter-equipped filter flange replacement and the corresponding camera calibration. During both flights, solar radiation conditions were stable and without any cloud coverage. The flight altitude of the UAV was set to 34 m (AGL).

In post-processing, the raw image data were flat-field-calibrated and converted from digital number (DN) to reflectance values using two different approaches, both based on the Empirical Line Method (Smith & Milton, 1999). A simple workflow was performed via a one-point calibration with a series of images taken from a spectrally precisely characterized Zenith™ polymer white panel with 95 % Lambertian reflectance before each flight. This white panel method is abbreviated as *WPM* in this study.

The more complex variant involved six differently graded (0, 10, 25, 50, 75 and 100 %.black shading) near-Lambertian 80×80 cm gray panels positioned directly next to the experimental field. They were recorded several times during the UAV flights. These gray panels were then identified in five corresponding images for each waveband. Their averaged DN was determined (see Figure 5.22) by a Python script (version 3.7, Python Software Foundation) based on the *roipoly* module. A transfer function per wavelength channel was then calculated with these values (see Figure 5.21) and the grayscale panels' reflectance data previously measured using ASD FieldSpec3 (Malvern Panalytical Ltd, Malvern, United Kingdom) (ASD).

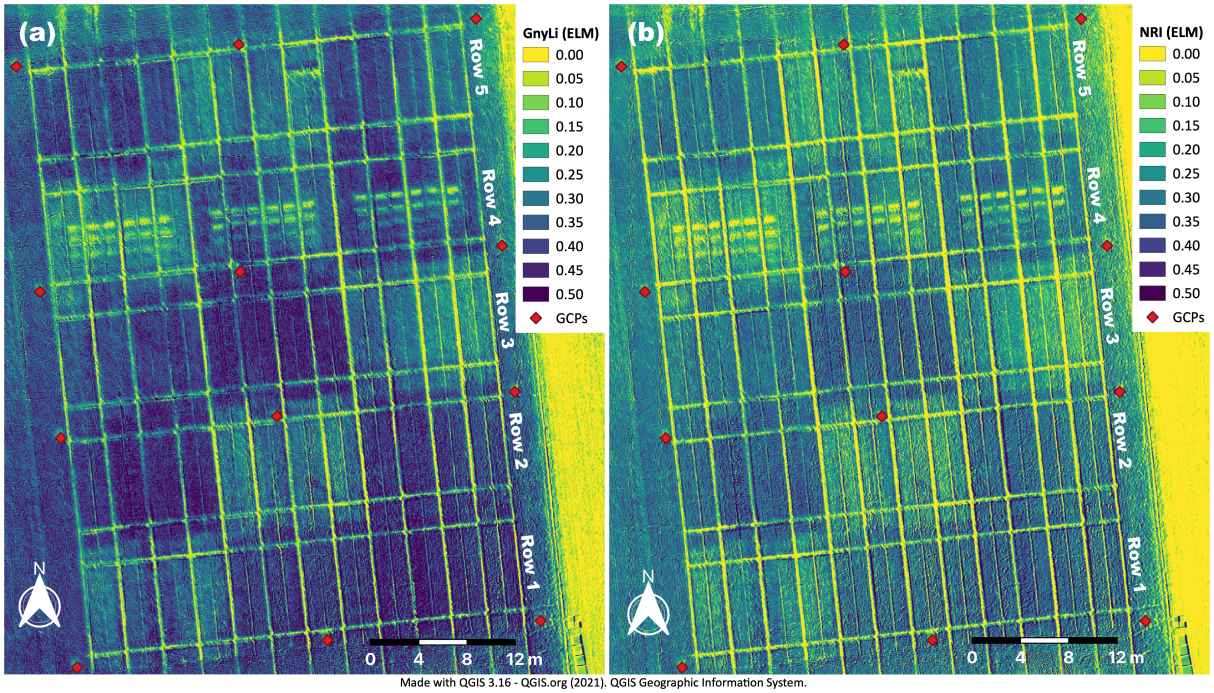


Figure 5.6: (**a**) GnyLi and (**b**) NRI orthomosaics processed from the four ELM-calibrated waveband orthomosaics (910, 980, 1100 and 1200 nm) derived from the camera system's spectral image data.

These functions were then used to convert the four DN image data sets to reflectance data. This workflow will be subsequently abbreviated as *ELM*. Additionally, for calibration purposes, a series of dark images were acquired before each flight. All post-processing steps were performed in the Python programming language using IPython (Perez & Granger, 2007) in a JupyterLab environment (Kluyver et al., 2016). After calibration, each of the four reflectance image data sets for both calibration methods was processed separately in a photogrammetric software suite (Metashape v1.6.2, Agisoft LLC, St. Petersburg, Russia) to an orthomosaic. Coordinates of twelve permanent and evenly distributed ground control points (GCPs, see Figure 5.2) were used for precise georeferencing in Metashape. After processing, these eight single-waveband orthomosaics were used to derive two sets of GnyLi and NRI VI orthomosaics in QGIS (version 3.14, QGIS Association, www.qgis.org) for both calibration methods. Figure 5.6 shows an example of the two orthomosaics for the ELM calibration method. The averaged VI values for each plot were then extracted via the zonal statistics tool. These VI data sets could then be used to evaluate and validate the relationship between SWIR-based vegetation indices and crop traits in the subsequent regression analyses.

5.2.6 Crop Trait Estimation Workflow

A comprehensive analysis workflow was designed and performed to evaluate the new camSWIR system (see section 5.2.4) for monitoring crop traits. Figure 5.7 gives an overview of the central data acquisition and analysis steps. The analysis workflow comprises six main data sets (I-VI) and one data set for validation, as described in the following.

(I) This data set represents the UAV data acquisition of RGB images using a P4RTK for stereo-photogrammetric analysis, resulting in crop height data (UAV crop height). This part (*crop height workflow*) is described in detail above in section 5.2.3, and these crop height data are of central importance for further data analysis.

(II) In the field experiment, manual and destructive samplings of crop height and biomass were conducted. As described in section 5.2.2, biomass was weighed before and after drying to determine fresh and dry biomass. The difference between fresh and dry biomass is considered the crop moisture content (crop moisture: CM). Dry biomass samplings were further analyzed for N_C in the laboratory.

(III) The third input data set for the analysis workflow originates from the newly developed camSWIR system flown on June 02. The multi-camera system was optimized to derive two NIR/SWIR vegetation indices, the NRI and the GnyLi (compare section 5.2.4). Section 5.2.5 describes the *spectral workflow* that transforms the raw DN image data sets into plot-wise VI reflectance data sets. For more details on the performance of the two VIs, see also (Koppe et al., 2010; Gnyp et al., 2014; Bendig et al., 2015; Camino et al., 2018; Aasen & Bareth, 2018; Jenal et al., 2019, 2020).

(IV) Regression models (RM) were created for the destructive field sampling plots (18 plots per date: n = 108) from (I) the UAV-derived crop height data and from (II) the manual and destructive sampling data, resulting in four regression models for biomass (fresh and dry), crop moisture, and N_C. In Figure 5.8, the 108 sampling plots of Row 4 are shown. Each color represents a sampling date, starting with orange for April 08 and ending with dark green for July 02.

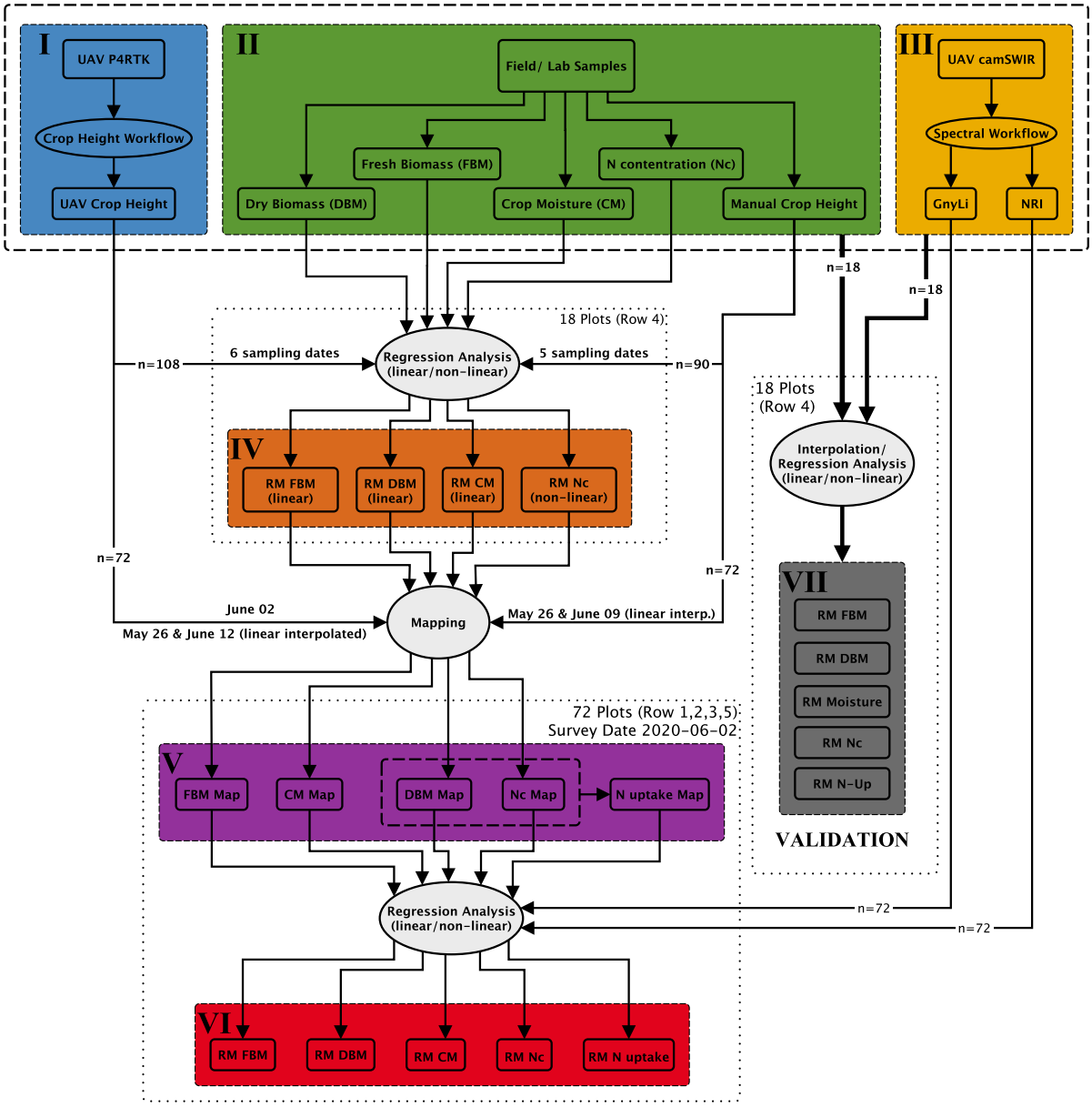


Figure 5.7: Simplified scheme of the developed crop trait estimation workflow.

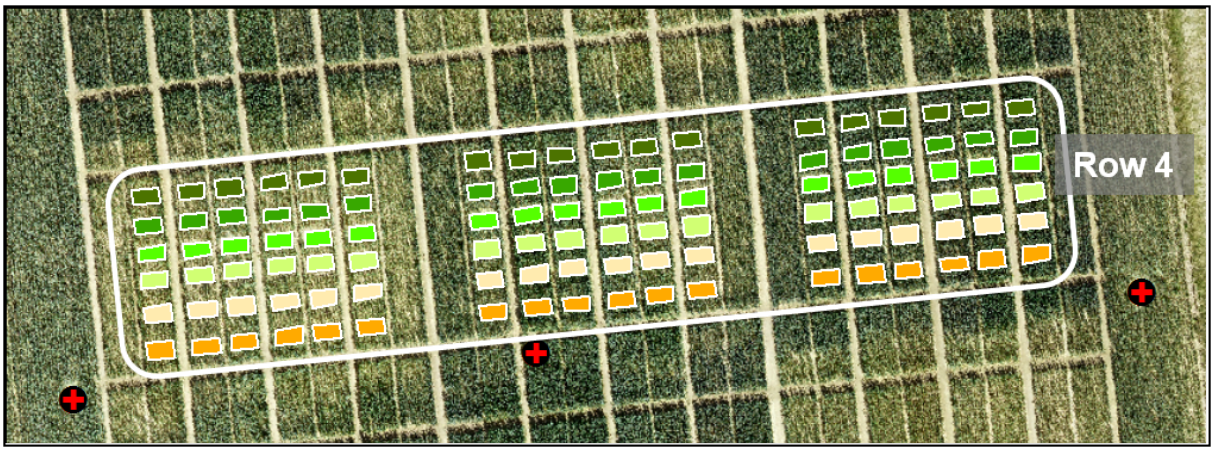


Figure 5.8: Image of the 108 sampling plots (18 per date, color-coded).

(V) These four regression models from step (IV) were then applied to the remaining 7.0×1.5 m plots of Row 1, 2, 3, and 5 using the P4RTK CH data (I) as well as the manual CH data (II) as input. This approach allowed biomass (fresh and dry), crop moisture (CM), and N_C to be estimated for the 72 test plots (18 per row). This step is possible because numerous studies have already proven the robustness of using CH as an estimator for biomass (Bendig et al., 2014; Tilly et al., 2014; Schirrmann et al., 2016; Hunt & Daughtry, 2018; Näsi et al., 2018; Roth & Streit, 2018; Yue et al., 2017) and using biomass as an estimator for N_C and N uptake (Aasen & Bareth, 2018; Tilly & Bareth, 2019; Jenal et al., 2020). With the derived data for dry biomass and N_C, the N uptake could be calculated in line with Lemaire & Gastal (1997) for the 72 test plots. Due to the abnormal UAV-derived crop heights for June 02, an additional data set was generated by interpolating the UAV-derived crop height of May 26 and June 12 linearly for June 02. This data set is named UAV crop height interpolated (P4RTK [i]).

(VI) The camSWIR-based VIs (NRI and GnyLi) were regressed against the five crop traits (V). Regression coefficients were used to evaluate the camSWIR's potential for monitoring crop traits.

(VII) The proposed analysis workflow (I—VI) was validated by regression analyses of the five different field parameters (FBM, DBM, CM, N_C, and N uptake) from the 18 destructive sampling plots and the two NIR/SWIR VIs, GnyLi, and NRI, considering two different spectral calibrations methods. Quality measures for better comparison were calculated (see section 5.2.7). Again, the values for June 02 were linearly interpolated between the two sampling dates of May 26 and June 12. The N uptake was derived from the 18 values of DBM and N_C. In this validation, the sampled field and lab data were directly analyzed against the VIs.

5.2.7 Statistical Measures

To evaluate the estimation accuracy of the derived regression models, we calculated the coefficient of determination R^2,

$$R^2 = \left(\frac{\sum_{i=1}^{n}(x_i - \bar{x})(y_i - \bar{y})}{\sqrt{\sum_{i=1}^{n}(x_i - \bar{x})^2}\sqrt{\sum_{i=1}^{n}(y_i - \bar{y})^2}} \right)^2, \tag{5.1}$$

the root-mean-square error (RMSE),

$$RMSE = \sqrt{\frac{\sum_{i=1}^{n}(x_i - y_i)^2}{n}}, \tag{5.2}$$

and the normalized *RMSE* (*NRMSE*),

$$NRMSE = \frac{RMSE}{\bar{y}} \times 100\ \%, \tag{5.3}$$

for a comprehensive comparison of the individual models (Richter et al., 2011). Where x_i is the *ith* estimated variable, y_i is the *ith* observed variable by the RM, $\bar{x}$ is the average of estimated variable x, and $\bar{y}$ represents the average of observed variable y. The variable n specifies the number of elements in a data set.

5.3 Results

5.3.1 UAV Crop Height Data Evaluation

UAV-derived CH data sets (see section 5.2.3) were used to estimate fresh and dry biomass, crop moisture, an indirect estimation of N_C, and N uptake for the 72 non-destructively sampled plots of rows 1, 2, 3, and 5 (see Figure 5.7). Therefore, the UAV-derived CH data were evaluated using results from manual CH measurements (see section 5.2.2). These manual measurements were performed on April 08, April 28, May 13, May 26, and June 09 for all 90 experimental field plots. UAV-based CH were significantly linearly correlated with manual CH for the five observation dates ($R^2 = 0.95$, $RMSE = 0.001$, $p < 0.001$) (Figure 5.9a,b). This linear relation indicates that UAV-based CH can be accurately derived from UAV image data for the sampling plots (n = 90, Figure 5.9a). Additionally, the determined UAV CH for the remaining 72 plots (n = 360, Figure 5.9b) were also highly correlated to the respective manually measured CH values so that they could be used to estimate the five crop traits for each of the 72 plots (Figure 5.7 (V)).

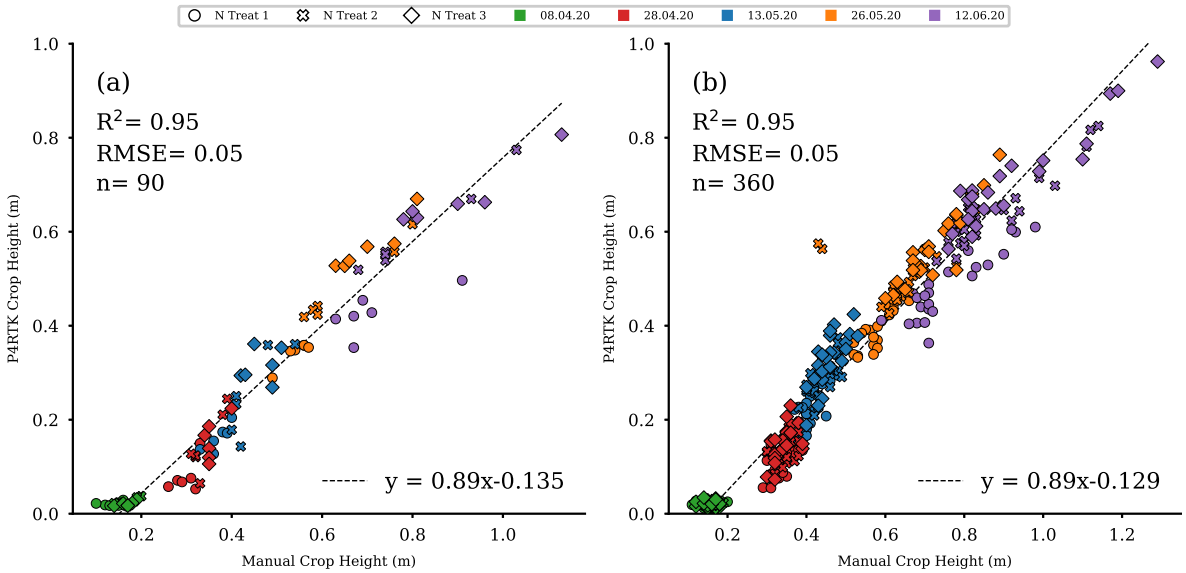


Figure 5.9: (**a**) Scatter plot for the manually measured CH versus the UAV-based CH for the 18 destructive sampling plots for all five comparable dates. (**b**) Scatter plot for the manually measured CH versus the UAV-based CH for the remaining 72 test plots for all five comparable dates ($p < 0.001$ for all regression models).

The results of the CH analysis are shown for six dates in Figure 5.10. The figure shows that the derived CH data capture the winter wheat growing stages well and that "non-growing" objects such as foot- or driving paths are easy to recognize. Even the small, destructive sampling areas in Row 2 (compare Figure 5.2) are clearly recognizable. Detailed validation of the generated CH data is presented in Figure 5.9.

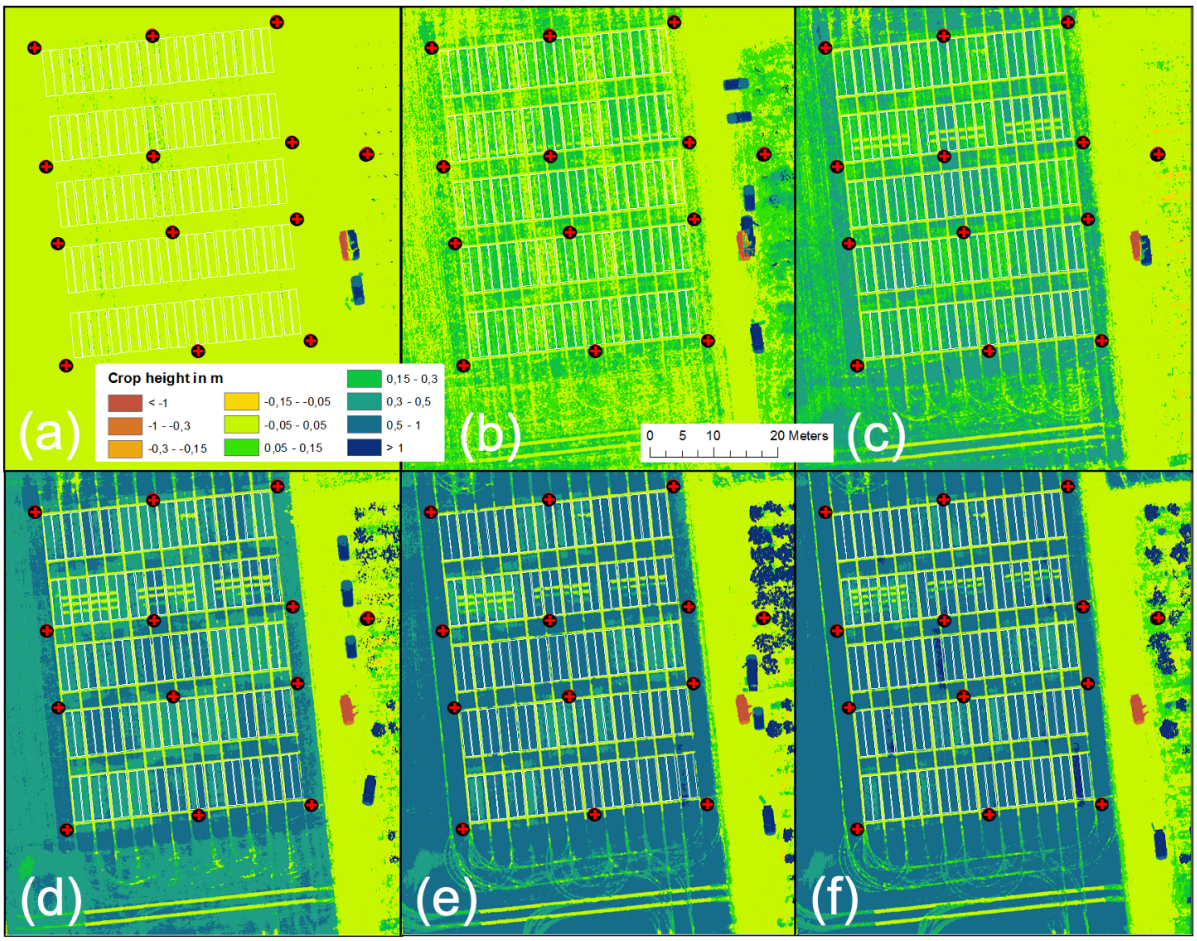


Figure 5.10: UAV-derived development of crop height in meters over the growing season 2020 for (**a**) April 07, (**b**) April 28, (**c**) May 13, (**d**) May 26, (**e**) June 12, and (**f**) July 01.

An unexpected decrease in the UAV-derived CH was related to data obtained on June 02, the UAV-based VNIR/SWIR data sampling date. This decrease is unrealistic and contrasts with all other data sets, indicating progressive plant growth throughout the growing season. Figure 5.11 shows the DOP and derived CH. Visually, the data look good, but detailed analysis shows a non-linear error, giving some plots an unrealistic drop in crop growth compared to that of May 26. The latter represents an erroneous output of the methodology. A more in-depth analysis resulted in a systematic error for all plots of the zero N-input variants (N1). Figure 5.11a (also compare Figure 5.2) shows that these plots have a characteristic bright reflectance due to the lower vegetation cover.

Moreover, these are the plots that show the lowest CH in Figure 5.11b–d present an enlarged part of row 2, where the bright, almost outshining, soil reflectance of the N1 plots seems to dominate, resulting in false modeling of the ground instead of the crop canopy. As a consequence, the affected plant heights are modeled too shallowly. For July 01, only variety no. 3 shows the same faulty behavior for the N1 fertilizer plots in all row replicates. Further examination of all plot data for CH on June 02 confirms this finding. Firstly, in Figure 5.12, all CH values for all plots in row 2 are plotted. The N2 and N3 N-variant plots show good and expected CH values, while all N1 plots show this significant decrease in crop growth, which is impossible.

Secondly, a complete visualization of all CH data of rows 1, 2, 3, and 5 is displayed in Figure 5.20 in Appendix 5.8.1. In particular, the N1 plot values show these significantly low CH values, with two exceptions included in Figure 5.20. Considering this effect, we used the data of June 02 with caution and created additionally a linearly interpolated, more realistic CH data set for June 02 using May 26 and June 12 data. This issue is addressed further in the discussion.

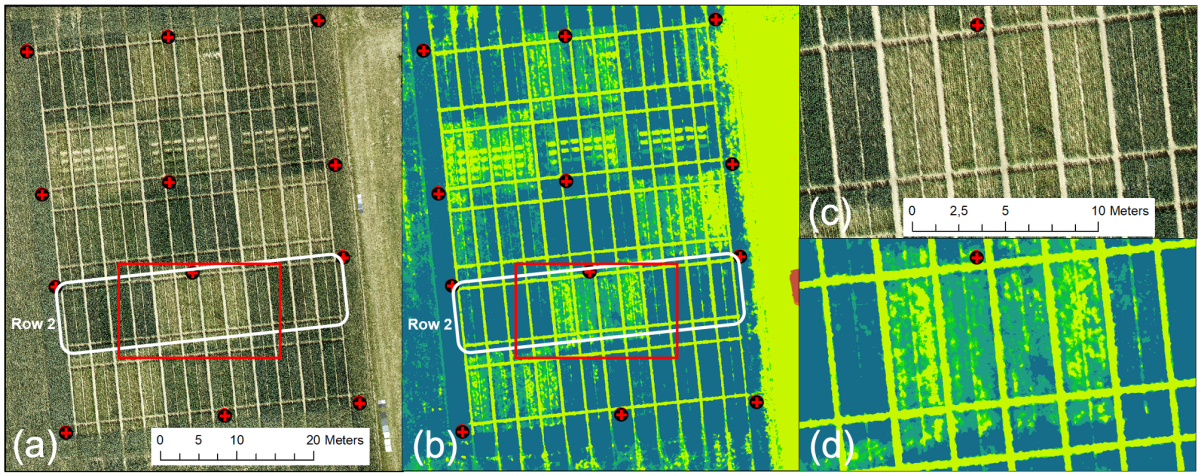


Figure 5.11: UAV-derived CH data for June 02 (CH legend from Figure 5.4 applies): (**a**) DOP, (**b**) derived CH map, (**c**) enlarged area of DOP (red rectangle in (**a**), (**d**) enlarged area of CH map (red rectangle in (**b**).

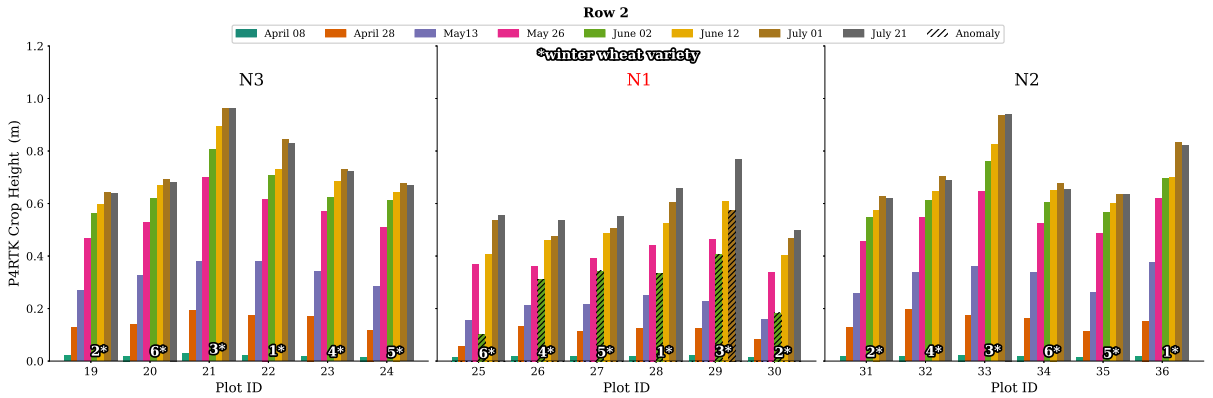


Figure 5.12: Bar chart representation of CH derived by the UAV for row 2 for all flight dates. For all N1 treatment plots' varieties, the crop height workflow resulted in an unexpected drop in plant growth for June 02. This phenomenon is also evident in all N1 stages of the other rows (see Figure 5.20). Variety no. 3 also shows negative growth for July 01 for all N1 treatments. The corresponding erroneous crop height values are marked with a hatched overlay in black.

5.3.2 Crop Traits Estimation Models

Regression fits between FBM, DBM, and CM with UAV-based (Figure 5.13a,d,g) and manually measured (Figure 5.13b,e,h) CH indicate a statistically significant linear relation. In contrast, as shown in Figure 5.13c,f,i, there was a non-linear decrease in N_C over the growing season. This curve shape is also known as the nitrogen dilution effect and is best described by a power function (Lemaire et al., 2008). Therefore, three non-linear regression models, based on a power-law fit, for estimating N_C were derived from FBM, DBM, and CM (see section 5.3.4 for further details).

Accuracy measures indicate lower errors and higher regression coefficients for model-based estimates of FBM, DBM, and CM if they are based on UAV-derived CH compared with those based on manually measured CH data (Table 5.3).

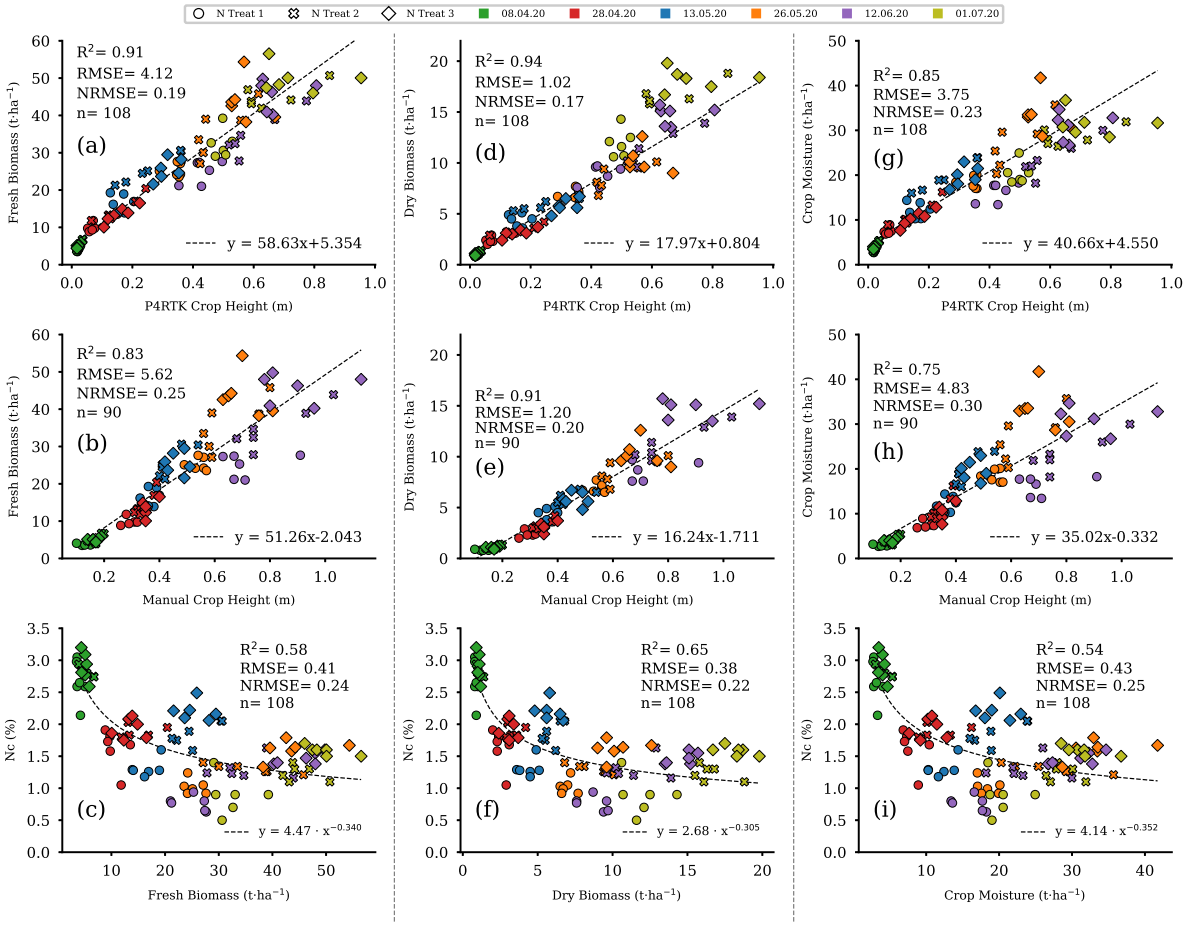


Figure 5.13: Scatter plots of the linear regression models for P4RTK and manual CH against the fresh and dry biomass, as well as crop moisture data of the 18 destructive sampling plots for the five and six sampling dates, respectively. Each column contains a non-linear regression model for estimating N_C from the three different biomass parameters. **Left column:** regression models for fresh biomass (**a**–**c**). **Center column:** regression models for dry biomass (**d**–**f**). **Right column:** regression models for crop moisture (**g**–**i**). ($p < 0.001$ for all regression models)

Table 5.3: Regression performance results for the estimation models for fresh (FBM) and dry biomass (DBM), crop moisture (CM) and N concentration (N_C) against UAV-based and manually measured CH data. ($p < 0.001$ for all regression models)

	FBM (t ha^{-1})		DBM (t ha^{-1})		CM (t ha^{-1})		N_C (%)		
	P4RTK	Manual	P4RTK	Manual	P4RTK	Manual	FBM	DBM	CM
R^2	0.91	0.83	0.94	0.91	0.85	0.75	0.58	0.65	0.54
RMSE	4.12	5.62	1.02	1.20	3.75	4.83	0.41	0.38	0.43
NRMSE (%)	19	25	17	20	23	30	24	22	25

5.3.3 Regression Analyses of Vegetation Indices and Biomass

Based on the regression models from section 5.3.2 derived from the 18 destructive sampling plots, the respective data were estimated for the remaining 72 test plots. These data sets were then used in a further step to evaluate the VI data sets of the GnyLi and the NRI (ELM and WPM calibration) as estimators. Since the three biomass models (fresh, dry, moisture) are based on CH as the estimator, the biomass data sets were derived using three different CH data sets for the survey on June 02.

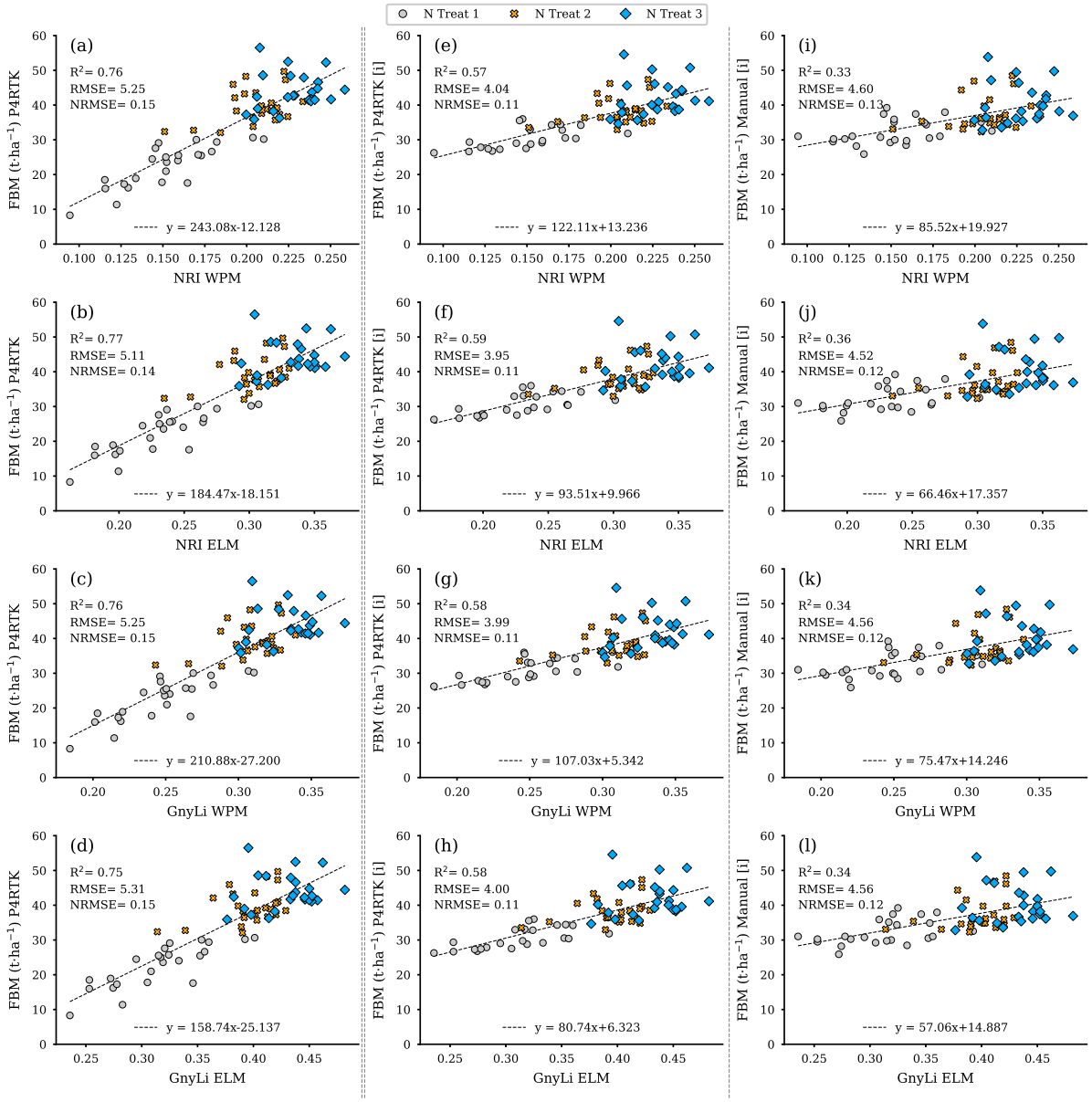


Figure 5.14: Scatter plots for the fresh biomass (FBM) data estimated for the 72 non-destructive test plots with the FBM-model based on three different crop height data sets with the spectral camera VIs acquired on June 02. **Left column:** crop height directly derived from P4RTK RGB data set of June 02 (**a**–**d**). **Center column:** linear interpolated crop height from P4RTK RGB data set of May 26 and June 12 (**e**–**h**). **Right column:** linear interpolated crop height manually measured on May 26 and June 09 (**i**–**l**). ($p < 0.001$ for all regression models)

The first data set is the CH determined by the P4RTK image data on June 02. However, due to the erroneous height data, the CH from two dates specified to be correct (May 26 and June 12) were linearly interpolated for June 02 and used in the model to estimate the biomass parameters. Since CH data for June 02 was also not available for the manual measurement, these data were also linearly interpolated from the two manual CH data sets (May 26 and June 09) and then used to estimate the values for FBM, DBM, and CM for the remaining 72 test plots. In combination with the four VI data sets, this resulted in twelve models for each biomass parameter. Figure 5.14 displays the twelve plots for the FBM data sets estimated by the three different CH data sets. The best-performing CH data set seems to be from June 02 (left column) with an R^2 of 0.75 to 0.77 throughout all parameters. However, the *RMSE* is significantly reduced by more than 20 % compared to the P4RTK-based models and less than 15 % to the manual-height-based models. Since these data are considered erroneous (see section 5.3.1), they are included for completeness only.

Table 5.4: Results of the linear regression analyses for both calibration methods (WPM, ELM) of both VIs (G: GnyLi, N: NRI) and the estimated (by three different CH) crop traits: fresh and dry biomass and the crop moisture. Three CH: P4: P4RTK crop height, M: manual crop height, [i]: interpolated crop height values. ($p < 0.001$ for all regression models)

		FBM ($t\,ha^{-1}$)			DBM ($t\,ha^{-1}$)			CM ($t\,ha^{-1}$)		
VI	CH	R^2	*RMSE*	*NRMSE* (%)	R^2	*RMSE*	*NRMSE* (%)	R^2	*RMSE*	*NRMSE* (%)
N_{ELM}	P4	0.77	5.11	14.49	0.77	1.58	15.83	0.77	3.53	13.96
G_{ELM}	P4	0.75	5.31	15.07	0.75	1.65	16.46	0.75	3.67	14.51
N_{WPM}	P4	0.76	5.25	14.87	0.76	1.63	16.25	0.76	3.62	14.33
G_{WPM}	P4	0.76	5.25	14.88	0.76	1.63	16.26	0.76	3.62	14.33
N_{ELM}	P4[i]	0.59	3.95	10.66	0.59	1.22	11.60	0.59	2.73	10.29
G_{ELM}	P4[i]	0.58	4.00	10.80	0.58	1.24	11.75	0.58	2.76	10.42
N_{WPM}	P4[i]	0.57	4.04	10.91	0.57	1.25	11.87	0.57	2.79	10.53
G_{WPM}	P4[i]	0.58	3.99	10.77	0.58	1.24	11.71	0.58	2.75	10.39
N_{ELM}	M[i]	0.36	4.52	12.35	0.36	1.43	13.59	0.36	3.09	11.84
G_{ELM}	M[i]	0.34	4.56	12.44	0.34	1.44	13.70	0.34	3.11	11.94
N_{WPM}	M[i]	0.33	4.60	12.56	0.33	1.46	13.82	0.33	3.14	12.04
G_{WPM}	M[i]	0.34	4.56	12.45	0.34	1.44	13.70	0.34	3.11	11.94

The center and right columns of Figure 5.14 present the scatter plots for the FBM derived from the interpolated CH data (P4RTK, manual) and the two VIs with both calibration methods. It can be seen that the FBM values derived from the P4RTK CH data (center) with an R^2 of 0.57 to 0.59 are considerably more accurate than the FBM values based on the manually measured CH (right column) with an R^2 of 0.33 to 0.36. Additionally, the UAV-based regression models have the lowest *RMSE* 3.95 to 4.04 $t\,ha^{-1}$ and *NRMSE* (11 %) values. More significant errors are mainly linked to the plots receiving greater nitrogen amounts (N3, blue diamond markers).
Figure 5.15 displays, like Figure 5.14, the models for the VIs as estimators, but here for the dry biomass (DBM) estimated from the three different CH data sets for the remaining 72 test plots. Due to the underlying relationship of CH as the joint estimator, these models exhibit similar performance behavior to those shown in Figure 5.14, even compared to each other. The left

column again shows the co-incidence of the VIs with the erroneous CH data from June 02 with a better R^2 compared to the other two models based on interpolated CH values.

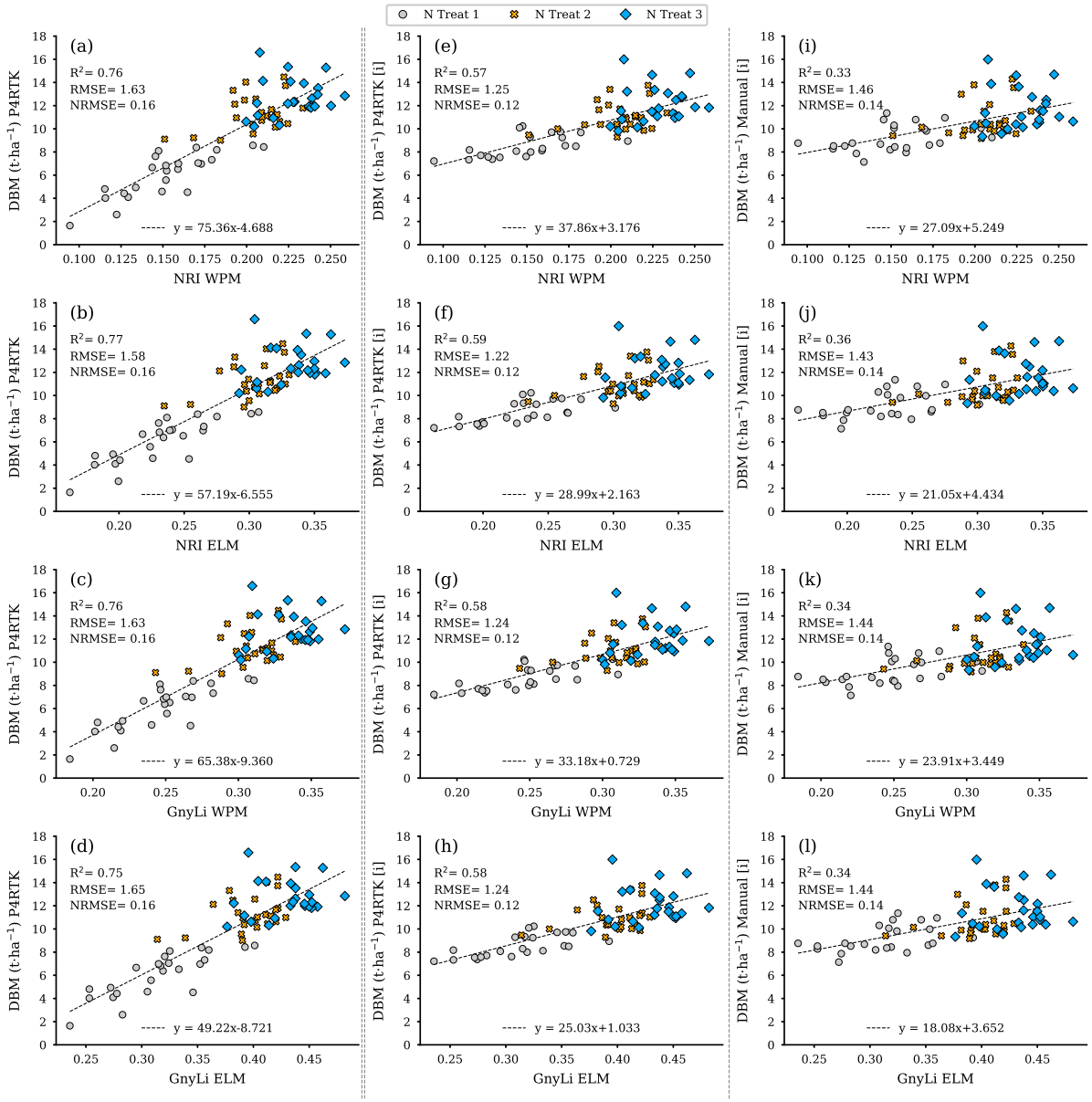


Figure 5.15: Scatter plots for the dry biomass (DBM) data estimated for the 72 non-destructive test plots with the DBM-model based on three different CH data sets with the spectral camera VIs acquired on June 02. **Left column:** CH directly derived from P4RTK RGB data set of June 02 (**a**–**d**). **Center column:** linearly interpolated CH from P4RTK RGB data set of May 26 and June 12 (**e**–**h**). **Right column:** linearly interpolated CH manually measured on May 26 and June 09 (**i**–**l**). ($p < 0.001$ for all regression models)

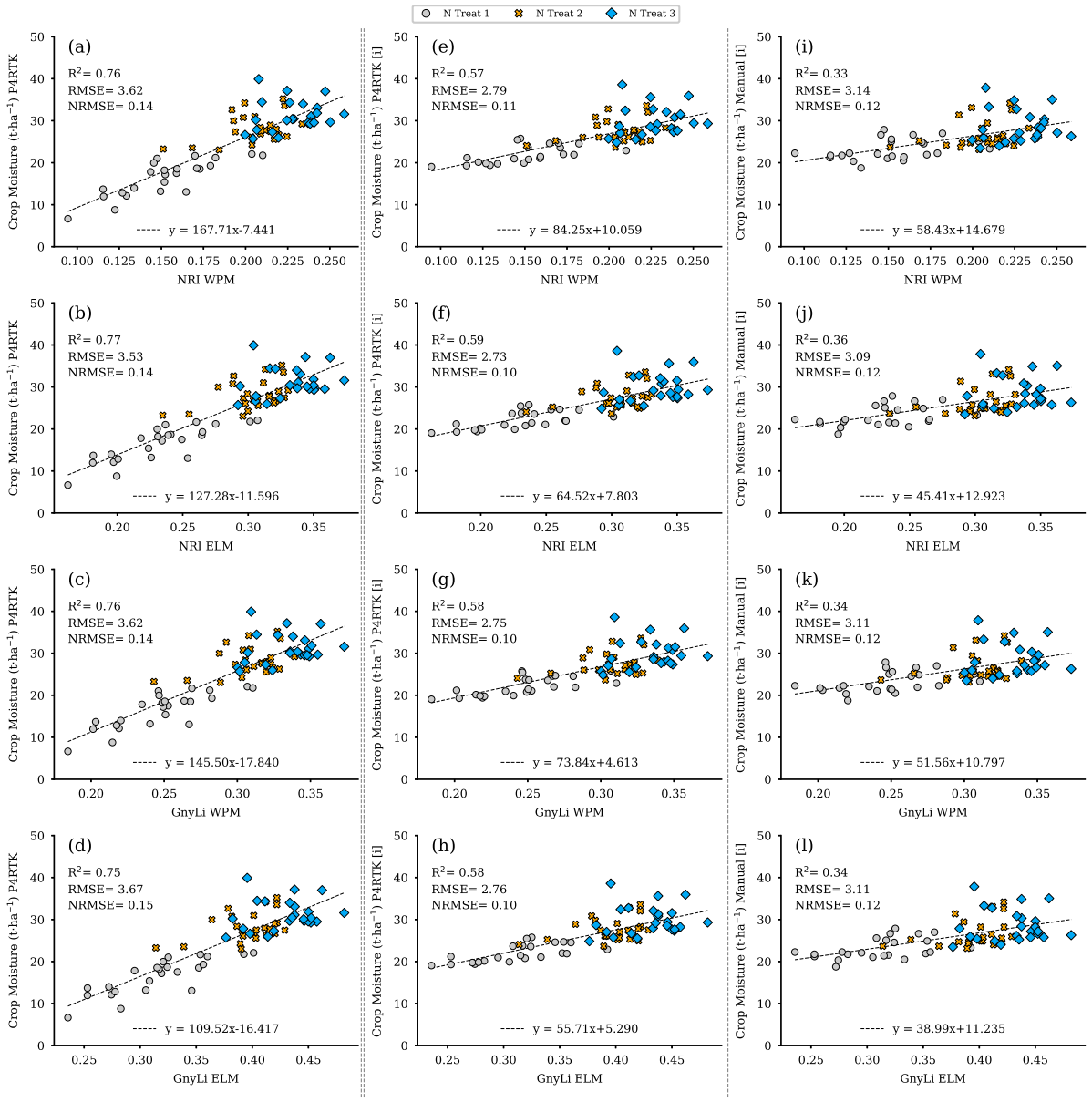


Figure 5.16: Scatter plots for the crop moisture (CM) data were estimated for the 72 non-destructive test plots with the CM model based on three different CH data sets with the spectral camera VIs acquired on June 02. **Left column:** CH directly derived from P4RTK RGB data set of June 02 (**a**–**d**). **Center column:** linear interpolated CH from P4RTK RGB data set of May 26 and June 12 (**e**–**h**). **Right column:** linear interpolated CH manually measured on May 26 and June 09 (**i**–**l**). ($p < 0.001$ for all regression models)

Figure 5.16 shows the resulting regression models based on both VIs as crop moisture estimators. Since crop moisture is directly related to wet and dry biomass, the performance of these models is almost identical to the models shown in Figures 5.14 and 5.15 but again in a different magnitude relationship. Table 5.4 summarizes the regression analyses' results for the three parameters FBM, DBM, and CM.

5.3.4 Regression Analyses of Vegetation Indices and N_C and N uptake

As shown in Figure 5.13f, the best predictor for N_C was DBM. The corresponding non-linear regression model had the highest R^2 of 0.65 and the lowest RMSE of 0.38 compared to the

RM based on FBM (R^2: 0.58, *RMSE*: 0.41) or CM (R^2: 0.54, *RMSE*: 0.43). Since the DBM was estimated with three different CH data sets, as shown in section 5.3.3, this also resulted in three data sets for the estimated N_C. These data sets were then finally further investigated with regression analyses, with the two VIs, GnyLi, and NRI (WPM, ELM), as estimators. Again, this results in twelve regression models for the flight date on June 02, shown in Figure 5.17. The equations exhibit a negative slope. This phenomenon resulted from the decrease in N_C with an advanced plant growth state for the N2 and N3 plots, but not for the zero-fertilization N1 plots.

Table 5.5: Results of the simple linear regression analyses for both calibration methods (ELM, WPM) of both VIs (NRI, GnyLi) and the estimated (by three different CH) crop traits: N_C and N uptake. Three crop heights: P4: P4RTK crop height, M: manual crop height, [i]: interpolated crop height values. ($p < 0.001$ for all regression models)

		N_C (%)			N uptake ($kg\,ha^{-1}$)		
VI	CH	R^2	*RMSE*	*NRMSE* (%)	R^2	*RMSE*	*NRMSE* (%)
NRI_{ELM}	P4	0.73	0.11	7.67	0.78	14.98	11.41
$GnyLi_{ELM}$	P4	0.71	0.11	7.88	0.76	15.60	11.88
NRI_{WPM}	P4	0.73	0.11	7.66	0.77	15.33	11.68
$GnyLi_{WPM}$	P4	0.72	0.11	7.75	0.77	15.38	11.71
NRI_{ELM}	P4[i]	0.67	0.04	3.21	0.61	10.82	7.86
$GnyLi_{ELM}$	P4[i]	0.66	0.04	3.25	0.60	10.95	7.96
NRI_{WPM}	P4[i]	0.65	0.04	3.31	0.59	11.09	8.06
$GnyLi_{WPM}$	P4[i]	0.66	0.04	3.24	0.60	10.93	7.94
NRI_{ELM}	M[i]	0.42	0.05	3.75	0.37	12.67	9.21
$GnyLi_{ELM}$	M[i]	0.41	0.05	3.78	0.36	12.77	9.28
NRI_{WPM}	M[i]	0.39	0.05	3.83	0.35	12.89	9.38
$GnyLi_{WPM}$	M[i]	0.41	0.05	3.78	0.36	12.77	9.29

The regression models based on the erroneous CH data from the RGB image data acquired on June 02 appear to perform well, as in the previous analyses, with R^2 of 0.71 to 0.73. However, they should be considered as an artifact. Compared to the results with the interpolated CH data from section 5.3.3, the analysis data for the VIs estimators for the UAV-based N_C estimators are better, with R^2 of 0.65 to 0.67, than the comparable estimators for biomass (see Figures 5.14–5.16). The regression models based on the VIs and the N_C estimated with the manually measured CH data again perform weakest, with an R^2 of 0.39 to 0.42 (Table 5.5). These results are slightly higher than the regression analyses of the VIs and the biomass parameters (section 5.3.3). The *RMSE* for the estimated N_C based on interpolated CH data sets (P4RTK, Manual) is comparatively low.

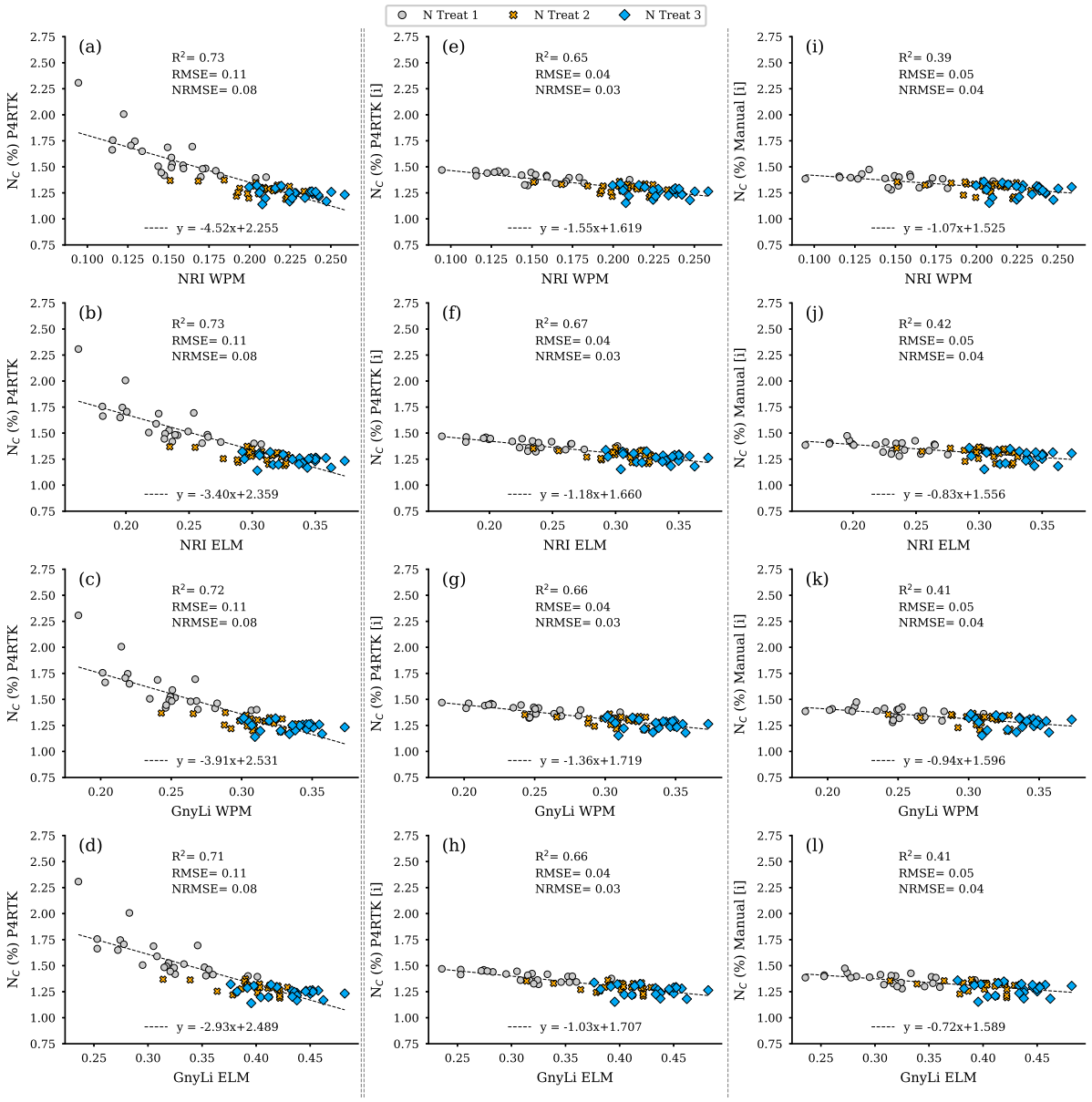


Figure 5.17: Scatter plots for the N concentration (N_C) data estimated for the 72 non-destructive test plots with the N_C-model, based on the DBM estimator RM for three different CH data sets, with the spectral camera VIs acquired on June 02. **Left column:** CH directly derived from P4RTK RGB data set of June 02 (**a**–**d**). **Center column:** linear interpolated CH from P4RTK RGB data set of May 26 and June 12 (**e**–**h**). **Right column:** linear interpolated CH manually measured on May 26 and June 09 (**i**–**l**). ($p < 0.001$ for all regression models)

Figure 5.18 shows the regression analysis results for N uptake using the two VIs, GnyLi and NRI (WPM, ELM), as estimators. The N uptake was calculated from the values for DBM and N_C of the 72 test plots. These two features were also derived using the established regression models from section 5.3.2 and the three different CH for the June 02 survey date. Each CH-related model is arranged in its corresponding column in Figure 5.18.

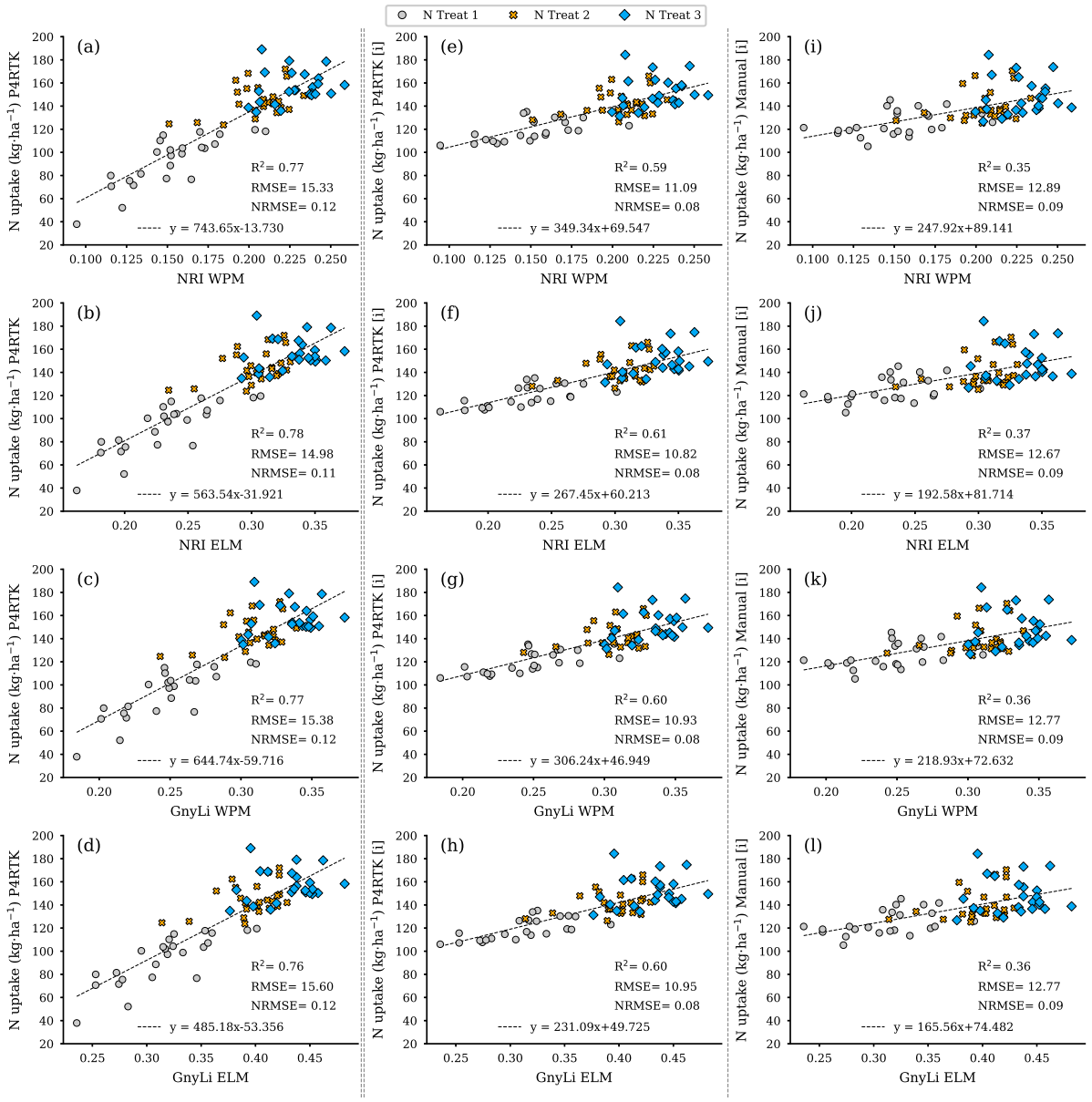


Figure 5.18: Scatter plots for the N uptake data estimated for the 72 non-destructive test plots with the N_C and DBM RM-model, based on the DBM estimator RM for three different CH data sets, with the spectral camera VIs acquired on June 02. **Left column:** CH directly derived for June 02 P4RTK RGB data set (**a**–**d**). **Center column:** linear interpolated CH from May 26 and June 12 P4RTK RGB data sets (**e**–**h**). **Right column:** linear interpolated CH manually measured on May 26 and June 09 (**i**–**l**). ($p < 0.001$ for all regression models)

5.3.5 Regression Analyses of Vegetation Indices and Ground Truth Data

To validate the results from the previous regression analyses (compare section 5.2.6, step VI), the spectral information of the two VIs, GnyLi, and NRI (ELM, WPM), was derived from the remaining standing biomass in the 18 destructive samplings plots on June 02 (see Figure 5.7, dark green and previous sampling area). These four VI data sets were then analyzed with the linearly interpolated ground truth data sets of May 26 and June 12 from these plots in simple linear regression models. Figure 5.19 shows the scatter plots of the individual analyses of the VIs as an estimator for the ground truth data of FBM, DBM, CM, N_C, and N uptake. As explained

in section 5.2.6, CM was derived from FBM and DBM, and the N uptake was processed from Nc and DBM. The results consistently show a high R^2 of at least 0.73 to a maximum of 0.87. Table 5.6 summarizes the particular linear regression results for each VI as an estimator for the respective crop trait.

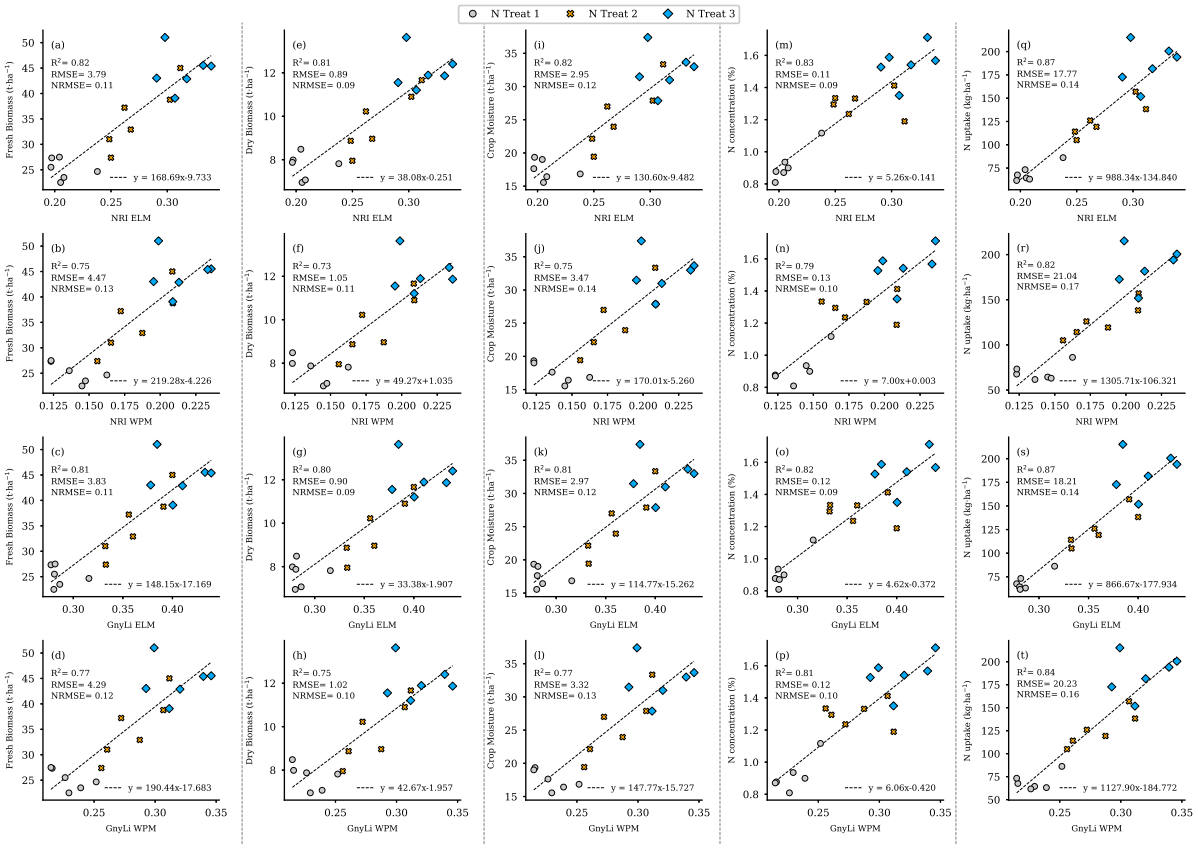


Figure 5.19: Scatter plots for the VI data for June 02 as estimators for the individual crop traits linearly interpolated from May 26 and June 12 of the 18 destructive sampling plots. (**a**–**d**) camSWIR VIs and FBM, (**e**–**h**) camSWIR VIs and DBM, (**i**–**l**) camSWIR VIs and crop moisture, (**m**–**p**) camSWIR VIs and N_C, (**q**–**t**) camSWIR VIs and N uptake. ($p < 0.001$ for all regression models)

5.4 Discussion

In this study, a newly developed VNIR/SWIR imaging system for UAVs, the camSWIR, is evaluated for crop trait monitoring of winter wheat. The focus is on two vegetation indices (VIs), the NRI (Koppe et al., 2010) and the GnyLi (Gnyp et al., 2014), which used near and short-wave infrared (NIR/SWIR) wavelengths (see Table 5.2). Previous studies showed that these indices outperformed VIs using bands from the visible and near-infrared (VIS/NIR) domain (Jenal et al., 2020; Tilly & Bareth, 2019; Tilly et al., 2015; Bendig et al., 2015; Gnyp et al., 2014; Koppe et al., 2010, 2012). Moreover, several authors indicate the SWIR domain's potential for crop trait monitoring (Aasen & Bareth, 2018; Berger et al., 2020; Roberts et al., 2018; Thenkabail et al., 2019; Mahajan et al., 2017; Pimstein et al., 2011; Li et al., 2018).

Table 5.6: Regression analyses' results for the VIs as estimators for the sampled ground truth data (FBM: fresh biomass, DBM: dry biomass, N_C: N concentration, CM: crop moisture, NUP: N uptake) of the 18 destructive sample plots. ($p < 0.001$ for all regression models)

VI	Trait	R^2	*RMSE*	*NRMSE* (%)
NRI_{ELM}	FBM	0.82	3.79	10.82
NRI_{WPM}	FBM	0.75	4.47	12.77
$GnyLi_{ELM}$	FBM	0.81	3.83	10.92
$GnyLi_{WPM}$	FBM	0.77	4.29	12.25
NRI_{ELM}	DBM	0.81	0.89	8.99
NRI_{WPM}	DBM	0.73	1.05	10.64
$GnyLi_{ELM}$	DBM	0.80	0.90	9.14
$GnyLi_{WPM}$	DBM	0.75	1.02	10.33
NRI_{ELM}	CM	0.82	2.95	11.74
NRI_{WPM}	CM	0.75	3.47	13.77
$GnyLi_{ELM}$	CM	0.81	2.97	11.82
$GnyLi_{WPM}$	CM	0.77	3.32	13.18
NRI_{ELM}	N_C	0.83	0.11	9.11
NRI_{WPM}	N_C	0.79	0.13	10.06
$GnyLi_{ELM}$	N_C	0.82	0.12	9.23
$GnyLi_{WPM}$	N_C	0.81	0.12	9.67
NRI_{ELM}	N uptake	0.87	0.02	13.95
NRI_{WPM}	N uptake	0.82	0.02	16.52
$GnyLi_{ELM}$	N uptake	0.87	0.02	14.30
$GnyLi_{WPM}$	N uptake	0.84	0.02	15.88

The presented results in this case study for winter wheat demonstrate this new sensor's potential to derive crop traits such as biomass, N_C, N uptake, and crop moisture. Although not typically used, these wavelengths' potential for monitoring agricultural systems has also been shown in other studies. For example, Ceccato et al. (2001) indicate the SWIR domain's potential to derive leaf water content. Honkavaara et al. (2016) indicate the same for monitoring surface moisture of a peat production area. Camino et al. (2018) demonstrated the advantage of the SWIR domain for retrieval of crop nitrogen. Finally, Psomas et al. (2011) and Koppe et al. (2010) proved the NIR/SWIR bands' suitability for biomass monitoring in grasslands and winter wheat. The selection of the applied bandpass filters in this study represents a compromise due to availability and cost compared to the original studies by Koppe et al. (2010) and Gnyp et al. (2014), which used field spectroradiometer and hyperspectral satellite data. If available in future studies, narrower ($\leq$10 nm), more wavelength-specific, bandpass filters should be used to investigate an effect on the estimation performance of the VIs with the wavelengths applied in (Koppe et al., 2010; Gnyp et al., 2014). In particular, when it comes to spectral features involving leaf chemicals such as proteins that also have an indirect link to N_C, using narrowband filters with the appropriate center wavelengths (Curran, 1989; Fourty et al., 1996) is crucial. Otherwise, when broader bandwidths are applied, this information about the fine spectral features is lost in the superimposed spectrum (Ollinger, 2010). Furthermore, water absorption has to be considered as it overlays all other features to a large extent in the SWIR domain (Li et al., 2018).

The NRI and GnyLi performed well as an estimator for different crop traits for the 72 test plots (Figure 5.7, step V and VI) in our study. In a first approach, we calculated comparatively high R^2 values (NRI, GnyLi) for FBM (R^2: 0.77, 0.75), DBM (R^2: 0.77, 0.75), N_C (R^2: 0.73, 0.71), N uptake (R^2: 0.78, 0.76), and crop moisture (R^2: 0.77, 0.75) with low *NRMSE*s ranging from 8 to 16 %. However, these good results for one date (June 02) result from a supposed spurious effect in the P4RTK RGB image data processed in the crop height workflow described in section 5.2.3. The low vegetation cover in the N1-treatment where nitrogen supply was omitted caused a significant CH error in the SfM/MVS analysis. This effect is most likely due to the strong reflectance of the high soil coverage and should be further investigated in the future. However, for all other observation dates, the P4RTK image data tracks crop growth with high accuracy (R^2: 0.95 for the 18 destructive sampling plots and R^2: 0.95 for the remaining 72 test plots) compared to the crop heights measured by hand with a folding ruler. The *RMSE* of 0.05 m is within the expected resolution for stereo-photogrammetric height measurement from image data for both regression models (see Figure 5.9).

To avoid the negative effect in the CH data, a second validation data set was produced by linearly interpolating the CH for June 02 to provide more reliable CH data. The regression models based on this interpolated data set resulted in moderately lower R^2 values for FBM (R^2: 0.59, 0.58), dry DBM (R^2: 0.59, 0.58), N_C (R^2: 0.67, 0.66), N uptake (R^2: 0.61, 0.60), and crop moisture (R^2: 0.59, 0.58). A reduction in *RMSE* (more than 20 %) and *NRMSE* (4 percentage points) was also observed in the regression models of the interpolated data sets. Thus, while the variability in crop traits explained by the model was lower, absolute and mean-normalized prediction errors decreased. This decrease was mainly due to lower errors for predicting crop traits in the N1 treatment (see Figures 5.14—5.18).

Compared to these findings, the regression analysis results used to validate both VIs using the ground-truth-based crop traits data from the 18 destructively sampled plots (see Figure 5.2 and Figure 5.7 step VII) consistently showed an even higher accuracy, ranging from R^2: 0.73 to R^2: 0.87, and lower *RMSE* values. This difference originates from a weaker correlation between UAV-derived CH data, which are the base for estimating the crop traits of the 72 test plots for June 02. Therefore, this slightly weaker correlation affects the estimation accuracy of the final step of the crop trait estimation workflow (Figure 5.7 step VI), in which the UAV-derived crop traits are estimated using the VIs in regression models. In contrast, the base regression models of the destructively derived crop traits for all sampling dates performed better (see Figure 5.13) with the UAV-derived CH (R^2: 0.54 to 0.94). Based on these CH, crop traits were estimated in turn for regression analyses with the VIs for the remaining 72 test plots. This slightly weaker relationship affects the last analysis step's estimation accuracy (Figure 5.7 step VI).

The same relationship can be observed in the regression analyses based on the manually measured CH. The comparison of the two CH data sets' performance revealed significant differences in estimation accuracy related to the VIs, whereby the crop traits' regression models based on the manually measured CH performs worse (R^2: 0.33 to 0.42) than the P4RTK-based crop traits (R^2: 0.57 to 0.67). This difference is described by Bareth et al. (2016). It occurs because UAV-derived CH data, unlike point-wise manually measured ones, represent a mean plant height value of an entire plot accounting for the plant density resulting from zonal statistics. Another solution

to provide CH data for reliably estimating crop traits might be utilizing UAV-LiDAR data (Bates et al., 2021; Zhou et al., 2020; Zhang et al., 2021) and should be investigated in future research.

Li et al. (2010) investigated the performance of established VIs and tested for optimal wavelength combinations in the VIS/NIR domain to retrieve N_C for certain growing stages. In their study on winter wheat, the authors found that all of the 77 published VIs and the best waveband combinations performed poorly ($R^2 < 0.29$). Similar results are described by Mistele & Schmidhalter (2008) for maize. Gnyp et al. Gnyp et al. (2013) investigated field spectra in rice and found similar moderate to poor R^2 when applying VIs across all growing stages ($R^2 < 0.5$). Reaching a higher R^2 of up to 0.8 was only possible by using step-wise multiple linear regression (MLR) or narrow NIR/SWIR bands for the complete data set, summarizing all growing stages. Stroppiana et al. (2018) present similar results from several studies, showing moderate to low R^2 for N retrieval for distinct growing stages. In general, most studies report only moderate to poor R^2 for a single survey date. Thus, the ability of VIs in the VIS/NIR domain to estimate crop N_C is limited. In particular, this applies to studies based on single survey dates. Considering the results from this study, we, therefore, suggest evaluating in more detail the performance of systems operating in the SWIR domain in future studies on date-specific crop trait estimation.

The results show that the recently introduced imaging system produces reliable VNIR/SWIR image data for the four selected wavebands. While only grayscale panels, destructively sampled crop data and estimated crop traits based on CH data could be used in this study, Jenal et al. (2020) additionally used field-spectroradiometer measurements (350 to 2500 nm) of grassland canopies. In the latter study, very high correlations between both independent reflectance data sets have already been demonstrated. In this study, the spectral quality of the image data was shown again, and similar excellent results were produced for the grayscale panel calibration (ELM) method (Figure 5.21) as described in Jenal et al. (2020). In determining the panel reflectances in the WPM-calibrated images (Figure 5.22) and regressing them with the panel reflectances, the quality of the WPM calibration method was successfully tested (Figure 5.23). The easy-to-use calibrated VNIR/SWIR spectral image data sets could be processed to derive plot-specific vegetation index reflectance values. An appropriate methodology was elaborated in previous studies (Jenal et al., 2019, 2020). The high sensitivity over almost the entire NIR/SWIR range of the InGaAs sensors used provides a high signal-to-noise ratio, which is crucial according to Stroppiana et al. (2018), and such sensors are a missing technology for crop trait monitoring. NIR-enhanced silicon-based VIS imagers are mainly affected by this issue due to a drop in sensitivity at their spectral detection limits. However, non-enhanced InGaAs sensors (900 to 1700 nm) also reach their spectral limits in the NIR, with steep sensitivity drops at both spectral ends. For this reason, VIS-NIR-enhanced InGaAs sensors (600 to 1700 nm) have advantages as they partially overcome these problems, especially in the NIR/SWIR domain.

Comparing the tested image reflectance calibration techniques (ELM and WPM, see section 5.2.5), both performed similarly (Tables 5.4—5.6), with slight differences in R^2 values dependent on the data set but not systematic. Thus, distinct recommendations on specific index-calibration method combinations could not be identified. This observation is again consistent with the findings of Jenal et al. (2020).

5.5 Conclusions and Outlook

The results presented in this study indicate that the VNIR/SWIR multi-camera system camSWIR is suitable for acquiring spectral image data in the NIR/SWIR. The derived vegetation indices were demonstrated to be capable of estimating agronomic relevant crop traits in winter wheat. In comparison with destructively measured crop trait data, both tested VIs (GnyLi and NRI) reached high estimation accuracies (R^2: 0.73 to 0.87) in the regression models for validation.
The findings of this study further imply that by applying the proposed multilevel crop trait estimation workflow, biomass-related crop traits can be estimated in regression models using SfM/MVS-derived CH data from UAV RGB imagery. Such applications are beneficial for a reliable assessment of crop traits using UAV data, since the availability of ground truth data is most often the limiting factor. In this study, this workflow's implementation led to bivariate regression models based on both NIR/SWIR VIs and the estimated crop traits, based on UAV-derived crop heights, which reached high accuracies (R^2: 0.57 to 0.67).
The CH data for June 02, which were considered unrealistic since they suggested a drop in the seasonal crop height development, raise the intriguing research question of this method's limitations. Therefore, this phenomenon requires further investigation and methodological improvements in order to avoid compromising effects. Alternatively, CH derived from UAV LiDAR data should also be investigated.
The results presented here are based on data from a single observation data. Thus, they are noteworthy but not yet representative and need to be confirmed by further studies. Future evaluations of the camSWIR imaging system using multi-temporal and multi-year data acquisition campaigns on a winter wheat field trial are planned. To allow for a comparison with established methods, such evaluations optimally also include data from airborne VNIR imaging systems and spectral ground truth using a portable spectroradiometer in the field.
Given that future evaluations confirm the results of this study, spectral data collected by the VNIR/SWIR multi-camera system can provide additional information for more accurate yield estimation or efficient fertilizer management in precision agriculture.

5.6 Author Contributions

Conceptualization, G.B. and A.J.; methodology, A.J.; validation, H.E.A., A.B. and A.J.; formal analysis, A.J. and G.B.; investigation, A.J., H.E.A., A.B., G.B., and H.H. ; data curation, A.J.; visualization, A.J.; writing–original draft preparation, A.J. and G.B.; writing–review and editing, H.E.A., A.B., H.H., and J.B. ; supervision, G.B., H.H., and J.B.; funding acquisition, G.B. and J.B. All authors have read and agreed to the published version of the manuscript.

5.7 Funding, Acknowledgements, and Conflict of Interest

This research was partly funded by the Federal Ministry of Education and Research (BMBF) [Grant number 031B0734F] as part of the consortium research project "GreenGrass".
The authors would like to thank the technical staff of Campus Klein-Altendorf for handling the experimental field throughout the growing season from seeding to harvest.
The authors declare no conflict of interest.

5.8 Appendix

5.8.1 P4RTK Crop Height—Bar Plots

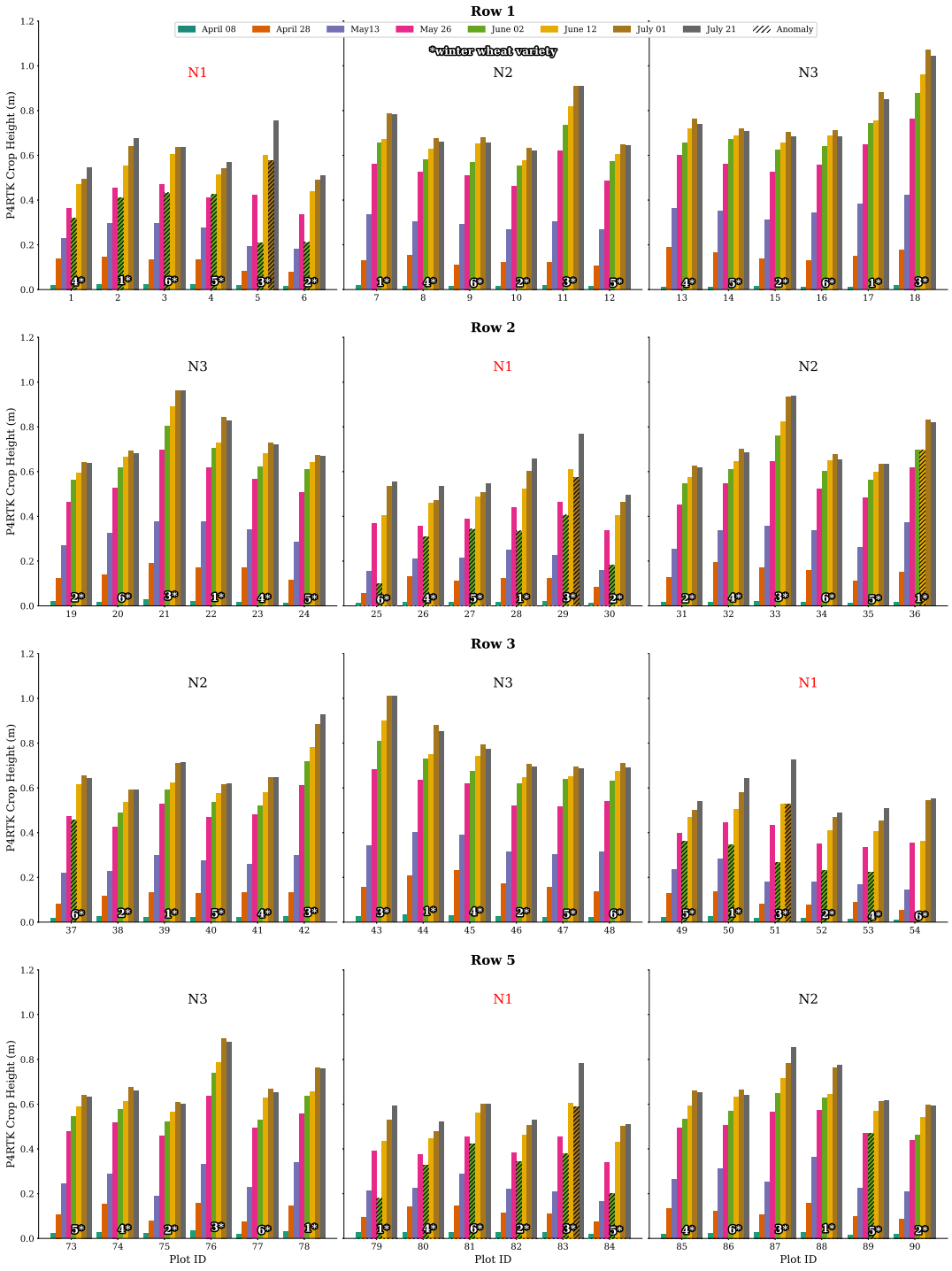


Figure 5.20: Graphical visualization of CH values for all relevant flight dates and all winter wheat varieties of rows 1, 2, 3, and 5 of the experimental field. The unexpectedly derived negative plant growth for the June 02 flight date by the *crop height workflow* is mainly found in the N1 plots, with three exceptions. Another noticeable phenomenon is the drop-in crop growth of variety no. 3 in all N1 stages of flight date July 01. The corresponding erroneous CH values are marked with a hatched overlay in black.

5.8.2 Reflectance Calibration by Grayscale Panels (ELM)

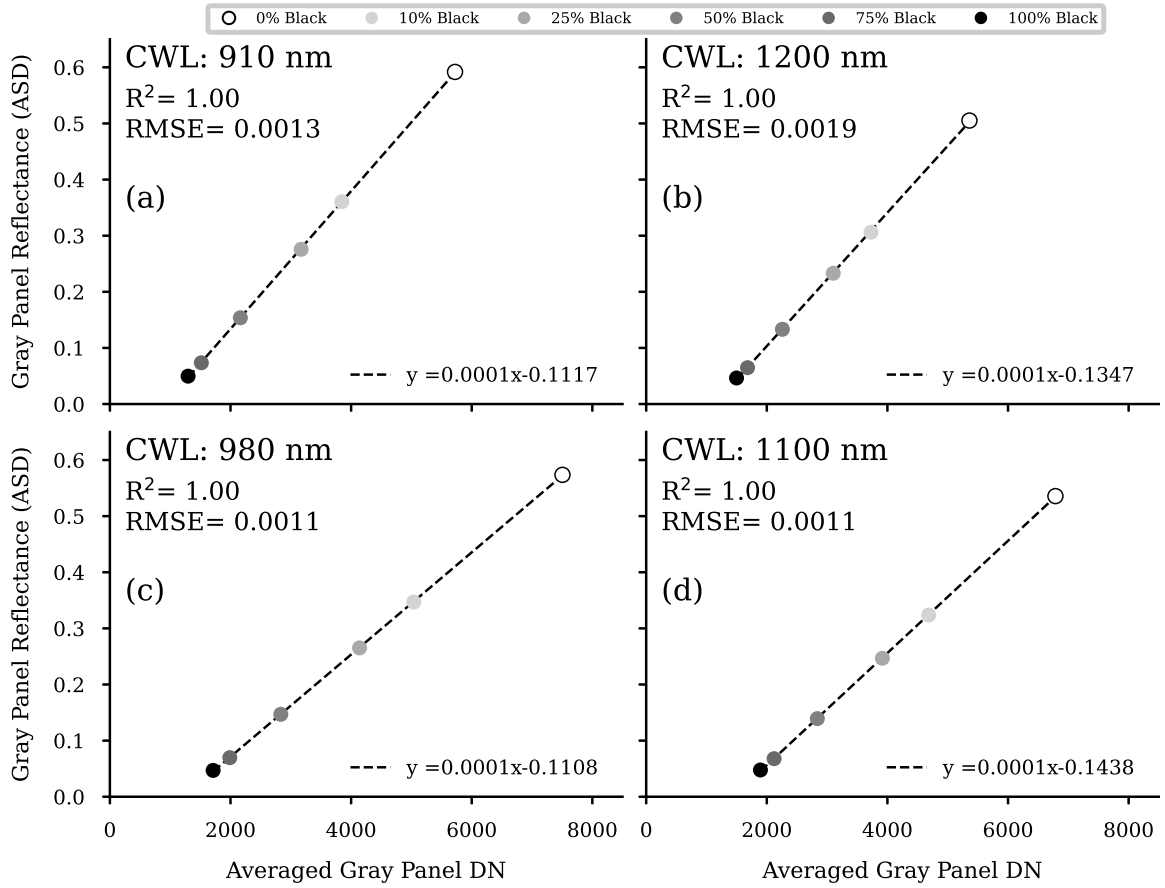


Figure 5.21: Regression analyses of the grayscale panel DN values measured in the flat-field corrected image data and the reflectance of the gray panels, measured by a portable ASD FieldSpec3 spectroradiometer (Malvern Panalytical Ltd, Malvern, United Kingdom) (ASD). For each of the four wavelength bands (**a**–**d**), five images were analyzed, and the resulting DNs of the respective gray panels were averaged. ($p < 0.001$ for all regression models)

5.8.3 WPM Calibration Method Test



Figure 5.22: Last step of a developed Python script to determine the averaged pixel values of selected areas. Here, the resulting grayscale panels' reflectance values for one WPM-calibrated image are displayed. The same script is used when determining the average digital numbers of the grayscale panels in the flat-field calibrated images for deriving the transfer function for converting the DN to reflectance values.

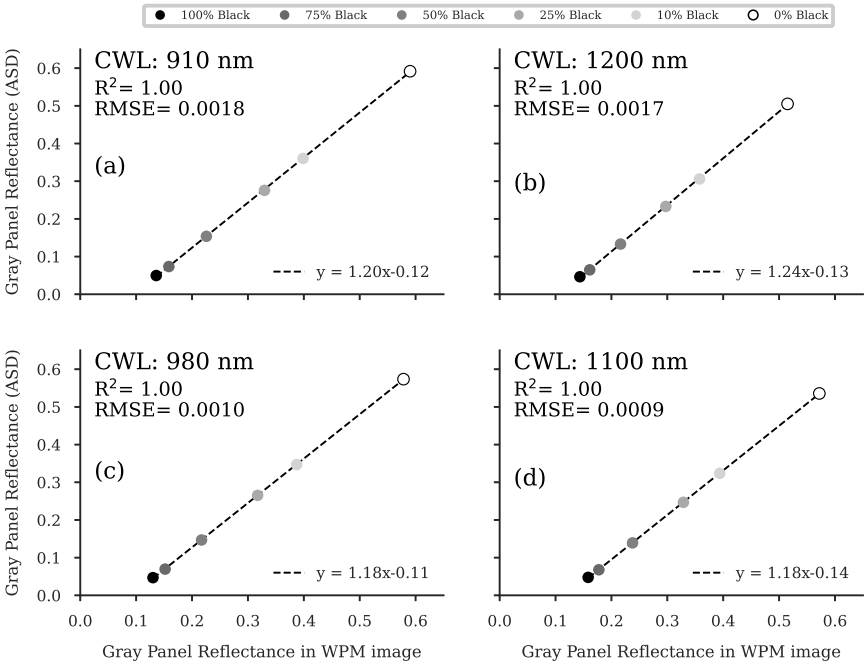


Figure 5.23: Regression analyses of the gray panel reflectance values in the WPM-calibrated images and the reflectance of the gray panels, measured by a portable ASD FieldSpec3 spectroradiometer (Malvern Panalytical Ltd, Malvern, United Kingdom) (ASD). For each of the four wavelength bands (**a**–**d**), five images were analyzed, and the resulting reflectance of the respective gray panel was averaged. ($p < 0.001$ for all regression models)

5.9 References

Aasen, H. & Bareth, G. (2018). Spectral and 3D Nonspectral Approaches to Crop Trait Estimation Using Ground and UAV Sensing. *Hyperspectral Remote Sensing of Vegetation*, volume III Title: Biophysical and Biochemical Characterization and Plant Species Studies, 103–131. CRC Press Taylor & Francis Group, (second edition ed.). https://doi.org/10.1201/9780429431180-4

Aasen, H., Burkart, A., Bolten, A., & Bareth, G. (2015). Generating 3D hyperspectral information with lightweight UAV snapshot cameras for vegetation monitoring: From camera calibration to quality assurance. *ISPRS Journal of Photogrammetry and Remote Sensing*, 108, 245–259. https://doi.org/10.1016/j.isprsjprs.2015.08.002

Ahrends, H. E., Eugster, W., Gaiser, T., Rueda-Ayala, V., Hüging, H., Ewert, F., & Siebert, S. (2018). Genetic yield gains of winter wheat in Germany over more than 100 years (1895–2007) under contrasting fertilizer applications. *Environmental Research Letters*, 13(10), 104003. https://doi.org/10.1088/1748-9326/aade12

Aklilu Tesfaye, A. & Gessesse Awoke, B. (2020). Evaluation of the saturation property of vegetation indices derived from sentinel-2 in mixed crop-forest ecosystem. *Spatial Information Research*. https://doi.org/10.1007/s41324-020-00339-5

Atzberger, C. (2013). Advances in Remote Sensing of Agriculture: Context Description, Existing Operational Monitoring Systems and Major Information Needs. *Remote Sensing*, 5(2), 949–981. https://doi.org/10.3390/rs5020949

Bareth, G., Bendig, J., Tilly, N., Hoffmeister, D., Aasen, H., & Bolten, A. (2016). A Comparison of UAV- and TLS-derived Plant Height for Crop Monitoring: Using Polygon Grids for the Analysis of Crop Surface Models (CSMs). *Photogrammetrie - Fernerkundung - Geoinformation*, 2016(2), 85–94. https://doi.org/10.1127/pfg/2016/0289

Bareth, G., Bolten, A., & Bendig, J. (2011). Potentials for low-cost Mini-UAVs. *Proceedings on the Workshop of Remote Sensing Methods for Change Detection and Process Modelling*, 1–8. https://doi.org/10.5880/TR32DB.KGA92.2

Bareth, G. & Schellberg, J. (2018). Replacing Manual Rising Plate Meter Measurements with Low-cost UAV-Derived Sward Height Data in Grasslands for Spatial Monitoring. *PFG – Journal of Photogrammetry, Remote Sensing and Geoinformation Science*, 86(3), 157–168. https://doi.org/10.1007/s41064-018-0055-2

Bates, J. S., Montzka, C., Schmidt, M., & Jonard, F. (2021). Estimating Canopy Density Parameters Time-Series for Winter Wheat Using UAS Mounted LiDAR. *Remote Sensing*, 13(4), 710. https://doi.org/10.3390/rs13040710

Bendig, J., Bolten, A., & Bareth, G. (2013). UAV-based Imaging for Multi-Temporal, very high Resolution Crop Surface Models to monitor Crop Growth Variability. *Photogrammetrie - Fernerkundung - Geoinformation*, 2013(6), 551–562. https://doi.org/10.1127/1432-8364/2013/0200

Bendig, J., Bolten, A., Bennertz, S., Broscheit, J., Eichfuss, S., & Bareth, G. (2014). Estimating Biomass of Barley Using Crop Surface Models (CSMs) Derived from UAV-Based RGB Imaging. *Remote Sensing*, 6(11), 10395–10412. https://doi.org/10.3390/rs61110395

Bendig, J., Yu, K., Aasen, H., Bolten, A., Bennertz, S., Broscheit, J., Gnyp, M. L., & Bareth, G. (2015). Combining UAV-based plant height from crop surface models, visible, and near infrared vegetation indices for biomass monitoring in barley. *International Journal of Applied Earth Observation and Geoinformation*, 39, 79–87. https://doi.org/10.1016/j.jag.2015.02.012

Berger, K., Verrelst, J., Féret, J.-B., Wang, Z., Wocher, M., Strathmann, M., Danner, M., Mauser, W., & Hank, T. (2020). Crop nitrogen monitoring: Recent progress and principal developments in the context of imaging spectroscopy missions. *Remote Sensing of Environment*, 242, 111758. https://doi.org/10.1016/j.rse.2020.111758

Camino, C., González-Dugo, V., Hernández, P., Sillero, J., & Zarco-Tejada, P. J. (2018). Improved nitrogen retrievals with airborne-derived fluorescence and plant traits quantified from VNIR-SWIR hyperspectral imagery in the context of precision agriculture. *International Journal of Applied Earth Observation and Geoinformation*, 70(February), 105–117. https://doi.org/10.1016/j.jag.2018.04.013

Candiago, S., Remondino, F., De Giglio, M., Dubbini, M., & Gattelli, M. (2015). Evaluating Multispectral Images and Vegetation Indices for Precision Farming Applications from UAV Images. *Remote Sensing*, 7(4), 4026–4047. https://doi.org/10.3390/rs70404026

Ceccato, P., Flasse, S., Tarantola, S., Jacquemoud, S., & Grégoire, J.-M. (2001). Detecting vegetation leaf water content using reflectance in the optical domain. *Remote Sensing of Environment*, 77(1), 22–33. https://doi.org/10.1016/S0034-4257(01)00191-2

Curran, P. J. (1989). Remote sensing of foliar chemistry. *Remote Sensing of Environment*, 30(3), 271–278. https://doi.org/10.1016/0034-4257(89)90069-2

Foley, J. A. (2011). CAN WE FEED THE WORLD SUSTAIN THE PLANET? *Scientific American*, 305(5), 60–65. https://www.jstor.org/stable/26002878

Fourty, T., Baret, F., Jacquemoud, S., Schmuck, G., & Verdebout, J. (1996). Leaf optical properties with explicit description of its biochemical composition: Direct and inverse problems. *Remote Sensing of Environment*, 56(2), 104–117. https://doi.org/10.1016/0034-4257(95)00234-0

Geipel, J., Link, J., & Claupein, W. (2014). Combined Spectral and Spatial Modeling of Corn Yield Based on Aerial Images and Crop Surface Models Acquired with an Unmanned Aircraft System. *Remote Sensing*, 6(11), 10335–10355. https://doi.org/10.3390/rs61110335

Gilliot, J. M., Michelin, J., Hadjard, D., & Houot, S. (2020). An accurate method for predicting spatial variability of maize yield from UAV-based plant height estimation: A tool for monitoring agronomic field experiments. *Precision Agriculture*. https://doi.org/10.1007/s11119-020-09764-w

Gnyp, M., Bareth, G., Li, F., Lenz-Wiedemann, V. I., Koppe, W., Miao, Y., Hennig, S. D., Jia, L., Laudien, R., Chen, X., & Zhang, F. (2014). Development and implementation of a multiscale biomass model using hyperspectral vegetation indices for winter wheat in the North China Plain. *International Journal of Applied Earth Observation and Geoinformation*, 33, 232–242. https://doi.org/10.1016/j.jag.2014.05.006

Gnyp, M. L., Yu, K., Aasen, H., Yao, Y., Huang, S., Miao, Y., & Bareth, C. . G. (2013). Analysis of Crop Reflectance for Estimating Biomass in Rice Canopies at Different Phenological Stages. *Photogrammetrie - Fernerkundung - Geoinformation*, 2013(4), 351–365. https://doi.org/10.1127/1432-8364/2013/0182

Haboudane, D., Miller, J. R., Pattey, E., Zarco-Tejada, P. J., & Strachan, I. B. (2004). Hyperspectral vegetation indices and novel algorithms for predicting green LAI of crop canopies: Modeling and validation in the context of precision agriculture. *Remote Sensing of Environment*, 90(3), 337–352. https://doi.org/10.1016/j.rse.2003.12.013

Hank, T. B., Berger, K., Bach, H., Clevers, J. G. P. W., Gitelson, A., Zarco-Tejada, P., & Mauser, W. (2019). Spaceborne Imaging Spectroscopy for Sustainable Agriculture: Contributions and Challenges. *Surveys in Geophysics*, 40(3), 515–551. https://doi.org/10.1007/s10712-018-9492-0

Herrmann, I., Karnieli, A., Bonfil, D. J., Cohen, Y., & Alchanatis, V. (2010). SWIR-based spectral indices for assessing nitrogen content in potato fields. *International Journal of Remote Sensing*, 31(19), 5127–5143. https://doi.org/10.1080/01431160903283892

Hoffmeister, D., Bolten, A., Curdt, C., Waldhoff, G., & Bareth, G. (2010). High-resolution Crop Surface Models (CSM) and Crop Volume Models (CVM) on field level by terrestrial laser scanning. *Proc.SPIE*, volume 7840. https://doi.org/10.1117/12.872315

Honkavaara, E., Eskelinen, M. A., Pölönen, I., Saari, H., Ojanen, H., Mannila, R., Holmlund, C., Hakala, T., Litkey, P., Rosnell, T., Viljanen, N., & Pulkkanen, M. (2016). Remote Sensing of 3-D Geometry and Surface Moisture of a Peat Production Area Using Hyperspectral Frame Cameras in Visible to Short-Wave Infrared Spectral Ranges Onboard a Small Unmanned Airborne Vehicle (UAV). *IEEE Transactions on Geoscience and Remote Sensing*, 54(9), 5440–5454. https://doi.org/10.1109/TGRS.2016.2565471

Huang, S., Miao, Y., Yuan, F., Gnyp, M. L., Yao, Y., Cao, Q., Wang, H., Lenz-Wiedemann, V. I. S., & Bareth, G. (2017). Potential of RapidEye and WorldView-2 Satellite Data for Improving Rice Nitrogen Status Monitoring at Different Growth Stages. *Remote Sensing*, 9(3), 227. https://doi.org/10.3390/rs9030227

Hunt, E. R. & Daughtry, C. S. T. (2018). What good are unmanned aircraft systems for agricultural remote sensing and precision agriculture? *International Journal of Remote Sensing*, 39(15-16), 5345–5376. https://doi.org/10.1080/01431161.2017.1410300

Hütt, C., Waldhoff, G., & Bareth, G. (2020). Fusion of Sentinel-1 with Official Topographic and Cadastral Geodata for Crop-Type Enriched LULC Mapping Using FOSS and Open Data. *ISPRS International Journal of Geo-Information*, 9(2), 120. https://doi.org/10.3390/ijgi9020120

Jenal, A., Bareth, G., Bolten, A., Kneer, C., Weber, I., & Bongartz, J. (2019). Development of a VNIR/SWIR Multispectral Imaging System for Vegetation Monitoring with Unmanned Aerial Vehicles. *Sensors*, 19(24), 5507. https://doi.org/10.3390/s19245507

Jenal, A., Lussem, U., Bolten, A., Gnyp, M. L., Schellberg, J., Jasper, J., Bongartz, J., & Bareth, G. (2020). Investigating the Potential of a Newly Developed UAV-based VNIR/SWIR Imaging System for Forage Mass Monitoring. *PFG – Journal of Photogrammetry, Remote Sensing and Geoinformation Science*, 88(5), 493–507. https://doi.org/10.1007/s41064-020-00128-7

Kandylakis, Z., Falagas, A., Karakizi, C., & Karantzalos, K. (2020). Water Stress Estimation in Vineyards from Aerial SWIR and Multispectral UAV Data. *Remote Sensing*, 12(15), 2499. https://doi.org/10.3390/rs12152499

Kluyver, T., Ragan-Kelley, B., Pérez, F., Bussonnier, M., Frederic, J., Hamrick, J., Grout, J., Corlay, S., Ivanov, P., Abdalla, S., & Willing, C. (2016). Jupyter Notebooks—a publishing format for reproducible computational workflows. *Proceedings of the 20th International Conference on Electronic Publishing*, 4. https://doi.org/10.3233/978-1-61499-649-1-87

Koppe, W., Gnyp, M. L., Hennig, S. D., Li, F., Miao, Y., Chen, X., Jia, L., & Bareth, G. (2012). Multi-Temporal Hyperspectral and Radar Remote Sensing for Estimating Winter Wheat Biomass in the North China Plain. *Photogrammetrie - Fernerkundung - Geoinformation*, 2012(3), 281–298. https://doi.org/10.1127/1432-8364/2012/0117

Koppe, W., Li, F., Gnyp, M. L., Miao, Y., Jia, L., Chen, X., Zhang, F., & Bareth, G. (2010). Evaluating Multispectral and Hyperspectral Satellite Remote Sensing Data for Estimating Winter Wheat Growth Parameters at Regional Scale in the North China Plain. *Photogrammetrie - Fernerkundung - Geoinformation*, 2010(3), 167–178. https://doi.org/10.1127/1432-8364/2010/0047

Kumar, L., Schmidt, K., Dury, S., & Skidmore, A. (2001). Imaging Spectrometry and Vegetation Science. *Imaging Spectrometry: Basic Principles and Prospective Applications*, Remote Sensing and Digital Image Processing, 111–155. Springer Netherlands. https://doi.org/10.1007/978-0-306-47578-8_5

Lemaire, G. & Gastal, F. (1997). N uptake and distribution in plant canopies. *Diagnosis of the Nitrogen Status in Crops*, 3–43. Springer Berlin Heidelberg. https://doi.org/10.1007/978-3-642-60684-7_1

Lemaire, G., Jeuffroy, M.-H., & Gastal, F. (2008). Diagnosis tool for plant and crop N status in vegetative stage: Theory and practices for crop N management. *European Journal of Agronomy*, 28(4), 614–624. https://doi.org/10.1016/j.eja.2008.01.005

Li, D., Wang, X., Zheng, H., Zhou, K., Yao, X., Tian, Y., Zhu, Y., Cao, W., & Cheng, T. (2018). Estimation of area- and mass-based leaf nitrogen contents of wheat and rice crops from water-removed spectra using continuous wavelet analysis. *Plant Methods*, 14(1), 76. https://doi.org/10.1186/s13007-018-0344-1

Li, F., Miao, Y., Hennig, S. D., Gnyp, M. L., Chen, X., Jia, L., & Bareth, G. (2010). Evaluating hyperspectral vegetation indices for estimating nitrogen concentration of winter wheat at different growth stages. *Precision Agriculture*, 11(4), 335–357. https://doi.org/10.1007/s11119-010-9165-6

Lussem, U., Bareth, G., Bolten, A., Schellberg, J., et al. (2017). Feasibility study of directly georeferenced images from low-cost unmanned aerial vehicles for monitoring sward height in a long-term experiment on grassland. *Grassland Science in Europe*, 22, 354–356. https://iris.unito.it/retrieve/handle/2318/1657936/383986/EGF2017-proceedingsFULL-rid.pdf#page=379

Maes, W. H. & Steppe, K. (2019). Perspectives for Remote Sensing with Unmanned Aerial Vehicles in Precision Agriculture. *Trends in Plant Science*, 24(2), 152–164. https://doi.org/10.1016/j.tplants.2018.11.007

Mahajan, G. R., Pandey, R. N., Sahoo, R. N., Gupta, V. K., Datta, S. C., & Kumar, D. (2017). Monitoring nitrogen, phosphorus and sulphur in hybrid rice (Oryza sativa L.) using hyperspectral remote sensing. *Precision Agriculture*, 18(5), 736–761. https://doi.org/10.1007/s11119-016-9485-2

Mistele, B. & Schmidhalter, U. (2008). Spectral measurements of the total aerial N and biomass dry weight in maize using a quadrilateral-view optic. *Field Crops Research*, 106(1), 94–103. https://doi.org/10.1016/j.fcr.2007.11.002

Mulla, D. J. (2013). Twenty five years of remote sensing in precision agriculture: Key advances and remaining knowledge gaps. *Biosystems Engineering*, 114(4), 358–371. https://doi.org/10.1016/j.biosystemseng.2012.08.009

Mutanga, O. & Skidmore, A. K. (2004). Narrow band vegetation indices overcome the saturation problem in biomass estimation. *International Journal of Remote Sensing*, 25(19), 3999–4014. https://doi.org/10.1080/01431160310001654923

Näsi, R., Viljanen, N., Kaivosoja, J., Alhonoja, K., Hakala, T., Markelin, L., & Honkavaara, E. (2018). Estimating Biomass and Nitrogen Amount of Barley and Grass Using UAV and Aircraft Based Spectral and Photogrammetric 3D Features. *Remote Sensing*, 10(7), 1082. https://doi.org/10.3390/rs10071082

Ollinger, S. V. (2010). Sources of variability in canopy reflectance and the convergent properties of plants. *New Phytologist*, 20.

Perez, F. & Granger, B. E. (2007). IPython: A System for Interactive Scientific Computing. *Computing in Science & Engineering*, 9(3), 21–29. https://doi.org/10.1109/MCSE.2007.53

Pimstein, A., Karnieli, A., Bansal, S. K., & Bonfil, D. J. (2011). Exploring remotely sensed technologies for monitoring wheat potassium and phosphorus using field spectroscopy. *Field Crops Research*, 121(1), 125–135. https://doi.org/10.1016/j.fcr.2010.12.001

Psomas, A., Kneubühler, M., Huber, S., Itten, K., & Zimmermann, N. E. (2011). Hyperspectral remote sensing for estimating aboveground biomass and for exploring species richness patterns of grassland habitats. *International Journal of Remote Sensing*, 32(24), 9007–9031. https://doi.org/10.1080/01431161.2010.532172

Richter, K., Hank, T. B., Atzberger, C., & Mauser, W. (2011). Goodness-of-fit measures: What do they tell about vegetation variable retrieval performance from Earth observation data. *SPIE Remote Sensing*, 81740R. https://doi.org/10.1117/12.897980

Roberts, D. A., Roth, K. L., Wetherley, E. B., Meerdink, S. K., & Perroy, R. L. (2018). Hyperspectral Vegetation Indices. *Hyperspectral Indices and Image Classifications for Agriculture and Vegetation*, (Chapter Hyperspectral Vegetation Indices). CRC Press. https://doi.org/10.1201/9781315159331-1

Roth, L. & Streit, B. (2018). Predicting cover crop biomass by lightweight UAS-based RGB and NIR photography: An applied photogrammetric approach. *Precision agriculture.*, 19(1), 93–114. https://doi.org/10.1007/s11119-017-9501-1

Sagan, V., Maimaitijiang, M., Sidike, P., Eblimit, K., Peterson, K. T., Hartling, S., Esposito, F., Khanal, K., Newcomb, M., Pauli, D., Ward, R., Fritschi, F., Shakoor, N., & Mockler, T. (2019). UAV-Based High Resolution Thermal Imaging for Vegetation Monitoring, and Plant Phenotyping Using ICI 8640 P, FLIR Vue Pro R 640, and thermoMap Cameras. *Remote Sensing*, 11(3), 330. https://doi.org/10.3390/rs11030330

Schirrmann, M., Giebel, A., Gleiniger, F., Pflanz, M., Lentschke, J., & Dammer, K.-H. (2016). Monitoring Agronomic Parameters of Winter Wheat Crops with Low-Cost UAV Imagery. *Remote Sensing*, 8(9), 706. https://doi.org/10.3390/rs8090706

Sims, D. A. & Gamon, J. A. (2002). Relationships between leaf pigment content and spectral reflectance across a wide range of species, leaf structures and developmental stages. *Remote Sensing of Environment*, 81(2), 337–354. https://doi.org/10.1016/S0034-4257(02)00010-X

Smith, G. M. & Milton, E. J. (1999). The use of the empirical line method to calibrate remotely sensed data to reflectance. *International Journal of Remote Sensing*, 20(13), 2653–2662. https://doi.org/10.1080/014311699211994

Stroppiana, D., Fava, F., Boschetti, M., & Brivio, P. A. (2018). Estimation of Nitrogen Content in Herbaceous Plants Using Hyperspectral Vegetation Indices. *Hyperspectral Indices and Image Classifications for Agriculture and Vegetation*, (Chapter Estimation of Nitrogen Content in Herbaceous Plants Using Hyperspectral Vegetation Indices). CRC Press. https://doi.org/10.1201/9781315159331-8

ten Harkel, J., Bartholomeus, H., & Kooistra, L. (2020). Biomass and Crop Height Estimation of Different Crops Using UAV-Based Lidar. *Remote Sensing*, 12(1), 17. https://doi.org/10.3390/rs12010017

Thenkabail, P. S., Lyon, J. G., & Huete, A. (2019). *Hyperspectral Remote Sensing of Vegetation*. CRC Press.

Thenkabail, P. S., Smith, R. B., & De Pauw, E. (2000). Hyperspectral vegetation indices and their relationships with agricultural crop characteristics. *Remote Sensing of Environment*, 71(2), 158–182. https://doi.org/10.1016/S0034-4257(99)00067-X

Tilly, N., Aasen, H., & Bareth, G. (2015). Fusion of Plant Height and Vegetation Indices for the Estimation of Barley Biomass. *Remote Sensing*, 7(9), 11449–11480. https://doi.org/10.3390/rs70911449

Tilly, N. & Bareth, G. (2019). Estimating Nitrogen from Structural Crop Traits at Field Scale—A Novel Approach Versus Spectral Vegetation Indices. *Remote Sensing*, 11(17), 2066. https://doi.org/10.3390/rs11172066

Tilly, N., Hoffmeister, D., Cao, Q., Huang, S., Lenz-Wiedemann, V., Miao, Y., & Bareth, G. (2014). Multitemporal crop surface models: Accurate plant height measurement and biomass estimation with terrestrial laser scanning in paddy rice. *Journal of Applied Remote Sensing*, 8(1), 083671. https://doi.org/10.1117/1.JRS.8.083671

Veloso, A., Mermoz, S., Bouvet, A., Le Toan, T., Planells, M., Dejoux, J.-F., & Ceschia, E. (2017). Understanding the temporal behavior of crops using Sentinel-1 and Sentinel-2-like data for agricultural applications. *Remote Sensing of Environment*, 199, 415–426. https://doi.org/10.1016/j.rse.2017.07.015

Viljanen, N., Honkavaara, E., Näsi, R., Hakala, T., Niemeläinen, O., & Kaivosoja, J. (2018). A Novel Machine Learning Method for Estimating Biomass of Grass Swards Using a Photogrammetric Canopy Height Model, Images and Vegetation Indices Captured by a Drone. *Agriculture*, 8(5), 70. https://doi.org/10.3390/agriculture8050070

Weiss, M., Jacob, F., & Duveiller, G. (2020). Remote sensing for agricultural applications: A meta-review. *Remote Sensing of Environment*, 236, 111402. https://doi.org/10.1016/j.rse.2019.111402

Yue, J., Yang, G., Li, C., Li, Z., Wang, Y., Feng, H., & Xu, B. (2017). Estimation of Winter Wheat Above-Ground Biomass Using Unmanned Aerial Vehicle-Based Snapshot Hyperspectral Sensor and Crop Height Improved Models. *Remote Sensing*, 9(7), 708. https://doi.org/10.3390/rs9070708

Zhang, X., Bao, Y., Wang, D., Xin, X., Ding, L., Xu, D., Hou, L., & Shen, J. (2021). Using UAV LiDAR to Extract Vegetation Parameters of Inner Mongolian Grassland. *Remote Sensing*, 13(4), 656. https://doi.org/10.3390/rs13040656

Zhou, L., Gu, X., Cheng, S., Yang, G., Shu, M., & Sun, Q. (2020). Analysis of Plant Height Changes of Lodged Maize Using UAV-LiDAR Data. *Agriculture*, 10(5), 146. https://doi.org/10.3390/agriculture10050146

6 Discussion

This dissertation developed and evaluated a VNIR/SWIR multi-camera 2D imaging system that is compact and flexible enough to be operated on UAVs to broadly exploit the SWIR domain for crucial spectral vegetation traits (see Figure 6.1). Furthermore, with its extended spectral range, it can provide spectral data in the form of easy-to-process spectral narrowband image data from VNIR to SWIR, resulting in robust spectral products such as well-proven VIs for research or to support, for example, site-specific crop management in PA or more advanced SF applications. In the course of this work, the prototype was named camSWIR.

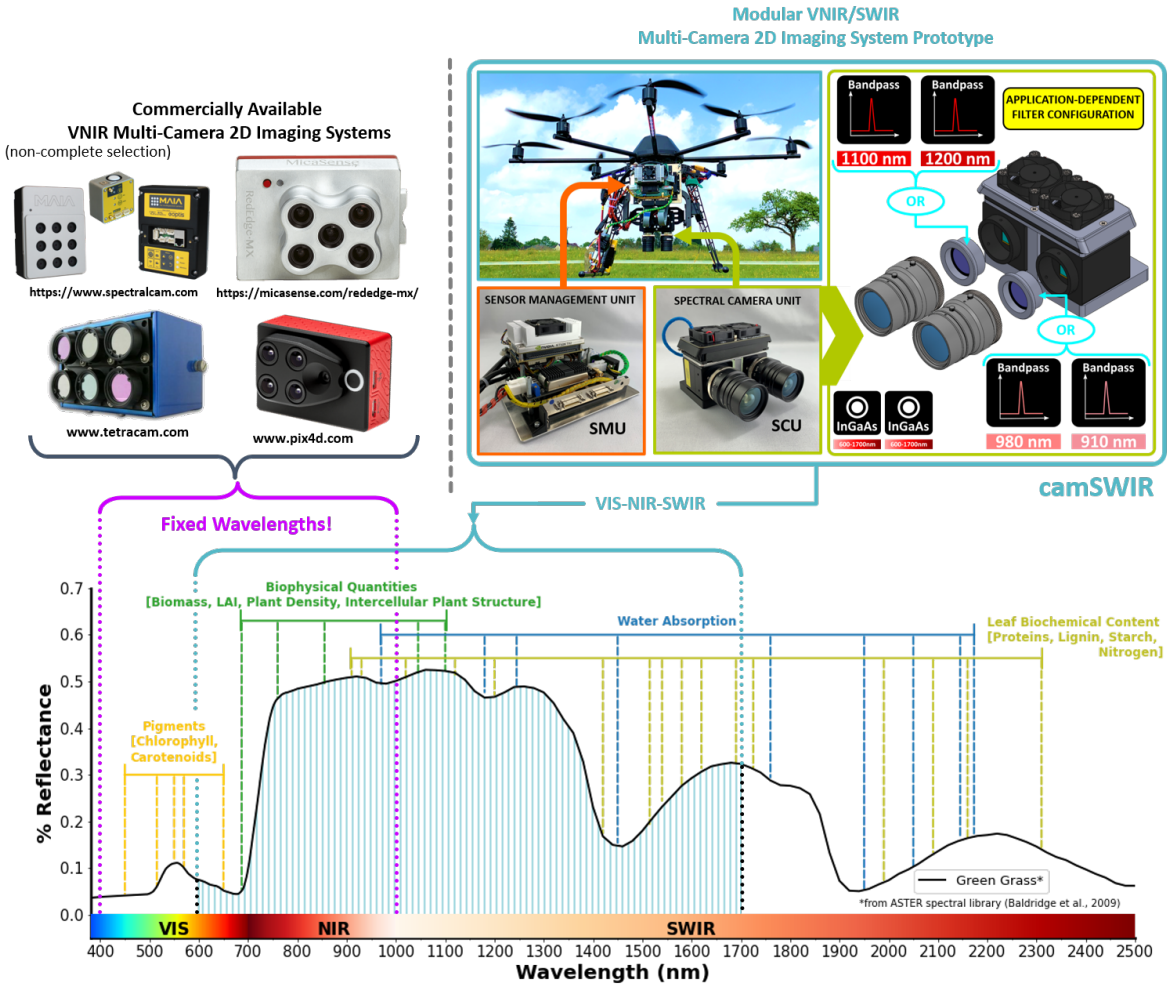


Figure 6.1: Solution to the existing spectral gap for vegetation monitoring with multispectral multi-camera systems. Comparison of a selection of commercial multi-camera systems for vegetation monitoring and the developed SWIR-based multi-camera system prototype relating to the spectral characteristics of vegetation (own illustration, inspired by Hank et al. 2019, Kumar et al. 2001 and Curran 1989).

Among the possible technologies for two-dimensional aerial spectral imaging (Bodkin et al., 2009; Hagen & Kudenov, 2013; Aasen et al., 2018), realistically, only two have prevailed so far and are currently intended for both scientific and commercial use: the hyperspectral line scanner, and the multi-camera multispectral 2D imaging system. Other technologies, such as FPIs-based hyperspectral SWIR snapshot imagers, are also up-and-coming in this regard but are currently still the subject of intense research and development (Honkavaara et al., 2016; Näsi et al., 2016). Hyperspectral systems are more suitable for applications in basic research or specialized niche applications as, on the one hand, they provide narrowband and high-resolution spectral data. However, on the other hand, they are associated with higher acquisition costs, increased weight and space requirements, and complex data acquisition and post-processing (Esposito et al., 2021). In contrast, multi-camera systems are easy to implement in UAV-based carrier platforms. Moreover, the directly acquired two-dimensional spectral image data can be processed in straightforward photogrammetric workflows in which vegetation indices and crop surface models can be derived to estimate plant height, above-ground biomass, and nitrogen content. In this context, the high spatial resolution also allows for better differentiation of vegetation, soil, and shadows and additionally enables phenotyping applications. On the other hand, although only a small selection of spectral bands is necessary to acquire established wavelengths for deriving well-proven vegetation indices, the reduced and fixed spectral resolution can hinder application versatility. Moreover, although an ever-growing variety of commercially available multispectral multi-camera systems for drone-based vegetation monitoring already exist, none of them has a spectral response in the SWIR domain because of the silicon-based image sensors. Figure 6.2 compares the spectral response of the implemented, and fixed bandpass filter wavelengths of commercially available multispectral multi-camera systems with the off-the-shelf available and interchangeable narrow bandpass filters for the SWIR-based camera system prototype camSWIR. Depending on the desired application (e.g., wavelengths or VIs), different filters can be implemented directly.

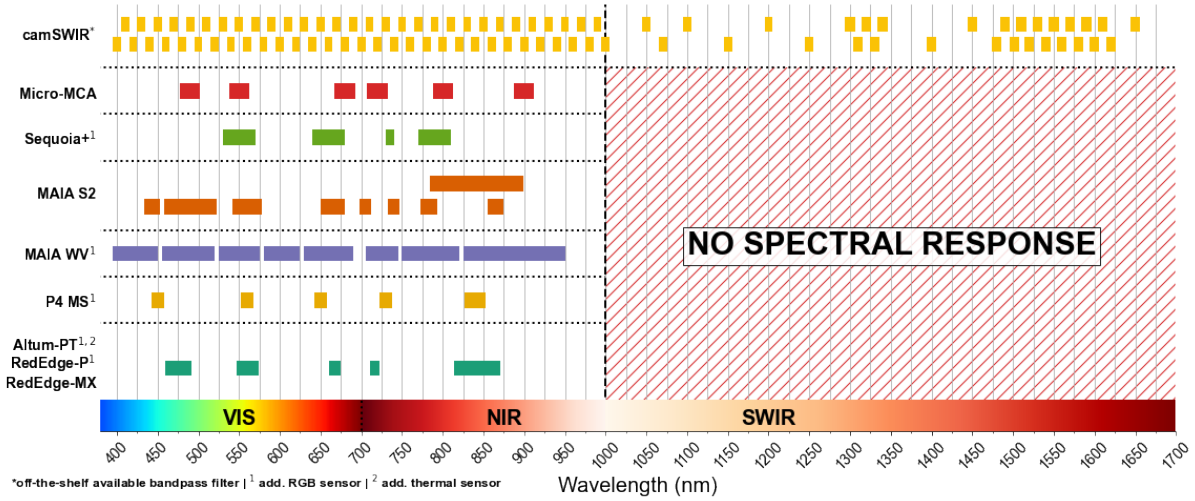


Figure 6.2: Comparison of the spectral response of the fixed bands of commercially available VNIR multi-camera systems and the interchangeable filters directly available for the developed SWIR-based camera system prototype camSWIR. (own illustration)

However, as stated by several studies, narrow SWIR bands can deliver spectral vegetation features for robust crop trait estimation, such as biomass, crop moisture, and nitrogen content (Herrmann et al., 2010; Camino et al., 2018; Berger et al., 2020a; Hornero et al., 2021). Unfortunately, because of the expensive and bulky InGaAs camera modules and their formerly high acquisition cost, an exclusive focus on the visible and near-infrared spectral regions has resulted in an underutilization of the SWIR band; thus, in many studies, there is a spectral observation gap caused by a lack of appropriate UAV-based multi-camera sensor systems.
An extensive literature review of the current state of the art revealed that high-resolution multi-camera systems for the SWIR range were neither commercially available nor the subject of research and development prior to this work. Nevertheless, it was also found that with the current technological advancement of available InGaAs modules, for the first time, the determining shortcomings have been minimized to the extent that camera modules are available that are suitable for the development of SWIR-sensitive multi-camera systems for UAV applications.
Chapters 3 to 5 above summarize the prototype development and evaluation results. Chapter 3 describes the design of the system and initial testing as the basis for this thesis. Finally, in the two subsequent evaluation studies, the system was deemed successful after it successfully estimated above-ground biomass on a permanent grassland field trial (chapter 4) as well as five different crop traits (fresh and dry biomass, N concentration, N uptake, and crop moisture) in a winter wheat experimental field (chapter 5). In this chapter, the prototype development of the VNIR/SWIR camera system is firstly discussed in section 6.1. Various important aspects beyond those outlined in chapter 3 are then discussed and expanded upon in detail.
Furthermore, in addition to pointing out limitations, this chapter outlines improvements to the camera system prototype that were implemented over the course of this work, as well as future improvements and extensions. Finally, (section 6.2) discusses the evaluation of the camera system prototype from chapters 4 and 5 with regard to the potential for estimating plant traits on two different experimental agricultural fields and the related influencing factors, as well as future improvements concerning data acquisition and analysis.

6.1 Camera System Development and Improvement

6.1.1 Development Process

Chapter 3 gives detailed insight into the development process of the multi-camera sensor system. As of December, 2017, an analysis of the components available on the market for building a SWIR-sensitive camera system was performed. The following criteria were essential for the use of the individual cameras in the later overall system:

- best spectral response
- best pixel resolution
- low noise without cryogenic or thermoelectric cooling
- reduced power consumption with the smallest possible dimensions and weight (SWaP)
- camera housing for optimal filter placement or bare board

Since the range of SWaP-InGaAs cameras under consideration that also had an extended spectral response into VIS, was quite limited, compromises had to be made with respect to some specific requirements. For example, only the analog CameraLink interface was available for the favored camera modules. This limitation resulted in increased space and weight requirements in the SMU, since non-embedded frame grabber hardware was needed to control and read out the two cameras. As a positive feature, camera modules that do not have the usual spectral sensitivity of 900 to 1700 nm could be chosen but extend this range into the VIS domain, between 400 and 600 nm, depending on the manufacturer and batch. Unfortunately, camera modules covering the entirety of the SWIR domain cannot be realized with single InGaAs sensors, as explained in section 2.1.2. Nevertheless, as shown in Figure 6.1, many important spectral vegetation features are already situated in the range, up to 1700 nm. For applications beyond 1700 nm, cryogenically cooled MCT sensors in scanner systems must be used, which are accordingly expensive, heavy, and power-demanding.

Extensive tests in the climate chamber and in front of an integrating sphere confirmed the presumed performance according to the manufacturer's specifications. When measuring the resulting dark signal in the climate chamber with different temperature profiles, the values for the exposure times envisaged for later usage (1 to 3 ms) were in the single-digit percentage range relative to the possible 2^{14} bit signal maximum. Therefore, this unwanted but inevitable, temperature-dependent sensor signal in the absence of light poses no problem for brightly illuminated daylight sceneries. Accordingly, it is only necessary to ensure that the camera modules are optimally adjusted with regard to the exposure time so that the maximum possible signal level is saturated to approximately 70 to 80 %. This critical adjustment must be made in the control software before the flight by applying a real-time histogram adaptation process.

Although the exposure time can vary considerably depending on illumination conditions, such as an overcast or clear sky, the tested InGaAs camera modules are ideally suited for daylight operations because of their high dynamic range of 3735:1 (72 dB) (Raptor Photonics, 2019), which allows for high contrast applications. However, exposure time, once adjusted to the current illumination conditions, is not automatically readjusted in the current system design during flight and therefore requires stable illumination conditions. Possible solutions for this issue are further discussed in detail in section 6.2.2.

Another essential task is reflectance calibration of raw DN image data. This calibration is performed in post-processing using image data from Lambertian grayscale tiles acquired during flight, and is used in surveys for subsequent comparability of survey flights that differ in time and location. To properly perform such a reflectance calibration in this thesis, the two sensors were also tested separately on an integrating sphere for their response to a uniform light source. In this way, several exposure-time-related lookup tables (Kokka et al., 2019), in the form of correction images, could be generated for each channel configuration to correct minor pixel differences and to obtain a homogeneous sensor image. This so-called flat-field correction eliminates the sensor-side error influences, such as manufacturing-related pixel sensitivity differences (Emerson & Little, 1999) and non-uniform exposure, such as lens- or filter-related vignetting (Aasen et al., 2015).

These variations in the image data must be corrected before the actual reflectance calibration to determine the true reflectances emanating from the scene. The two different filter mounting solutions were also examined in more detail during the flat-field measurements. Unexpected artifacts occurred with the more straightforward mounting solution. This important finding is documented in more detail in section 6.1.2 as an extension to section 3.2.1.3 and Figure 3.3.
Seamless integration of camera systems into existing flight platforms is always a challenge (Jenal et al., 2022), and UAVs, in particular, have even more demanding requirements due to limited space and energy resources. The additional required battery payload was marginal compared to the system's total weight, which was a critical factor in terms of energy consumption. The quest for a more efficient solution that saves space and weight, and thus complies with the permissible takeoff weight of UAVs, was achieved during the course of the research work, in parallel with the evaluation studies conducted by redesigning the SMU. This process is further described in section 6.1.3.
The following sections 6.1.2 to 6.1.4, discuss relevant points pertaining to the construction of the system and its optimization, complementing chapter 3, and further possible hardware improvements beyond this thesis are pointed out.

6.1.2 Optical Filter Considerations

Since the positioning of the optical filters can be an essential factor in the imaging quality of the optical system, two possible mounting positions for the filter assemblies were investigated with special care. As described in chapter 3, both realized possibilities were thoroughly investigated. As the development of InGaAs sensor manufacturing is continuously progressing, two SWIR-sensitive cameras were procured to assemble the system, which were also improved for the VIS-NIR range, extending the spectral sensitivity range to the visible domain down to about 600 nm. However, the enhanced sensitivity leads to a problem that makes it challenging to filter the desired wavelength. Standard optical interference filters are based on the sensitivities of the standard sensor materials used for the spectral domains. This means that these bandpass filters for the VNIR range become transmissive in the SWIR range, and even SWIR bandpass filters can lose their ability to block light from higher wavelengths. Therefore, combining different filter types for the desired wavelength is necessary. In this case, for every CWL, a shortpass and a bandpass were chosen. A filter stack of both filter elements was then assembled to combine their transmission properties.
Figure 6.3a shows the filters' wavelength-dependent transmittance values for the VIS to SWIR domain provided by the manufacturer (Edmund Optics, 2022), which were not available for all filters for the complete spectral response of the selected InGaAs sensors (905 nm and 980 nm).Figures 6.3b,c show spectroradiometer measurements performed in front of the opening of an integrating sphere to determine the resulting transmission spectra of the manually combined filter stacks. Figure 6.3b shows a clear transmission of the NIR filter stacks in the SWIR range, which is due to the insufficient blocking properties of the selected shortpass filter (SP1100). As a result of the ideal-suited transmission characteristics of the shortpass filter (SP1300), Figure 6.3c shows ideal transmission profiles of both filter stacks that seem suitable for the planned application and favors this short pass for all NIR and SWIR filter stacks.

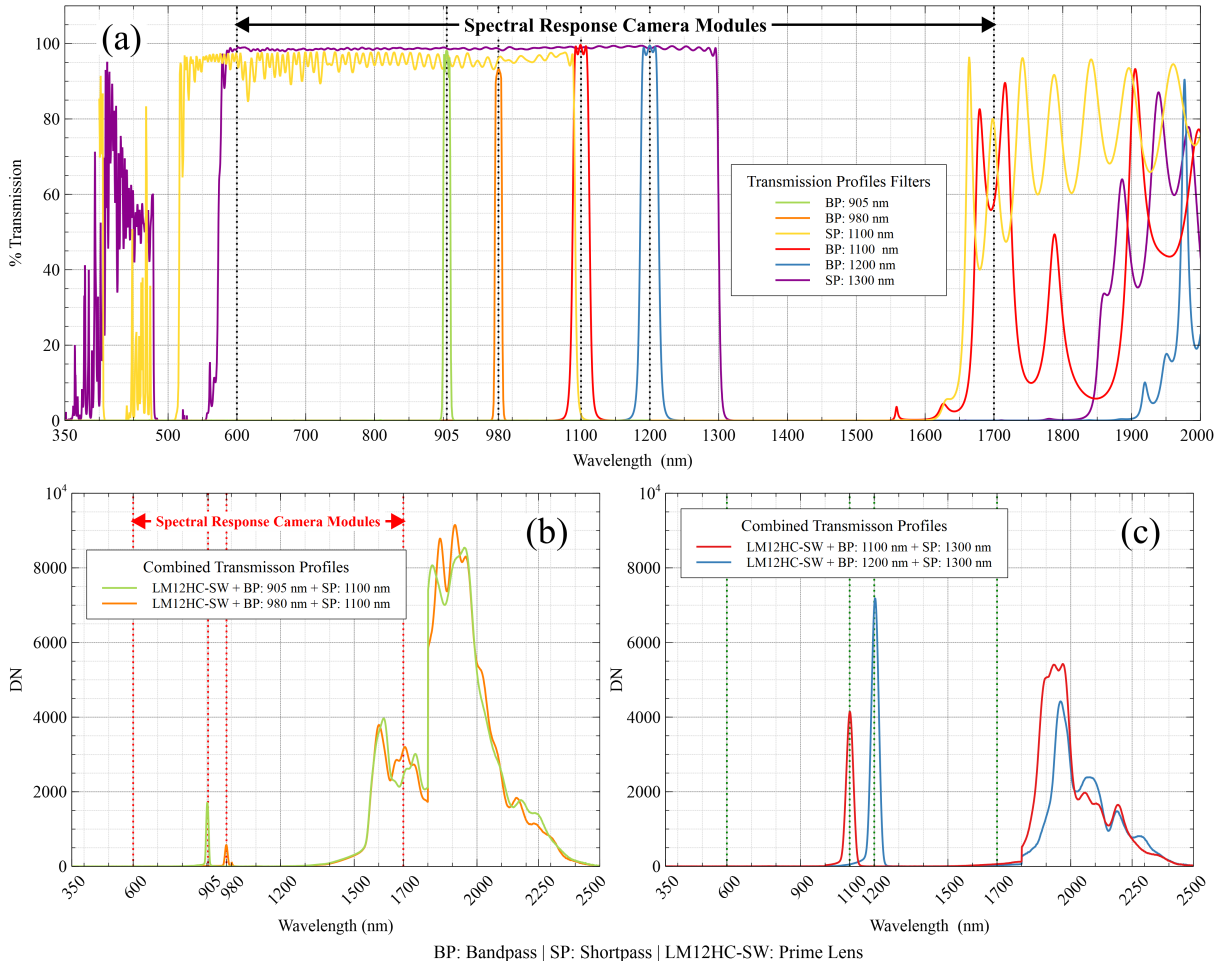


Figure 6.3: (**a**) Selected suitable filter types for the front-mounted filter modules based on the manufacturer's transmission data. Since the individual bandpass filters tend to become transparent in the SWIR, another filter element, in this case, a shortpass filter, is needed to protect the sensitivity range of the camera modules from the effects of interfering light. (**b**) Spectrometer test for the two filter stacks for the NIR domain. The selected short pass filter cannot block light beyond 1300 nm and is therefore not suitable. (**c**) Spectrometer test for the two filter stacks for the SWIR domain. The selected shortpass can block the entire sensitivity range of the InGaAs sensor and should be used for all filter stacks.

In the course of the evaluation, these front-mounted filter assemblies turned out to be unsuitable for use in the camera system—primarily because of the combination of the two mismatched individual bandpass and shortpass filter elements, which were required to block the entirety of the InGaAs sensor's sensitivity from incident light as described above. The main problem with this method became apparent when taking flat-field images at the integrating sphere. The assembled filter stacks generated circular artifacts in the recorded image data because of back reflections between the lens and the filter disks. These artifacts are non-linear effects and highly dependent on the incoming light intensity reflected from the observed scene; thus, they are nearly impossible to correct. Figure 6.4 displays two flat-field images recorded at an integrating sphere and the corresponding image profiles along the two image diagonals. The ring-shaped artifacts are evident in the flat-field images and present in both image profiles accordingly. Therefore, although the fastest filter change would have been possible with this variant, it was not pursued further and was discarded since the necessary quality of the image data could not be achieved.

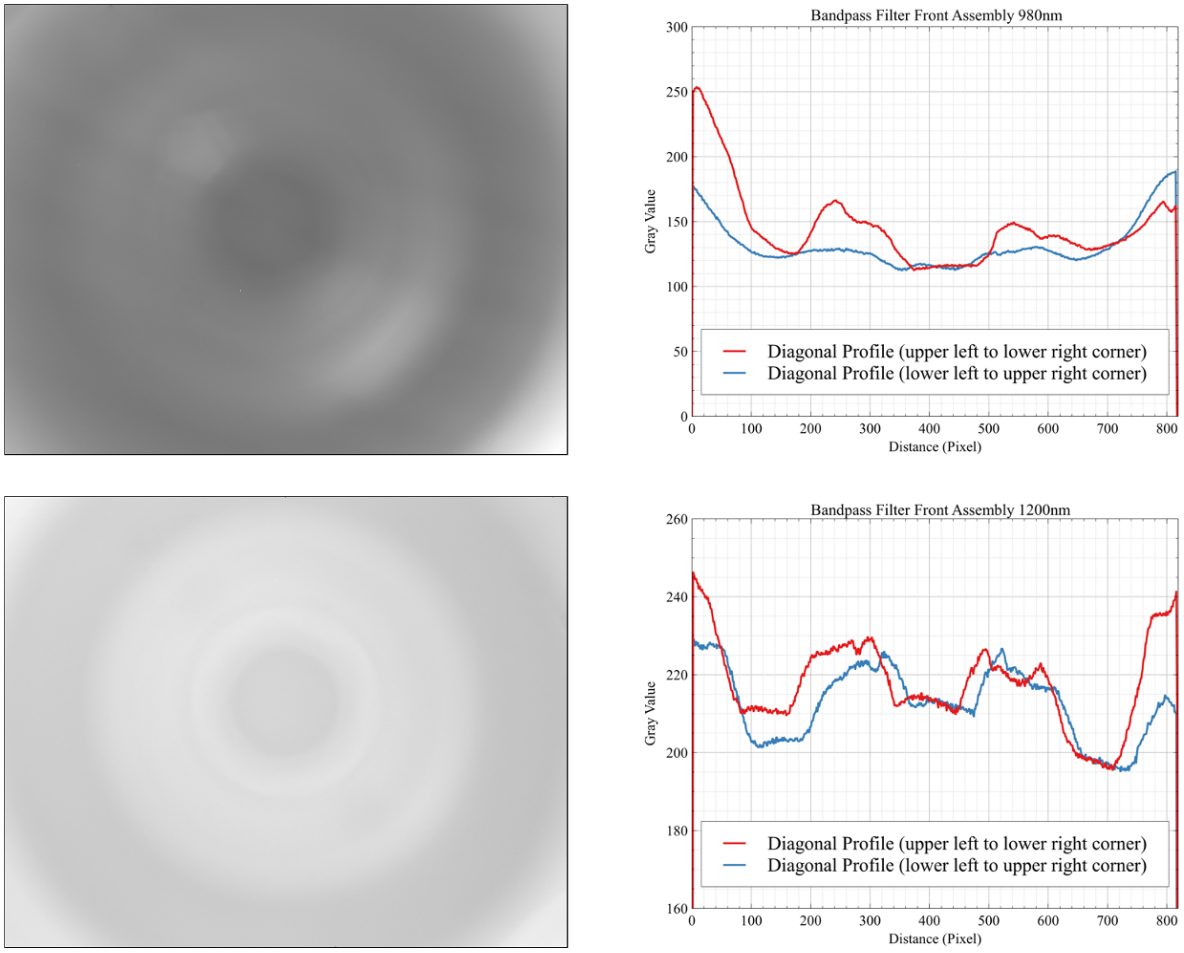


Figure 6.4: Visible artifacts in flat-field calibration images of the tested filter front-assembly caused by back reflections

Based on the composition and features of the optical filter solutions, the apparent use of hybrid band-pass filters between the lens and sensor proved to be the most suitable. In this setup, a more homogeneous sensor illumination and wavelength stability of the passband to avoid a blue shift (Stark et al., 2015) is achieved, and no artifacts were detected in the flat-field images (see section 3.2.1.3). These hybrid filters are composed of dichroic (interference) and colored glass (absorbance) filters and can block the entire spectral sensitivity range of VNIR/SWIR cameras, except for the desired center wavelength CWL with a bandwidth of 10 nm (Thorlabs, 2022). They are also perfectly matched, without undesirable air gaps affecting the refractive properties. From this unexpected result, it follows that the optical path for such systems with a broad spectral range requires a scrupulous investigation to check in advance for any spurious influences that cannot be directly detected in regular operation because of an overlay of the artifacts with the recorded scene.

6.1.3 Improved Sensor Management Unit

Another limitation was the comparatively bulky sensor management unit (SMU). This bulkiness was mainly due to the aforementioned CameraLink cameras available at the time of system design and the frame grabber hardware required for readout, unavailable for embedded systems. Therefore, specially developed printed circuit boards (PCBs) for interconnection were used to compensate for this disadvantage as much as possible and to make the design as compact as possible.

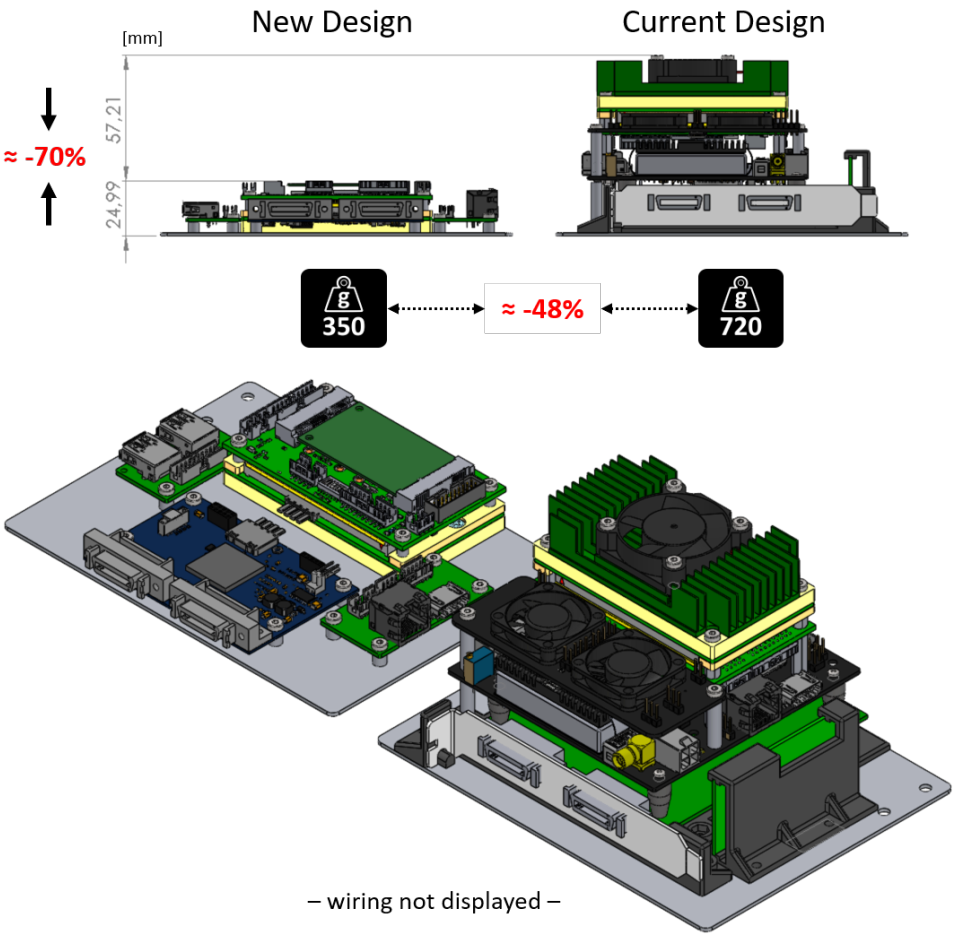


Figure 6.5: Comparison of two CAD designs: the first SMU and the newly designed alternative based on an embedded frame grabber module with reduced size and weight.

Fortunately, manufacturers seem to have recognized the demand for miniaturized parts, as these frame grabber modules have evolved drastically during the course of this work. As a result, new embedded versions were made available that can be easily integrated into embedded systems. CAD models of these newly available components were used to develop an improved SMU in CAD software in order to test its suitability for the overall system in advance. Figure 6.5 compares the new CAD model of the current SMU version with an improved version based on new hardware. As can be seen, significantly more space and weight is saved compared to the previous SMU version. This new SMU has already been successfully built and meets the shape and dimensions designed in the CAD drawing.
Figures 6.6a,b show a side-by-side comparison between the old and the new SMU version. In addition, the latter is shown mounted on a UVA during a flight campaign for test purposes in Figure 6.6c. Figure 6.6d displays a resulting orthomosaic derived from the captured spectral image data (CWL: (910 ± 2) nm; FWHM: (10 ± 2) nm) from the test flight. There are further possibilities for miniaturization, such as choosing a different, smaller computing unit if available or replacing the camera modules used with more powerful ones, which could eliminate the frame grabber hardware and trim the overall system to lower power consumption. This improvement would even make it possible to combine both components, SCU and SMU, into one compact embedded unit.

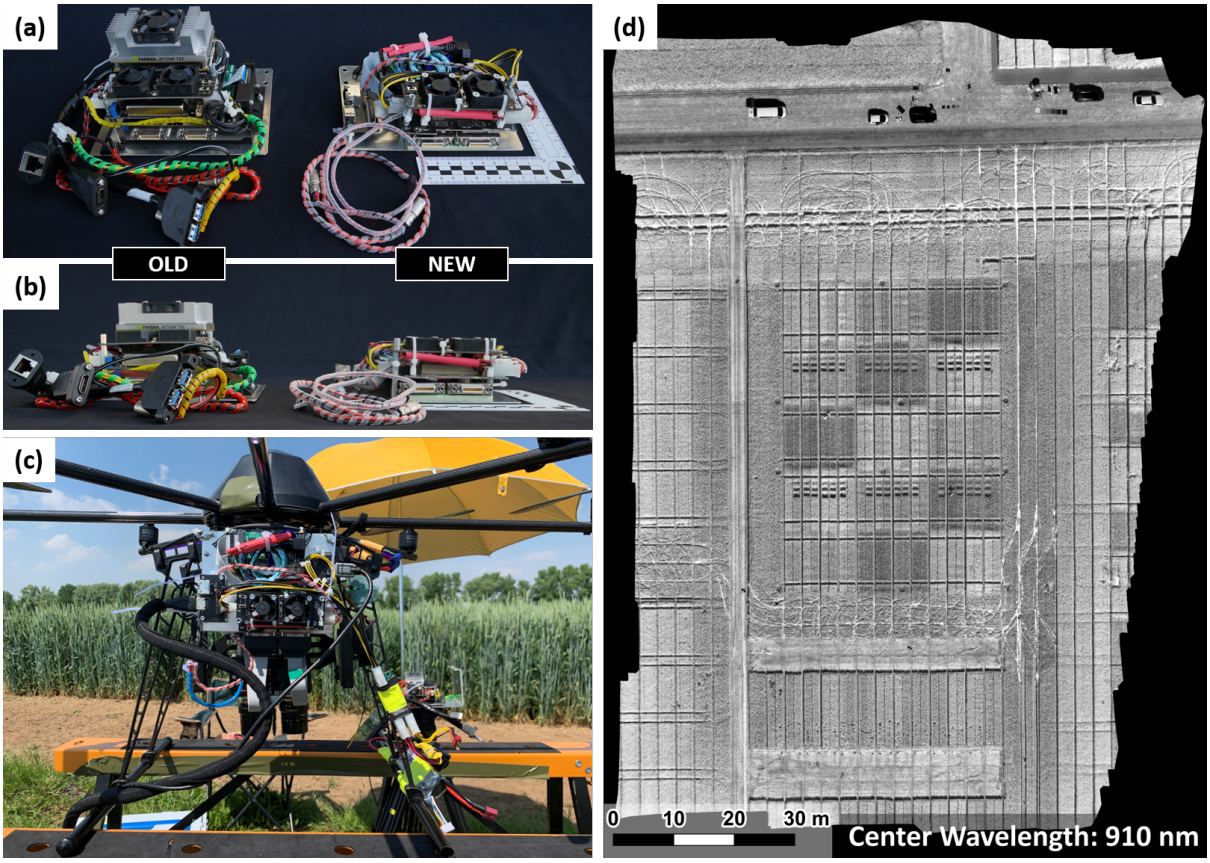


Figure 6.6: (**a**) and (**b**) Direct comparison of the old and new SMU versions. (**c**) New SMU version mounted onto a UAV for performance testing. (**d**) Derived orthomosaic from the image data acquired by the camera system with the new SMU Version.

6.1.4 Extension of Spectral Channels

An explicit limitation of the camera system prototype is that only two camera modules could be implemented in the system, and thus only two spectral channels could be acquired per flight. Therefore, several consecutive flights must be performed in a short period per flight date, to capture more than two spectral bands. This approach requires stable illumination conditions and a thorough instrument calibration on the ground and in the air when changing the filter flanges used for more sophisticated VIs—namely, those incorporating more than two wavebands. On the one hand, this shortcoming is due to the still comparatively more expensive camera hardware, which is approximately a factor of 10 higher than silicon-based hardware. On the other hand, integrating the housed camera modules is still more complex with regard to space requirements and weight. This problem could be solved by integrating houseless OEM camera modules, if available. However, with some minor modifications, the system's control hardware (SMU) can potentially operate up to four such CameraLink camera modules in parallel.
Fortunately, image sensor technology's state-of-the-art is constantly evolving. Particularly in the field of SWIR sensors, improved production processes in recent years have made it possible to process the semiconductor material InGaAs ever more effectively and thus to develop better sensors that deliver high-quality image data at room temperature (Wang et al., 2019). There will be further enhancements in this area in the next few years, but whether the composite semiconductor material InGaAs will become a mass product in sensor production is yet to be seen.

The first promising signs are the improved InGaAs sensors IMX990 and IMX991 from Sony, intended for the industrial mass market and will be used primarily in process control of the production of food or liquid products (Sony, 2022). However, the development of multispectral multi-camera systems will also benefit from this trend. Because the accessibility of more performant imaging sensors directly enables manufacturers of industrial camera modules to build correspondingly powerful and compact camera modules.
The first industrial camera manufacturers have recently (as of December, 2021) started offering camera modules with these two IMX99X sensors (e.g., Alvium 1800 C-130 VSWIR, Allied Vision, Stadtroda, Germany). While these are in the same price range as the currently used modules, they are supposed to consistently perform better in almost all specifications, such as four times the resolution, only a quarter of the weight, and even a fifth of the current volumetric dimensions. For example, with this four times higher spatial resolution, the area to be monitored could also be covered more efficiently and in less time. In addition, the increased pixel count could also increase the GSD, which is especially important when processing CSM and phenotyping applications. All in all, these more performant camera modules would further increase the application flexibility of the system. Another valuable aspect of the Alvium 1800 series is the availability of enclosureless board-level variants of these modules, which can be integrated with the desired number into a complete embedded system in a less complex way. Table 6.1 compares the implemented modules to the latest state-of-the-art modules to illustrate the current technological progress.

Table 6.1: Comparison between the currently implemented camera module in the prototype (Raptor Photonics, 2022) and a current state-of-the-art module (Allied Vision, 2022a).

Parameter	**Raptor Photonics Owl640 Mini**	**Alvium 1800 C-130 VSWIR**
Sensor	- unknown -	Sony IMX990
Sensor type	InGaAs	InGaAs
TE Cooling	None	None
Resolution (H×V)	640×512	1296×1032
Pixel size	15 µm×15 µm	5 µm×5 µm
Bit depth	14 Bit	12 Bit
Spectral response	600 to 1700 nm	400 to 1700 nm
Shutter mode	Global Shutter	Global Shutter
Interface	CameraLink	MIPI CSI-2 or USB-3
Power Supply	12 V	5 V
Mass	170 g	40 g
Dimensions (L×W×H)	42×42×67 (mm)	26×29×29 (mm)

When it comes to driving the technological advancement of SWIR imaging, optical remote sensing plays only a minor role as an incentive force. Nonetheless, it is advantageous that, in addition to spectral vegetation monitoring, the SWIR range offers further advantages that are of interest for various application areas with high order volumes. This interest is basically related to the fact that Particles, molecules, or atoms scatter light. However, if they are much smaller than the wavelength, Rayleigh scattering occurs, and light is scattered less at the more prolonged wavelengths of SWIR wavelengths than at the smaller VIS ones.

Therefore, SWIR wavelengths are more likely to penetrate smoke, haze, and fog until the particles have a diameter on the order of the wavelength and until the wavelength-dependent scattering decreases significantly, known as Mie scattering (Hansen & Malchow, 2008; Maître, 2017). Unlike in the LWIR range, even high-contrast, high-resolution images are possible in the SWIR because of the reflection and absorption of photons, similar to the visible spectrum. These excellent imaging properties of SWIR sensors in harsh environmental conditions make them ideal for assisting autonomous driving in vehicles. However, as this segment is very competitive and dictated by a strict price regime, rethinking and finding new solutions is necessary for the long term.
Therefore, there have been repeated attempts to replace InGaAs sensors with other sensor technologies in recent years (Wang et al., 2021). One promising technology here is quantum dot thin-film technology, in which a photosensitive material is deposited directly onto a silicon-based CMOS readout circuit, eliminating the need for time-consuming and error-prone bonding of InGaAs onto it (Tretyakov et al., 2020, 2019; Liu et al., 2021). This process enables spectral sensitivity similar to VIS-NIR enhanced InGaAs image sensors, but with a significant cost reduction, resulting in a price range identical to that of silicon-based sensors (Goossens et al., 2017). This price reduction would also favor integrating multiple sensors directly onto a PCB and would allow the systems to be miniaturized further. Here, however, the camera modules resulting from this technology still need to be released by manufactures and must be tested for suitability for use in UAV-based vegetation monitoring.

6.2 Camera System evaluation

6.2.1 Evaluation of Crop Trait Estimation Performance

The newly developed camera system prototype was evaluated in two field experiments with different agricultural vegetation types. The parameters of the UAV-based multi-camera system were used to pre-plan flight patterns for both field trials to reach the desired GSD of 0.04 $\mathrm{m{\cdot}px^{-1}}$. The first field trial for evaluation was conducted on permanent grassland. Two VI orthomosaics of the NRI and GnyLi indices were then derived from the four recorded wavelength bands in the NIR and SWIR, which formed the basis for further analysis. In bivariate regression analyses, the derived VIs were very accurate (R^2: 0.71 to 0.75) in estimating above-ground biomass (dry matter yield), which was available in the form of sampled ground truth data across all 156 plots in the chessboard field trial (see Figure 4.2). Lussem et al. (2018) found an R^2 between 0.36 and 0.65 for estimating dry matter (DM) yield via UAV-RGB-based and field-spectroradiometer-based VIs in the same field experiment under similar conditions (second cut, 2017). In another study on this particular grassland field trial, Lussem et al. (2019) found an R^2 between 0.57 and 0.70 for estimating DM yield for the first cut in 2018, using a UAV-based VNIR multispectral multi-camera system. Spectral ground truth measurements were acquired in selected plots, and both spectrometer and camera-based VIs were analyzed in regression analyses against DM yield. The resulting accuracies were compared to each other. Although the spectrometer data performed better than the camera VIs, as expected, because of the low number of sampling spots within the plots with larger measurement cross-sections, these findings should be further investigated with a more refined experimental design.

In the second experiment on a winter wheat trial field, four orthomosaics of different wavelengths were again derived from two flights. Here, 18 plots provided ground truth data in the form of fresh and dry biomass, and nitrogen concentration, that was used to create estimation models of five plant traits combined with crop height data based on multi-temporal UAV RGB data. These models were applied to the remaining plots to estimate the five crop traits per plot. These plots could then be analyzed again with both the NRI and GnyLi indices in bivariate regression models, indicating the possibility of generating ground truth data for evaluation purposes, with moderate to good accuracies (R^2: 0.57 to 0.59). This approach should be investigated further by validating the derived models on an independent winter wheat field trial. The validation of the two VI data sets with the crop traits derived from real ground truth data from the 18 destructive sampling plots showed an even higher accuracy, an R^2 from 0.75 to 0.85. This result should also be taken into account and investigated in more detail in future experimental setups so that the number of possible plots for ground-truthing should, at best, be doubled.
Although only one set of spectral image data was collected throughout the growing season for each field trial, the results of the regression analyses for both the permanent grassland and winter wheat field trials are auspicious for estimating vegetation traits. Therefore, the camera system's performance throughout each phenological stage during the growing season requires further investigation. In addition, it remains to be seen what data quality the system will provide at other stages of the growth process and whether these will produce similar analysis results. Since leaf chemistry and plant structure are known to vary considerably at each growth stage (Jones, 2010), the estimation models developed will also most likely need to be adapted to this fact (Gnyp et al., 2014b; Li et al., 2010). Therefore, to better evaluate this extended application within the growing season as well as the repeatability of the results, analyses with multi-annual, multi-temporal spectral image data sets of the camera system must be obtained and analyzed.
The fundamental statistical analyses performed in the course of this work in the form of bivariate regression analyses provide an initial positive assessment of the suitability of the camera system for non-destructive estimation of crop traits based on simple statistical models from an unmanned aerial carrier platform. However, more sophisticated statistical methods, such as multiple linear regressions or machine learning approaches, such as random forests, have been investigated by Bendig et al. (2015) and Yue et al. (2018). Such approaches combine structural plant heights and spectral data, and they have already been proven to be robust estimators of crop traits, such as biomass and nitrogen concentration (Aasen & Bareth, 2018; Näsi et al., 2018). In particular, machine learning regression methods, such as Gaussian process regression, the aforementioned random forests, and artificial neural networks are offering great potential for developing even better-performing estimation models (Verrelst et al., 2019; Berger et al., 2020,a). Although such models are already applied for investigating biomass and N estimation, for example, in grass (Borra-Serrano et al., 2019) and maize (Han et al., 2019; Zhang et al., 2021), for leaf nitrogen concentration and plant height (Osco et al., 2020), and for protein content (Zhou et al., 2021), they have only investigated surrogate relationships via chlorophyll and structural features like the LAI. As a consequence, these studies did not investigate narrow SWIR bands directly related to the estimated plant traits to improve the prediction quality.

This shortcoming of the non-integrated SWIR range is mainly due to the lack of easy-to-use and suitable sensor solutions for the SWIR domain. Hyperspectral scanners covering this spectral range are still very cost-intensive. They also collect a large amount of data during operation, which has to be handled somehow and is also redundant in most applications. In light of these challenges, the camera system developed in this thesis can make a valuable contribution and be used in a targeted approach because of its adaptability to specific applications.

6.2.2 Reflectance integrity of image data

The imaging system acquires raw spectral image data in the form of discrete brightness values, so-called digital numbers (DNs), which can already be assigned to a specific wavelength when narrowband bandpass filters are used. However, no quantitative assumptions can be made from this data. Therefore, to establish comparability and consistency of the image data, the data must be converted into a physical relation independent of external parameters that distort the reflective properties of the observed vegetation. These include, for example, exposure time, illumination conditions, and the properties of the optical system. Accordingly, the raw image data is converted to reflectance afterward, which is already defined in chapter 2. Therefore, two calibration methods based on the empirical line method (Smith & Milton, 1999) are evaluated in chapters 4 and 5. One with multiple panels in different shades of gray (ELM) in flight, and one with a single white panel (WPM) before a flight. Both have provided comparable results concerning the calibrated data and in the following regression analyses with slightly better accuracies in the WPM calibrated image data.
Nonetheless, the ELM method is preferred because the calibration data is recorded during the flight and not on the ground, as with the WPM method (Fawcett & Anderson, 2019). For the ELM method, grayscale tiles with a known (near-)Lambertian radiation characteristic were used, which must then be contained in at least a few images so that an empirical line calibration in reflectances can subsequently take place based on these reflectance references tiles. The Zenith Lite™ white panel with a Lambertian reflectance of nearly 95% is still necessary for an in-field, flat-field calibration after changing the bandpass filters on the ground. However, to perform an empirical line correction, after Smith & Milton (1999), every acquired aerial image should contain such calibration tiles to account for fluctuations in the illumination conditions during image acquisition. Since this setup is neither feasible nor possible for aerial imaging tasks in general, both data acquisition campaigns for the evaluation studies were performed under highly stable solar radiation conditions around solar noon, and flight time was kept as short as possible to minimize such influences (Fawcett & Anderson, 2019). The similar procedure and comparable results of Porto et al. (2020) confirm this approach. Moreover, more sophisticated calibration techniques, as postulated by Honkavaara et al. (2012) and Kizel et al. (2018), could be established to account for unstable illumination conditions as well as to perform a more robust calibration against external disturbances that influence the reflectance signal of the observed canopy surface (Honkavaara & Khoramshahi, 2018). Nevertheless, it is impossible to wait for optimal radiation weather, especially in PA or SF, and the agricultural areas to be monitored can only be covered by longer flight times. The larger these areas to be monitored, the more these effects must be accounted for.

In addition, it is desirable to automate the data processing as much as possible, which includes reflectance calibration so that the user does not have to spend significant time and effort but obtains data quickly for upcoming management decisions. For completeness, it remains to be mentioned that even under the best radiation weather conditions, slight fluctuations in illumination, imperceptible to the human eye, are still possible. These fluctuations are assumed to be negligible, but they can emerge practically unpredictable during flight and may lead to an undesirable degree of uncertainty in the reflectance data. Therefore, most commercial multispectral systems have an additional irradiance sensor that detects the current illumination conditions. Versions of such a sensor are also called down-welling light sensor (DLS) (MicaSense, 2020), incident light sensor (ILS) (MAIA, 2020; Tetracam, 2020), and sunshine sensor (Parrot, 2020). They work best when the sky is either wholly overcast or cloud-free.
In order to be able to effectively operate the VNIR/SWIR multispectral multi-camera system in unstable light conditions or for capturing more extensive areas, in the medium term, such an additional incident light measurement should be established. Experimental irradiance measurement systems for UAV imaging applications in the VNIR already exist (Arthur et al., 2014; Suomalainen et al., 2018). They consist exclusively of a spectrometer, which can potentially be adapted to the SWIR domain for use with the camera system prototype. Lightweight and miniaturized spectrometers in "fingertip size" (C12880MA, Hamamatsu Photonics, Hamamatsu City, Japan), which could be ideally used in this context, are unfortunately only available for the VNIR domain at the moment.
However, conventional SWIR-capable instruments add more weight and result in higher power consumption, thus shortening the UAV's flight time. Therefore, these reflectance correction measurements could initially be performed on the ground as an interim solution, since the experimental fields under investigation are still relatively small and can be covered in less than ten minutes. For this purpose, portable field spectrometers and pyrometers positioned on the ground near the observed area could be used (Arroyo-Mora et al., 2019). A more lightweight variant, close to the camera system during flight, could consist of InGaAs photodiodes spectrally matched to the filter wavebands used for the cameras. Here, InGaAs photodiodes with integrated FPIs (MEMS-FPI, Hamamatsu Photonics, Hamamatsu City, Japan) could facilitate this tuning of the desired wavelength without changing filter disks when changing the bandpass wavelength of a camera module.

6.2.3 Spectral Resolution and Bandwidth

The question arises whether a high amount of spectral information is reasonable and efficaciously applicable in agricultural vegetation monitoring, especially for PA applications to support management decisions. Compared to hyperspectral systems, multispectral multi-camera systems are characterized by the fact that the acquired two-dimensional image data can be processed directly in photogrammetry software. These systems need no additional data from high-precision INS to process the raw data further. However, the use of multi-camera systems results in a significantly smaller number of available spectral channels. Nevertheless, the sheer abundance of spectral information acquired by hyperspectral scanners is often an avoidable bottleneck in further processing and analysis of the data, primarily when specific research questions or use cases are being addressed.

Thenkabail et al. (2018) found that "an overwhelming proportion of the hyperspectral narrowbands can be redundant" and further identified 28 narrow wavelength bands from a literature review that are optimal for studying vegetation and agricultural crops. The number of these bands can be further reduced if one wants to observe application-specific properties, which rely on established wavelength combinations, so-called narrowband VIs.
Numerous VIs have been developed in recent years to help detect various vegetation features, such as biomass or canopy nitrogen (Tucker, 1979; Serrano et al., 2002). In such cases, a multispectral multi-camera system can be optimally adapted and tuned to these waveband combinations and easily operated on-board of a UAV if narrow filter bandwidths ($\leq$10 nm) can be realized (Hunt & Daughtry, 2018). However, this solution requires the ability to customize the system to the required application, which is not possible with commercially available multi-camera systems. In most cases, these multi-camera systems are self-contained with fully comprehensive workflows, from data acquisition to finished spectral products, ensuring easy operation, especially for non-expert users. In this way, extensive recalibrations of these systems, which are necessary when changing filters, should be avoided. However, recalibration makes sense in several years of device lifetime simply because of aging effects (Mamaghani & Salvaggio, 2019).
Furthermore, the full potential of the vegetation spectrum can only be exploited if such systems also provide spectral information from the shortwave infrared domain. In this respect, the newly developed camera system provides complete access to spectral adaptions and modifications. Integration of new spectral channels and corresponding system calibration is possible at any time, as chapters 3, 4, and 5 demonstrate. In this regard, for future studies, additional SWIR wavelengths should be integrated into the system—namely, those that are directly related to plant-bound nitrogen, such as wavelengths at 1510 nm and 1680 nm (Fourty et al., 1996). These bands allow, for example, the calculation of the normalized difference nitrogen index (NDNI) for better estimation of leaf nitrogen content (Serrano et al., 2002; Liang et al., 2018).
Multi-camera systems are mostly equipped with broadband spectral channels. Hyperspectral scanners, in contrast, provide narrow bandwidths $\leq$10 nm by design (Berger et al., 2020). However, a distinction must also be made between spectral sampling and the actual bandwidth of the sampled wavelengths, leading to a possible overlapping of spectral bands and thus spectral information in hyperspectral data (Liang, 2003a). Thenkabail et al. (2018) recommend a nominal bandwidth of 10 nm for hyperspectral systems, which makes it possible to achieve a good balance between sensor illumination and discrimination of individual vegetation features. If the filter bandwidths are too narrow, only a tiny amount of light will reach the individual pixels and will be increasingly dominated by sensor noise sources.
On the other hand, if the filter bandwidth is too broad, a superposition of many features is possible and can lead, for example, to a saturation phenomenon (Mutanga & Skidmore, 2004). As described in chapter 3, the self-developed multispectral system uses high-performance hybrid bandpass filters with an FWHM of 10 nm each to meet these requirements for detecting subtle spectral features. Filters with even narrower bandwidths and more precise center wavelengths can be provided by various manufacturers. However, such specificity may involve higher costs and lead times due to the custom production of these elements, so this trade-off must be considered.

In addition to the InGaAs camera modules for the VNIR/SWIR domain, with perspective, a camera module for the LWIR domain could also be integrated. This wavelength range (approximately 7.5 to 13.5 µm, see Figure 2.2) could then be used to analyze the thermal radiation emitted from vegetation canopies in conjunction with the passive narrowband multispectral data for pathogen detection (Hornero et al., 2021), water status and drought stress (Crusiol et al., 2020), and crop phenotyping (Maimaitijiang et al., 2017). These camera modules usually contain VOx-based microbolometers. Because of the particular thermistor-based sensor concept, calibration is moderately more complex, depending on the sensor module (Han et al., 2021). On the hardware and software side, this means only moderate integration effort. Like InGaAs sensors, these sensors have undergone significant technological progress and are also available in a convenient size for integration into UAVs, such as the radiometric Boson® 640 (Teledyne FLIR LLC, Wilsonville, OR, USA), made possible by the SWaP approach (Hagen, 2020).

6.3 Prospects for PA and SF applications

As mentioned in section 1.1, PA has a history of almost 40 years, and it has evolved only slowly in its early days, mainly due to technological constraints (Finger et al., 2019). On the other hand, socioeconomic motivations and dynamics also play a decisive role, which meanwhile have also become the focus of more scientific attention (Klerkx et al., 2019). For example, in the field of agriculture, it is easier for generations that have been socialized with modern technology to embrace the technological progress openly and to integrate it into their everyday working lives. Nevertheless, the available technologies must generate a direct added value in the form of higher profit, no matter how performant or inexpensive they are (Bucci et al., 2020). Otherwise, they will not even be implemented, or they will be quickly abandoned. However, achieving all of these demands a level of technology that is only beginning to pay off with the current (miniaturized) computing power, algorithms (machine learning), networking capabilities (5G), and high-precision positioning systems and automation (John Deere, 2022)—to name just the most important ones. All these information and communication technologies culminate in data-driven closed-loop agricultural management systems that rely primarily on spatially resolved sensor data on crop conditions from the field (Saiz-Rubio & Rovira-Más, 2020). Therefore, spectral data from optical instruments contribute to one of the essential building blocks of such management cycles. In this context, UAVs as airborne carrier platforms are an advantageous technology that is being intensively researched and, in some cases, already successfully implemented (Tsouros et al., 2019; Radoglou-Grammatikis et al., 2020).

In particular, UAV-based multispectral multi-camera systems are ideally suited for this purpose because of their ease of use and spatially high-resolution two-dimensional spectral image data. Practical management approaches in this regard have been investigated and elaborated, for example, by Thompson & Puntel (2020) or Barzin et al. (2020) for corn.

The concept of the multi-camera system prototype developed in this thesis fits well into such site-specific management workflows in PA or SF. It combines the advantages of commercially available multi-camera systems and extends the spectral range of the acquired spectral image data to the under-exploited SWIR domain, which contains essential spectral vegetation features.

It also allows for versatile adaptation to different applications through an exchangeable optical filter system for farming systems. Its modular design is not necessarily tied to a specific type of UAV or airborne platform in general. Still, it can also be adapted to other platforms like ground-based vehicles, such as tractors or field robots.
Furthermore, the application range can also be extended to other areas like for example forestry. Since the SWIR range is excellent for detecting vegetation moisture and thus drought stress, this camera system could be used for many forestry-specific applications, such as monitoring forest health with early detection of tree diseases or pest infestations (Ismail & Mutanga, 2011; Hornero et al., 2021; Poblete et al., 2021; Huo et al., 2021), monitoring forest fuel loading, detecting early forest fires (Allison et al., 2016),and identifying tree species (Näsi et al., 2016). Forsström et al. (2021) recommend integrating the SWIR domain to monitor the forest understory, which plays a key role in forest ecosystems.
In the future, however, the success and application range of UAV-based optical sensors in SF will also depend on the degree of automation that will be technically and legally possible in this area. Such semi- or fully automated services could be located at agricultural cooperatives or specialized firms. Nevertheless, other technologies are also in the starting phases in the field of agricultural vegetation monitoring and offer a potential competition to UAV-based systems, at least in commercial applications. Nanosatellites or CubeSats, for example, are becoming more and more established in monitoring vegetation (Maes & Steppe, 2019). However, the multi-camera system developed in this work could also be used in this application area with appropriate adaptations.

7 | Conclusion and Outlook

A sustainable agricultural sector can significantly mitigate current global threats ranging from resource scarcity to climate change, thus ensuring long-term food security for the world's population. Precision agriculture, which emerged in the 1980s with the dawn of digitization, is one such mitigation measure. This concept pursues the idea of breaking up the homogeneous treatment of agricultural land and instead establishing site-specific, heterogeneous managing practices according to actual demands. Having progressed slowly in recent decades, this concept is now evolving more quickly and is being taken further by more advanced information and communication technologies. As a result, precision agriculture is transforming into smart agriculture. These data-driven concepts highly relate to high-resolution timely and spatial information from within the field. Remotely sensed data can meet this high demand for field-level data. In addition to a variety of different sensor concepts, optical sensors have proven particularly successful for this task—especially multispectral multi-camera 2D systems carried by UAVs.

Overall, these versatile and partially highly integrated imaging systems have become an integral part of UAV-based vegetation monitoring and thus a means of choice to address agronomic research or agricultural applications in combination with UAVs in precision agriculture. However, the systems currently available, whether commercial or experimental, suffer from several shortcomings. The most important shortcoming is the limited spectral application range, spanning exclusively the VIS and NIR, which does not account for crucial spectral vegetation features in the SWIR domain directly linked to above-ground biomass, water content, and leaf chemicals like proteins and notably nitrogen. In this context, the multispectral multi-camera system prototype developed for this work solves this deficiency. The main feature of this camera system is the extended spectral range into the under-exploited SWIR domain to detect crucial and subtle spectral vegetation features for estimating important crop traits. The individual channels' spectral bandwidth is realized by narrow bandpass filters, with which VNIR camera systems are rarely, if ever, equipped. The SWIR domain was previously inaccessible with the current VNIR multi-camera technology, resulting in a quasi spectral gap in the SWIR. This development was only possible thanks to fast-evolving InGaAs sensor technology, leading to more suitable image sensors over the past years. Hybrid narrowband versions with high optical quality were chosen for the bandpass filters so that fine spectral features could still be detected, comparable to hyperspectral systems. This spectral granularity and the additional interchangeability of filters turn the camera system into a suitable tool for research applications.

The two field studies conducted in a permanent grassland trial and a winter wheat experiment on the non-destructive estimation of plant traits, such as fresh and dry biomass and nitrogen concentration using bivariate regression models, were positively evaluated with high accuracies.

The results provide initial starting points for further in-depth investigations in multi-temporal and multi-annual surveys, including additional wavelengths by adapting more bandpass filters for important spectral features, as well as more advanced analysis methods using machine learning techniques.

Over the course of this work, the camera system prototype was significantly optimized in terms of weight and dimensions. In addition, due to rapid advances in technology, the number of spectral channels can potentially be expanded by selecting newly available, more powerful camera modules, which offer four times the spatial resolution with significantly lower power and space requirements per channel. This improvement could further increase the spatial and spectral resolution, which is ideal for acquiring large amounts of spectral data for the foundation of management decisions in precision agriculture and smart farming applications.

This rapid technological development indicates further that the current potential in the area of sensor technology is not yet exhausted, and future developments will give rise to more sophisticated applications in PA. With the ever-advancing networking of sensors and their integration into location-specific management cycles for demand- and time-critical management decisions. Particularly with future autonomously operating aircraft carrier platforms, UAV-based VNIR/SWIR multispectral multi-camera technology could take a significant leap forward and gain even greater importance as a fundamental component in the essential building blocks of site-specific crop management circles or in environmental monitoring applications in general.

Furthermore, the evaluation of the camera system prototype carried out on two experimental agricultural sites for this work represents only one field of application. Due to the sensitivity to the moisture content of the vegetation, as a result of the water absorption in the SWIR, it also imposes the extension of the application spectrum to significant challenges in forestry or agro-silvo-pastoral systems. Given the potential information gain, both spectral and spatial, it is strongly recommended to intensively investigate the prototype camera system in these applications as well and to compare the results with studies already performed on a variety of scenarios, such as VNIR- or SWIR-based multi- or hyperspectral investigations.

8 | References

References for Chapters: 1, 2, 6 and 7.

Aasen, H. & Bareth, G. (2018). Spectral and 3D Nonspectral Approaches to Crop Trait Estimation Using Ground and UAV Sensing. *Hyperspectral Remote Sensing of Vegetation*, volume III Title: Biophysical and Biochemical Characterization and Plant Species Studies, 103–131. CRC Press Taylor & Francis Group, (second edition ed.). https://doi.org/10.1201/9780429431180-4

Aasen, H. & Bolten, A. (2017). Multi-temporal high-resolution imaging spectroscopy with hyperspectral 2D imagers – From theory to application. *Remote Sensing of Environment*, 205(September 2017), 374–389. https://doi.org/10.1016/j.rse.2017.10.043

Aasen, H., Burkart, A., Bolten, A., & Bareth, G. (2015). Generating 3D hyperspectral information with lightweight UAV snapshot cameras for vegetation monitoring: From camera calibration to quality assurance. *ISPRS Journal of Photogrammetry and Remote Sensing*, 108, 245–259. https://doi.org/10.1016/j.isprsjprs.2015.08.002

Aasen, H., Honkavaara, E., Lucieer, A., & Zarco-Tejada, P. J. (2018). Quantitative Remote Sensing at Ultra-High Resolution with UAV Spectroscopy: A Review of Sensor Technology, Measurement Procedures, and Data Correction Workflows. *Remote Sensing*, 10(7), 1091. https://doi.org/10.3390/rs10071091

Adão, T., Hruška, J., Pádua, L., Bessa, J., Peres, E., Morais, R., Sousa, J. J., Adão, T., Hruška, J., Pádua, L., Bessa, J., Peres, E., Morais, R., & Sousa, J. J. (2017). Hyperspectral Imaging: A Review on UAV-Based Sensors, Data Processing and Applications for Agriculture and Forestry. *Remote Sensing*, 9(11), 1110. https://doi.org/10.3390/rs9111110

Aday, S. & Aday, M. S. (2020). Impact of COVID-19 on the food supply chain. *Food Quality and Safety*, 4(4), 167–180. https://doi.org/10.1093/fqsafe/fyaa024

ADZ (2022). *Agricultural Systems of the Future*. https://www.agrarsysteme-der-zukunft.de/en/home. Last accessed on 14 January 2022.

Alavipanah, S. K., Matinfar, H. R., Rafiei Emam, A., Khodaei, K., Hadji Bagheri, R., & Yazdan Panah, A. (2010). Criteria of selecting satellite data for studying land resources. *Desert*, 15(2), 83–102. https://doi.org/10.22059/jdesert.2011.23005

Allied Vision (2022a). *Alvium 1800 C SWIR: High-performance CSI-2 SWIR camera module for embedded applications*. https://www.alliedvision.com/en/products/camera-series/alvium-1800-c-swir/. Last accessed on 17 January 2022.

Allied Vision (2022b). *STEP files for Allied Vision Alvium cameras*. https://www.alliedvision.com/en/support/alvium-step-file-toolbox/. Last accessed on 09 February 2022.

Allison, R. S., Johnston, J. M., Craig, G., & Jennings, S. (2016). Airborne Optical and Thermal Remote Sensing for Wildfire Detection and Monitoring. *Sensors*, 16(8), 1310. https://doi.org/10.3390/s16081310

Arroyo-Mora, J. P., Kalacska, M., Inamdar, D., Soffer, R., Lucanus, O., Gorman, J., Naprstek, T., Schaaf, E. S., Ifimov, G., Elmer, K., & Leblanc, G. (2019). Implementation of a UAV–Hyperspectral Pushbroom Imager for Ecological Monitoring. *Drones*, 3(1), 12. https://doi.org/10.3390/drones3010012

Arthur, A. M., Robinson, I., Rossini, M., Davis, N., & MacDonald, K. (2014). A dual-field-of-view spectrometer system for reflectance and fluorescence measuremnents (piccolo doppio) and corrrection of etaloning. 9.

Assmann, J. J., Kerby, J. T., Cunliffe, A. M., & Myers-Smith, I. H. (2018). Vegetation monitoring using multispectral sensors — best practices and lessons learned from high latitudes. *Journal of Unmanned Vehicle Systems*, 7(1), 54–75. https://doi.org/10.1139/juvs-2018-0018

ASTER (2021). *ASTER: Advanced Spaceborne Thermal Emission and Reflection Radiometer*. https://asterweb.jpl.nasa.gov/index.asp. Last accessed on 10 November 2021.

Atzberger, C. (2013). Advances in Remote Sensing of Agriculture: Context Description, Existing Operational Monitoring Systems and Major Information Needs. *Remote Sensing*, 5(2), 949–981. https://doi.org/10.3390/rs5020949

Baldridge, A., Hook, S., Grove, C., & Rivera, G. (2009). The ASTER spectral library version 2.0. *Remote Sensing of Environment*, 113(4), 711–715. https://doi.org/10.1016/j.rse.2008.11.007

Bareth, G., Bolten, A., & Bendig, J. (2011). Potentials for low-cost Mini-UAVs. *Proceedings on the Workshop of Remote Sensing Methods for Change Detection and Process Modelling*, 1–8. https://doi.org/10.5880/TR32DB.KGA92.2

Bareth, G. & Hütt, C. (2021). Upscaling and Validation of RTK-direct Georeferenced UAV-based RGB Image Data with Planet Imagery using Polygongrids for Pasture Monitoring. *The International Archives of the Photogrammetry, Remote Sensing and Spatial Information Sciences*, XLIII-B3-2021, 533–538. https://doi.org/10.5194/isprs-archives-XLIII-B3-2021-533-2021

Barzin, R., Pathak, R., Lotfi, H., Varco, J., & Bora, G. C. (2020). Use of UAS Multispectral Imagery at Different Physiological Stages for Yield Prediction and Input Resource Optimization in Corn. *Remote Sensing*, 12(15), 2392. https://doi.org/10.3390/rs12152392

Bayer, B. (1976). United States Patent 3971065: Colour Imaging Array.

Bendig, J., Bolten, A., & Bareth, G. (2012). Introducing a low-cost Mini-UAV for thermal- and multispectral-imaging. *International Archives of the Photogrammetry, Remote Sensing and Spatial Information Sciences - ISPRS Archives*, volume 39, 345–349.

Bendig, J., Yu, K., Aasen, H., Bolten, A., Bennertz, S., Broscheit, J., Gnyp, M. L., & Bareth, G. (2015). Combining UAV-based plant height from crop surface models, visible, and near infrared vegetation indices for biomass monitoring in barley. *International Journal of Applied Earth Observation and Geoinformation*, 39, 79–87. https://doi.org/10.1016/j.jag.2015.02.012

Berger, K., Verrelst, J., Féret, J.-B., Hank, T., Wocher, M., Mauser, W., & Camps-Valls, G. (2020a). Retrieval of aboveground crop nitrogen content with a hybrid machine learning method. *International Journal of Applied Earth Observation and Geoinformation*, 92, 102174. https://doi.org/10.1016/j.jag.2020.102174

Berger, K., Verrelst, J., Féret, J.-B., Wang, Z., Wocher, M., Strathmann, M., Danner, M., Mauser, W., & Hank, T. (2020b). Crop nitrogen monitoring: Recent progress and principal developments in the context of imaging spectroscopy missions. *Remote Sensing of Environment*, 242, 111758. https://doi.org/10.1016/j.rse.2020.111758

Berni, J., Zarco-Tejada, P., Suarez, L., & Fereres, E. (2009). Thermal and Narrowband Multispectral Remote Sensing for Vegetation Monitoring From an Unmanned Aerial Vehicle. *IEEE Transactions on Geoscience and Remote Sensing*, 47(3), 722–738. https://doi.org/10.1109/TGRS.2008.2010457

Bhan, R., Saxena, R., Jalwani, C., & Lomash, S. (2009). Uncooled infrared microbolometer arrays and their characterisation techniques. *Defence Science Journal*, 59(6), 580.

Bitarafan, M. & DeCorby, R. (2017). On-Chip High-Finesse Fabry-Perot Microcavities for Optical Sensing and Quantum Information. *Sensors*, 17(8), 1748. https://doi.org/10.3390/s17081748

Blanc, N., Giffard, P., Seitz, P., Buchschacher, P., Nguyen, V., & Hoheisel, M. (2009). Semiconductor Image Sensing. *More than Moore: Creating High Value Micro/Nanoelectronics Systems*, 239–278. Springer US. https://doi.org/10.1007/978-0-387-75593-9_8

Bodkin, A., Sheinis, A., Norton, A., Daly, J., Beaven, S., & Weinheimer, J. (2009). Snapshot hyperspectral imaging: The hyperpixel array camera. *SPIE Defense, Security, and Sensing*, 73340H. https://doi.org/10.1117/12.818929

Born, M. & Wolf, E. (2019). Elements of the theory of interference and interferometers. *Principles of Optics: 60th Anniversary Edition*, 286–411. Cambridge University Press, (seventh ed.). https://doi.org/10.1017/9781108769914.010

Borra-Serrano, I., Swaef, T. D., Muylle, H., Nuyttens, D., Vangeyte, J., Mertens, K., Saeys, W., Somers, B., Roldán-Ruiz, I., & Lootens, P. (2019). Canopy height measurements and non-destructive biomass estimation of Lolium perenne swards using UAV imagery. *Grass and Forage Science*, 74(3), 356–369. https://doi.org/10.1111/gfs.12439

Braga, P., Crusiol, L. G. T., Nanni, M. R., Caranhato, A. L. H., Fuhrmann, M. B., Nepomuceno, A. L., Neumaier, N., Farias, J. R. B., Koltun, A., Gonçalves, L. S. A., & Mertz-Henning, L. M. (2021). Vegetation indices and NIR-SWIR spectral bands as a phenotyping tool for water status determination in soybean. *Precision Agriculture*, 22(1), 249–266. https://doi.org/10.1007/s11119-020-09740-4

Brew, A. N. & Neyland, H. M. (1980). Manual of photogrammetry. *Aerial Photography*, 279–303. American Society of Photogrammetry, Falls Church.

Broge, N. & Leblanc, E. (2001). Comparing prediction power and stability of broadband and hyperspectral vegetation indices for estimation of green leaf area index and canopy chlorophyll density. *Remote Sensing of Environment*, 76(2), 156–172. https://doi.org/10.1016/S0034-4257(00)00197-8

Bucci, G., Bentivoglio, D., Belletti, M., & Finco, A. (2020). Measuring a farm's profitability after adopting precision agriculture technologies: A case study from Italy. *ACTA IMEKO*, 9(3), 65–74. https://doi.org/10.21014/acta_imeko.v9i3.799

Buitrago, M. F., Skidmore, A. K., Groen, T. A., & Hecker, C. A. (2018). Connecting infrared spectra with plant traits to identify species. *ISPRS Journal of Photogrammetry and Remote Sensing*, 139, 183–200. https://doi.org/10.1016/j.isprsjprs.2018.03.013

Camino, C., González-Dugo, V., Hernández, P., Sillero, J., & Zarco-Tejada, P. J. (2018). Improved nitrogen retrievals with airborne-derived fluorescence and plant traits quantified from VNIR-SWIR hyperspectral imagery in the context of precision agriculture. *International Journal of Applied Earth Observation and Geoinformation*, 70(February), 105–117. https://doi.org/10.1016/j.jag.2018.04.013

Campbell, J. B. & Wynne, R. H. (2011). *Introduction to Remote Sensing, Fifth Edition*. Guilford Press.

Chawade, A., van Ham, J., Blomquist, H., Bagge, O., Alexandersson, E., & Ortiz, R. (2019). High-Throughput Field-Phenotyping Tools for Plant Breeding and Precision Agriculture. *Agronomy*, 9(5), 258. https://doi.org/10.3390/agronomy9050258

Chen, J.-R., Chao, P. C.-P., Tsai, C.-H., & Chen, W.-D. (2014). Design and realization of a high resolution (640 × 480) SWIR image acquisition system. *Microsystem Technologies*, 20(8), 1583–1595. https://doi.org/10.1007/s00542-014-2179-7

Cohen, Y. & Alchanatis, V. (2018). Spectral and spatial methods for hyperspectral and thermal image-analysis to estimate biophysical and biochemical properties of agricultural crops. *Biophysical and Biochemical Characterization and Plant Species Studies*, 73–101. CRC Press.

Collet, M. G. (1986). Solid-state image sensors. *Sensors and Actuators*, 10(3), 287–302. https://doi.org/10.1016/0250-6874(86)80051-8

Colomina, I. & Molina, P. (2014). Unmanned aerial systems for photogrammetry and remote sensing: A review. *ISPRS Journal of Photogrammetry and Remote Sensing*, 92, 79–97. https://doi.org/10.1016/j.isprsjprs.2014.02.013

Crusiol, L. G. T., Nanni, M. R., Furlanetto, R. H., Sibaldelli, R. N. R., Cezar, E., Mertz-Henning, L. M., Nepomuceno, A. L., Neumaier, N., & Farias, J. R. B. (2020). UAV-based thermal imaging in the assessment of water status of soybean plants. *International Journal of Remote Sensing*, 41(9), 3243–3265. https://doi.org/10.1080/01431161.2019.1673914

Curran, P. J. (1989). Remote sensing of foliar chemistry. *Remote Sensing of Environment*, 30(3), 271–278. https://doi.org/10.1016/0034-4257(89)90069-2

Cushing, D. (2011). *Enhanced Optical Filter Design*. Number v. PM 201 in SPIE. SPIE Press.

DAKIS (2022). *Digital Agricultural Knowledge and Information System*. https://adz-dakis.com/. Last accessed on 14 January 2022.

Dandin, M., Abshire, P., & Smela, E. (2007). Optical filtering technologies for integrated fluorescence sensors. *Lab on a Chip*, 7(8), 955. https://doi.org/10.1039/b704008c

Delamere, M. (2014). Low-noise small SWaP SWIR imagers for light-starved high-sensitivity applications. 9070, 907006. https://doi.org/10.1117/12.2057493

Deng, L., Mao, Z., Li, X., Hu, Z., Duan, F., & Yan, Y. (2018). UAV-based multispectral remote sensing for precision agriculture: A comparison between different cameras. *ISPRS Journal of Photogrammetry and Remote Sensing*, 146, 124–136. https://doi.org/10.1016/j.isprsjprs.2018.09.008

DJI (2021). *P4 Multispectral - DJI*. https://www.dji.com/de/p4-multispectral. Last accessed on 05 February 2022.

DJI (2022). *DJI - Offizielle Webseite*. https://www.dji.com/de. Last accessed on 18 January 2022.

Dubbini, M., Pezzuolo, A., De Giglio, M., Gattelli, M., Curzio, L., Covi, D., Yezekyan, T., & Marinello, F. (2017). Last generation instrument for agriculture multispectral data collection. *Agricultural Engineering International: CIGR Journal*, 19(1), 87–93.

Durini, D. & Arutinov, D. (2020). 1 - Fundamental principles of photosensing. *High Performance Silicon Imaging (Second Edition)*, Woodhead Publishing Series in Electronic and Optical Materials, 3–24. Woodhead Publishing, (second edition ed.). https://doi.org/10.1016/B978-0-08-102434-8.00001-5

Earth Observing System (2021). *Panchromatic Imagery And Its Band Combination In Remote Sensing*. https://eos.com/make-an-analysis/panchromatic/. Last accessed on 05 January 2022.

Edmund Optics (2022). *Optiken - Bildverarbeitung - Photonik - Optomechanik - Laser | Edmund Optics*. https://www.edmundoptics.de/. Last accessed on 05 February 2022.

Emerson, G. P. & Little, S. J. (1999). Flat-Fielding for CCDs in AAVSO Observations, I. *Journal of the American Association of Variable Star Observers (JAAVSO)*, 27(1), 49–54.

Emilien, A.-V., Thomas, C., & Thomas, H. (2021). UAV & satellite synergies for optical remote sensing applications: A literature review. *Science of Remote Sensing*, 3, 100019. https://doi.org/10.1016/j.srs.2021.100019

EnMap (2022). *Mission - EnMAP*. https://www.enmap.org/mission/. Last accessed on 10 January 2022.

ESA (2017). *User Guides - Sentinel-2 MSI - Sentinel Online - Sentinel Online*. https://sentinel.esa.int/web/sentinel/user-guides/sentinel-2-msi. Last accessed on 04 October 2021.

Esposito, M., Crimaldi, M., Cirillo, V., Sarghini, F., & Maggio, A. (2021). Drone and sensor technology for sustainable weed management: A review. *Chemical and Biological Technologies in Agriculture*, 8(1), 18. https://doi.org/10.1186/s40538-021-00217-8

Fawcett, D. & Anderson, K. (2019). Investigating impacts of calibration methodology and irradiance variations on lightweight drone-based sensor derived surface reflectance products. *Remote Sensing for Agriculture, Ecosystems, and Hydrology XXI*, 13. https://doi.org/10.1117/12.2533106

Ferrier, S. (2020). Prioritizing where to restore Earth's ecosystems. *Nature*, 586(7831), 680–681. https://doi.org/10.1038/d41586-020-02750-2

Finger, R., Swinton, S. M., El Benni, N., & Walter, A. (2019). Precision Farming at the Nexus of Agricultural Production and the Environment. *Annual Review of Resource Economics*, 11(1), 313–335. https://doi.org/10.1146/annurev-resource-100518-093929

Foley, J. A., Ramankutty, N., Brauman, K. A., Cassidy, E. S., Gerber, J. S., Johnston, M., Mueller, N. D., O'Connell, C., Ray, D. K., West, P. C., Balzer, C., Bennett, E. M., Carpenter, S. R., Hill, J., Monfreda, C., Polasky, S., Rockström, J., Sheehan, J., Siebert, S., Tilman, D., & Zaks, D. P. M. (2011). Solutions for a cultivated planet. *Nature*, 478(7369), 337–342. https://doi.org/10.1038/nature10452

Forsström, P. R., Juola, J., & Rautiainen, M. (2021). Relationships between understory spectra and fractional cover in northern European boreal forests. *Agricultural and Forest Meteorology*, 308–309, 108604. https://doi.org/10.1016/j.agrformet.2021.108604

Fourty, T., Baret, F., Jacquemoud, S., Schmuck, G., & Verdebout, J. (1996). Leaf optical properties with explicit description of its biochemical composition: Direct and inverse problems. *Remote Sensing of Environment*, 56(2), 104–117. https://doi.org/10.1016/0034-4257(95)00234-0

Fowler, J. E. (2014). Compressive pushbroom and whiskbroom sensing for hyperspectral remote-sensing imaging. *2014 IEEE International Conference on Image Processing (ICIP)*, 684–688. https://doi.org/10.1109/ICIP.2014.7025137

Fussell, J., Rundquist, D., & Harrington, J. (1986). On defining remote sensing. *Photogrammetric Engineering and Remote Sensing*, 52(9), 1507–1511.

Geipel, J., Link, J., Wirwahn, J., & Claupein, W. (2016). A Programmable Aerial Multispectral Camera System for In-Season Crop Biomass and Nitrogen Content Estimation. *Agriculture*, 6(1), 4. https://doi.org/10.3390/agriculture6010004

Gholizadeh, A., Saberioon, M., Borůvka, L., Wayayok, A., & Mohd Soom, M. A. (2017). Leaf chlorophyll and nitrogen dynamics and their relationship to lowland rice yield for site-specific paddy management. *Information Processing in Agriculture*, 4(4), 259–268. https://doi.org/10.1016/j.inpa.2017.08.002

Gitay, H., Brown, S., Easterling, W., & Jallow, B. (2001). Chapter 5: Ecosystems and Their Goods and Services. *Climate Change 2001: Impacts, Adaptation, and Vulnerability*, 108. Cambridge University Press.

Gnyp, M., Bareth, G., Li, F., Lenz-Wiedemann, V. I., Koppe, W., Miao, Y., Hennig, S. D., Jia, L., Laudien, R., Chen, X., & Zhang, F. (2014a). Development and implementation of a multiscale biomass model using hyperspectral vegetation indices for winter wheat in the North China Plain. *International Journal of Applied Earth Observation and Geoinformation*, 33, 232–242. https://doi.org/10.1016/j.jag.2014.05.006

Gnyp, M. L., Miao, Y., Yuan, F., Ustin, S. L., Yu, K., Yao, Y., Huang, S., & Bareth, G. (2014b). Hyperspectral canopy sensing of paddy rice aboveground biomass at different growth stages. *Field Crops Research*, 155, 42–55. https://doi.org/10.1016/j.fcr.2013.09.023

Godfray, H. C. J., Beddington, J. R., Crute, I. R., Haddad, L., Lawrence, D., Muir, J. F., Pretty, J., Robinson, S., Thomas, S. M., & Toulmin, C. (2010). Food Security: The Challenge of Feeding 9 Billion People. *Science*, 327(5967), 812–818. https://doi.org/10.1126/science.1185383

Goesele, M., Snavely, N., Curless, B., Hoppe, H., & Seitz, S. M. (2007). Multi-View Stereo for Community Photo Collections. *2007 IEEE 11th International Conference on Computer Vision*, 1–8. https://doi.org/10.1109/ICCV.2007.4408933

Goldstein, N., Wiggins, R., Woodman, P., Saleh, M., Nakanishi, K., Fox, M. E., Tannian, B. E., Ziph-Schatzberg, L., & Soletski, P. (2018). Compact visible to extended-SWIR hyperspectral sensor for unmanned aircraft systems (UAS). *Algorithms and Technologies for Multispectral, Hyperspectral, and Ultraspectral Imagery XXIV*, 52. https://doi.org/10.1117/12.2305615

Goossens, S., Navickaite, G., Monasterio, C., Gupta, S., Piqueras, J. J., Pérez, R., Burwell, G., Nikitskiy, I., Lasanta, T., Galán, T., Puma, E., Centeno, A., Pesquera, A., Zurutuza, A., Konstantatos, G., & Koppens, F. (2017). Broadband image sensor array based on graphene–CMOS integration. *Nature Photonics*, 11(6), 366–371. https://doi.org/10.1038/nphoton.2017.75

Goossens, T., Geelen, B., Lambrechts, A., & Van Hoof, C. (2019). Vignetted-aperture correction for spectral cameras with integrated thin-film Fabry-P\'erot filters. *Applied Optics*, 58(7), 1789. https://doi.org/10.1364/AO.58.001789

Goossens, T. & Van Hoof, C. (2019). Exit pupil localization to correct spectral shift in thin-film Fabry-Perot spectral cameras. *OSA Continuum*, 2(7), 2217. https://doi.org/10.1364/OSAC.2.002217

Goward, S. N. (1985). Shortwave infrared detection of vegetation. *Advances in Space Research*, 5(5), 41–50. https://doi.org/10.1016/0273-1177(85)90255-8

Grant, B. G. (2016). *Getting Started with UAV Imaging Systems: A Radiometric Guide*. Spie Press Book. dx.doi.org/10.1117/2.2201704.01

GreenGrass (2022). *Neue Perspektiven einer innovativen Weidehaltung für mehr Nachhaltigkeit*. https://www.greengrass-project.de/. Last accessed on 14 January 2022.

Gupta, N., Ashe, P. R., & Tan, S. (2010). A Miniature Snapshot Multispectral Imager. 7660, 76602G–76602G–12. https://doi.org/10.1117/12.852661

Hagen, N. (2020). Dynamic radiometric calibration and radiometric matching of multiple microbolometer detector arrays. *Proc.SPIE*, volume 11502. https://doi.org/10.1117/12.2567811

Hagen, N. & Kudenov, M. W. (2013). Review of snapshot spectral imaging technologies. *Optical Engineering*, 52(9), 090901. https://doi.org/10.1117/1.OE.52.9.090901

Hambrecht, L., Brown, R. P., Piel, A. K., & Wich, S. A. (2019). Detecting 'poachers' with drones: Factors influencing the probability of detection with TIR and RGB imaging in miombo woodlands, Tanzania. *Biological Conservation*, 233, 109–117. https://doi.org/10.1016/j.biocon.2019.02.017

Han, L., Yang, G., Dai, H., Xu, B., Yang, H., Feng, H., Li, Z., & Yang, X. (2019). Modeling maize above-ground biomass based on machine learning approaches using UAV remote-sensing data. *Plant Methods*, 15(1), 10. https://doi.org/10.1186/s13007-019-0394-z

Han, Y., Tarakey, B. A., Hong, S.-J., Kim, S.-Y., Kim, E., Lee, C.-H., & Kim, G. (2021). Calibration and Image Processing of Aerial Thermal Image for UAV Application in Crop Water Stress Estimation. *Journal of Sensors*, 2021, e5537795. https://doi.org/10.1155/2021/5537795

Hank, T. B., Berger, K., Bach, H., Clevers, J. G. P. W., Gitelson, A., Zarco-Tejada, P., & Mauser, W. (2019). Spaceborne Imaging Spectroscopy for Sustainable Agriculture: Contributions and Challenges. *Surveys in Geophysics*, 40(3), 515–551. https://doi.org/10.1007/s10712-018-9492-0

Hansen, M. P. & Malchow, D. S. (2008). Overview of SWIR detectors, cameras, and applications. 6939, 69390I. https://doi.org/10.1117/12.777776

Harwin, S. & Lucieer, A. (2012). Assessing the Accuracy of Georeferenced Point Clouds Produced via Multi-View Stereopsis from Unmanned Aerial Vehicle (UAV) Imagery. *Remote Sensing*, 4(6), 1573–1599. https://doi.org/10.3390/rs4061573

Hecht, E. (2018). *Optik*. De Gruyter. https://doi.org/doi:10.1515/9783110526653

Herrmann, I., Karnieli, A., Bonfil, D. J., Cohen, Y., & Alchanatis, V. (2010). SWIR-based spectral indices for assessing nitrogen content in potato fields. *International Journal of Remote Sensing*, 31(19), 5127–5143. https://doi.org/10.1080/01431160903283892

Honkavaara, E., Eskelinen, M. A., Pölönen, I., Saari, H., Ojanen, H., Mannila, R., Holmlund, C., Hakala, T., Litkey, P., Rosnell, T., Viljanen, N., & Pulkkanen, M. (2016). Remote Sensing of 3-D Geometry and Surface Moisture of a Peat Production Area Using Hyperspectral Frame Cameras in Visible to Short-Wave Infrared Spectral Ranges Onboard a Small Unmanned Airborne Vehicle (UAV). *IEEE Transactions on Geoscience and Remote Sensing*, 54(9), 5440–5454. https://doi.org/10.1109/TGRS.2016.2565471

Honkavaara, E., Hakala, T., Saari, H., Markelin, L., Mäkynen, J., & Rosnell, T. (2012). A process for radiometric correction of UAV image blocks. *Photogrammetrie, Fernerkundung, Geoinformation*, (2), 115–127. https://doi.org/10.1127/1432-8364/2012/0106

Honkavaara, E. & Khoramshahi, E. (2018). Radiometric Correction of Close-Range Spectral Image Blocks Captured Using an Unmanned Aerial Vehicle with a Radiometric Block Adjustment. *Remote Sensing*, 10(2), 256. https://doi.org/10.3390/rs10020256

Hornero, A., Zarco-Tejada, P. J., Quero, J. L., North, P. R. J., Ruiz-Gómez, F. J., Sánchez-Cuesta, R., & Hernandez-Clemente, R. (2021). Modelling hyperspectral- and thermal-based plant traits for the early detection of Phytophthora-induced symptoms in oak decline. *Remote Sensing of Environment*, 263, 112570. https://doi.org/10.1016/j.rse.2021.112570

Hunt, E. R. & Daughtry, C. S. T. (2018). What good are unmanned aircraft systems for agricultural remote sensing and precision agriculture? *International Journal of Remote Sensing*, 39(15-16), 5345–5376. https://doi.org/10.1080/01431161.2017.1410300

Hunt, E. R. & Rock, B. N. (1989). Detection of changes in leaf water content using Near- and Middle-Infrared reflectances. *Remote Sensing of Environment*, 30(1), 43–54. https://doi.org/10.1016/0034-4257(89)90046-1

Huo, L., Persson, H. J., & Lindberg, E. (2021). Early detection of forest stress from European spruce bark beetle attack, and a new vegetation index: Normalized distance red & SWIR (NDRS). *Remote Sensing of Environment*, 255, 112240. https://doi.org/10.1016/j.rse.2020.112240

Hwang, T.-L., Schwarz, S. E., & Rutledge, D. B. (1979). Microbolometers for infrared detection. *Applied Physics Letters*, 34(11), 773–776. https://doi.org/10.1063/1.90669

Inoue, Y. (2020). Satellite- and drone-based remote sensing of crops and soils for smart farming – a review. *Soil Science and Plant Nutrition*, 66(6), 798–810. https://doi.org/10.1080/00380768.2020.1738899

Inoue, Y., Darvishzadeh, R., & Skidmore, A. (2018). Hyperspectral assessment of ecophysiological functioning for diagnostics of crops and vegetation. *Biophysical and Biochemical Characterization and Plant Species Studies*, 25–71. CRC Press.

INTRA (2022). *Groupe Intra : ACCUEIL*. https://www.groupe-intra.com/eng. Last accessed on 18 January 2022.

Iqbal, F., Lucieer, A., & Barry, K. (2018). Simplified radiometric calibration for UAS-mounted multispectral sensor. *European Journal of Remote Sensing*, 51(1), 301–313. https://doi.org/10.1080/22797254.2018.1432293

Ismail, R. & Mutanga, O. (2011). Discriminating the early stages of Sirex noctilio infestation using classification tree ensembles and shortwave infrared bands. *International Journal of Remote Sensing*, 32(15), 4249–4266. https://doi.org/10.1080/01431161.2010.486413

Jaakkola, A., Hyyppä, J., Kukko, A., Yu, X., Kaartinen, H., Lehtomäki, M., & Lin, Y. (2010). A low-cost multi-sensoral mobile mapping system and its feasibility for tree measurements. *ISPRS Journal of Photogrammetry and Remote Sensing*, 65(6), 514–522. https://doi.org/10.1016/j.isprsjprs.2010.08.002

Jackson, R. D. & Huete, A. R. (1991). Interpreting vegetation indices. *Preventive Veterinary Medicine*, 11(3), 185–200. https://doi.org/10.1016/S0167-5877(05)80004-2

Janesick, J. R. (2007). *Photon Transfer: DN → [Lambda]*. Number 170 in SPIE PM. SPIE.

Jenal, A., Bareth, G., Bolten, A., Kneer, C., Weber, I., & Bongartz, J. (2019). Development of a VNIR/SWIR Multispectral Imaging System for Vegetation Monitoring with Unmanned Aerial Vehicles. *Sensors*, 19(24), 5507. https://doi.org/10.3390/s19245507

Jenal, A., Hüging, H., Ahrends, H. E., Bolten, A., Bongartz, J., & Bareth, G. (2021). Investigating the Potential of a Newly Developed UAV-Mounted VNIR/SWIR Imaging System for Monitoring Crop Traits—A Case Study for Winter Wheat. *Remote Sensing*, 13(9), 1697. https://doi.org/10.3390/rs13091697

Jenal, A., Kneer, C., Weber, I., Asgari, M., Knieps, M., & Bongartz, J. (2022). An Adaptive Sensor Framework for Gyrocopter-Based Optical Remote Sensing: Introduction and Applications. *PFG – Journal of Photogrammetry, Remote Sensing and Geoinformation Science*. https://doi.org/10.1007/s41064-021-00187-4

Jenal, A., Lussem, U., Bolten, A., Gnyp, M. L., Schellberg, J., Jasper, J., Bongartz, J., & Bareth, G. (2020). Investigating the Potential of a Newly Developed UAV-based VNIR/SWIR Imaging System for Forage Mass Monitoring. *PFG – Journal of Photogrammetry, Remote Sensing and Geoinformation Science*, 88(5), 493–507. https://doi.org/10.1007/s41064-020-00128-7

Jiang, S., Jiang, C., & Jiang, W. (2020). Efficient structure from motion for large-scale UAV images: A review and a comparison of SfM tools. *ISPRS Journal of Photogrammetry and Remote Sensing*, 167, 230–251. https://doi.org/10.1016/j.isprsjprs.2020.04.016

John Deere (2022). *John Deere Reveals Fully Autonomous Tractor at CES 2022*. https://www.deere.com/en/news/all-news/autonomous-tractor-reveal/. Last accessed on 13 January 2022.

Jones, H. G. (2010). *Physicochemical and Environmental Plant Physiology. By Park S. Nobel.* (fourth ed.), volume 46. Academic Press. https://doi.org/10.1017/S0014479709990950

Jones, H. G. & Vaughan, R. A. (2010). *Remote Sensing of Vegetation: Principles, Techniques, and Applications*. Oxford university press. https://global.oup.com/academic/product/remote-sensing-of-vegetation-9780199207794?q=remote%20sensing&lang=en&cc=de#

Jones, H. P., Jones, P. C., Barbier, E. B., Blackburn, R. C., Rey Benayas, J. M., Holl, K. D., McCrackin, M., Meli, P., Montoya, D., & Mateos, D. M. (2018). Restoration and repair of Earth's damaged ecosystems. *Proceedings of the Royal Society B: Biological Sciences*, 285(1873), 20172577. https://doi.org/10.1098/rspb.2017.2577

Joseph, G. (2020). How to Specify an Electro-optical Earth Observation Camera? A Review of the Terminologies Used and its Interpretation. *Journal of the Indian Society of Remote Sensing*, 48(2), 171–180. https://doi.org/10.1007/s12524-020-01105-8

Kandemir, T., Schuster, M. E., Senyshyn, A., Behrens, M., & Schlögl, R. (2013). The Haber–Bosch Process Revisited: On the Real Structure and Stability of "Ammonia Iron" under Working Conditions. *Angewandte Chemie International Edition*, 52(48), 12723–12726. https://doi.org/10.1002/anie.201305812

Kandylakis, Z., Falagas, A., Karakizi, C., & Karantzalos, K. (2020). Water Stress Estimation in Vineyards from Aerial SWIR and Multispectral UAV Data. *Remote Sensing*, 12(15), 2499. https://doi.org/10.3390/rs12152499

Khosla, R. (2010). Precision agriculture: Challenges and opportunities in a flat world. *19th World Congress of Soil Science, Soil Solutions for a Changing World, Brisbane, Australia*.

Kizel, F., Benediktsson, J. A., Bruzzone, L., Pedersen, G. B. M., Vilmundardóttir, O. K., & Falco, N. (2018). Simultaneous and Constrained Calibration of Multiple Hyperspectral Images Through a New Generalized Empirical Line Model. *IEEE Journal of Selected Topics in Applied Earth Observations and Remote Sensing*, 11(6), 2047–2058. https://doi.org/10.1109/JSTARS.2018.2804666

Klerkx, L., Jakku, E., & Labarthe, P. (2019). A review of social science on digital agriculture, smart farming and agriculture 4.0: New contributions and a future research agenda. *NJAS - Wageningen Journal of Life Sciences*, 90–91, 100315. https://doi.org/10.1016/j.njas.2019.100315

Knox, N. M., Skidmore, A. K., Schlerf, M., de Boer, W. F., van Wieren, S. E., van der Waal, C., Prins, H. H. T., & Slotow, R. (2010). Nitrogen prediction in grasses: Effect of bandwidth and plant material state on absorption feature selection. *International Journal of Remote Sensing*, 31(3), 691–704. https://doi.org/10.1080/01431160902895480

Koch, B. & Khosla, R. (2003). The Role of Precision Agriculture in Cropping Systems. *Journal of Crop Production*, 9(1-2), 361–381. https://doi.org/10.1300/J144v09n01_02

Kokka, A., Pulli, T., Honkavaara, E., Markelin, L., Kärhä, P., & Ikonen, E. (2019). Flat-field calibration method for hyperspectral frame cameras. *Metrologia*, 56(5), 055001. https://doi.org/10.1088/1681-7575/ab3261

Koppal, S. J. (2014). Lambertian reflectance. *Computer Vision: A Reference Guide*, 441–443. Springer US. https://doi.org/10.1007/978-0-387-31439-6_534

Koppe, W., Gnyp, M. L., Hennig, S. D., Li, F., Miao, Y., Chen, X., Jia, L., & Bareth, G. (2012). Multi-Temporal Hyperspectral and Radar Remote Sensing for Estimating Winter Wheat Biomass in the North China Plain. *Photogrammetrie - Fernerkundung - Geoinformation*, 2012(3), 281–298. https://doi.org/10.1127/1432-8364/2012/0117

Koppe, W., Li, F., Gnyp, M. L., Miao, Y., Jia, L., Chen, X., Zhang, F., & Bareth, G. (2010). Evaluating Multispectral and Hyperspectral Satellite Remote Sensing Data for Estimating Winter Wheat Growth Parameters at Regional Scale in the North China Plain. *Photogrammetrie - Fernerkundung - Geoinformation*, 2010(3), 167–178. https://doi.org/10.1127/1432-8364/2010/0047

Kowa (2022). *CAD data LM12HC-SW | 1" 12mm SWIR C-Mount Lens*. https://www.kowa-lenses.com/en/lm12hc-sw-industrial-lens-c-mount. Last accessed on 09 February 2022.

Kuester, M. (2016). Radiometric use of worldview-3 imagery. *DigitalGlobe: Longmont, CO, USA*. https://dg-cms-uploads-production.s3.amazonaws.com/uploads/document/file/207/Radiometric_Use_of_WorldView-3_v2.pdf

Kumar, L., Schmidt, K., Dury, S., & Skidmore, A. (2001). Imaging Spectrometry and Vegetation Science. *Imaging Spectrometry: Basic Principles and Prospective Applications*, Remote Sensing and Digital Image Processing, 111–155. Springer Netherlands. https://doi.org/10.1007/978-0-306-47578-8_5

Laffly, D. (2020). A Brief History of Remote Sensing. *TORUS 2 – Toward an Open Resource Using Services*, 1–21. Wiley, (first ed.). https://doi.org/10.1002/9781119720553.ch1

Landsat (2021). *Landsat Satellite Missions | U.S. Geological Survey*. https://www.usgs.gov/landsat-missions/landsat-satellite-missions

Langguth, F. & Goesele, M. (2014). Irradiance. *Computer Vision: A Reference Guide*, 428–429. Springer US. https://doi.org/10.1007/978-0-387-31439-6_527

Lassaletta, L., Billen, G., Grizzetti, B., Anglade, J., & Garnier, J. (2014). 50 year trends in nitrogen use efficiency of world cropping systems: The relationship between yield and nitrogen input to cropland. *Environmental Research Letters*, 9(10), 105011. https://doi.org/10.1088/1748-9326/9/10/105011

Lenton, T. M. (2011). Early warning of climate tipping points. *Nature Climate Change*, 1(4), 201–209. https://doi.org/10.1038/nclimate1143

Lenton, T. M., Rockström, J., Gaffney, O., Rahmstorf, S., Richardson, K., Steffen, W., & Schellnhuber, H. J. (2019). Climate tipping points — too risky to bet against. *Nature*, 575(7784), 592–595. https://doi.org/10.1038/d41586-019-03595-0

Li, D., Watson, C. J., Yan, M. J., Lalor, S., Rafique, R., Hyde, B., Lanigan, G., Richards, K. G., Holden, N. M., & Humphreys, J. (2013). A review of nitrous oxide mitigation by farm nitrogen management in temperate grassland-based agriculture. *Journal of Environmental Management*, 128, 893–903. https://doi.org/10.1016/j.jenvman.2013.06.026

Li, F., Miao, Y., Hennig, S. D., Gnyp, M. L., Chen, X., Jia, L., & Bareth, G. (2010). Evaluating hyperspectral vegetation indices for estimating nitrogen concentration of winter wheat at different growth stages. *Precision Agriculture*, 11(4), 335–357. https://doi.org/10.1007/s11119-010-9165-6

Liaghat, S. & Balasundram, S. (2010). A Review: The Role of Remote Sensing in Precision Agriculture. *American Journal of Agricultural and Biological Sciences*, 5(1), 50–55. https://doi.org/10.3844/ajabssp.2010.50.55

Liang, L., Di, L., Huang, T., Wang, J., Lin, L., Wang, L., & Yang, M. (2018). Estimation of Leaf Nitrogen Content in Wheat Using New Hyperspectral Indices and a Random Forest Regression Algorithm. *Remote Sensing*, 10(12), 1940. https://doi.org/10.3390/rs10121940

Liang, S. (2003a). Estimation of surface radiation budget: II. Longwave. *Quantitative Remote Sensing of Land Surfaces*, 345–397. John Wiley & Sons, Ltd. https://doi.org/10.1002/047172372X.ch10

Liang, S. (2003b). Introduction. *Quantitative Remote Sensing of Land Surfaces*, 1–24. John Wiley & Sons, Ltd. https://doi.org/10.1002/047172372X.ch1

Liang, S. (2004). *Quantitative Remote Sensing of Land Surfaces*. Wiley Series in Remote Sensing. Wiley-Interscience.

Liu, C., Guo, J., Yu, L., Li, J., Zhang, M., Li, H., Shi, Y., & Dai, D. (2021). Silicon/2D-material photodetectors: From near-infrared to mid-infrared. *Light: Science & Applications*, 10(1), 123. https://doi.org/10.1038/s41377-021-00551-4

Lowder, S. K., Skoet, J., & Raney, T. (2016). The Number, Size, and Distribution of Farms, Smallholder Farms, and Family Farms Worldwide. *World Development*, 87, 16–29. https://doi.org/10.1016/j.worlddev.2015.10.041

Lowe, D. G. (1999). Object recognition from local scale-invariant features. *Proceedings of the Seventh IEEE International Conference on Computer Vision*, volume 2, 1150–1157 vol.2. https://doi.org/10.1109/ICCV.1999.790410

Lukas, V., Novák, J., Neudert, L., Svobodova, I., Rodriguez-Moreno, F., Edrees, M., & Kren, J. (2016). The Combination of UAV Survey and Landsat Imagery for Monitoring of Crop Vigor in Precision Agriculture. *ISPRS - International Archives of the Photogrammetry, Remote Sensing and Spatial Information Sciences*, XLI-B8, 953–957. https://doi.org/10.5194/isprsarchives-XLI-B8-953-2016

Lussem, U., Bolten, A., Gnyp, M. L., Jasper, J., & Bareth, G. (2018). EVALUATION OF RGB-BASED VEGETATION INDICES FROM UAV IMAGERY TO ESTIMATE FORAGE YIELD IN GRASSLAND. *ISPRS - International Archives of the Photogrammetry, Remote Sensing and Spatial Information Sciences*, XLII-3, 1215–1219. https://doi.org/10.5194/isprs-archives-XLII-3-1215-2018

Lussem, U., Bolten, A., Menne, J., Gnyp, M. L., & Bareth, G. (2019). ULTRA-HIGH SPATIAL RESOLUTION UAV-BASED IMAGERY TO PREDICT BIOMASS IN TEMPERATE GRASSLANDS. *ISPRS - International Archives of the Photogrammetry, Remote Sensing and Spatial Information Sciences*, volume XLII-2-W13, 443–447. https://doi.org/10.5194/isprs-archives-XLII-2-W13-443-2019

Macleod, H. A. (2010). *Thin-Film Optical Filters* (4. ed ed.). Series in Optics and Optoelectronics. CRC Press.

Madsen, C. K. & Zhao, J. H. (1999). *Optical Filter Design and Analysis*. Wiley Series in Microwave and Optical Engineering. John Wiley & Sons, Inc. https://doi.org/10.1002/0471213756

Maes, W. H. & Steppe, K. (2019). Perspectives for Remote Sensing with Unmanned Aerial Vehicles in Precision Agriculture. *Trends in Plant Science*, 24(2), 152–164. https://doi.org/10.1016/j.tplants.2018.11.007

MAIA (2019). *MAIA - the multispectral camera*. https://www.spectralcam.com/. Last accessed on 17 September 2019.

MAIA (2020). *ILS - Incident Light Sensor*. https://www.spectralcam.com/ils-irradiant-light-sensor/. Last accessed on 05 November 2021.

Maimaitijiang, M., Ghulam, A., Sidike, P., Hartling, S., Maimaitiyiming, M., Peterson, K., Shavers, E., Fishman, J., Peterson, J., Kadam, S., Burken, J., & Fritschi, F. (2017). Unmanned Aerial System (UAS)-based phenotyping of soybean using multi-sensor data fusion and extreme learning machine. *ISPRS Journal of Photogrammetry and Remote Sensing*, 134, 43–58. https://doi.org/10.1016/j.isprsjprs.2017.10.011

Maître, H. (2017). *From Photon to Pixel: The Digital Camera Handbook, Revised and Updated 2nd Edition* (first ed.). John Wiley & Sons, Ltd. https://doi.org/10.1002/9781119402442

Mäkynen, J., Holmlund, C., Saari, H., Ojala, K., & Antila, T. (2011). Unmanned aerial vehicle (UAV) operated megapixel spectral camera. *Electro-Optical Remote Sensing, Photonic Technologies, and Applications v*, volume 8186, 295–303. https://doi.org/10.1117/12.897712

Mamaghani, B. & Salvaggio, C. (2019). Multispectral Sensor Calibration and Characterization for sUAS Remote Sensing. *Sensors*, 19(20), 4453. https://doi.org/10.3390/s19204453

Mamaghani, B., Sasaki, G., Connal, R., Kha, K., Knappen, J., Hartzell, R., Marcellus, E., Bauch, T., Raqueno, N., & Salvaggio, C. (2018). An initial exploration of vicarious and in-scene calibration techniques for small unmanned aircraft systems. *arXiv:1804.09585 [eess]*. http://arxiv.org/abs/1804.09585

Mamaghani, B., Saunders, M. G., & Salvaggio, C. (2019). Inherent Reflectance Variability of Vegetation. *Agriculture*, 9(11), 246. https://doi.org/10.3390/agriculture9110246

Manfreda, S., McCabe, M. F., Miller, P. E., Lucas, R., Pajuelo Madrigal, V., Mallinis, G., Ben Dor, E., Helman, D., Estes, L., Ciraolo, G., Müllerová, J., Tauro, F., De Lima, M. I., De Lima, J. L. M. P., Maltese, A., Frances, F., Caylor, K., Kohv, M., Perks, M., Ruiz-Pérez, G., Su, Z., Vico, G., & Toth, B. (2018). On the Use of Unmanned Aerial Systems for Environmental Monitoring. *Remote Sensing*, 10(4), 641. https://doi.org/10.3390/rs10040641

Martin, G. (2015). High Performance SWIR Imaging Cameras. *Raptor Photonics White Paper*, Raptor Photonics Ltd.: Milbrook, Larne, UK.

Meshroom (2022). *AliceVision | Meshroom - 3D Reconstruction Software*. https://alicevision.org/#meshroom. Last accessed on 25 January 2022.

MicaSense (2019). *Home - MicaSense*. https://micasense.com/. Last accessed on 15 January 2019.

MicaSense (2020). *Light Sensors: The Basics (DLS and Sunshine Sensor)*. https://support.micasense.com/hc/en-us/articles/115002782008-Light-Sensors-the-Basics-DLS-and-Sunshine-Sensor-. Last accessed on 05 November 2021.

Microdrones (2022). *UAV/Drohnenlösungen in den Bereichen Kartierung, Luftinspektion und unbemannte Ladung*. https://www.microdrones.com/de/. Last accessed on 18 January 2022.

MK OktoXL 6S12 (2022). *MK Okto XL 6S12 [OKTO_XL_6S12]*. https://shop.mikrokopter.de/index.php?main_page=product_info&products_id=840. Last accessed on 04 February 2022.

MODIS (2021). *MODIS Web*. https://modis.gsfc.nasa.gov/about/. Last accessed on 10 November 2021.

Moore, G. K. (1979). What is a picture worth? A history of remote sensing / Quelle est la valeur d'une image? Un tour d'horizon de télédétection. *Hydrological Sciences Bulletin*, 24(4), 477–485. https://doi.org/10.1080/02626667909491887

Morales, A., Guerra, R., Horstrand, P., Diaz, M., Jimenez, A., Melian, J., Lopez, S., & Lopez, J. F. (2020). A Multispectral Camera Development: From the Prototype Assembly until Its Use in a UAV System. *Sensors*, 20(21), 6129. https://doi.org/10.3390/s20216129

Mulla, D. J. (2013). Twenty five years of remote sensing in precision agriculture: Key advances and remaining knowledge gaps. *Biosystems Engineering*, 114(4), 358–371. https://doi.org/10.1016/j.biosystemseng.2012.08.009

Mutanga, O. & Skidmore, A. K. (2004). Narrow band vegetation indices overcome the saturation problem in biomass estimation. *International Journal of Remote Sensing*, 25(19), 3999–4014. https://doi.org/10.1080/01431160310001654923

Näsi, R., Honkavaara, E., Tuominen, S., Saari, H., Pölönen, I., Hakala, T., Viljanen, N., Soukkamäki, J., Näkki, I., Ojanen, H., & Reinikainen, J. (2016). Uas based tree species identification using the novel fpi based hyperspectral cameras in visible, nir and swir spectral ranges. *International Archives of the Photogrammetry, Remote Sensing and Spatial Information Sciences - ISPRS Archives*, 2016-Janua(July), 1143–1148. https://doi.org/10.5194/isprsarchives-XLI-B1-1143-2016

Näsi, R., Viljanen, N., Kaivosoja, J., Alhonoja, K., Hakala, T., Markelin, L., & Honkavaara, E. (2018). Estimating Biomass and Nitrogen Amount of Barley and Grass Using UAV and Aircraft Based Spectral and Photogrammetric 3D Features. *Remote Sensing*, 10(7), 1082. https://doi.org/10.3390/rs10071082

nFrames (2022). *nFrames - nFrames – Empowering Photogrammetry*. https://www.nframes.com/. Last accessed on 19 January 2022.

Nocerino, E., Dubbini, M., Menna, F., Remondino, F., Gattelli, M., & Covi, D. (2017). Geometric calibration and radiometric correction of the maia multispectral camera. *ISPRS - International Archives of the Photogrammetry, Remote Sensing and Spatial Information Sciences*, XLII-3/W3, 149–156. https://doi.org/10.5194/isprs-archives-XLII-3-W3-149-2017

Osco, L. P., Junior, J. M., Ramos, A. P. M., Furuya, D. E. G., Santana, D. C., Teodoro, L. P. R., Gonçalves, W. N., Baio, F. H. R., Pistori, H., Junior, C. A. d. S., & Teodoro, P. E. (2020). Leaf Nitrogen Concentration and Plant Height Prediction for Maize Using UAV-Based Multispectral Imagery and Machine Learning Techniques. *Remote Sensing*, 12(19), 3237. https://doi.org/10.3390/rs12193237

Paiva, E., Rodas, J., Kali, Y., Lesme, F., Lesme, J. L., & Rodríguez-Piñeiro, J. (2021). A Review of UAVs Topologies and Control Techniques. *2021 IEEE International Conference on Automation/XXIV Congress of the Chilean Association of Automatic Control (ICA-ACCA)*, 1–6. https://doi.org/10.1109/ICAACCA51523.2021.9465186

Palmer, J. M. & Grant, B. G. (2009). *The Art of Radiometry*. SPIE press Bellingham. https://doi.org/10.1117/3.798237

Park, H., Kim, N., Park, S., & Choi, J. (2020). Sharpening of Worldview-3 Satellite Images by Generating Optimal High-Spatial-Resolution Images. *Applied Sciences*, 10(20), 7313. https://doi.org/10.3390/app10207313

Parrot (2020). *Parrot Sequoia+ multispectral camera for drone mapping*. https://www.pix4d.com/product/sequoia. Last accessed on 05 November 2021.

Paschotta, R. (2008). *Encyclopedia of Laser Physics and Technology*, volume 1. Wiley-vch.

Pelton, J. N., Madry, S., Camacho-Lara, S., Pelton, J. N., & University, I. S., editors (2013). *Handbook of Satellite Applications*. Springer Reference. Springer.

PhenoRob (2022). *PhenoRob - Robotics and Phenotyping for Sustainable Crop Production*. https://www.phenorob.de/. Last accessed on 14 January 2022.

Pix4D (2022). *Image acquisition*. https://support.pix4d.com/hc/en-us/articles/115002471546-Image-acquisition. Accessed on 15 January 2022.

Poblete, T., Navas-Cortes, J. A., Camino, C., Calderon, R., Hornero, A., Gonzalez-Dugo, V., Landa, B. B., & Zarco-Tejada, P. J. (2021). Discriminating Xylella fastidiosa from Verticillium dahliae infections in olive trees using thermal- and hyperspectral-based plant traits. *ISPRS Journal of Photogrammetry and Remote Sensing*, 179, 133–144. https://doi.org/10.1016/j.isprsjprs.2021.07.014

Porto, L. R., Imai, N. N., Berveglieri, A., Miyoshi, G. T., Moriya, É. A., Tommaselli, A. M., & Honkavaara, E. (2020). Comparison between two radiometric calibration methods applied to UAV multispectral images. *Image and Signal Processing for Remote Sensing XXVI*, 66. https://doi.org/10.1117/12.2579346

PRISMA (2022). *PRISMA (Hyperspectral) - eoPortal Directory*. https://earth.esa.int/web/eoportal/satellite-missions/p/prisma-hyperspectral. Last accessed on 10 January 2022.

QGIS (2022). *Welcome to the QGIS project! A Free and Open Source Geographic Information System*. https://www.qgis.org/en/site/index.html. Last accessed on 12 December 2022.

Radoglou-Grammatikis, P., Sarigiannidis, P., Lagkas, T., & Moscholios, I. (2020). A compilation of UAV applications for precision agriculture. *Computer Networks*, 172, 107148. https://doi.org/10.1016/j.comnet.2020.107148

Raptor Photonics (2019). *InGaAs SWIR VIS-SWIR SWaP 640 TEC-less Camera for Low Power Lost Cost OEMs*. https://www.raptorphotonics.com/products/owl-640-tecless-vis-swir-ingaas/. Last accessed on 20 January 2022.

Raptor Photonics (2022). *InGaAs SWIR VIS-SWIR SWaP 640 TEC-less camera for low power OEMs*. https://www.raptorphotonics.com/products/owl-640-m/. Last accessed on 20 January 2022.

Rasmussen, J., Azim, S., Boldsen, S. K., Nitschke, T., Jensen, S. M., Nielsen, J., & Christensen, S. (2021). The challenge of reproducing remote sensing data from satellites and unmanned aerial vehicles (UAVs) in the context of management zones and precision agriculture. *Precision Agriculture*, 22(3), 834–851. https://doi.org/10.1007/s11119-020-09759-7

Reay, D. (2015). *Nitrogen and Climate Change*. Palgrave Macmillan UK. https://doi.org/10.1057/9781137286963

Reay, D. S., Davidson, E. A., Smith, K. A., Smith, P., Melillo, J. M., Dentener, F., & Crutzen, P. J. (2012). Global agriculture and nitrous oxide emissions. *Nature Climate Change*, 2(6), 410–416. https://doi.org/10.1038/nclimate1458

Reichman, J. (2000). Handbook of optical filters for fluorescence microscopy. *Chroma Technology Corporation*.

Revill, A., Florence, A., MacArthur, A., Hoad, S., Rees, R., & Williams, M. (2020). Quantifying Uncertainty and Bridging the Scaling Gap in the Retrieval of Leaf Area Index by Coupling Sentinel-2 and UAV Observations. *Remote Sensing*, 12(11), 1843. https://doi.org/10.3390/rs12111843

Richards, J. & Jai, X. (2006). *Remote Sensing Digital Image Analysis*. Springer-Verlag. https://doi.org/10.1007/3-540-29711-1

Roberts, D. A., Roth, K. L., Wetherley, E. B., Meerdink, S. K., & Perroy, R. L. (2018). Hyperspectral Vegetation Indices. *Hyperspectral Indices and Image Classifications for Agriculture and Vegetation*, (Chapter Hyperspectral Vegetation Indices). CRC Press. https://doi.org/10.1201/9781315159331-1

Roberts, D. A., Ustin, S. L., Ogunjemiyo, S., Greenberg, J., Dobrowski, S. Z., Chen, J., & Hinckley, T. M. (2004). Spectral and Structural Measures of Northwest Forest Vegetation at Leaf to Landscape Scales. *Ecosystems*, 7(5). https://doi.org/10.1007/s10021-004-0144-5

Robertson, G. P., Paul, E. A., & Harwood, R. R. (2000). Greenhouse Gases in Intensive Agriculture: Contributions of Individual Gases to the Radiative Forcing of the Atmosphere. *Science*. https://doi.org/10.1126/science.289.5486.1922

Rogalski, A. (2002). Infrared detectors: An overview. *Infrared Physics & Technology*, 43(3), 187–210. https://doi.org/10.1016/S1350-4495(02)00140-8

Rogalski, A. (2004). Optical detectors for focal plane arrays. *Opto-Electronics Review*, 12(2), 221–245. https://optor.wat.edu.pl/12(2)221.pdf

Rogalski, A. (2005). HgCdTe infrared detector material: History, status and outlook. *Reports on Progress in Physics*, 68(10), 2267–2336. https://doi.org/10.1088/0034-4885/68/10/R01

Rogalski, A. & Ciupa, R. (1999). Performance limitation of short wavelength infrared InGaAs and HgCdTe photodiodes. *Journal of Electronic Materials*, 28(6), 630–636. https://doi.org/10.1007/s11664-999-0046-6

Roth, L., Hund, A., & Aasen, H. (2018). PhenoFly Planning Tool: Flight planning for high-resolution optical remote sensing with unmanned areal systems. *Plant Methods*, 14(1). https://doi.org/10.1186/s13007-018-0376-6

Rouse, W., Haas, R. H., Schell, J. A., & Deering, D. W. (1974). Monitoring vegetation systems in the Great Plains with ERTS. *Third Earth Resources Technology Satellite-1 Symposium (NASA SP-351)*, 309–317.

Saiz-Rubio, V. & Rovira-Más, F. (2020). From Smart Farming towards Agriculture 5.0: A Review on Crop Data Management. *Agronomy*, 10(2), 207. https://doi.org/10.3390/agronomy10020207

SenseFly (2022). *senseFly – The Professional's Mapping Drone*. https://www.sensefly.com/. Last accessed on 18 January 2022.

Serrano, L., Peñuelas, J., & Ustin, S. L. (2002). Remote sensing of nitrogen and lignin in Mediterranean vegetation from AVIRIS data: Decomposing biochemical from structural signals. *Remote Sensing of Environment*, 81(2), 355–364. https://doi.org/10.1016/S0034-4257(02)00011-1

SHALOM (2022). *The Shalom Mission*. https://www.space.gov.il/en/research-and-development/1144. Last accessed on 02 February 2022.

Shi, X., Han, W., Zhao, T., & Tang, J. (2019). Decision Support System for Variable Rate Irrigation Based on UAV Multispectral Remote Sensing. *Sensors*, 19(13), 2880. https://doi.org/10.3390/s19132880

Shukla, P., Skea, J., Calvo Buendia, E., Masson-Delmotte, V., Portner, H., Roberts, D., Zhai, P., Slade, R., Connors, S., Van Diemen, R., et al. (2019). *IPCC, 2019: Summary for Policymakers. In: Climate Change and Land: An IPCC Special Report on Climate Change, Desertification, Land Degradation, Sustainable Land Management, Food Security, and Greenhouse Gas Fluxes in Terrestrial Ecosystems*. Intergovernmental Panel on Climate Change (IPCC).

Sims, D. A. & Gamon, J. A. (2002). Relationships between leaf pigment content and spectral reflectance across a wide range of species, leaf structures and developmental stages. *Remote Sensing of Environment*, 81(2), 337–354. https://doi.org/10.1016/S0034-4257(02)00010-X

Singh, K. K. & Frazier, A. E. (2018). A meta-analysis and review of unmanned aircraft system (UAS) imagery for terrestrial applications. *International Journal of Remote Sensing*, 39(15-16), 5078–5098. https://doi.org/10.1080/01431161.2017.1420941

Smith, G. M. & Milton, E. J. (1999). The use of the empirical line method to calibrate remotely sensed data to reflectance. *International Journal of Remote Sensing*, 20(13), 2653–2662. https://doi.org/10.1080/014311699211994

Snavely, N., Seitz, S. M., & Szeliski, R. (2006). Photo Tourism: Exploring Photo Collections in 3D. 25(3), 835–846. https://doi.org/10.1145/1141911.1141964

Solymosi, K., Kövér, G., & Romvári, R. (2019). The Progression of Vegetation Indices: A Short Overview. *Acta Agraria Kaposváriensis*, 23(1), 75–90. https://doi.org/10.31914/aak.2264

Sony (2022). *SenSWIR Image Sensor*. https://www.sony-semicon.co.jp/e/products/IS/industry/technology/swir.html. Last accessed on 10 January 2022.

Stafford, J. V. (2000). Implementing Precision Agriculture in the 21st Century. *Journal of Agricultural Engineering Research*, 76(3), 267–275. https://doi.org/10.1006/jaer.2000.0577

Stark, B., McGee, M., & Chen, Y. (2015). Short wave infrared (SWIR) imaging systems using small Unmanned Aerial Systems (sUAS). *2015 International Conference on Unmanned Aircraft Systems (ICUAS)*, 495–501. https://doi.org/10.1109/ICUAS.2015.7152328

Stars Project (2022). *Multispectral and panchromatic images*. https://www.stars-project.org/en/knowledgeportal/magazine/remote-sensing-technology/introduction/multispectral-and-panchromatic-images/. Last accessed on on 05 January 2021.

Stemmler, S. (2021). Development of a high-speed, high-resolution multispectral camera system for airborne applications. *Multimodal Sensing and Artificial Intelligence: Technologies and Applications II*, volume 11785, 233–236. https://doi.org/10.1117/12.2591990

Sugiura, R., Noguchi, N., & Ishii, K. (2005). Remote-sensing Technology for Vegetation Monitoring using an Unmanned Helicopter. *Biosystems Engineering*, 90(4), 369–379. https://doi.org/10.1016/j.biosystemseng.2004.12.011

Sun, Z., Wang, X., Wang, Z., Yang, L., Xie, Y., & Huang, Y. (2021). UAVs as remote sensing platforms in plant ecology: Review of applications and challenges. *Journal of Plant Ecology*, (rtab089). https://doi.org/10.1093/jpe/rtab089

Suomalainen, J., Hakala, T., Alves de Oliveira, R., Markelin, L., Viljanen, N., Näsi, R., & Honkavaara, E. (2018). A Novel Tilt Correction Technique for Irradiance Sensors and Spectrometers On-Board Unmanned Aerial Vehicles. *Remote Sensing*, 10(12), 2068. https://doi.org/10.3390/rs10122068

Swissdrones (2022). *Swissdrones – Long-range VTOL UAV*. https://www.swissdrones.com/. Last accessed on 18 January 2022.

Tattaris, M., Reynolds, M. P., & Chapman, S. C. (2016). A Direct Comparison of Remote Sensing Approaches for High-Throughput Phenotyping in Plant Breeding. *Frontiers in Plant Science*, 7. https://www.frontiersin.org/article/10.3389/fpls.2016.01131

Tetracam (2020). *Tetracam Micro-MCA Multispectral Camera Array*. https://www.tetracam.com/Products-Micro_MCA.htm. Last accessed on 05 November 2021.

The Royal Society (2009). *Reaping the Benefits Science and the Sustainable Intensification of Global Agriculture*. The Royal Society.

Thenkabail, P. S., Lyon, J. G., & Huete, A. (2018). Advances in hyperspectral remote sensing of vegetation and agricultural crops. *Fundamentals, Sensor Systems, Spectral Libraries, and Data Mining for Vegetation*, 3–37. CRC Press.

Thenkabail, P. S., Lyon, J. G., & Huete, A. (2019). *Hyperspectral Remote Sensing of Vegetation*. CRC Press.

Thenkabail, P. S., Mariotto, I., Gumma, M. K., Middleton, E. M., Landis, D. R., & Huemmrich, K. F. (2013). Selection of hyperspectral narrowbands (hnbs) and composition of hyperspectral twoband vegetation indices (HVIS) for biophysical characterization and discrimination of crop types using field reflectance and hyperion/EO-1 data. *IEEE Journal of Selected Topics in Applied Earth Observations and Remote Sensing*, 6(2), 427–439. https://doi.org/10.1109/JSTARS.2013.2252601

Thompson, L. J. & Puntel, L. A. (2020). Transforming Unmanned Aerial Vehicle (UAV) and Multispectral Sensor into a Practical Decision Support System for Precision Nitrogen Management in Corn. *Remote Sensing*, 12(10), 1597. https://doi.org/10.3390/rs12101597

Thorlabs (2022). *NIR Bandpass & Laser Line Filters: 700 - 1650 nm Center Wavelength*. https://www.thorlabs.com/newgrouppage9.cfm?objectgroup_id=1000. Last accessed on 07 January 2022.

Tretyakov, I., Shurakov, A., Perepelitsa, A., Kaurova, N., Svyatodukh, S., Zilberley, T., Ryabchun, S., Smirnov, M., Ovchinnikov, O., & Goltsman, G. (2019). Room Temperature Silicon Detector for IR Range Coated with Ag2S Quantum Dots. *physica status solidi (RRL) – Rapid Research Letters*, 13(9), 1900187. https://doi.org/10.1002/pssr.201900187

Tretyakov, I., Svyatodukh, S., Perepelitsa, A., Ryabchun, S., Kaurova, N., Shurakov, A., Smirnov, M., Ovchinnikov, O., & Goltsman, G. (2020). Ag2S QDs/Si Heterostructure-Based Ultrasensitive SWIR Range Detector. *Nanomaterials*, 10(5), 861. https://doi.org/10.3390/nano10050861

Triggs, B., McLauchlan, P. F., Hartley, R. I., & Fitzgibbon, A. W. (2000). Bundle Adjustment — A Modern Synthesis. *Vision Algorithms: Theory and Practice*, volume 1883, 298–372. Springer Berlin Heidelberg. https://doi.org/10.1007/3-540-44480-7_21

Trimble (2022). *Trimble Inpho | Trimble Geospatial*. https://de.geospatial.trimble.com/products-and-solutions/inpho. Last accessed on 02 February 2022.

Tsouros, D. C., Bibi, S., & Sarigiannidis, P. G. (2019). A Review on UAV-Based Applications for Precision Agriculture. *Information*, 10(11), 349. https://doi.org/10.3390/info10110349

Tucker, C. J. (1979). Red and photographic infrared linear combinations for monitoring vegetation. *Remote Sensing of Environment*, 8(2), 127–150. https://doi.org/10.1016/0034-4257(79)90013-0

Turner, D., Lucieer, A., & Watson, C. (2012). An Automated Technique for Generating Georectified Mosaics from Ultra-High Resolution Unmanned Aerial Vehicle (UAV) Imagery, Based on Structure from Motion (SfM) Point Clouds. *Remote Sensing*, 4(5), 1392–1410. https://doi.org/10.3390/rs4051392

Turner, D. G., Bakker, T. C., Dixon, P., & Ettenberg, M. H. (2008). The development of, and applications for, extended response (0.7 to 1.7μm) InGaAs focal plane arrays. 6940, 694037. https://doi.org/10.1117/12.779865

Ullman, S. (1979). The interpretation of structure from motion. *Proc. R. Soc. Lond. B*, 203(1153), 405–426. https://doi.org/10.1098/rspb.1979.0006

Uni Bonn (2022a). *Boden Campus Klein-Altendorf — Landwirtschaftliche Fakultät Universität Bonn*. https://www.aussenlabore.uni-bonn.de/cka/de/standort/copy_of_standortbeschreibung. Last accessed on 21 January 2022.

Uni Bonn (2022b). *Klima Campus Klein-Altendorf — Landwirtschaftliche Fakultät Universität Bonn*. https://www.aussenlabore.uni-bonn.de/cka/de/standort/wetterdaten. Last accessed on 21 January 2022.

van der Meer, F. & de Jong, S. M., editors (2001). *Imaging Spectrometry: Basic Principles and Prospective Applications* (fourth ed.). Springer Science & Business Media.

van Leeuwen, W. J. D. (2009). Visible, Near-IR, and Shortwave IR Spectral Characteristics of Terrestrial Surfaces. *The SAGE Handbook of Remote Sensing*, 32–50. SAGE Publications, Inc. https://doi.org/10.4135/9780857021052.n3

Vaughan, J. M. (1989). *The Fabry-Perot Interferometer: History, Theory, Practice and Applications* (first ed.). Routledge. https://doi.org/10.1201/9780203736715

Vermeiren, J. P. & Merken, P. (2017). InGaAs detectors and FPA's for a large span of applications: Design and material considerations. *International Conference on Space Optics — ICSO 2014*, volume 10563, 306–312. https://doi.org/10.1117/12.2304272

Verrelst, J., Malenovský, Z., Van der Tol, C., Camps-Valls, G., Gastellu-Etchegorry, J.-P., Lewis, P., North, P., & Moreno, J. (2019). Quantifying Vegetation Biophysical Variables from Imaging Spectroscopy Data: A Review on Retrieval Methods. *Surveys in Geophysics*, 40(3), 589–629. https://doi.org/10.1007/s10712-018-9478-y

VisualSFM (2022). *VisualSFM : A Visual Structure from Motion System - Documentation*. http://ccwu.me/vsfm/doc.html. Last accessed on 19 January 2022.

Walter, A., Finger, R., Huber, R., & Buchmann, N. (2017). Opinion: Smart farming is key to developing sustainable agriculture. *Proceedings of the National Academy of Sciences*, 114(24), 6148–6150. https://doi.org/10.1073/pnas.1707462114

Wang, C. & Myint, S. W. (2015). A Simplified Empirical Line Method of Radiometric Calibration for Small Unmanned Aircraft Systems-Based Remote Sensing. *IEEE Journal of Selected Topics in Applied Earth Observations and Remote Sensing*, 8(5), 1876–1885. https://doi.org/10.1109/JSTARS.2015.2422716

Wang, H., Yu, Y., You, S., Meng, J., Muska, M., Li, Q., & Yang, Q. (2021). Low-Temperature Growth of High-Quality Ag2HgS2 Crystals for Setup of Weak-Light UV–Visible–NIR Photodetectors. *Advanced Optical Materials*, 9(10), 2002080. https://doi.org/10.1002/adom.202002080

Wang, L. & Wei, Y. (2016). Revised normalized difference nitrogen index (NDNI) for estimating canopy nitrogen concentration in wetlands. *Optik*, 127(19), 7676–7688. https://doi.org/10.1016/j.ijleo.2016.05.115

Wang, P., Xia, H., Li, Q., Wang, F., Zhang, L., Li, T., Martyniuk, P., Rogalski, A., & Hu, W. (2019). Sensing Infrared Photons at Room Temperature: From Bulk Materials to Atomic Layers. *Small*, 15(46), 1904396. https://doi.org/10.1002/smll.201904396

Weik, M. H. (2001). Full-width at half-maximum. *Computer Science and Communications Dictionary*, 661–661. Springer US. https://doi.org/10.1007/1-4020-0613-6_7770

Westoby, M., Brasington, J., Glasser, N., Hambrey, M., & Reynolds, J. (2012). 'Structure-from-Motion' photogrammetry: A low-cost, effective tool for geoscience applications. *Geomorphology*, 179, 300–314. https://doi.org/10.1016/j.geomorph.2012.08.021

Wingtra (2022). *Wingtra – The professional VTOL drone for mapping and surveying*. https://wingtra.com/. Last accessed on 18 January 2022.

Witschi, H. (2000). Fritz Haber: December 9, 1868-January 29, 1934. *Toxicology*, 149(1), 3–15. https://doi.org/10.1016/s0300-483x(00)00227-4

Yue, J., Feng, H., Yang, G., & Li, Z. (2018). A Comparison of Regression Techniques for Estimation of Above-Ground Winter Wheat Biomass Using Near-Surface Spectroscopy. *Remote Sensing*, 10(1), 66. https://doi.org/10.3390/rs10010066

Zecha, C. W., Link, J., & Claupein, W. (2013). Mobile sensor platforms: Categorisation and research applications in precision farming. *Journal of Sensors and Sensor Systems*, 2(1), 51–72. https://doi.org/10.5194/jsss-2-51-2013

Zhang, C. & Kovacs, J. M. (2012). The application of small unmanned aerial systems for precision agriculture: A review. *Precision Agriculture*, 13(6), 693–712. https://doi.org/10.1007/s11119-012-9274-5

Zhang, Y., Xia, C., Zhang, X., Cheng, X., Feng, G., Wang, Y., & Gao, Q. (2021). Estimating the maize biomass by crop height and narrowband vegetation indices derived from UAV-based hyperspectral images. *Ecological Indicators*, 129, 107985. https://doi.org/10.1016/j.ecolind.2021.107985

Zhou, X., Kono, Y., Win, A., Matsui, T., & Tanaka, T. S. T. (2021). Predicting within-field variability in grain yield and protein content of winter wheat using UAV-based multispectral imagery and machine learning approaches. *Plant Production Science*, 24(2), 137–151. https://doi.org/10.1080/1343943X.2020.1819165

Zorabedian, P. (1995). 8 - Tunable External-Cavity Semiconductor Lasers. *Tunable Lasers Handbook*, Optics and Photonics, 349–442. Academic Press. https://doi.org/10.1016/B978-012222695-3/50009-X

A | Author's Contribution Chapter 3

Titel	Development of a VNIR/SWIR Multispectral Imaging System for Vegetation Monitoring with Unmanned Aerial Vehicles
Autoren	Alexander Jenal Georg Bareth Andreas Bolten Caspar Kneer Immanuel Weber Jens Bongartz
Status	online veröffentlicht am 13. Dezember 2019
Journal	MDPI Sensors
Jahr	2019
Band	19
Ausgabe	24
Artikel-nummer	5507
DOI	`https://doi.org/10.3390/s19245507`
Eigenanteil	- Konzeption und Entwicklung des Kamerasystems (komplett) - Aufbau des Kamerasystems (komplett) - Adaption des Kamerasystems an UAV - Datenaufnahme (Klimakammer, Spektrallabor, Testflug) - Datenauswertung (komplett) - Verfassen des Manuskriptes (Hauptautor) - Erstellung von Abbildungen und Tabellen (komplett) - Review/ Überarbeitung des Manuskriptes

B | Author's Contribution Chapter 4

Titel	Investigating the Potential of a Newly Developed UAV-based VNIR/ SWIR Imaging System for Forage Mass Monitoring
Autoren	Alexander Jenal Ulrike Lussem Andreas Bolten Martin Leon Gnyp Jürgen Schellberg Jörg Jasper Jens Bongartz Georg Bareth
Status	online veröffentlicht am 28. Oktober 2020
Journal	PFG – Journal of Photogrammetry, Remote Sensing and Geoinformation Science
Jahr	2020
Ausgabe, Seiten	88, 493–507
DOI	`https://doi.org/10.1007/s41064-020-00128-7`
Eigenanteil	- Konzeption und Design der Studie (teilweise) - Datenaufnahme bei Feldkampagne (Sensorseitig) - Datenaufbereitung und -prozessierung Kamerasystem (komplett) - Datenanalysen und -auswertungen (komplett) - Verfassen des Manuskriptes (Hauptautor) - Erstellung von Abbildungen und Tabellen (ausgenommen Abbilung 4.2) - Review/ Überarbeitung des Manuskriptes (komplett)

C | Author's Contribution Chapter 5

Titel	Investigating the Potential of a Newly Developed UAV-Mounted VNIR/SWIR Imaging System for Monitoring Crop Traits—A Case Study for Winter Wheat
Autoren	Alexander Jenal Hubert Hüging Hella Ellen Ahrends Andreas Bolten Jens Bongartz Georg Bareth
Status	online veröffentlicht am 27.04.2021
Journal	MDPI Remote Sensing
Jahr	2021
Band	13
Ausgabe	9
Artikel-nummer	1697
DOI	https://doi.org/10.3390/rs13091697
Eigenanteil	- Konzeption und Design der Studie (teilweise) - Datenaufnahme bei Feldkampagne (Sensorseitig, komplett) - Datenaufbereitung und -prozessierung Kamerasystem (komplett) - Datenanalysen und -auswertungen (komplett) - Verfassen des Manuskriptes (Hauptautor) - Erstellung von Abbildungen und Tabellen (ausgenommen Abbildung 5.3, Abbildung 5.2, teilweise) - Review/ Überarbeitung des Manuskriptes